GEORGIA INSTITUTE OF TECHNOLOGY — OFFICE OF CONTRACT ADMINISTRATION

PROJECT ADMINISTRATION DATA SHEET

[X] ORIGINAL [ ] REVISION NO. _____

Project No. E-25-~~M01~~ 10 (R6170-0A0) GTRC/~~GXX~~ DATE 7 / 24 / 86

Project Director: D.L. McDowell School/~~Lab~~ ME

Sponsor: National Science Foundation

Type Agreement: Grant #MSM-8601889

Award Period: From 7/1/86 To 12/31/88 * (Performance) 3/31/89 (Reports)

Sponsor Amount:	This Change	Total to Date
Estimated: $		$ 115,393
Funded: $		$ 115,393

Cost Sharing Amount: $ 35,970 Cost Sharing No: G-35-333

Title: Extension of State Variable Theories of High Temperature Multiaxial Cyclic Loading

ADMINISTRATIVE DATA OCA Contact John B. Schonk X-4820

1) Sponsor Technical Contact:

A. Thirumalai
National Science Foundation
ENG/MSM
Washington, DC 20550

202/357-9542

2) Sponsor Admin/Contractual Matters:

Joe Carrabino
National Science Foundation
DGC/ENG
Washington, DC 20550

202/357-9602

Defense Priority Rating: N/A Military Security Classification: N/A

(or) Company/Industrial Proprietary: N/A

RESTRICTIONS

See Attached NSF Supplemental Information Sheet for Additional Requirements.

Travel: Foreign travel must have prior approval – Contact OCA in each case. Domestic travel requires sponsor approval where total will exceed greater of $500 or 125% of approved proposal budget category.

Equipment: Title vests with GIT

COMMENTS:

*Includes 6 month unfunded flexibility period

No Funds may be expended after 12/31/88

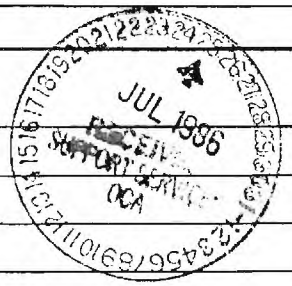

COPIES TO:

SPONSOR'S I. D. NO. 02.107.000.86R30

Project Director	Procurement/EES Supply Services	GTRC
Research Administrative Network	Research Security Services	Library
Research Property Management	Reports Coordinator (OCA)	Project File
Accounting	Research Communications (2)	Other A. Jones

88

GEORGIA INSTITUTE OF TECHNOLOGY
OFFICE OF CONTRACT ADMINISTRATION

NOTICE OF PROJECT CLOSEOUT

Date 6/23/89

ject No. E-25-M10 Center No. _____

ject Director D. L. McDowell School/Lab ME

nsor National Science Foundation

tract/Grant No. MSM - 8601889 GTRC XX GIT ____

me Contract No. _____

le Extension of State Variable Theories of High Temperature Multiaxial Cyclic Loading

ective Completion Date 12/31/88 (Performance) 3/31/89 (Reports)

seout Actions Required:

_ None
_ Final Invoice or Copy of Last Invoice
_ Final Report of Inventions and/or Subcontracts
_ Government Property Inventory & Related Certificate
_ Classified Material Certificate
_ Release and Assignment
_ Other _____

ludes Subproject No(s). _____

project Under Main Project No. _____

tinues Project No. _____ Continued by Project No. _____

tribution:

Project Director
Administrative Network
Accounting
Procurement/GTRI Supply Services
Research Property Management
Research Security Services

X Reports Coordinator (OCA)
X GTRC
X Project File
X Contract Support Division (OCA)
___ Other _____

PROGRESS REPORT ON NSF GRANT NO. MSM-8601889

EXTENSION OF STATE VARIABLE THEORIES TO HIGH TEMPERATURE MULTIAXIAL CYCLIC LOADING

Submitted to Division of Mechanics, Structures
and Materials Engineering

National Science Foundation
1800 G. Street, N.W.
Washington, D.C. 20550

September 1987

Submitted by

DAVID L. MCDOWELL

Associate Professor
The George W. Woodruff School of Mechanical Engineering
Georgia Institute of Technology
Atlanta, GA 30332

Strides have been made during the first year in both theoretical and experimental aspects of the proposed program. In summary, these accomplishments are as follows:

(i) the couching of bounding surface theory, previously applied accurately to the problem of multiaxial inelastic deformation of rate-independent metals, within the context of rate-dependent, viscoplastic behavior;

(ii) multiaxial cyclic viscoplasticity theory coupled with anisotropic creep damage;

(iii) baseline uniaxial tests on high temperature metals;

(iv) the set-up of high temperature multiaxial testing capability;

(v) student involvement; and

(vi) refereed papers and presentations.

It should be noted that two distinctive high temperature materials have been selected for this study. Type 304 stainless steel has been selected on the basis of the rather extensive existing uniaxial database and relevance to the power industry; it is a ductile, tough, low strength material at the temperature of interest, 600°C. In contrast, Waspaloy is a γ-γ' strengthened Ni-base superalloy which exhibits rather high strength levels but is significantly rate-sensitive at 650°C; in addition, this material is rather well-characterized uniaxially at this temperature. It is somewhat of a model material for studying behavior of Ni-base superalloys in the sense that its practical upper-use temperature is in the vicinity of 650-700°C. This enables studies of deformation response with more accurate control of temperature in the gage section than would be obtained with higher temperature Ni-base superalloys. The stainless steel has been procured and biaxial specimens are currently being machined. Waspaloy will be procured and machined pending verification of the

biaxial specimen design with type 304 stainless steel specimens; feedback is also being sought from NASA.

Each of the six items listed above is discussed next in more detail.

(i) Viscoplastic Bounding Surface Theory

A rate-dependent bounding surface model was developed in an effort to generalize unified creep-plasticity models to a theoretical framework which has successfully correlated cyclic stress-strain response under multiaxial nonproportional loading. It was shown that the presence of a dynamic recovery term in the backstress evolution equation is necessary for compatibility with a bounding surface approach. The bounding surface approach was further refined by (a) generalization of the concept of the image point for kinematic hardening, (b) rate-dependence of the direct hardening coefficient in the backstress evolution equation as motivated by viscous dislocation mechanics, and (c) introduction of nonlinear kinematic hardening with dependence on the instantaneous distance to the bounding surface. Development (b) above essentially admits a rate-dependent bounding surface radius.

This rate-dependent bounding surface model is in essence a generalization of some of the more accurate viscoplastic overstress models which have been developed largely in association with NASA and NSF sponsored programs in the last decade. This framework will be examined in some detail from an experimental perspective in the second year of this grant.

(ii) Coupling with Anisotropic Continuum Damage Mechanics

A coupling between a rate-dependent bounding surface theory and an anisotropic continuum creep damage approach has been developed jointly with NSF and Martin-Marietta (ORNL) support. The coupling assumes small cavity volume fraction, i.e. an

isotropic effect of damage on inelastic deformation, and incorporates description of tertiary creep and rupture.

(iii) **Baseline Uniaxial Testing**

Uniaxial baseline tests have to date been conducted on type 304 stainless steel at 600°C. Tests have included cyclic deformation, strain-controlled stress relaxation, monotonic tests with hold periods, and load-controlled rachetting. Additionally, complex computer-controlled experiments have been conducted which involve cycling at several strain rates with periodic strain hold periods to study the validity of overstress approaches.

(iv) **High-Temperature Multiaxial Testing**

A computer-controlled, high temperature axial-torsional load frame has been recently installed. We are in the process of determining optimal biaxial specimen design to maintain uniform temperature in the gage section. Also, previously developed software for control of complex, nonproportional strain-controlled tension-torsion histories is being modified to conform to the current hardware configuration and latest version of operating system for the PDP-11-23 computer. Significant experimental results on this system are anticipated in the next year for both materials under study.

(v) **Student Involvement**

Two Ph.D. students (one is also a Research Engineer) are currently supported at least partially by the program, and are involved in both the theoretical and experimental aspects. In addition, an M.S. student has been involved with the high temperature uniaxial baseline testing. The operation of the multiaxial testing laboratory is the responsibility of the

Research Engineer, R.L.T. Oehmke.

(vi) **Additional Funding**

NSF funded the original proposal at approximately a 50% level, indicating that requests for additional funds should be directed to other funding sources. The principal investigator has continued to pursue NASA funding in earnest, and has been informed by NASA that the additional funding is likely to be approved in Fall 1987. This will enable extension of the program and completion of original program goals within an additional 2-3 year time period.

(vii) **Papers and Presentations**

The following is a list of refereed papers related to bounding surface viscoplasticity which were produced/published or submitted during the first year of this grant (enclosed):

1. McDowell, D.L., Ho, Kwang-Il, and Stalley, J., "An Anisotropic, Damage-Coupled Viscoplastic Model for Creep-Dominated Cyclic Loading," presented at the ASTM Third Int. Symp. for Nonlinear Fracture Mechanics, October 1986 (accepted for publication in an ASTM STP).

2. McDowell, D.L. and Moosbrugger, J.C., "A Generalized Rate-Dependent Bounding Surface Model," to be presented at ASME Pressure Vessels and Piping Division Fall Conference, Knoxville, TN, October 1987.

3. McDowell, D.L., Ho, K., and Moosbrugger, J.C., "Continuum Damage Representation of Creep-Dominated, Nonproportional Cyclic Loading," to be presented at the Int. Seminar on High Temperature Fracture Mechanisms and Mechanics, Dourdan, France, October 1987.

The following related presentations were made:

1. "Creep-Dominated, Damage-Coupled Cyclic Viscoplasticity," Oak Ridge National Laboratory, October 1986.

2. "Potential for Materials Characterization Using Multiaxial Nonproportional Testing," ASTM Spring Meeting of Subcommittee E9-04 on Instrumentation, Cincinnati, OH, April, 1987.

3. "Developments in Two Surface Plasticity Theory", Rensselaer Polytechnic Institute, September 22, 1987.

4. "Developments in Two Surface Plasticity Theory", Cornell University, September 23, 1987.

5. "Developments in Two Surface Plasticity Theory", Brown University, September 28, 1987.

David L. McDowell[1], Kwang-Il Ho[2] and James Stalley[3]

AN ANISOTROPIC, DAMAGE-COUPLED VISCOPLASTIC MODEL FOR CREEP-DOMINATED CYCLIC LOADING

ABSTRACT: There are many practical applications in the power and propulsion industries which involve sustained periods of loading at high temperatures with periodic unloading-reloading sequences. Such histories may often be regarded as creep-dominated when only a small number of unloading-reloading events occurs over the life of the component. Typically, thermal constraint additionally results in rotation of the principal stress axes with respect to fixed material axes in regions of stress and temperature gradients such as nozzle inlets. This rotation may produce anisotropic states of both creep damage and inelastic deformation. Such rotations also occur in the creep zone for an advancing creep crack, or if far-field tractions change nonproportionally. In this paper, a continuum creep damage approach is coupled with a rate-dependent bounding surface theory to correlate nonproportional, axial-torsional experiments conducted on thin-walled tubular specimens of type 304 stainless steel at 593°C. A directionally-dependent scalar damage distribution evolves as a second order, symmetric tensor for each unique set of principal stress axes for this material based on quantitative metallographic assessment of the damage distribution. A general higher order symmetric damage growth law is also introduced.

KEY WORDS: Multiaxial, creep, cyclic plasticity, nonproportional, damage mechanics.

---

[1] Assistant Professor, School of Mechanical Engineering, Georgia Institute of Technology, Atlanta, Georgia 30332.
[2] Graduate Student, School of Mechanical Engineering, Georgia Institute of Technology, Atlanta, Georgia 30332.
[3] Graduate Student, School of Materials Engineering, Georgia Institute of Technology, Atlanta, Georgia 30332.

INTRODUCTION

Creep rupture is an important failure mechanism in the power and propulsion industries. Though linear and nonlinear creep damage summation rules based on time fraction are useful design concepts, their link with evolution of physical damage is tenuous. When the creep damage, including cavity growth and triple point cracking, develops anisotropically, it is necessary to follow the evolution of both the magnitude and orientation of damage. Description of anisotropic creep damage is particularly important in cases where the principal stresses rotate with respect to a material coordinate system during the creep history due to unloading-reloading thermal constraint, a change in geometry (e.g. crack extension), or a nonproportional change in applied tractions.

In this study, a formulation for anisotropic continuum creep damage is developed motivated from earlier work by Murakami and Ohno [1-2] and by Leckie and Onat [3]. The damage theory is coupled with a unified, two surface cyclic viscoplasticity formulation suitable for both nonproportional cyclic plasticity and creep. Axial torsional experiments on tubular type 304 stainless steel specimens were conducted at ORNL (Oak Ridge National Laboratory) at 593°C. Type 304 stainless steel was selected on the basis of its usage as a cladding material in the nuclear industry. First, the nature of the damage field is ascertained for both proportional and nonproportional creep loading histories from quantitative metallography on sectioned specimens. Then, the coupled damage and deformation models are presented, followed by correlation with nonproportional creep experiments.

STUDIES OF DAMAGE DISTRIBUTION

The tubular tension-torsion specimens from several experiments were sectioned to quantitatively determine the damage distribution. The intent of these measurements is an aid in development of the anisotropic damage rate equation. In this section, it will be shown that a second order tensor damage distribution is adequate for proportional loading (fixed principal stress directions). Later sections will delve into more detail of the experiments; this section will serve as experimental motivation of the damage growth law to be offered later. The coordinate system in the specimen mid-plane for computation of the damage distribution is shown in Fig. 1.

It has already been established that physical damage should be represented by an even rank tensor (c.f. Leckie and Onat [3]). It is possible to represent the magnitude of the damage distribution as a vector function on the unit sphere. Defining this function as ω,

$$\underset{\sim}{\omega}(\underset{\sim}{n}) = \frac{1}{S_g(\underset{\sim}{n})} \int_V dS_{gd}(\underset{\sim}{n}) \tag{1}$$

where $\underset{\sim}{n}$ is a unit vector, $S_g(\underset{\sim}{n})$ is the total grain boundary area in volume V, associated with unit normal vector $\underset{\sim}{n}$ and $dS_{gd}(\underset{\sim}{n})$ is the differential wedge cracked or cavitated grain boundary area associated with unit normal vector $\underset{\sim}{n}$. In the plane of the specimen wall, the distribution $\omega(\underset{\sim}{n})$ can be estimated from a micrograph as

$$\underset{\sim}{\omega}(\underset{\sim}{n}) = \frac{1}{L_g(\underset{\sim}{n})} \sum_{k=1}^{N} L_{gd}(\underset{\sim}{n})^{(k)} \tag{2}$$

where $L_g(\underset{\sim}{n})$ is the total grain boundary length in the micrograph associated with unit vector $\underset{\sim}{n}$, $L_{gd}(\underset{\sim}{n})^{(k)}$ is the length of the k^{th} damaged grain boundary segment in the micrograph perpendicular to $\underset{\sim}{n}$, and N is the total number of such segments in the micrograph. It must be emphasized that equation (2) is approximate since a micrograph reflects only the intersection of damaged grain boundary facets with a planar surface; there is an inherent assumption that the orientation distribution of damaged facets realizes its mean value in the plane of the specimen wall. Under the assertion of symmetry of ω,

$$\omega(\underset{\sim}{n}) = \omega(-\underset{\sim}{n}) \tag{3}$$

so that only two quadrants of the x_1x_2 coordinate system in Fig. 1 need be mapped.

It is desirable to obtain a representative sample of grains for quantitative damage measurement to ensure reliable results. To include a sufficient sample size of grain boundaries, a magnification of 200X was used for determining the wedge crack or microcrack damage distribution.

Sections were taken at two locations each at the inside and outside specimen diameter. At each section three to five different locations were photographed to provide a suitable sample lot. All sections were taken in the specimen gage section, but not in the immediate proximity of the final rupture crack.

Computer programs were written for a Weiss Videoplan to allow the user to move the cursor along grain boundaries and to mark wedge cracks or cavitated segments. The results were immediately digitized on floppy disk. Post-processing programs were written to convert the raw data in the wedge crack or cavity files to print to any output file the grain boundary segment length, fraction wedge cracked or cavitated, and the normal vector to the segment. All grain boundary segments in a

number of micrographs were digitized, regardless of whether or not any damage was present, resulting in a good statistical estimate of total grain boundary length at a given magnification. At rupture, wedge cracks on grain boundaries were readily apparent and measurable. Grain boundary cavitation, however, was not so accurately quantified because of grain boundary sliding and the small size of the cavities. Since wedge cracking is the dominant form of damage in the loading regime (stress level) of these specimens, the quantification of damage included only wedge cracks or microcracks. Although this underestimates the total damage, it is assumed that the directional distribution is representative of the total damage; this assumption was validated for a few specimens by digitization of r-type cavitated grain boundary facets at a magnification of 1000X. This result is reasonable since voids on grain boundaries may coalsce to form microcracks as rupture is approached.

The damage distribution ω is plotted for several histories in Figs. 2-3. For each history, arrows are drawn in the direction of the maximum principal stress. Several arrows appear for nonproportional histories with the associated time spent loading in each direction. All histories shown in Figs. 2-3 were associated with the same isochronous stress level. In these figures, the damage distribution is associated with discrete 15 degree increments; hence, each data point represents the contribution from microcracks oriented at $\pm$7.5 degrees from the stated angle. A smaller increment is not justified based on scatter in the data.

Referring to the proportional history GT-2, it is apparent that within the resolution of the data, a second rank tensor distribution is adequate for damage, i.e.

$$\omega(\underset{\sim}{n}) = \underset{\sim}{n}\cdot\underset{\sim}{D}\cdot\underset{\sim}{n} \qquad (4)$$

where

$$\underset{\sim}{D} = D_o(\eta\ \underset{\sim}{I} + (1-\eta)\ \underset{\sim}{n}^{(1)} \otimes \underset{\sim}{n}^{(1)}) \qquad (5)$$

$\underset{\sim}{I}$ is the identity tensor, η is the fraction of isotropic damage, $\underset{\sim}{n}^{(1)}$ is the unit vector in the direction of maximum principal stress, and $\otimes$ represents the outer product. An isotropic distribution of damage would not be as accurate for this case. A fourth or higher rank tensor is not warranted on the basis of this data. Here, D_o is the magnitude of the damage tensor in the maximum principal stress direction, i.e.

$$D_o = w(\underset{\sim}{n}^{(1)}) \qquad (6)$$

Note also that $\eta \simeq 0.61$ as determined by the fraction of damage perpendicular to $\underset{\sim}{n}^{(1)}$ compared to D_o. The second order tensor distribution with $\eta=0.61$ is plotted for history GT-2. This value of η was found in analysis of a ruptured uniaxial specimen, for which the principal axis of damage was found to be within 8° of the loading axis. It is seen in Figs. 2-3 that $\eta = 0.61$ is also acceptable for the biaxial damage distributions.

In experiment GT-2 shown in Fig. 2, the maximum principal stress direction is 16.7° clockwise from the specimen longitudinal axis shown in Fig. 1. In contrast, specimen GT-3 experienced a maximum principal stress rotation of 33.4° at 456 hours into the experiment and ruptured at a somewhat longer time. Due to the relatively large component of isotropic damage for this material, the damage distributions at rupture do not depart greatly from that of the symmetric, second rank tensor form in equation (5), even for nonproportional histories. This result is in part attributable to the relatively small rotations of the principal stress axis in these experiments. In the general case, there is no reason to expect a second rank tensor damage distribution to suffice, particularly for materials which damage quite anisotropically [3] such as copper.

DAMAGE GROWTH LAW

A second rank tensor damage rate equation for a constant isochronous stress level and isothermal conditions may be written as

$$\dot{\underset{\sim}{D}} = B(\sigma^*)^k(\underset{\sim}{\phi}:\underset{\sim}{\phi})^{\ell/2}\,[\eta\underset{\sim}{I} + (1-\eta)\sum_{j=1}^{3} M^{(j)}\underset{\sim}{n}^{(j)}\otimes\underset{\sim}{n}^{(j)}]\,\bar{M}^{(1)}$$

$$= \dot{D}_I\underset{\sim}{I} + \sum_{j=1}^{3}\dot{\underset{\sim}{D}}^{(j)}_{AN} \qquad (7)$$

where $\underset{\sim}{\sigma}$ is the Cauchy stress, B,k, ℓ and η are constants, $\underset{\sim}{n}^{(j)}$ is the unit vector in the j^{th} principal stress direction, and $M^{(j)}$ serves to apportion damage growth to multiple tensile principal stresses and is given by

$$M^{(j)} = \langle \underset{\sim}{n}^{(j)} \cdot \frac{\underset{\sim}{\sigma}}{|\sigma_j|} \cdot \underset{\sim}{n}^{(j)} \rangle \;; \quad \bar{M}^{(1)} = \langle \underset{\sim}{n}^{(1)} \cdot \frac{\underset{\sim}{\sigma}}{\sigma_{max}} \cdot \underset{\sim}{n}^{(1)} \rangle \qquad (8)$$

where $\sigma_{max} = \max_{i=1,2,3} |\sigma_i|$, σ_i are the ordered principal stresses,

and the Macauley bracket $\langle F \rangle = F$ if $F > 0$; $\langle F \rangle = 0$ otherwise. Factor $\bar{M}^{(1)}$ pertains only to rupture behavior for biaxial principal stress ratios less than -1. The scalar product is defined by $(\underset{\sim}{\phi}:\underset{\sim}{\phi}) = (\phi_{ij}\phi_{ij})$, and the outer product is denoted by $\otimes$.

The damage effect tensor $\underset{\sim}{\phi}$, as defined by Murakami and Ohno [1], is a generalization of the Kachanov-Rabotnov [4-5] scalar damage approach. In this work, unlike that of Murakami and Ohno, the damage effect tensor is based on a

damage distribution associated with a symmetric tensor of even but arbitrary rank rather than the second rank tensor obtained by integrating equation (7). This is thought to be more representative of the actual driving force for damage, which is not generally a second order tensor. The damage effect tensor is second rank and symmetric and is obtained heuristically from the damage distribution w in the current maximum principal stress direction in the following way:

$$\underset{\sim}{\phi} = (\underset{\sim}{I} - \underset{\sim}{D}^*(\underset{\sim}{n}^{(1)}))^{-1} \tag{9}$$

where

$$\underset{\sim}{D}^*(\underset{\sim}{n}^{(1)}) = w(\underset{\sim}{n}^{(1)}) \ (\eta \ \underset{\sim}{I} + (1-\eta) \ \underset{\sim}{n}^{(1)} \otimes \underset{\sim}{n}^{(1)}) \tag{10}$$

Finally, the isochronous stress σ^* is obtained from the work of Huddleston [6] as

$$\sigma^* = \frac{3}{2} S_1 \left(\frac{2}{3} \frac{\sigma_e}{S_1} \right)^a \exp\left[b \left(\frac{J_1}{S_s} - 1 \right) \right] \tag{11}$$

where

$$S_1 = \sigma_1 - \sigma_{kk}/3$$

$$\sigma_e = [(3/2) \ \underset{\sim}{s} : \underset{\sim}{s}]^{1/2}$$

$$\underset{\sim}{s} = \underset{\sim}{\sigma} - \frac{1}{3} \sigma_{kk} \underset{\sim}{I}$$

$$S_s = (\sigma_1^{\,2} + \sigma_2^{\,2} + \sigma_3^{\,2})^{1/2}$$

$$J_1 = \sigma_{kk}$$

This form of the isochronous stress has been rather thoroughly supported by a variety of biaxial creep experiments on tubular specimens of type 304 stainless steel at 593°C at ORNL, including axial tension, equi-biaxial tension (axial tension and pressure), internal pressure, torsion, axial tension and torsion, and axial compression and torsion. It should be noted that this form of σ^* was verified for loading magnitudes which would be expected to lead to matrix power law creep-governed grain boundary damage accumulation. For lower stress levels, it may be necessary to modify this form to account for coupled grain boundary diffusion-power law creep [7-9] mechanisms. For this study, however, the isochronous stress level selected is within the domain of power law creep. It should also be mentioned that the maximum principal stress, the effective stress, and the first invariant of stress are included in σ^*, just as in the isochronous stress definition forwarded by Leckie et al. [10-12].

The key element of the current approach which differs from second rank tensor damage models is the use of a symmetric, even rank tensorial growth rate for the damage distribution $\underset{\sim}{\omega}(\underset{\sim}{n})$ given by

$$\dot{\underset{\sim}{\omega}}(\underset{\sim}{n}) = \dot{D}_I + \sum_{j=1}^{3} (\underset{\sim}{n} \cdot \dot{\underset{\sim}{D}}_{AN}^{(j)} \cdot \underset{\sim}{n}) \, (\underset{\sim}{n} \cdot \underset{\sim}{n}^{(j)})^{2P} \qquad (12)$$

for P = 0 or any positive integer. Exponent P = 0 only if the actual damage distribution $\underset{\sim}{\omega}(\underset{\sim}{n})$ corresponds to that of a symmetric second order tensor. This is approximately the case for type 304 stainless steel at 593°C as discussed

earlier. For an isotropically damaging material with $\eta = 1$, the second term in equation (12) does not apply since the anisotropic component of the damage rate is zero. The results of Hayhurst et al. [12] for copper indicate a high degree of anisotropy, and hence a larger value of P. The second term in equation (12) maps the damage rate in up to three mutually orthogonal directions onto the direction of arbitrary unit vector $\underset{\sim}{n}$, and essentially performs the transformation of an even rank, symmetric, anisotropic damage rate tensor of order (2P+2) for each principal direction with associated positive principal stress.

Obviously, the nature of the integrated damage distribution $\omega(\underset{\sim}{n})$ will depend on whether the loading history was proportional or nonproportional and on the value of P. Rotation of the principal stress eigenvectors will in general result in multiple "peaks" in the damage distribution ω with respect to a fixed material coordinate system for $P > 0$. Use of a damage distribution as P increases involves some practical difficulties, however. The primary difficulty is the additional number of degrees of freedom necessary to represent the state of damage at a material point. Possible concessions to address this problem include use of a relatively small number of points on the unit sphere with some sort of interpolation scheme between points or assignment of uniform ω values to discrete segments of the unit sphere. In this work, the second alternative is selected, though the damage distribution is only second order. The work of Leckie [13] and Krajcinovic [14] in approximation of creep damage distributions as vector functions are noted.

It is important to realize that the damage rate distribution expressed in equation (12) does not imply that only principal stresses are effective driving forces for damage. Both the isotropic and anisotropic character of $\dot{\omega}$ reflect the contribution of shear stress with assisting normal tensile stress, constraint

earlier. For an isotropically damaging material with $\eta = 1$, the second term in equation (12) does not apply since the anisotropic component of the damage rate is zero. The results of Hayhurst et al. [12] for copper indicate a high degree of anisotropy, and hence a larger value of P. The second term in equation (12) maps the damage rate in up to three mutually orthogonal directions onto the direction of arbitrary unit vector $\underset{\sim}{n}$, and essentially performs the transformation of an even rank, symmetric, anisotropic damage rate tensor of order (2P+2) for each principal direction with associated positive principal stress.

Obviously, the nature of the integrated damage distribution $\omega(\underset{\sim}{n})$ will depend on whether the loading history was proportional or nonproportional and on the value of P. Rotation of the principal stress eigenvectors will in general result in multiple "peaks" in the damage distribution ω with respect to a fixed material coordinate system for $P > 0$. Use of a damage distribution as P increases involves some practical difficulties, however. The primary difficulty is the additional number of degrees of freedom necessary to represent the state of damage at a material point. Possible concessions to address this problem include use of a relatively small number of points on the unit sphere with some sort of interpolation scheme between points or assignment of uniform ω values to discrete segments of the unit sphere. In this work, the second alternative is selected, though the damage distribution is only second order. The work of Leckie [13] and Krajcinovic [14] in approximation of creep damage distributions as vector functions are noted.

It is important to realize that the damage rate distribution expressed in equation (12) does not imply that only principal stresses are effective driving forces for damage. Both the isotropic and anisotropic character of $\dot{\omega}$ reflect the contribution of shear stress with assisting normal tensile stress, constraint

between adjacent grains affected by relative orientation, extent of grain boundary sliding, etc. The magnitude of the principal stresses reflect the strength of driving forces, albeit shear and/or normal stress, or even coupled boundary diffusion-matrix creep damage growth at lower stress levels. Obviously, not all feasible damage mechanisms can be treated within the current framework, e.g. damage growth exclusively on maximum shear planes, although the most commonly reported, essential features of structurally significant behavior are captured. In this regard, it is possible that even the anisotropic character of the damage distribution is a function of isochronous stress level, i.e. $\eta = \eta(\sigma^*)$ and $P = P(\sigma^*)$, in accordance with different regimes of cavity growth mechanisms [7-9].

As stated earlier, equation (7) holds only for a constant isochronous stress level since constant values of B and ℓ imply that time fraction and damage (for proportional loading) are uniquely related; these restrictions cannot describe multiple isochronous stress level sequence effects (nonlinear damage accumulation) [15] if the rupture criterion is stress-independent. In this study, we will be concerned with experiments performed at constant isochronous stress and hence do not require stress-level dependence of ℓ, but such an extension offers no particular difficulty. To admit isochronous stress sequence effects, it is necessary to assign exponent ℓ as a function of σ^*. This is supported by experiments conducted by Chaboche et al. [15-16] in which the measured damage is observed to accumulate more slowly as a function of time fraction t/t_R as the isochronous stress level increases. The deleterious effects of low-high stress level sequences and the accumulation of greater physical damage under low stress than high stress conditions at the same time fraction are well documented [17].

Another key element of the damage formulation is the rupture criterion. Previous discussion has assumed that ω_{max} = constant at rupture. It is clear from

previous work [3,17] that the extent of creep damage just prior to the final rupture event depends on stress level, suggesting rupture critera of the following possible forms

$$R(\sigma_{max}, \Psi, \omega_{max}) = 0 \tag{13}$$

or

$$\max_{\text{all } \underset{\sim}{n}} (\omega(\underset{\sim}{n})\underset{\sim}{n}\cdot\underset{\sim}{\sigma}\cdot\underset{\sim}{n}, \Psi) = \text{constant} \tag{14}$$

or

$$\int_{A_u} (\omega(\underset{\sim}{n})\underset{\sim}{n}\cdot\underset{\sim}{\sigma}\cdot\underset{\sim}{n})dA = \text{constant} \tag{15}$$

where the integration in equation (15) is performed over the unit sphere. In equations (13)-(14), Ψ is defined by

$$\Psi = \frac{1}{4\pi} \int_{A_u} \omega(\underset{\sim}{n})\, dA \tag{16}$$

and represents the mean value of the $\omega(\underset{\sim}{n})$ distribution. Clearly, Ψ is directly related to the first invariant of $\underset{\sim}{D}$ for proportional creep loading histories for P = 0. The relationship for such histories is given by

$$\Psi = D_{kk}/3 \tag{17}$$

For completely isotropic creep damage, $\eta = 1$, $\Psi = D_I$. It should be noted that $\dot{\Psi} = \dot{D}_{kk}/3$ independent of loading path if $P = 0$. It should also be noted that σ_{max} in equation (13) is the maximum tensile principal stress.

If one of the stress level-dependent rupture criteria stated in equations (13)-(15) is used, then the damage at rupture is not constant and the time fraction at any given damage level, even for constant ℓ, depends on the isochronous stress for proportional loading. The stress level-dependent rupture criteria approach is more difficult to implement since experimental investigation of the damage distribution at different stress levels is quite involved. Existing data are somewhat sketchy and incomplete. The logical approximation to the physically more precise stress level-dependent rupture criterion is the first approach, i.e. the assumption of a constant damage at failure. This approximation is most likely accurate, even for variable load histories, since the damage growth is highly nonlinear only near the final rupture event. Therefore, from a practical viewpoint, the use of a constant damage at rupture is likely to be sufficient, especially in view of the inherent scatter in creep rupture tests. Hence, the rupture criterion

$$\omega_{max} = \max_{\text{all } \underset{\sim}{n}} \omega(\underset{\sim}{n}) = 1 \qquad (18)$$

is selected in this work.

Another important consideration is that of aging or microstructural transformations which occur during the creep history. These aging effects may include grain boundary and/or matrix precipitation, precipitate growth, and microstructural coarsening. Furthermore, the rate of transformation observed during pre-aging events without stress or inelastic deformation does not

necessarily correspond to that observed in the presence of continued creep or cyclic deformation. In general, if low stress, long term creep rupture predictions are to be made on the basis of high stress, short term tests, then it is necessary to include these aging effects via proper description of precipitation/aging kinetics. This can be accomplished in micromechanical fashion by inclusion of explicit state variables representing precipitate size and spacing, for example, which couple with the damage rate. It may also be accomplished phenomenologically by modification of the damage rate coefficient and exponents to reflect aging. The addition of void nucleation sites associated with ongoing precipitation may assume the form of a sequence of delta functions in the damage rate equation.

Type 304 stainless steel does exhibit precipitation and growth of $M_{23}C_6$ carbides along grain boundaries at 593°C. In the present study, the aging effects in type 304 stainless steel at 593°C are not explicitly considered since the constants and parameters in the damage rate equation are fit to predominately uniaxial creep results at a given isochronous stress level; the model predictions are then obtained for multiaxial nonproportional test results at the same isochronous stress level and temperature starting from the same initial condition. Hence, aging effects are implicitly embedded in the model parameters. This is also true for the creep behavior in the viscoplasticity approach to be discussed in the next section. In the general case of widely varying isochronous stress levels or temperatures, aging kinetics must be explicitly considered. This is not the subject of this paper but indeed deserves the focus of parallel investigations.

Finally, it should be noted that under conditions of finite strain (e.g. large stretch and rotation), the damage distribution must evolve in reference to a

material coordinate system, necessitating an appropriate finite strain formulation.

DAMAGE-COUPLED, RATE-DEPENDENT PLASTICITY MODEL

To describe the rate-dependent, high-temperature creep-plasticity response for histories which involve both creep and cyclic plasticity, it is necessary to introduce a theory capable of modeling a wide range of behavior. For multiaxial cyclic plasticity, it has previously been demonstrated that a bounding surface approach [18-23] provides very good correlation of nonproportional deformation behavior. Since such behavior is of great concern to the current investigation, a new strain-hardening model based on a rate-dependent bounding surface with a Mroz translation rule for backstress is adopted. Key features of this theory include isotropic hardening reflected through growth of the backstress magnitude rather than a scalar parameter in the flow rule, and backstress magnitudes in creep and cyclic plasticity appreciably higher than those in conventional unified creep-plasticity models [c.f. 24-30] in accord with experimental results under nonproportional loading. Rate-dependence is reflected primarily through the bounding surface, strain-hardening is reflected through growth of the bounding surface, and smooth yielding response is obtained through use of the Mroz distance vector in the backstress hardening rate coefficient.

Briefly, the damage-coupled bounding surface model can be stated in multiaxial form as

$$\dot{\underset{\sim}{\epsilon}}^{n} = \frac{3}{2} K \langle \bar{\sigma}\mathcal{D} - K_o \rangle^{n} (\underset{\sim}{s} - \underset{\sim}{\alpha})/\bar{\sigma} \qquad (19)$$

where

$$\bar{\sigma} = [(3/2)(\underset{\sim}{s} - \underset{\sim}{\alpha}):(\underset{\sim}{s} - \underset{\sim}{\alpha})]^{1/2} = \sqrt{3/2}\ ||\underset{\sim}{s} - \underset{\sim}{\alpha}|| \tag{20}$$

$$\bar{\alpha} = [(3/2)\underset{\sim}{\alpha}:\underset{\sim}{\alpha}]^{1/2} \tag{21}$$

Here deviatoric stress $\underset{\sim}{s} = \underset{\sim}{\sigma} - (\sigma_{kk}/3)\underset{\sim}{I}$, and backstress $\underset{\sim}{\alpha}$ is deviatoric. The inelastic strain $\underset{\sim}{\varepsilon}^n$ includes both conventional creep and plastic strain as in other unified theories. The effective overstress and backstress are denoted as $\bar{\sigma}$ and $\bar{\alpha}$, respectively. Note that the effect of damage is reflected by a multiplicative factor $\mathscr{D}$ and the product $\bar{\sigma}\mathscr{D}$ can be thought of as a net stress although the term is somewhat loosely used here. As stated by Leckie [13], the influence of the damage tensor on the creep rate is isotropic and monotonically increasing, even into the tertiary regime. This has been demonstrated even for materials which damage in a highly anisotropic manner [12]. Furthermore, Murakami [2] has conducted a set of experiments on plates with intentional configurations of machined holes to approximate the anisotropic net section loss occurring in creep cavitation or wedge cracking processes and has found that the coupling between deformation and damage is related to the first invariant of damage. Hence, we define the factor $\mathscr{D}$ as

$$\mathscr{D} = 1 + C\,\Psi^m \tag{22}$$

where Ψ is defined in equation (16). Note that the effect of damage on the tertiary creep rate will remain unaltered upon rotation of the principal stress axes with this formulation as is experimentally observed. It should be that an auxiliary condition (i.e. rupture criterion) would have to be used with the current coupled equations to accomplish node release in a finite element creep

crack growth application.

The competition between hardening and recovery terms in the backstress rate equation is crucial in this bounding surface formulation and is expressed as

$$\mathscr{D}\dot{\underset{\sim}{\alpha}} = H(\bar{\alpha}\mathscr{D},\delta\ )||\dot{\underset{\sim}{\epsilon}}^{n}||\underset{\sim}{\nu} - R(\bar{\alpha}\mathscr{D})\underset{\sim}{\alpha}\mathscr{D} \tag{23}$$

where

$$H(\bar{\alpha}\mathscr{D},\delta\ ) = \beta_0 + \beta_1\exp(-\beta_4\langle 1 - \beta_3\left\{\frac{\delta}{K^*}\right\}\rangle^{\beta_5}) + \beta_2\exp(-\beta_6\bar{\alpha}^*) \tag{24}$$

$$\delta = \sqrt{3/2}\ ||\ \sqrt{2/3}\ \ K^*\underset{\sim}{N} - \underset{\sim}{s}\mathscr{D}||\ , \quad \underset{\sim}{N} = (\underset{\sim}{s} - \underset{\sim}{\alpha})/||\underset{\sim}{s} - \underset{\sim}{\alpha}|| \tag{25}$$

$$\bar{\alpha}^* = K^* - \delta - \bar{\sigma}\mathscr{D} \tag{26}$$

$$R(\bar{\alpha}\mathscr{D}) = \beta_7\exp(-\beta_8\bar{\alpha}\mathscr{D})(\bar{\alpha}\mathscr{D})^{\beta_9} \tag{27}$$

The radius of the bounding surface, K^*, evolves with accumulated plastic strain (creep hardening) and responds through the effective overstress to changes in inelastic strain rate, i.e.

$$K^* = \beta_{10}[K_{mf} - (K_{mf} - K_{mo})\exp(-\beta_{11}\bar{\epsilon}^{n})]\mathscr{D}[1 + \beta_{12}\bar{\sigma}^{\ \beta_{13}}] \tag{28}$$

where

$$\bar{\epsilon}^{n} = \int_0^t \sqrt{(2/3)\ \dot{\underset{\sim}{\epsilon}}^{n}:\dot{\underset{\sim}{\epsilon}}^{n}}\ dt' \tag{29}$$

The directional index for the backstress hardening rate is a rate-dependent Mroz form

$$\underset{\sim}{\nu} = \left[\frac{\sqrt{2/3}\, K^{*}\, \underset{\sim}{N} - s\underset{\sim}{\mathscr{D}}}{\sqrt{2/3}\, \delta} \right] \tag{30}$$

The bounding surface and the surface of constant dimension K_0 which prescribes elastic response are shown in Fig. 4 along with the vector $\underset{\sim}{\nu}$ in deviatoric space.

In this formulation, $K, K_0, n, C, m, \beta_0, \beta_1, \beta_2, \beta_3, \beta_4, \beta_5, \beta_6, \beta_7, \beta_8, \beta_9, \beta_{10}, \beta_{11}, \beta_{12}, \beta_{13}, K_{mo}$, and K_{mf} are isothermal material constants. Non-isothermal generalization can be achieved primarily by invoking temperature dependence of the backstress recovery term [27] and some of the constants, although this is not necessary in the current isothermal work. Note that K_0 does not evolve, resulting in a domination of the inelastic response by evolution of the backstress. This feature allows the overstress tensor to properly model inelastic strain rate direction for rapidly changing nonproportional loading directions or for a departure from a previous loading path for which steady state creep conditions were reached.

The hardening function which governs smooth transition from a very "stiff" region of backstress rate to an asymptotic response is the second term in equation (24) where the Mroz distance vector is normalized by bounding surface radius. Constants $\beta_1, \beta_4, \beta_5$, and β_3 govern this transition and are selected to match a monotonic, strain-controlled uniaxial test at a single strain rate in addition to a cyclic, strain-controlled uniaxial test at a single strain rate. The cyclic test is used primarily to determine β_3, which ensures that the normalization will be satisfactory for both monotonic and cyclic behavior. Constant β_0 describes asymptotic response and constants β_2 and β_6 are employed in a second order term to model the backstress level dependence of hardening rate observed experimentally

when hardening dominates recovery. Constants K_{mf}, K_{mo}, and β_{11} introduce strain hardening into the model and can be determined either from a uniaxial monotonic or cyclic test. Constants β_{10}, β_{12}, and β_{13} are determined from flow stress/strain rate sensitivity data at the temperature of interest; since strain rate sensitivity of K^* is directly related to that of stress in this model, these constants can be determined in a straightforward manner after the constants in the flow rule have been defined to fit a range of desired (observed) backstress behavior obtained from "dip" tests, multiaxial creep or cyclic plasticity experiments involving a sudden change in inelastic strain rate direction, etc. Constants C and m are determined by matching the integrated inelastic strain rate behavior with tertiary creep data; the work of Murakami [2] indicates that $m = 1$ is a good approximation for small volume fractions of damage but a power law ($m > 1$) may be necessary for larger volume fractions.

CORRELATIONS WITH EXPERIMENTAL DATA

Tension-torsion tests were conducted at ORNL on tubular specimens of type 304 stainless steel (ORNL Ref. heat 9T2796) at 593°C. The specimens were annealed at 1093°C for 30 minutes, and were subsequently air cooled at >100°C/min to room temperature. Refer to previous work by Huddleston [6] for further experimental details.

Since the effective rupture strains encountered in this study are less than 20% for most experiments, the assumption of small strains will be made with only small error. The axial strain is defined as the change in gage length divided by the original gage length. Engineering shear strain is obtained by dividing the

angle of twist by the gage length and multiplying by the mean radius. The axial and shear stresses are assumed uniform over the cross-section, the usual thin-walled assumption. In all that follows, all stresses will be considered nominal, i.e. second Piola-Kirchoff.

Determination of Constants:

i. Damage Growth Equation

Interrupted creep tests are generally necessary to assess exponent ℓ at a given isochronous stress level; ℓ can also be determined in an approximate way by periodically unloading from the creep curve [15] or by matching the integrated damage-coupled creep equations (19)-(30) with observed onset of tertiary response assuming m=1 in equation (22). The value m=1 arises from the Murakami study [2] mentioned earlier. Stress exponent k is easily identified as the slope of the $\log(t_R)$ vs. $\log(\sigma)$ curve obtained from uniaxial tests. Isotropic damage fraction η is identified as the ratio of the transverse damage to the longitudinal damage in a uniaxial test, and is identified by the quantitative metallographic techniques described earlier. Once k is known, coefficent B can be found at the isochronous stress level associated with ℓ by integrating and matching rupture times from uniaxial tests with the assumed rupture criterion $\omega_{max} = 1$.

For an isochronous stress of 176.1 MPa at 593°C, the constants are $B = 2.71 \times 10^{-28}$ sec^{-1} and $\ell = 4.8$. Units of stress and damage rate are MPa and sec^{-1}, respectively. Constants independent of isochronous stress include $k = 8.5551$ and $\eta = 0.61$. Exponent ℓ was estimated by matching the tertiary response of uniaxial tests with the integrated damage-coupled creep equations.

ii. Damage-Coupled Plasticity Equations

The general methodology of determining the constants is discussed in a previous section. Strain rate sensitivity data of Steichen [31] for annealed type 304 stainless steel was used to determine constants β_{10}, β_{12}, and β_{13}. Constant K_o selected as representative of initial yielding of the annealed material; constants K and n were selected on the basis of the relatively high ratio between backstress magnitude and deviatoric stress magnitude observed in nonproportional biaxial creep experiments by Oytana et al. [32] on a somewhat similar material. The high value of n results in the relatively small dependence of overstress on inelastic strain rate which was discussed earlier. Constants β_0, β_1, β_2, β_3, β_4, β_5, β_6, K_{mf}, K_{mo}, and β_{11} were determined from data obtained by Corum [33] on the same ORNL reference heat of annealed material at 593°C; a monotonic test and subsequent cyclic response at 8.33×10^{-5} sec^{-1} was used. The near-perfect agreement between the model and experiment displayed in Fig. 5 is a consequence of this fitting process. It should be noted, though, that not all unified creep-plasticity models are capable of this degree of representation of actual cyclic response. Constants β_7, β_8, and β_9 were determined after the hardening terms were established by fitting the secondary creep rate (without damage) versus stress relationship established from numerous uniaxial tests at ORNL at 593°C; in the uniaxial case, at steady state creep conditions, equality of hardening and recovery rates results in the expression (neglecting damage)

$$\frac{3}{2} H(\alpha, \delta) \dot{\epsilon}_{11}^{n} = \beta_7 \exp(-\beta_8 \alpha) \alpha^{(\beta_9 + 1)} \qquad (31)$$

from which the recovery constants were computed from three stress levels ranging

from 69 MPa to 241 MPa. Note the α in equation (31) is the uniaxial equivalent value.

As previously mentioned, the damage coefficient C in equation (22) was obtained with the assumption m = 1 by fitting the tertiary portion of the creep response. In summary, the material constants at 593°C for the damage-coupled creep-plasticity model are:

$K = 5\times10^{-48}$	$\beta_{10} = 0.00361$
$K_o = 13.8$	$\beta_{11} = 7.0$
$n = 30$	$\beta_{12} = 0.225$
$\beta_o = 1104$	$\beta_{13} = 1.91$
$\beta_1 = 6.9\times10^{6}$	$K_{mf} = 517$
$\beta_2 = 1044$	$K_{mo} = 145$
$\beta_3 = 1.18$	$C = 0.32$
$\beta_4 = 23.16$	$m = 1$
$\beta_5 = 1.25$	$\beta_8 = -0.0207$
$\beta_6 = 0.0196$	$\beta_9 = 5.088$
$\beta_7 = 1.552\times10^{-19}$	

where the units of stress are in MPa and time in sec.

To further illustrate the behavior of the model, monotonic and cyclic tests at different strain rates and creep tests at several stress levels are predicted in Figs. 5-6 at 593°C. Note the smooth yielding response in monotonic tests. The secondary creep rates in the creep tests are also quite accurate since the recovery function was determined for a wide range of stress levels.

iii. Correlation with Biaxial Creep Experiments

Model predictions and experimental data for four different biaxial creep experiments are shown in Figs. 7-11. In these figures, inelastic axial and shear strain components are plotted versus time in addition to the axial and shear stress history. It is noted that the rupture time is generally well-predicted in addition to the secondary and tertiary creep rates and inelastic strain upon initial loading. The rupture time for specimen GT-3 is underpredicted but is overpredicted for specimen GT-4A which was subjected to a similar nonproportional loading history. The inelastic behavior and rupture is well-predicted for proportionally loaded specimens GT-1 and GT-2. The correlation obtained for GT-6, a somewhat complex creep-dominated cyclic loading history, is excellent. In all these experiments, the isochronous stress was held constant at 176.15 MPa and the principal stress directions were rotated at some point(s) in the loading history.

CONCLUSIONS

The present study has demonstrated that anisotropic creep damage can be successfully treated within the framework of continuum damage mechanics, even for creep-dominated cyclic loading histories typical of nuclear components. Damage accumulation is predominately isotropic for type 304 stainless steel at 593°C, but the anisotropic component of damage has been identified by quantitative metallography and a general framework derived for any observed level of anisotropy. A scalar damage distribution has been introduced which evolves in

rate form as a symmetric second rank tensor for this material, but can be effectively extended via constant P to higher rank, even, symmetric tensors. A bounding surface cyclic viscoplasticity theory has been offered for the multiaxial creep-plasticity deformation, and damage has been directly incorporated. Good correlation of rupture time, secondary creep, and tertiary creep has been obtained for proportional and nonproportional, isothermal, constant isochronous nominal stress loading histories.

ACKNOWLEDGMENTS

The authors are grateful to Martin Marietta Energy Systems (ORNL Subcontract No. 19X-55966C; program manager Dr. R.L. Huddleston) for support in development of the anisotropic damage formulation. Support of the U.S. National Science Foundation (NSF MSM-8601889; MSM-8552714) in development of the rate-dependent cyclic viscoplasticity theory is also appreciated.

REFERENCES

1. Murakami, S., and Ohno, N., "A Continuum Theory of Creep and Creep Damage," Creep in Structures, IUTAM, 1980, pp. 422-444 (Eds. Ponter and Hayhurst).

2. Murakami, S., "Notion of Continuum Damage Mechanics and its Application to Anisotropic Creep Damage Theory," ASME J. of Engineering Materials and Technology, Vol. 105, April 1983, pp. 99-105.

3. Leckie, F. A., and Onat, E. T., "Tensorial Nature of Damage Measuring Internal Variables," Physical Non-Linearities in Structural Analysis, IUTAM, 1980, pp. 140-155 (Eds. Hult and Lemaitre).

4. Kachanov, L., Fundamental of Fracture Mechanics, Nauka, Moscow, 1974.

5. Rabotnov, Y. N., Creep Problems in Structural Members, Amsterdam, North Holland Publishing Co., 1969.

6. Huddleston, R. L., "An Improved Multiaxial Creep-Rupture Strength Criterion," ASME J. Pressure Vessels and Piping, Paper 84-PVP-106, 1984.

7. Miller, D. A., and Langdon, T. G., "Independent and Sequential Cavity Growth Mechanisms," Scripta Metallurgica, Vol. 14, 1980, pp. 143-148.

8. Svensson, L. E., and Dunlop, G. L., "Mechanisms for the Growth of Intergranular Creep Cavities," Creep in Structures, IUTAM, 1980, pp. 445-462 (Eds. Ponter and Hayhurst).

9. Cocks, A.C.F., and Ashby, M.F., "On Creep Fracture by Void Growth," J. Progress in Materials Science, Vol. 27, 1981, pp. 189-245.

10. Trampczynski, W. A., Hayhurst, D.R., and Leckie, F.A., "Creep Rupture of Copper and an Aluminum Alloy under Non-Proportional Loading," Univ. of Leicester, Dept. of Engr., Report No. 80-8, 1980.

11. Hayhurst, D. R., Leckie, F. A., and McDowell, D. L., "Damage Growth Under Nonproportional Loading," ASTM STP 853, 1985.

12. Trampczynski, W. A., and Hayhurst, D.R., "Creep Deformation and Rupture Under Non-Proportional Loading," Creep in Structures, IUTAM, 1980, pp. 388-405 (Eds. Ponter and Hayhurst).

13. Leckie, F. A., "The Constitutive Equations for High Temperatures and Their Relationship to Design," Proc. Int. Conf. on Constitutive Laws for Engineering Materials, Eds. Desai and Gallagher, Univ. of Arizona, Tucson, Jan. 1983, p. 93.

14. Krajcinovic, D., "Creep of Structures - A Continuous Damage Mechanics Approach," J. Structural Mechanics, 11(1), 1983, pp. 1-11.

15. Lemaitre, J., and Chaboche, J. -L., "A Non-Linear Model of Creep-Fatigue Damage Cumulation and Interaction," Mechanics of Visco-Plastic Media and Bodies, Ed. Jan Hult, Springer, Berlin, 1975, pp. 297-301.

16. Chaboche, J. -L., "Continuous Damage Mechanics - A Tool to Describe Phenomena Before Crack Initiation," Nuclear Engr. and Design, Vol. 64, 1981, pp. 233-247.

17. Woodford, D.A., "Creep Damage and the Remaining Life Concept," ASME J. Engr. Materials and Technology, Vol. 101, Oct. 1979, pp. 311-316.

18. Dafalias, Y.F., and Popov, E.P., "A Model of Nonlinearly Hardening Materials for Complex Loading," Acta Mechanica, Vol. 21, 1975, pp. 173-192.

19. Dafalias, Y.F., "The Concept and Application of the Bounding Surface in Plasticity Theory," Physical Non-Linearities in Structural Analysis, Eds. J. Hult and J. Lemaitre, IUTAM Symposium, Senlis, France, Springer Verlag, 1981, pp. 56-63.

20. Tseng, N.T., and Lee, G.C., "Simple Plasticity Model of the Two-Surface Type," ASCE Journal of Engineering Mechanics, Vol. 109, No. 3, June 1983, pp. 795-810.

21. Mroz, Z., "An Attempt to Describe the Behaviour of Metals Under Cyclic Loads Using a More General Workhardening Model," Acta Mechanica, Vol. 7, 1967, pp. 199-212.

22. McDowell, D. L., "A Two Surface Model for Transient Nonproportional Cyclic Plasticity: Part 1," ASME J. Applied Mechanics paper No. 85-APM-9, 1985.

23. McDowell, D. L., "A Two Surface Model for Transient Nonproportional Cyclic Plasticity: Part 2," ASME J. Applied Mechanics Paper No. 85-APM-10, 1985.

24. Pugh, C. E., and Robinson, D.N., "Some Trends in Constitutive Equation Model Development for High-Temperature Behavior Model Development for High-Temperature Behavior of Fast-Reactor Structural Alloys," Nuc. Engr. and Design, Vol. 48, 1978, pp. 269-276.

25. Krieg, R. D., Swearengen, J. C., and Rohde, R. W., "A Physically-Based Internal Variable Model for Rate-Dependent Plasticity," Inelastic Behavior of Pressure Vessel and Piping Components (Eds. Chang and Krempl), PVP-PB-028, ASME, 1978, pp. 15-28.

26. Lagneborg, R., "A Modified Recovery-Creep Model and its Evaluation," Metal Science Journal, Vol. 6, 1972, pp. 127-133.

27. Miller, A., "An Inelastic Constitutive Model for Monotonic, Cyclic, and Creep Deformation," ASME J. of Engineering Materials and Technology, Vol. 98, 1976, pp. 97-113.

28. Ponter, A.R.S., and Leckie, F.A., "Constitutive Relationships for the Time-Dependent Deformation of Metals," J. of Eng. Mat. and Technology, Trans. ASME, Volume 98, 1976.

29. Hart, E.W., "Constitutive Relations for Non-Elastic Deformations of Metals," J. of Eng. Mat. and Technology, Trans. ASME, Volume 98, 1976.

30. Chan, K.S., Bodner, S.R., Walker, K.P., and Lindholm, U.S., "A Survey of Unified Constitutive Theories," Proc. 2nd Symp. on Nonlinear Constitutive Relations for High Temperature Applications, NASA Lewis Research Center, June 13-15, 1984.

31. Steichen, J.M., "Tensile Properties of Thermally Exposed type 304 Stainless Steel," ASME J. Engr. Materials and Technology, Oct. 1976, pp. 357-360.

32. Oytana, C., Delobelle, P., and Mermet, A., "Constitutive Equations Study in Biaxial Stress Experiments," ASME J. Engr. Materials and Technology, Vol. 104, Jan. 1982, pp. 1-11.

33. Corum, J. M., "Material Property Data for Elastic-Plastic-Creep Analyses of Stiffened Sham-Lag Panel," Appendix C to report #ORNL-SUB-3754-1, by R. L. Egger, 1974, p. 222.

LIST OF FIGURES

FIG. 7- Applied biaxial nominal stress history (top) and predicted versus experimental inelastic strains (bottom) for specimen GT-1. Actual and predicted rupture times are 892 hr and 998 hr, respectively.

FIG. 8- Applied biaxial nominal stress history (top) and predicted versus experimental inelastic strains (bottom) for specimen GT-2. Actual and predicted rupture times are 1173 hr and 998 hr, respectively.

FIG. 9- Applied biaxial nominal stress history (top) and predicted versus experimental inelastic strains (bottom) for specimen GT-3. Actual and predicted rupture times are 1398 hr and 1043 hr, respectively.

FIG. 10- Applied biaxial nominal stress history (top) and predicted versus experimental inelastic strains (bottom) for specimen GT-4A. Actual and predicted rupture times are 851 hr and 1043 hr, respectively.

FIG. 11- Applied biaxial nominal stress history (top) and predicted versus experimental inelastic strains (bottom) for specimen GT-6. Actual and predicted rupture times are 1088 hr and 1060 hr, respectively.

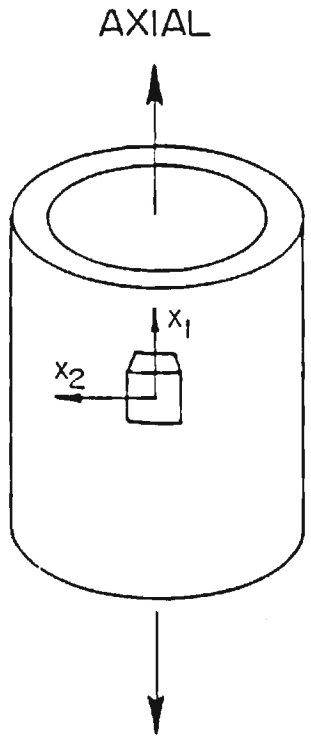

FIG. 1- Coordinate system for the tubular tension torsion specimen; x_1 and x_2 are the axial and circumferential coordinates, respectively, in the specimen mid-plane.

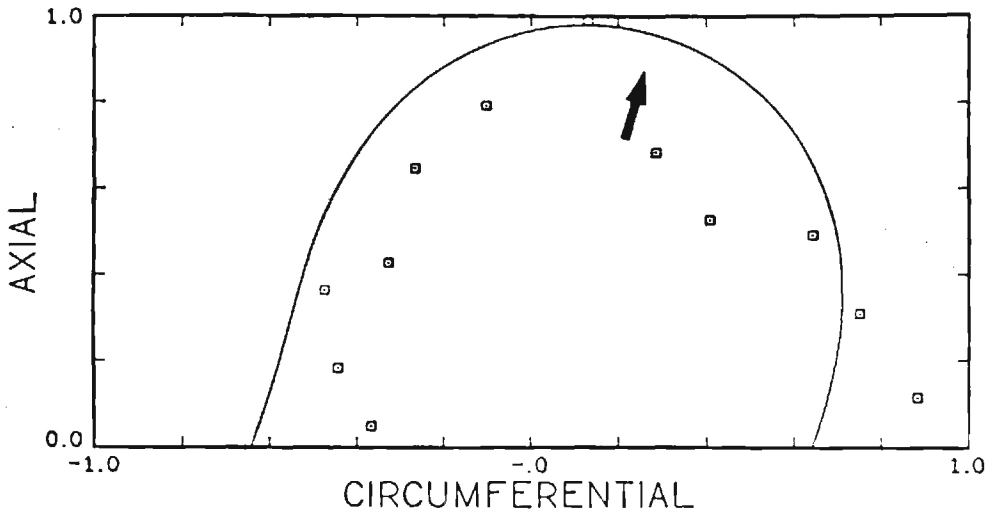

FIG. 2- Polar plot of damage distribution ω for proportional loading history GT-2 with nominal axial and shear stresses of 156.8 MPa and -52.3 MPa, respectively. Note the arrow in the maximum principal stress direction. The solid line represents a symmetric second order tensor distribution.

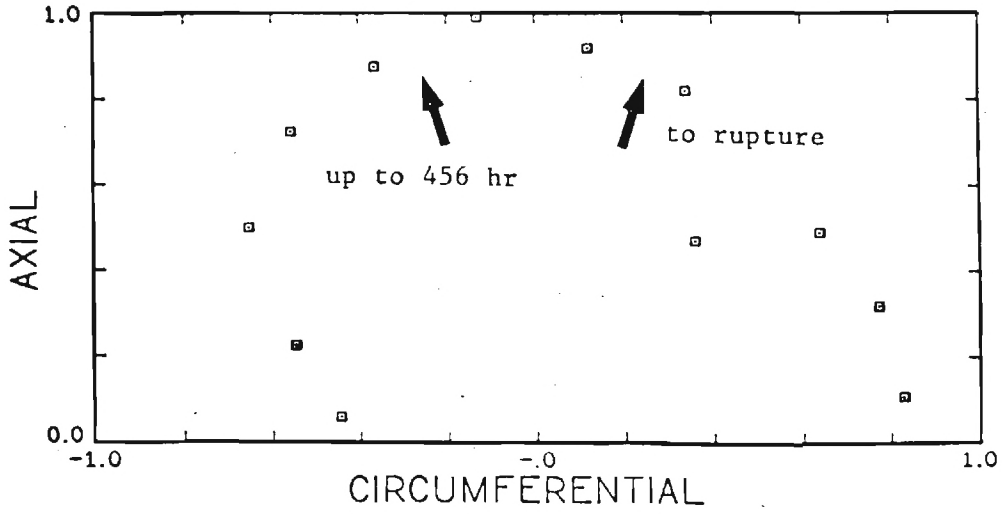

(a)

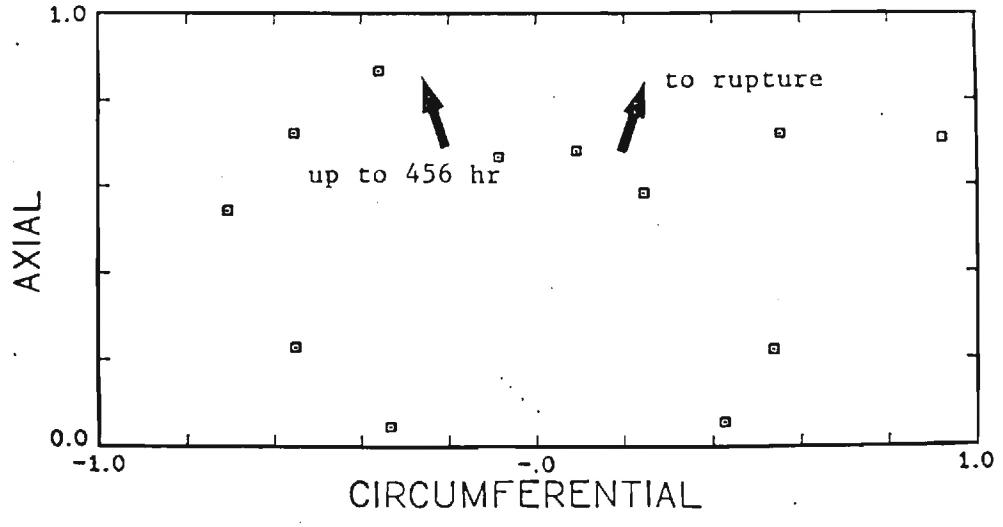

(b)

FIG. 3- Polar plots of damage distribution ω for nonproportional histories (a) GT-3 and (b) GT-4A. Note the arrows in the maximum principal stress directions for each history along with the fraction of rupture time spent in each orientation.

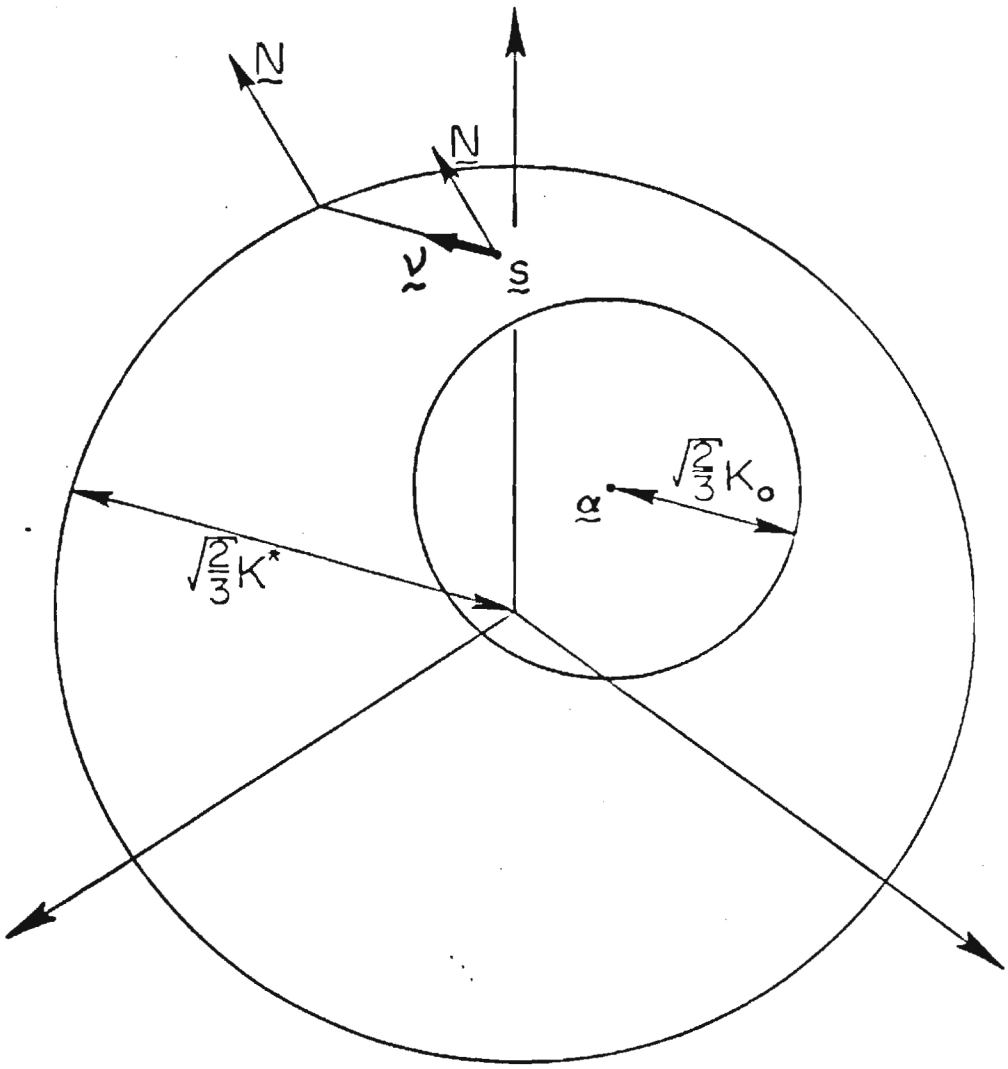

FIG. 4- Bounding and loading surfaces in deviatoric stress space.

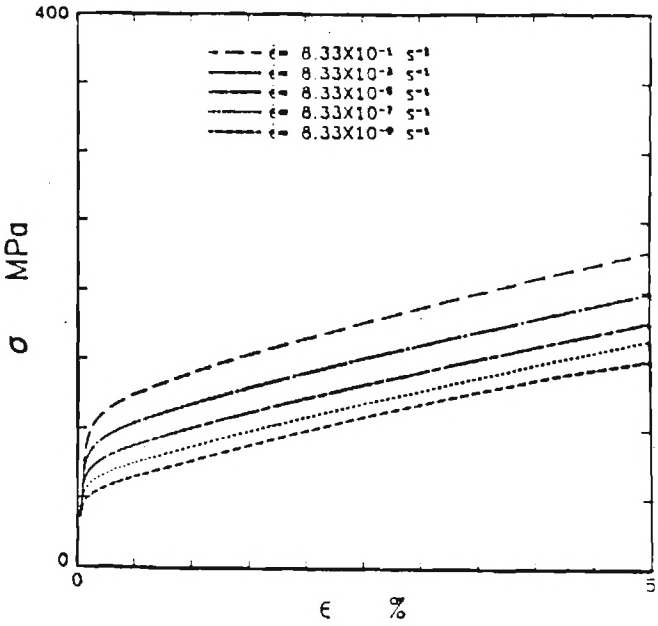

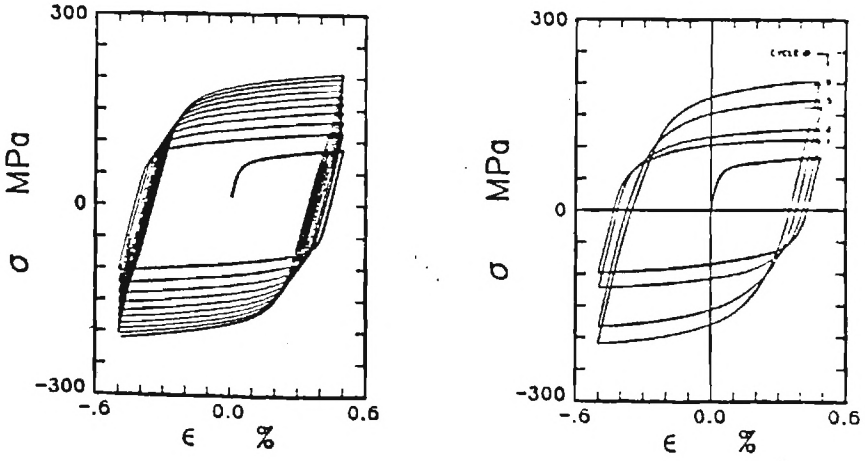

FIG. 5- (Top) predicted uniaxial monotonic response and (bottom) predicted (left) and experimental [27,33] (right) uniaxial strain-controlled hysteresis loops at a strain rate of $8.33X10^{-5}$ sec^{-1} for type 304 stainless steel at 593°C.

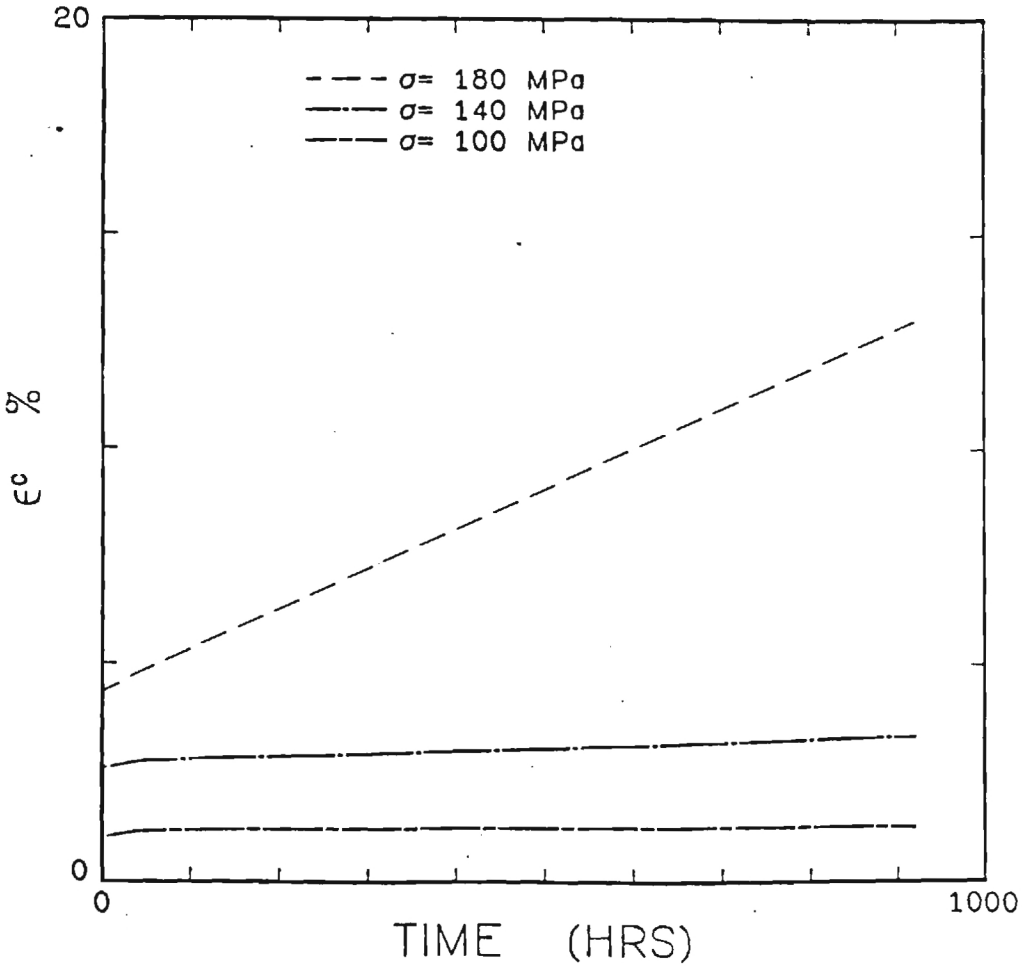

FIG. 6- Predicted uniaxial creep response for type 304 stainless steel at 593°C.

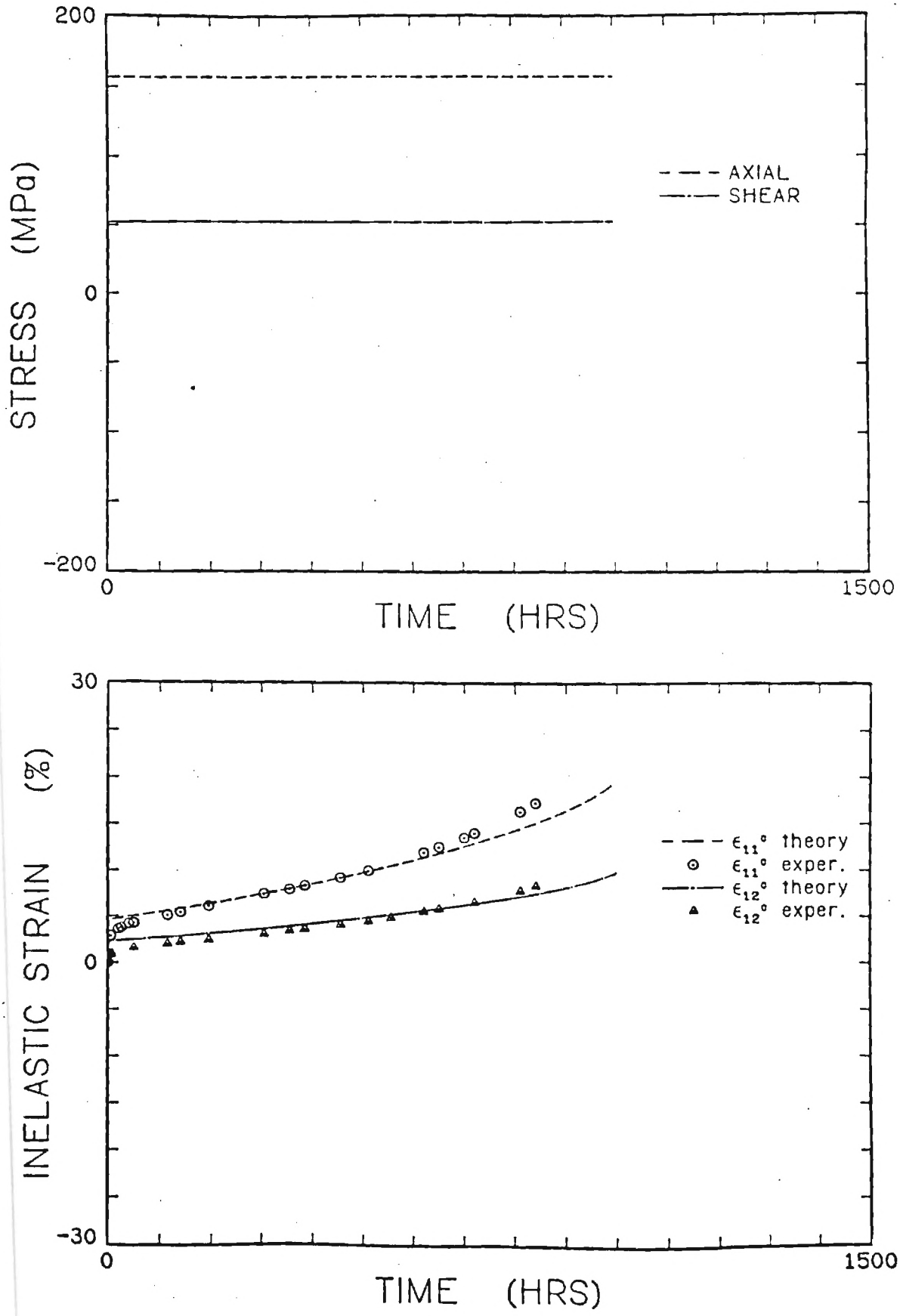

FIG. 7- Applied biaxial nominal stress history (top) and predicted versus experimental inelastic strains (bottom) for specimen GT-1. Actual and predicted rupture times are 892 hr and 998 hr, respectively.

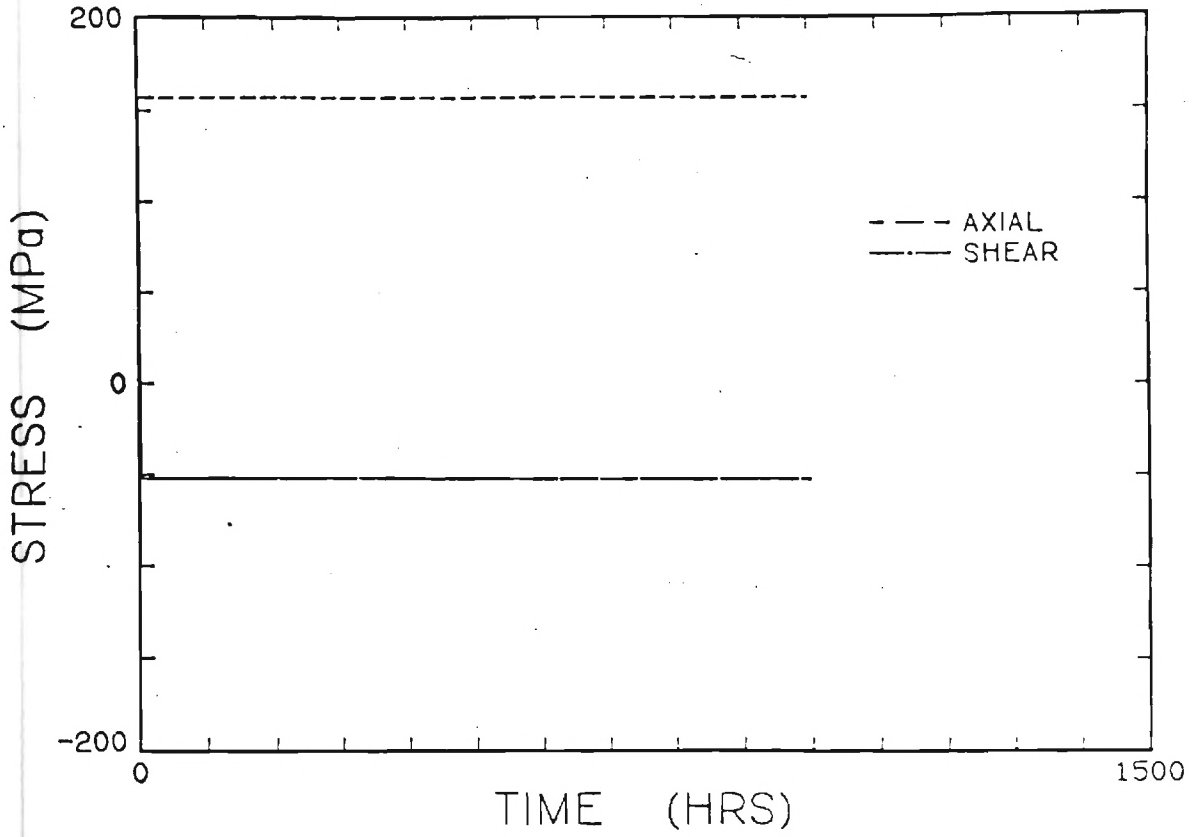

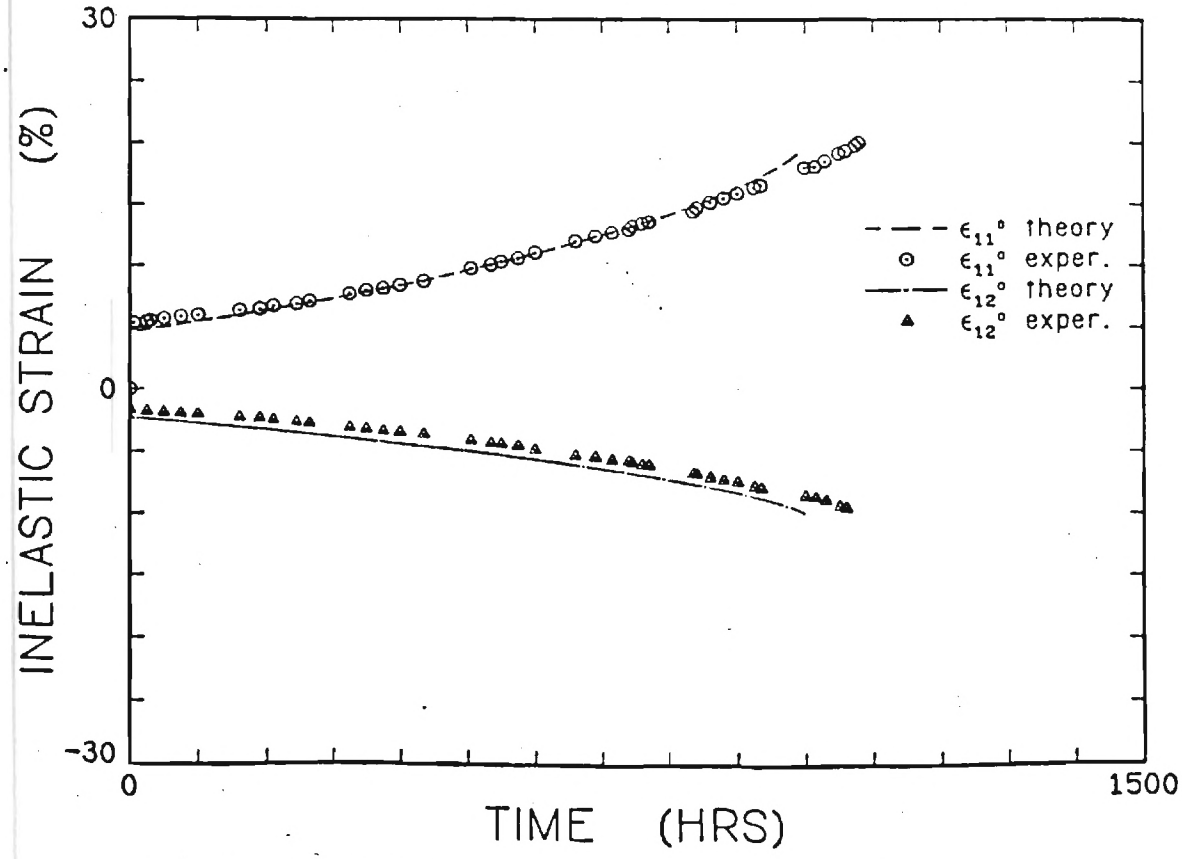

FIG. 8- Applied biaxial nominal stress history (top) and predicted versus experimental inelastic strains (bottom) for specimen GT-2. Actual and predicted rupture times are 1173 hr

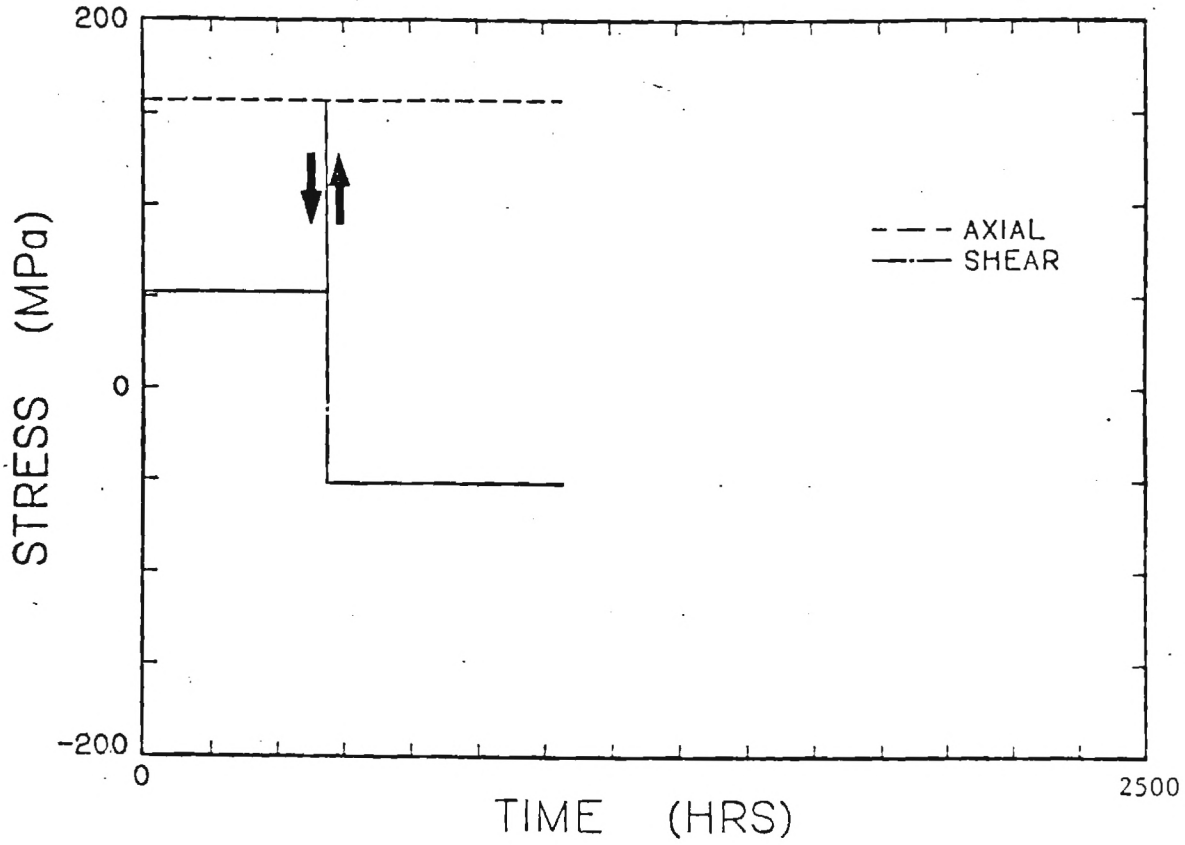

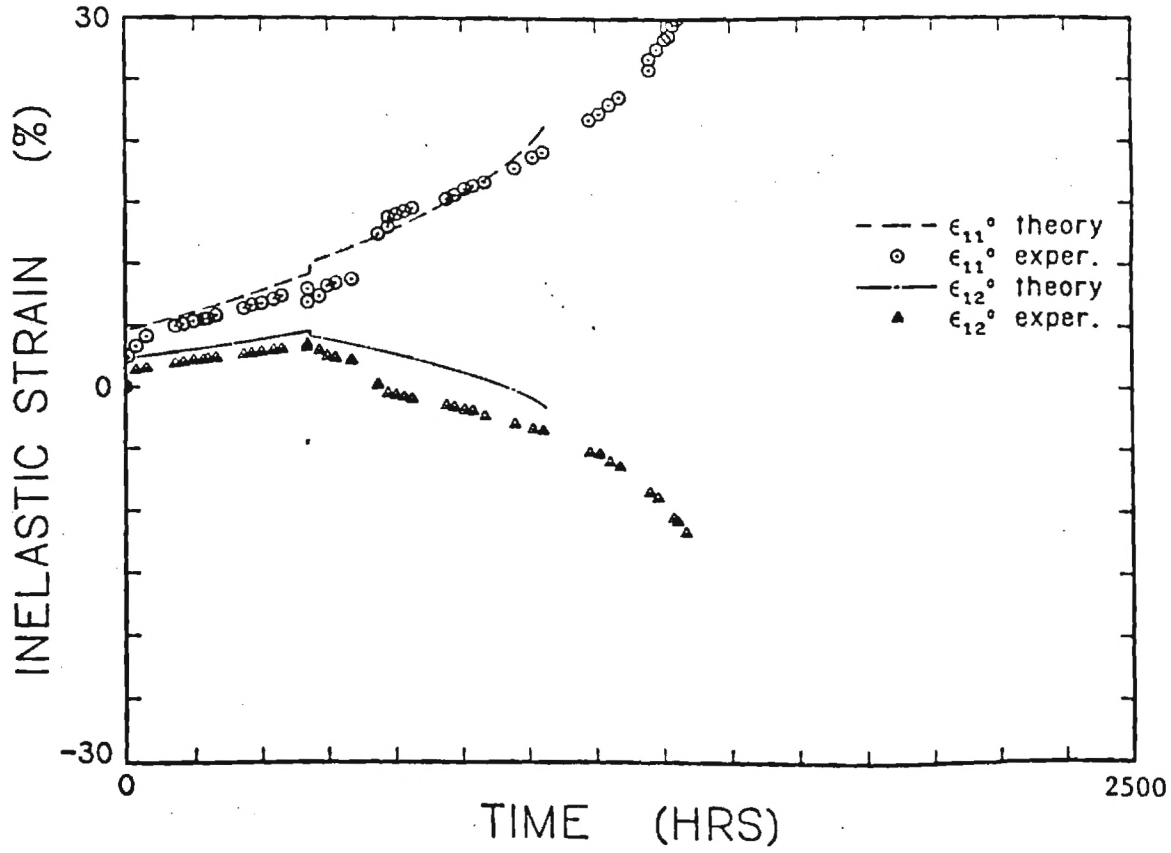

FIG. 9- Applied biaxial nominal stress history (top) and predicted versus experimental inelastic strains (bottom) for specimen GT-3. Actual and predicted rupture times are 1398 hr

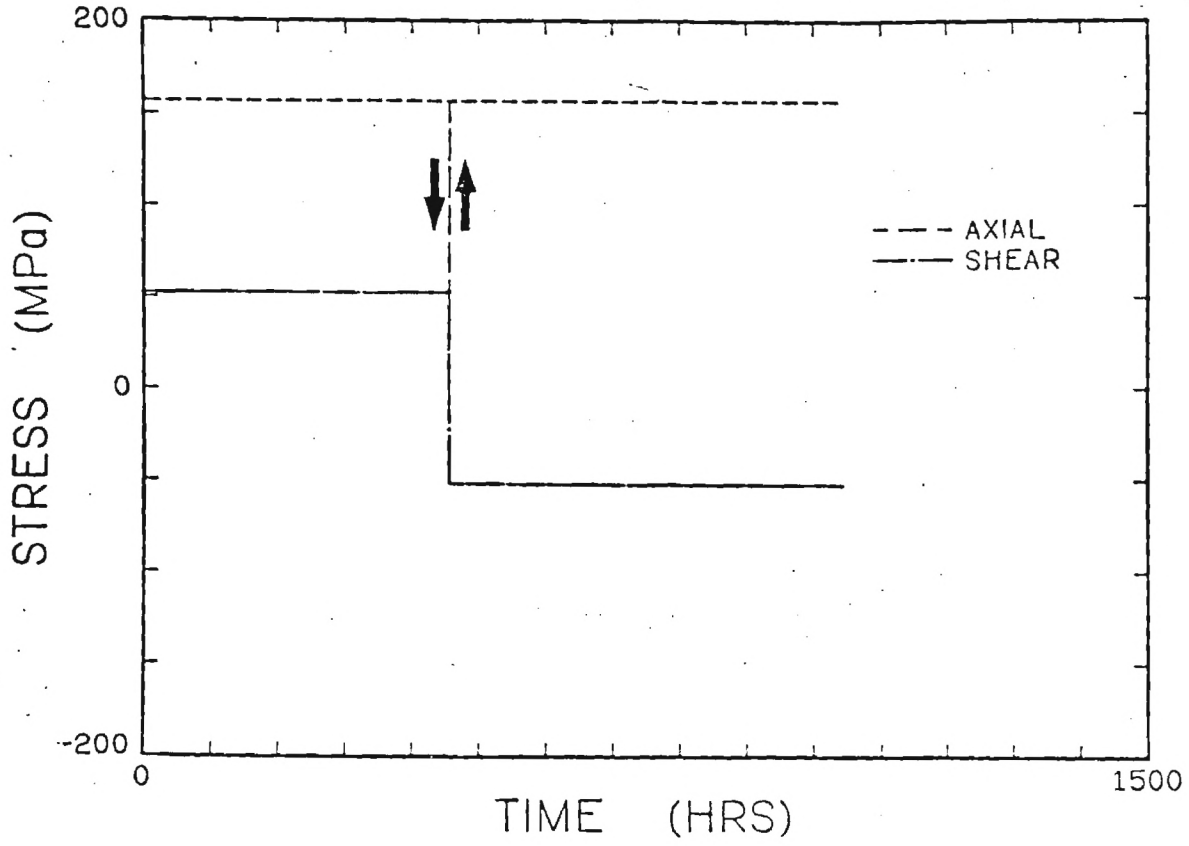

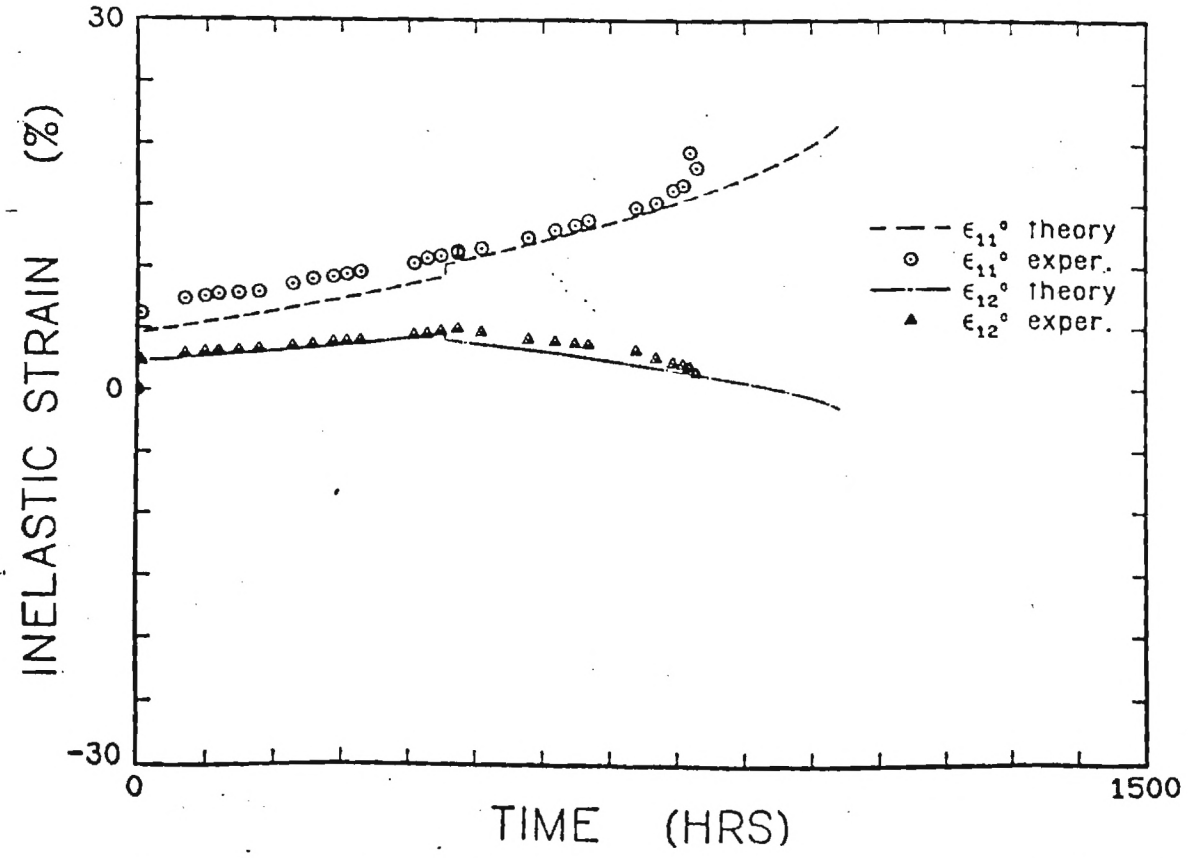

FIG. 10- Applied biaxial nominal stress history (top) and predicted versus experimental inelastic strains (bottom) for specimen GT-4A. Actual and predicted rupture times are 851 hr

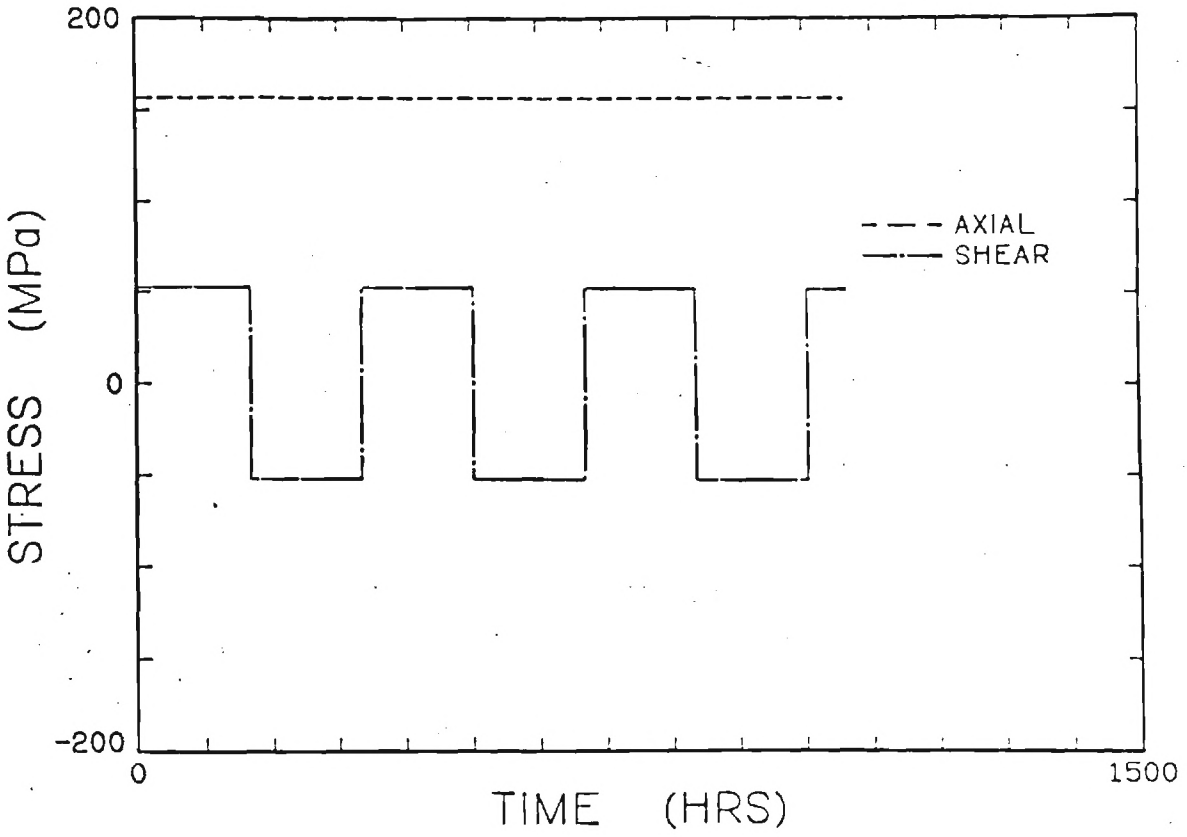

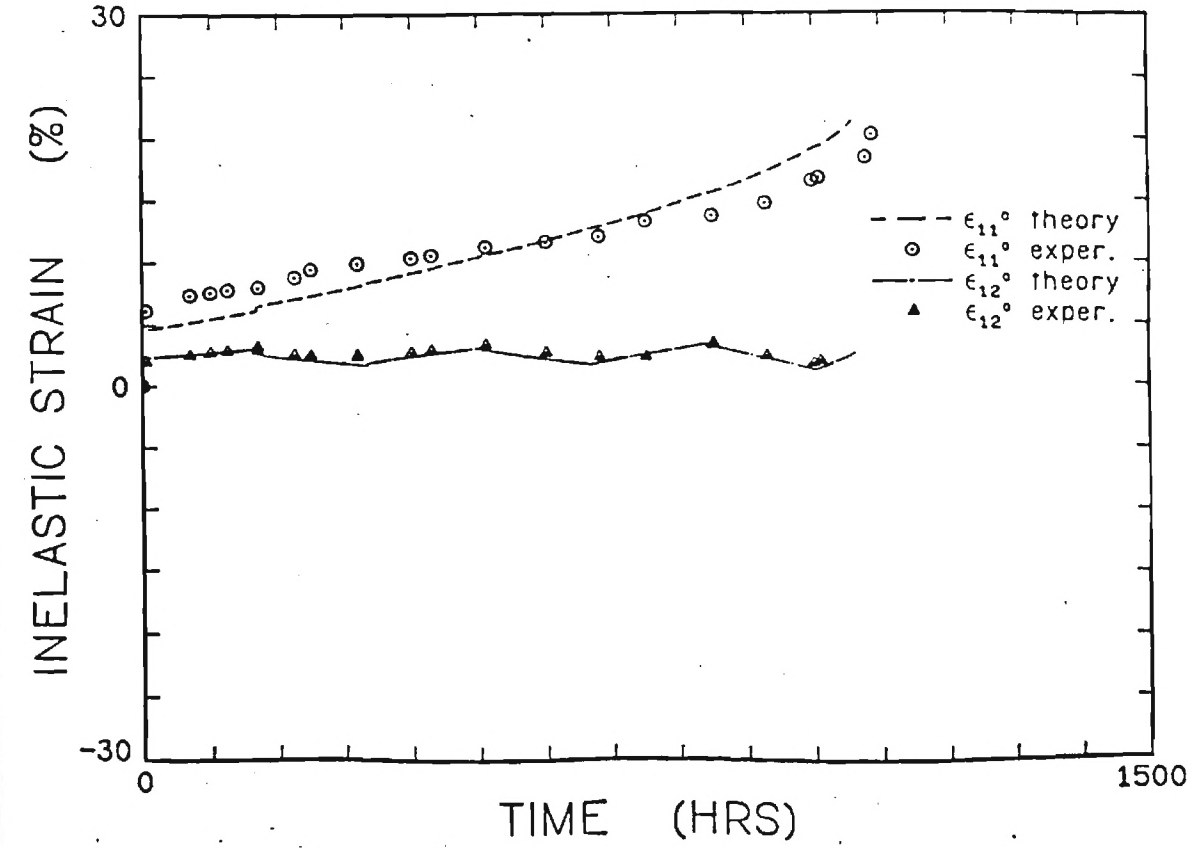

FIG. 11- Applied biaxial nominal stress history (top) and predicted versus experimental inelastic strains (bottom) for specimen GT-6. Actual and predicted rupture times are 1088 hr

Submitted for Review for Presentation/Publication
ASME PVP Division, Fall Conf., Knoxville, TN Oct. 21-23, '87.

A GENERALIZED RATE-DEPENDENT BOUNDING SURFACE MODEL

D.L. McDowell
Associate Professor

J.C. Moosbrugger
Graduate Research Assistant

Georgia Institute of Technology
Atlanta, Georgia 30332

ABSTRACT

The usual format of unified creep-plasticity models with direct hardening/dynamic recovery is briefly reviewed. A rate-dependent bounding surface theory is proposed and its relationship to these "conventional" unified theories is explored. Tensorial state variables in the model are related to thermal and athermal, short and long range obstacles to dislocation motion. Several interesting features regarding multiaxial generalization, nonproportional loading and asymptotic behaviors are discussed. The definition of the image point in the new model is generalized to allow inclusion of arbitrary directional indices for kinematic hardening.

INTRODUCTION

Classical constitutive models for rate-independent inelastic or viscous flow of initially isotropic, polycrystalline metals assume the existence of inelastic or viscous potentials, respectively, which govern the inelastic strain rate and evolution of any internal variables. In cases where the inelastic strain rates vary significantly across regimes which could either be considered rate-independent or viscous, there are two approaches. First, the inelastic and viscous potentials may be summed with no coupling as in classical models. The alternative is to couple the potentials either through internal variable coupling or via combination into a single, rate-dependent potential.

The latter approach is the focus of so-called unified creep-inelasticity or state variable models in which the inelastic strain rate encompasses straining associated with overcoming viscous (thermal) and predominately plastic (athermal) barriers [1-8]. Typically, one of the major problems with such unified approaches is the difficulty encountered in accurately predicting viscous or creep behavior when the material constants and parameters are primarily determined from higher strain rate data or vice versa. In addition, the predominate use of uniaxial tests has led to inaccuracies in modeling material behavior under nonproportional loading. The viewpoint taken here is that careful examination of experimental behaviors over a wide range of strain rates, including biaxial nonproportional histories, in conjunction with micromechanical considerations can lead to a more general unified

framework.

It is useful to consider a conceptual framework for existing models. Typically, two internal variables are chosen as a minimum set. One, associated with kinematic hardening or deformation induced anisotropy is often termed the backstress, internal stress or equilibrium stress and is associated with the fluctuating stress field produced by the accumulation of dislocation lines at or near glide obstacles in the operant slip planes. The other internal variable is associated with isotropic hardening effects. In rate-independent plasticity, it is typically associated with the yield surface dimension. In the unified theories it is analogously included, most often, as a viscous drag stress, implying that the inherent resistance to dislocation glide is dependent upon the deformation history. These internal variables are associated with microstructurally local stresses produced by dislocation rearrangements.

As a somewhat specific form, consider the isothermal framework employed by Walker [7] and Chaboche [8], albeit with slightly different functional dependencies. These theories are selected as representative of a direct hardening/dynamic recovery format. For simplicity, we restrict consideration to the small strain case. The inelastic strain rate $\dot{\underset{\sim}{\epsilon}}^{n}$ and internal or equilibrium stress rate $\dot{\underset{\sim}{\alpha}}$ are given by

$$\dot{\underset{\sim}{\epsilon}}^{n} = f(||\underset{\sim}{s} - \underset{\sim}{\alpha}||, K)\ (\underset{\sim}{s} - \underset{\sim}{\alpha}) \tag{1}$$

$$\dot{\underset{\sim}{\alpha}} = C(\rho)\ [a\,\underset{\sim}{n} - h(\rho)\underset{\sim}{\alpha}]\ ||\dot{\underset{\sim}{\epsilon}}^{n}|| - R(||\underset{\sim}{\alpha}||)\underset{\sim}{\alpha} \tag{2}$$

where

$$||\dot{\underset{\sim}{\epsilon}}^{n}|| = (\dot{\underset{\sim}{\epsilon}}^{n} : \dot{\underset{\sim}{\epsilon}}^{n})^{1/2}, \tag{3}$$

$R(||\underset{\sim}{\alpha}||)$ is a static thermal recovery function, and $\rho = \int ||\dot{\underset{\sim}{\epsilon}}^{n}||dt$.

It should be noted that C is considered independent of ρ in nearly all viscoplastic theories of this form. The static thermal recovery term provides a Bailey-Orowan [7] format for the balance of microstructural hardening and recovery processes.

The term $-Ch\underset{\sim}{\alpha}||\dot{\underset{\sim}{\epsilon}}||$ in equation (2) is referred to as a dynamic recovery term and provides nonlinear kinematic hardening behavior even at high inelastic strain rates where static thermal recovery effects are negligible. This term was first proposed by Armstrong and Frederick [10]. The isotropic hardening parameter is denoted by K and depends on the accumulated inelastic strain path length, i.e. $K = \hat{K}(\rho)$. Likewise, as seen in equation (2), the nonlinear kinematic hardening is in general

dependent on ρ. The coefficient of direct hardening, a', is generally regarded as isothermally constant. The inelastic strain rate function f usually is expressed as a power law or exponential-type function of effective overstress $||\underset{\sim}{s} - \underset{\sim}{\alpha}||$ normalized by K.

It should be noted that hardening effects associated with accumulation of inelastic strain are reflected in both the flow rule through K and in the evolution of $\underset{\sim}{\alpha}$ through the ρ-dependent coefficients. Both $C(\rho)$ and $a'(\rho)$ saturate to constant values as $\rho \to \infty$. At strain rates high enough to neglect static thermal recovery and at "large" strains, $||\underset{\sim}{\alpha}||$ achieves the rate-independent limit $||\underset{\sim}{\alpha}|| = a'(\rho)$ in the limit as $\rho \to \infty$. Hence, the asymptotic or saturation behavior of $\underset{\sim}{\alpha}$ at high strain rates is assumed to be independent of inelastic strain path history and strain rate.

The equivalence with a two surface Mroz-type hardening theory with a bounding surface has been established for a kinematic internal variable whose evolution is prescribed by the hardening/dynamic recovery format of equation (2) with $h(\rho) = 1$; this equivalence was first pointed out by Marquis [11] and was subsequently discussed by Chaboche and Rousselier [12]. This equivalence is extremely important in view of the accuracy of correlations obtained with two surface theories based on a Mroz-type kinematic hardening rule for multiaxial nonproportional cyclic plasticity [13-18]. Furthermore, it reveals that isotropic hardening in the above formulation may appear in both the flow rule and the kinematic hardening rule; its presence in the former affects the inelastic strain rate and in the latter affects the rate of kinematic hardening. Based on this equivalence with a simple two surface theory form and with the previously demonstrated inaccuracy of Prager hardening for $\underset{\sim}{\alpha}$ [19] in multiaxial experiments, the dynamic recovery term is viewed as essential for proper multiaxial generalization. We should note, of course, that this term has already been established as necessary for proper correlation of experimental uniaxial data (c.f. James et al. [20]). Based on experimental observations, it appears that a heuristic necessary condition for multiaxial generalization of any rate-dependent theory is that it collapse to a multiple loading surface interpretation with Mroz- or near Mroz-type kinematic hardening behavior; inclusion of the dynamic recovery term is necessary to satisfy this condition.

With the foregoing equivalence with bounding surface theory established, it is necessary to appeal to microstructural considerations to obtain physically based multiaxial generalizations. Such generalizations should comply with (i) the presence of thermal and athermal obstacles to dislocation motion with different amplitudes and spatial periodicities, (ii) rate-dependence of dislocation substructures, and (iii) the possibility of tensorial indices other than $\underset{\sim}{\alpha}$ for dynamic recovery associated with dislocation cross-slip or climb around obstacles. These three features will be respectively addressed by

(i) decomposition of $\underset{\sim}{\alpha}$ into thermal and athermal, predominately short and long range components, respectively;
(ii) rate-dependence of the direct hardening coefficient for the internal stress component associated with dislocation interactions with thermal,

predominately short range barriers; and
(iii) generalization of the definition of the "image point" on the bounding surface toward which the short range internal stress may translate.

All of these features are addressed in the context of a rate-dependent bounding surface model in the next section.

RATE-DEPENDENT BOUNDING SURFACE MODEL

Short and Long Range Internal Stresses

We adopt the view that the net force on mobile dislocations required to achieve a given mean velocity is isothermally invariant; it is the rate of directional (kinematic) material hardening (due to the interaction of mobile dislocations with other dislocations and other microstructural defects) which changes with deformation history, resulting in increasing flow stress, for example, under cyclic hardening conditions. The isotropic or nondirectional hardening affects the size of the stress space domain in which the internal stress can evolve rather than the initial "yielding" behavior. The coupling of viscous and plastic effects is accomplished via distinction between internal stress fields associated with thermal barriers to dislocation glide and those which are primarily athermal. This distinction arises from recognition that obstacles to dislocation glide may or may not be bypassed depending on the relative magnitude of the activation energy associated with the prevailing bypass mechanism.

We refer to the work of Chen, Gilman and Head [21], Gillis and Gilman [22], Solomon and Nix [23] and Ahlquist and Nix [24] regarding the influence of the internal stress field on mean dislocation velocity. Though the total internal stress field associated with dislocation arrangement is necessarily self-equilibrated, the component of internal stress which is manifested in macroscopic response, as viewed by Solomon and Nix and by the authors, is related to the magnitude and frequency of the peaks of the actual distribution rather than the mean values in any grain. This component of internal stress can, in fact, produce inelastic strain rate in the absence of macroscopically applied stress. Lowe and Miller [26-27], among others, have recognized the role of short and long range barriers in the development of internal stress fields. They cite the work of Mughrabi who observed distinct long and short wavelength periodicities in the curvature of free primary dislocations in neutron irradiated copper as direct microstructural evidence. Short range barriers (several Burgers vectors in extent) are considered to be primarily of a thermal nature. That is, thermally activated processes can assist dislocations in bypassing or penetrating these barriers. Long range barriers are considered to be primarily of an athermal nature, i,e. the activation energies associated with the processes by which dislocations can bypass or penetrate these barriers are high and characterized by weak temperature dependence.

There is experimental evidence [23,24,28-29,31] indicating that the magnitude of internal stress $\underset{\sim}{g}$ is a very significant fraction of the applied stress. Though $\underset{\sim}{g}$ is not observable in the strict sense, its magnitude may be estimated indirectly via the flow potential. The reported experimental estimates of $\underset{\sim}{g}$ are typically on the order of 60% to 80% of the magnitude of the applied stress $||\underset{\sim}{s}||$ at various rates of prestrain.

The short range, predominately thermal barriers provide the rate-controlling feature of viscoplastic, rate-sensitive deformation behavior. Dislocations moving in the vicinity of short range barriers are alternately hindered and assisted by the fluctuating short range internal stress fields set up by pile-ups at precipitates, entanglements, etc. There is a marked transitory short range microstructural rearrangement associated with a change of macroscopic strain rate or loading direction, in contrast to the rather more slowly evolving long range microstructure. This argument is very similar to the distinction drawn by Lowe and Miller [26-27] between very short range, thermal and short range, athermal internal stresses. At extremely high strain rates typical of shock loading, for example, the dislocation density is extremely high and the cell structure is very fine [30]. These nonlinear, strain rate-dependent changes in the character of the stalemating capability of short range barriers can be appropriately included in the direct hardening term in equation (2) through coefficient a'.

In addition, isotropic hardening associated with immobilization of dislocations at short range obstacles affects the rate of stalemating processes at the short range barriers; hence, the hardening rate of the short range internal stress increases as the immobile dislocation density increases. This effect may be incorporated in coefficient a' through dependence on the inelastic strain path history, for example.

The notion that the viscous drag force should be reflected by the short range internal stress introduces the possibility that the overstress is not necessarily a strong function of inelastic strain rate, as implied by theories which assume that the internal stress hardening functions are linear in strain rate. The validity of either viewpoint, however, is extremely difficult to assess on the basis of only uniaxial experiments since the directional indices for all of the terms are collinear. Since the evolution of short range internal stress in the former approach is highly transient and nonlinearly strain rate-dependent, uniaxial unloading or stress dip experiments to determine the internal stress may be subject to error unless great care is given to precise control and temporal resolution of data acquistion. Nonproportional loading experiments, in contrast, provide more information regarding the internal stress magnitude since the inelastic strain rate is collinear with $(\underset{\sim}{s} - \underset{\sim}{g})$. Analyses we have conducted on experimental data on Ni-base superalloy Hastelloy X at 650°C [31] subjected to sinusoidal, cyclic nonproportional tension-torsion loading at different effective strain rates indicated that the internal stress is a very significant fraction of the peak applied effective stress ($\sim$ 60% to 80%) and that the coefficients of the direct hardening/dynamic recovery terms were rate-dependent. Consequently, the overstress was not as large nor did it vary with strain rate as much as predicted with rate-

independent coefficients. These tests were conducted at strain rates high enough to validate neglect of static thermal recovery terms. Additionally, analysis of nonproportional cyclic loading experiments on type 304 stainless steel by McDowell [16-17] revealed that the magnitude of the internal stress $\underset{\sim}{\alpha}$ even after a tremendous amount of cyclic hardening was approximately 70% to 80% of the peak applied effective stress.

Obviously, a complete micromechanical treatment of the various processes involved and the coupling between them is beyond the scope of any continuum model. In the continuum model to be discussed here, we will attempt to describe the macroscopic material behavior through a viscoplastic potential which captures strain rate sensitivity over a wide range of strain rates. Coupling of viscous and plastic effects is accomplished by prescribing evolution equations for two kinematic hardening internal variables. One is associated with material hardening due to interaction of mobile dislocations with short range barriers. The other is associated with interactions of mobile dislocations with long range barriers. These interactions are described by the sum of these two kinematic hardening variables,

$$\underset{\sim}{\alpha} = \underset{\sim}{\alpha}^{sr} + \underset{\sim}{\alpha}^{*} \tag{4}$$

which represents the center of a viscoplastic potential surface in deviatoric stress space. Short and long range internal stresses are denoted by $\underset{\sim}{\alpha}^{sr}$ and $\underset{\sim}{\alpha}^{*}$, respectively. The evolution equations for these kinematic hardening variables reflect the dominant thermal or athermal nature of associated short or long range barriers. The postulated evolution equation for the short range internal stress will lead to a rate-dependent bounding surface of a von-Mises form which bounds the region of evolution of the short range internal stress in deviatoric stress space.

Rate-Dependent Bounding Surface Interpretation

The interpretation of the proposed preceding framework in terms of a rate-dependent bounding surface model is surprisingly direct and concise. In this section, we introduce a bounding surface formulation with a generalized image point for kinematic hardening of the short range internal stress. The rate-dependent flow rule is

$$\dot{\underset{\sim}{\varepsilon}}^{n} = \left[\frac{3}{2} \right]^{1/2} A \langle J_{\alpha} - \kappa \rangle^{n} \exp\left[B \langle J_{\alpha} - \kappa \rangle^{n+1} \right] \underset{\sim}{n} \tag{5}$$

where

$$J_{\alpha}(\underset{\sim}{\alpha}) = \left[\frac{3}{2} (\underset{\sim}{s} - \underset{\sim}{\alpha}):(\underset{\sim}{s} - \underset{\sim}{\alpha}) \right]^{1/2} = \left[\frac{3}{2} \right]^{1/2} ||\underset{\sim}{s} - \underset{\sim}{\alpha}|| \qquad (6)$$

and

$$\underset{\sim}{n} = \frac{\underset{\sim}{s} - \underset{\sim}{\alpha}}{||\underset{\sim}{s} - \underset{\sim}{\alpha}||} \qquad (7)$$

There is no consistency condition to be met in the rate-dependent case, i.e. the stress point may lie outside of the rate-independent yield surface $J_{\alpha}(\underset{\sim}{s}-\underset{\sim}{\alpha}) = \kappa$. Here, A, B and n are regarded as constants in the isothermal case. We admit the possibility that κ may be a repository for isotropic hardening although, as discussed later, we do not seek to place the emphasis on this point offered by the vast majority of unified theories. This flow rule, as discussed by Nouailhas [32], approximates the hyperbolic sine function often used for more accurate correlation of strain rate sensitivity over a wide range of inelastic strain rates. Essentially, the exponential flow potential results in a variable viscosity exponent, when viewed in terms of more conventional power law representations. It should be noted that Lowe and Miller [26-27] have similarly based the flow potential on the sum of short and long range internal stresses.

The hardening rates for long and short range internal stresses are respectively given by

$$\dot{\underset{\sim}{\alpha}}^{*} = C^{*} \dot{\underset{\sim}{\epsilon}}^{n} - \underset{\sim}{N}^{*}(\underset{\sim}{\alpha}^{*}) \qquad (8)$$

$$\dot{\underset{\sim}{\alpha}}^{sr} = C(\delta^{g}) \left[a\underset{\sim}{\lambda}^{g} - \underset{\sim}{\alpha}^{sr} \right] ||\dot{\underset{\sim}{\epsilon}}^{n}|| - \underset{\sim}{N}^{sr}(\underset{\sim}{\alpha}^{sr}) \qquad (9)$$

where $\underset{\sim}{N}^{*}$ and $\underset{\sim}{N}^{sr}$ are static thermal recovery functions and parameters δ^{g} and $\underset{\sim}{\lambda}^{g}$ are associated with the bounding surface defined by $J_{\alpha}(\underset{\sim}{s}-\underset{\sim}{\alpha}^{*}) = R^{*}$. Note the similarity of the evolution law for short range internal stress with that for $\underset{\sim}{\alpha}$ in the framework outlined in equations (1)-(3). Note that coeficient "a" in equation (9) in general includes isotropic hardening associated with both short and long range barriers. In

addition, "a" is in general strain rate-dependent to incorporate rate-dependence of the saturation dislocation density. These features of the model will be discussed later.

Define the bounding surface radius R^* and the image point $\underset{\sim}{s}^g$ on the bounding surface by

$$\left[\frac{2}{3}\right]^{1/2} R^* = a + ||\underset{\sim}{s} - \underset{\sim}{\alpha}|| \,, \tag{10}$$

$$\underset{\sim}{s}^g = \left[\frac{2}{3}\right]^{1/2} R^* \underset{\sim}{\lambda}^g + \underset{\sim}{\alpha}^* = (a + ||\underset{\sim}{s} - \underset{\sim}{\alpha}||)\underset{\sim}{\lambda}^g + \underset{\sim}{\alpha} - \underset{\sim}{\alpha}^{sr} \tag{11}$$

where "a" is the coefficient of the direct hardening term in equation (9). The norm of the vector from $\underset{\sim}{\alpha}^{sr}$ to the image point configuration, as shown geometrically in Figure 1, may be expressed in terms of internal variables within the present model framework, i.e.

$$\delta^g = || a\underset{\sim}{\lambda}^g - \underset{\sim}{\alpha}^{sr} || \tag{12}$$

and the unit vector $\underset{\sim}{\nu}^g$ in this direction is given by

$$\underset{\sim}{\nu}^g = \frac{a\underset{\sim}{\lambda}^g - \underset{\sim}{\alpha}^{sr}}{\delta^g} \tag{13}$$

As $\delta \to 0$, $||\underset{\sim}{\alpha}^{sr}|| \to a$ which attributes to "a" the meaning of saturation level of short range internal stress. Obviously, from equation (10), "a" is a component of the bounding surface radius. The bounding surface in this framework can be associated with saturation of internal stress and continuing hardening at long range obstacles.

It has been consistently noted [19-39] in studies of rate-independent nonproportional loading data that a hardening modulus based on the Mroz distance vector, i.e. the special case $\underset{\sim}{\lambda} = \underset{\sim}{n}$, provides good correlation of data. In other words, the nonproportionality of the next loading increment affects the inelastic strain rate. In the current rate-dependent framework, this dependence on δ^g (which is also rate-dependent)

is admitted through $C(\delta^g)$. From equations (10) and (13), it is clear that equation (9) may be written as

$$\dot{\underset{\sim}{\alpha}}^{sr} = \delta^g \, C(\delta^g) \, ||\dot{\underset{\sim}{\epsilon}}^n|| \, \underset{\sim}{\nu}^g - \underset{\sim}{N}^{sr}(\underset{\sim}{\alpha}^{sr}) \qquad (14)$$

The hardening rule in equation (14) is essentially equivalent to that offered by McDowell et al. [33-34] for modeling creep-plasticity interaction of type 304 stainless steel at 593°C, although in that earlier work the idenification with the direct hardening/dynamic recovery format was not made. Furthermore, in this earlier work by McDowell, the flow potential was made to depend only on the short range internal stress as defined in this work.

A generalized image point formulation may permit more accurate representation of dislocation rearrangements over a wide range of strain rates. Experiments [19,35,39] have shown that the direction of the rate of g may be more closely related to that of the deviatoric stress rate than the inelastic strain rate, at least within some ranges of strain rates or loading regimes. Perhaps the most compelling reason for mathematical generalization of the image point concept is the possibility of deriving a particular (not necessarily Mroz-type) image point from first principles, e.g. a mechanically and micromechanically consistent analysis of slip for a polycrystalline aggregate subjected to nonproportional loading. Such a development would also serve as a more fundamental foundation for bounding surface theory in addition to its proven capability for experimental correlation.

Figure 1 depicts the geometrical interpretation of this bounding surface theory in the deviatoric stress plane.

A very important additional aspect of this approach is the inclusion of rate-dependence and isotropic hardening in the bounding surface through parameter "a". The hardening coefficient "a" may be written as

$$a = a_o \left[F(||\underset{\sim}{s} - \underset{\sim}{\alpha}||) + \Sigma(q, \Lambda, ||\underset{\sim}{s}-\underset{\sim}{\alpha}||, ||\underset{\sim}{\alpha}^{sr}||) + \varsigma F\Sigma\right] \qquad (15)$$

a_o is a temperature-dependent constant and Σ is a temperature-dependent history functional of inelastic strain amplitude q, nonproportionality factor Λ (as described elsewhere [15-16]), overstress, and the magnitude of short range internal stress. The term $a_o\Sigma$ is the component of "a" which is affected by isotropic hardening and is representative of the average immobile dislocation density at both short and long range barriers of predominately athermal character. Hence, the possibility

that isotropic hardening depends on inelastic strain rate history is included. Parameter ς prescribes the coupling between isotropic hardening and the instantaneous strain rate. From the work of Krempl and Lu [36], $\varsigma = 0$ for type 304 stainless steel at room temperature and there is no coupling between the viscous and plastic components; as pointed out by Krempl, ς is not necessarily zero for all materials [37]. Krempl [37] also points out the general impropriety of including isotropic hardening effects in the flow rule since this implies that the viscous overstress versus inelastic strain rate relation is always affected by isotropic hardening. The present theory interprets this coupling chiefly as an effect on the short range internal stress rate; although the flow rule with constant κ cannot instantaneously reflect this coupling with a sudden change in strain rate, the rapid evolution of the short range internal stress may render extremely difficult differentiation of the results of the two approaches based on uniaxial tests only. The present theory assumes that isotropic hardening processes affect viscous drag force on dislocations predominately via g^{sr} rather than attenuation of overstress via κ. Such a distinction is most easily assessed by analysis of results from multiaxial nonproportional loading histories; as discussed in a previous section, multiaxial nonproportional experimental evidence exists to motivate this inclusion of isotropic hardening [36,39] and rate-dependence [31] in the evolution equation for g^{sr}. Krempl [37-38] also introduces the possibility of including both rate-dependence and isotropic hardening in the coefficient of direct hardening for the equilibrium or internal stress rate.

Function F introduces the nonlinear effect of effectively increasing activation energy of thermal barriers with increasing inelastic strain rate in addition to a decrease in mean free path between short range obstacles; in other words, the directional hardening is strain rate-dependent because the set of effective stalemating obstacles is not invariant with strain rate. Function F can be directly interpreted as the strain rate sensitivity of the asymptotic or bounding, i.e. "large" strain, stress-strain response. The function F also can reflect inverse strain rate sensitivity.

For very high strain rates at which the flow potential is quite nonlinear in overstress J_α, this feature permits description of the highly workhardened microstructure and the corresponding high internal stress field, in contrast to the strain rate invariant directional hardening incorporated in numerous other theories. Refer to Clifton [40] for a review of the operative dislocation mechanisms at high strain rates.

The present model is complete with prescription of specific forms for $C(\delta^g)$, F, Σ and recovery functions $\mathbb{N}^{sr}$ and $\mathbb{N}^*$.

Creep, Stress Relaxation, and High Strain Rate Behaviors

Since the current model applies to a continuum of inelastic strain rates ranging from the creep rates to high strain rates, it is necessary to examine the asymptotic behavior of the model in these regimes. We

present an abbreviated outline of asymptotic behaviors in this paper.

Consider first the asymptotic behavior of the rate-dependent model at high enough strain rates to neglect static thermal recovery effects. The magnitude of the short range internal stress saturates in the asymptotic regime of flow stress to

$$||\underset{\sim}{\alpha}^{sr}|| = a \tag{16}$$

which is obviously a function of both isotropic hardening and inelastic strain rate or overstress. Hence, in this approach there is no rate-independent form for the state variable $\underset{\sim}{\alpha}$ at high strain rates in contrast to several analogous theories [7-8].

The transient nature of creep and stress relaxation is dependent on overstress $||\underset{\sim}{s} - \underset{\sim}{\alpha}||$. Hence, both the transient, short range and steady long range hardening processes embedded in $\underset{\sim}{\alpha}$ contribute. Since the growth of $\underset{\sim}{\alpha}$ is nonlinear and depends on inelastic strain rate, creep or stress relaxation behavior will obviously depend on prior loading history. For example, creep tests conducted at the same stress levels after different prior loading histories will exhibit different transient responses.

Let us first consider the stress (load)- controlled creep test. After primary creep transients reflecting rearrangement of dislocation structures at short range obstacles have subsided, steady state conditions will be reached. Steady state corresponds to saturation of the internal stress $\underset{\sim}{\alpha}$, i.e.

$$\dot{\underset{\sim}{\alpha}} = \underset{\sim}{0} = C^{*}\dot{\underset{\sim}{\epsilon}}^{n} + C\left[a\underset{\sim}{\lambda}^{g} - \underset{\sim}{\alpha}^{sr} \right]||\dot{\underset{\sim}{\epsilon}}^{n}|| - \underset{\sim}{N}^{sr}(\underset{\sim}{\alpha}^{sr}) - \underset{\sim}{N}^{*}(\underset{\sim}{\alpha}^{*}) \tag{17}$$

such that the static thermal recovery functions must balance all hardening processes. In the approach to steady state creep conditions it would generally be expected that the internal stress would approach collinearity with the deviatoric stress, i.e. $\underset{\sim}{\lambda}^{g} \rightarrow \underset{\sim}{n}$. Since the hardening vs. recovery processes at short and long range barriers are physically distinct, we may assume that both the long and short range internal stresses eventually saturate at some steady state. However, the asymptotic approach to the steady state may occur at different rates for the long and short range backstresses. Most relevant observations indicate that dislocation arrangements at short range barriers approach steady state fairly quickly, with this evolution reflected in the primary

creep behavior. On the other hand, the long range internal stress may approach a steady state more slowly. The net effect is that the creep response may appear to have reached steady state at rather small strains, but may never quite reach such a state metallurgically nor in terms of the present model since the damage effect may be reflected in the creep response prior to steady state. In an engineering sense, we may operationally define a steady state creep response as corresponding to the minimum creep rate observed in a standard test, i.e. just prior to the tertiary stage. Then we may assume that the balance of hardening and thermal recovery holds for dislocation structures at both short and long range barriers, i.e.

$$C\left[a\underset{\sim}{\lambda}^{g} - \underset{\sim}{\alpha}^{sr} \right] ||\dot{\underset{\sim}{\epsilon}}^{n}|| = \underset{\sim}{N}^{sr}(\underset{\sim}{\alpha}^{sr}) \qquad (18)$$

$$C^{*}\dot{\underset{\sim}{\epsilon}}^{n} = \underset{\sim}{N}^{*}(\underset{\sim}{\alpha}^{*}) \qquad (19)$$

In view of the nonlinearity of the recovery terms, it is clear that the internal stress at steady state creep is rate-dependent. Furthermore, since the left hand side of equation (18) is nonlinearly rate-dependent, the recovery term $\underset{\sim}{N}^{sr}$ need not necessarily be as large as in most theories, nor of the same nonlinear form.

Primary creep behavior is largely related to the overstress-dependent parameter C which governs transient response of the short range internal stress. The marked transient rate of stress relaxation during strain hold periods is also heavily dependent on C, while the static thermal recovery terms govern the rate of recovery at long times as discussed by Walker [7]; it should be noted that large static thermal recovery terms can lead to unrealistic stress relaxation at long times in conventional unified theories. The creep and relaxation behaviors are analogous processes both physically and in the constitutive equations; essentially, only the boundary conditions are different.

At very high strain rates (e.g. $> 10^{1} - 10^{2}$ sec^{-1}), formulations in which C and "a" are constants essentially lead to a strain rate-independent evolution of $\underset{\sim}{\alpha}$. This implies that the resistance to dislocation motion is offered by rate-independent barriers. The present model considers a "viscous" resisting force associated with the viscoplastic component of the internal stress, $\underset{\sim}{\alpha}^{sr}$, which increases in concert with the applied stress. This rate-dependent increase in the strength of short range barriers may be attributed to decreased mean free path of stalemating events and to inertial forces on dislocations as discussed by Clifton [40]; the latter effects may be extremely localized

and quite unstable.

There is a fundamental physical difference between the two approaches. Namely, the first approach suggests that the hardened microstructure, reflected by $\underset{\sim}{\alpha}$, is essentially invariant with respect to strain rate once static thermal recovery terms can be safely neglected. This infers that the set of obstacles or mechanisms which resist dislocation motion and the nature of these obstacles is invariant with respect to strain rate. Yet, as mentioned earlier, the dislocation density and cell size of specimens tested at extremely high strain rates is markedly different from that of specimens tested at moderate strain rates to the same level of strain. The extent of microstructural hardening is significantly greater and of a different spatial character at the very high strain rate. Clifton [40] attributes this chiefly to increasing mobile dislocation density at increasing strain rate. This can be reflected physically through rate-dependence of the internal stress evolution, in particular in the dependence of Σ on overstress.

It may also be shown [41] that neglect of rate-dependence in coefficient "a" and static thermal recovery terms results in a rate-independent bounding surface formulation which includes kinematic hardening of both the yield surface and bounding surface. Interestingly, this particular formulation involves both a Prager-type and image point directed kinematic hardening increment for the yield surface [42].

SOME IMPLICATIONS OF THE BOUNDING SURFACE FORMULATION

Some important features of the bounding surface model will be examined in this section with some brief illustrative numerical calculations. Special attention is focused on the dependence of coefficient C in equation (9) on δ^g and associated implications for accurate modeling of the initial yielding portion of the stress-strain response.

Figures 2-6 illustrate some examples of model behavior for uniaxial and for multiaxial cyclic strain-controlled histories and will be discussed shortly. In these calculations, we choose $C(\delta^g)$ of the form

$$C(\delta^g/2a) = C_o \left\{ 1 + C_f \left[1 - \exp\left[-C_d(\delta^g/2a)^m\right] \right] \right\} \qquad (20)$$

where δ^g in this case is defined in accordance with a Mroz-type rule, i.e. $\underset{\sim}{\lambda}^g = \underset{\sim}{n}$.

It should be emphasized that the model constants were determined from several sources [14-16,43-44] in order to be somewhat representative of the behavior of type 304 and 316 stainless steels for the purpose of illustrating certain features of the model. They do not, however, represent an optimal set for accurately describing the actual behavior of either material at a particular temperature and range of strain rates since this is not the intent of the present work. Hence, the methodology

of determination of constants reported here is of an inherently approximate nature; refer to Ref. [33] for details of more precise isothermal characterization of a given material. Constants A, B and n were determined from constant strain rate monotonic test results reported by Abrahamson [43] with the assumption that

$$\| \underset{\sim}{s} - \underset{\sim}{\alpha} \| = 0.4 \, \sigma_f \tag{21}$$

where σ_f is the flow stress at 4% plastic strain. This assumption is based on the approximate asymptotic level of $\underset{\sim}{\alpha}$ noted in experiments [23-25,29,31,39].

Rate-dependence in the coefficient of the direct hardening term for the short range backstress is included via dependence of the limit surface radius on overstress, i.e.

$$a = (2/3)^{1/2} R^* - \| \underset{\sim}{s} - \underset{\sim}{\alpha} \| \tag{22}$$

$$R^* = R_1^* + R_2^* \tag{23}$$

$$R_2^* = M \, J_{\alpha}^{m_1} \tag{24}$$

Isotropic hardening effects, including dependence on inelastic strain path length and nonproportionality of the loading history, are included through evolution of R_1^* by incorporating the model due to McDowell [44] arrived at through the analysis of data from nonproportional cyclic strain controlled histories imposed on type 304 stainless steel at room temperature [19,39], i.e.

$$\dot{R}_1^* = \bar{\mu} \left[\bar{R}_1^*(\Lambda) - R_1^* \right] \| \dot{\underset{\sim}{\epsilon}}^n \| \tag{25}$$

where

$$\bar{R}_1^* = R_o + h_1(\Lambda)^{h_2} \tag{26}$$

and Λ denotes dependence on nonproportionality of the loading history.

The definition of $\bar{R}_1^*$ in equation (26) is taken from Ref. [44] with the simplification h_2 = constant in this work. The value of h_2 is taken as representative of the level of nonproportionality associated with a biaxial path to be considered in this study.

An initial limit surface radius was taken to be R_1^* = 34.5 MPa and a constant effective strain rate of 0.002 sec^{-1} was used for all calculations. Note that ζ = 0 in this formulation, as supported by experiments on austenitic stainless steels [36]. Again, it is emphasized that the model constants are selected to be representative in only an approximate way of a wide range of temperatures and strain rates for austenitic types 304/316 stainless steels in the absence of static thermal recovery effects. A summary of model constants selected for example calculations is as follows:

κ = 10 MPa	$\underset{\sim}{N}^* = \underset{\sim}{0}$, $\underset{\sim}{N}^{sr} = \underset{\sim}{0}$
$\bar{\mu}$ = 10	$C^* = 3000$ MPa
ν = 0.29 (elastic Poisson's ratio)	
G = 75.2 X 10^3 MPa (elastic shear modulus)	
A = 3.6 X 10^{-10}	B = 2.73 X 10^{-10}
n = 4.5	m_1 = 0.85
C_o = 72	M = 2.5
C_f = 36	R_o = 175 MPa
C_d = 10	h_1 = 175 MPa
m = 1.8	h_2 = 0.6

Units of stress and time are MPa and sec, respectively.

Referring to Figures 2-3, it is clear that the present framework is suitable for representation of nonproportional cyclic loading histories. A strain-controlled, room temperature tension-torsion square path history enforced on a thin-walled tubular, type 304 stainless steel specimen by Ohashi et al. [45] is shown with the results of the rate-dependent bounding surface theory juxtaposed. Though the amplitudes of the predicted and experimental results are not in precise agreement, owing to the approximate nature of the parameter selection procedure which was independent of these particular experimental results, the character of the response is accurately predicted. This is not surprising, of course, since the bounding surface theory is expected to perform well for such nonproportional cyclic loading histories [16-19,39,44]. The dependence of C on δg in the current model, to be discussed in the next paragraph, and the generalized image point offer the potential for very precise correlation of the detailed features of nonproportional loading histories.

In Figure 4, the cyclic hardening behavior characteristic of this class of materials from the annealed condition is displayed by the model for constant amplitude cycling at ± 0.5% strain. The smooth transition from initial yielding to the asymptotic response is noted in particular. It must be emphasized that the radius κ of the purely elastic regime is extremely small as noted above. This smooth transition emerges primarily

from the dependence of C on δ^g in equation (20). It must be emphasized that this dependence is not embodied in current unified theories, but is extremely relevant to the practical problems of modeling mean stress relaxation and rachetting at cyclic strain amplitudes of small magnitude. For example, Chaboche and co-workers [32,46] effectively decompose the internal stress $\underline{\alpha}$ into an arbitrary number (usually two) of components which evolve with independent hardening/dynamic recovery rules to more accurately capture the work-hardening response just after initial yielding at each reversal. In the present theory, this is accomplished in essence by the introduction of the two tensorial variables $\underline{\alpha}^{sr}$ and $\underline{\alpha}^*$; however, the introduction of dependence of C on δ^g is the key to accurate modeling of the transition from initial yielding to asymptotic behavior in the context of a single direct hardening/dynamic recovery evolution equation for $\underline{\alpha}^{sr}$. The component $\underline{\alpha}^*$ defines the asymptotic response exclusively. A continuous dependence on δ^g is reflected in $C(\delta^g)$ in the spirit of rate-independent two surface theories. Furthermore, it is most likely necessary to decompose the internal stress $\underline{\alpha}$ into more than two components à la Chaboche to achieve the accuracy and generality offered by the current framework with $C(\delta^g)$. Finally, the decomposition offered herein is based on short and long range internal stresses, motivated by dislocation arguments; Chaboche and associates evidently decomposed $\underline{\alpha}$ to obtain a better fit to experimental data.

To illustrate the consequences of the dependence of C on δ^g, model computations were made for strain-controlled, monotonic uniaxial tests with C = constant and with $C = C(\delta^g)$. In Figure 5, the responses are shown for C = constant ($C_d = 0$) for various C values. It is noted that the approach to the asymptotic or bounding behavior may be varied with C in this case, but the "initial yielding" behavior is strongly affected; even moderate C values, for example, lead to a marked discontinuity in the stress-strain response at small strains. The use of high C values to minimize this discontinuity results in unrealistically rapid approach to asymptotic behavior, a feature often noted in current unified theories. Figure 6 depicts the range of stress-strain behaviors which can be achieved with $C = C(\delta^g)$ by varying C_d in equation (20) with C_o, C_f and m listed above; in contrast to Figure 5, note that both a high initial tangent modulus and a smooth transition from elastic behavior to elastic-viscoplastic behavior is obtained for a range of C_d values, whereas this cannot be accomplished with any constant C value. Hence, the full nonlinear transition may be described accurately by the evolution of the short range internal stress. This of course has important implications for prediction of stress relaxation, rachetting, and inelastic strain ranges for creep-fatigue calculations under both proportional and nonproportional loading histories of typically small to moderate strain amplitude or magnitude.

In this work, we have discussed behavior for only a single strain rate for rather restricted histories when static thermal recovery is negligible. Some of the subtleties of the current approach have been highlighted. The model captures cyclic behavior, including nonproportional loading paths, and the full elastic-viscoplastic transition to asymptotic stress-strain response. The creep behavior has been discussed elsewhere [33-34].

CONCLUSIONS

A rate-dependent bounding surface model has been proposed as an accurate multiaxial generalization of unified creep-plasticity theory. Its relationship to several existing unified theories with hardening/dynamic recovery format is explored. Several key departures from these existing theories are noted, motivated by experimental observations. The definition of the image point associated with the bounding surface in the new model is generalized to allow inclusion of arbitrary directional indices for kinematic hardening. In addition, the bounding surface radius is allowed to depend on both the inelastic strain rate and the effective inelastic strain path length. As a result, there is no unique rate-independent asymptotic behavior at high strain rate. Furthermore, static thermal recovery terms are not required to balance a direct hardening term linear in inelastic strain rate, a requirement of many existing theories which limits accuracy of combined correlation of both cyclic and creep behaviors.

ACKNOWLEDGMENTS

The authors are grateful for the support of the U.S. National Science Foundation (NSF MSM-8601889; MSM-8552714) for support of this work.

REFERENCES

1. Lindholm, U.S., Chan, K.S., Bodner, S.R., Weber, R.M., Walker, K.P., and Cassenti, B.N., "Constitutive Modeling for Isotropic Materials," NASA CR-174980, SwRI-7476/30, 1985.
2. Pugh, C. E., and Robinson, D.N., "Some Trends in Constitutive Equation Model Development for High-Temperature Behavior Model Development for High-Temperature Behavior of Fast-Reactor Structural Alloys," Nuc. Engr. and Design, Vol. 48, 1978, pp. 269-276.
3. Krieg, R. D., Swearengen, J. C., and Rohde, R. W., "A Physically-Based Internal Variable Model for Rate-Dependent Plasticity," Inelastic Behavior of Pressure Vessel and Piping Components (Eds. Chang and Krempl), PVP-PB-028, ASME, 1978, pp. 15-28.
4. Lagneborg, R., "A Modified Recovery-Creep Model and its Evaluation," Metal Science Journal, Vol. 6, 1972, pp. 127-133.
5. Bodner, S.R., and Partom, Y., "Constitutive Equations for Elastic-Viscoplastic Strain Hardening Materials," ASME J. of Applied Mechanics, Vol. 42, 1975, pp. 385-389.
6. Hart, E.W., "Constitutive Relations for Non-Elastic Deformations of Metals," J. Eng. Mat. and Technology, Trans. ASME, Volume 98, 1976.
7. Walker, K.P., "Research and Development Program for Nonlinear Structural Modeling with Advanced Time-Temperature Dependent Constitutive Relationships," NASA Report CR-165533, NASA Lewis RC, Nov. 1981.

8. Chaboche, J.L., "Description Thermodynamicque et Phénomènologique de la Viscoplasticité Cyclique avec Endommagement," Publication No. 1978-3 of the Office National d'Etudes et de Researches Aerospatiales, France, 1978.
9. Chaboche, J.L., "Viscoplastic Constitutive Equations for the Description of Cyclic and Anisotropic Behaviour of Metals," Bull. de l' Acad. Polonaise des Sciences, Série Sc. et Techn., Vol. 25, No. 1, 1977, pp. 33-42.
10. Armstrong, P.J., and Frederick, C.O., "A Mathematical Representation of the Multiaxial Bauschinger Effect," C.E.G.B. Report RD/B/N 731, 1966.
11. Marquis, D., "Sur un Modèle de Plasticité rendant compte du Comportement Cyclique," 3ème Congrès Francais de Mécanique, Nancy, 1979.
12. Chaboche, J. L., and Rousselier, G., "On the Plastic and Viscoplastic Constitutive Equations- Part I: Rules Developed With Internal Variable Concept," ASME J. Pressure Vessel Technology, Vol. 105, 1983, pp. 153-158.
13. Dafalias, Y.F., and Popov, E.P., "A Model of Nonlinearly Hardening Materials for Complex Loading," Acta Mechanica, Vol. 21, 1975, pp. 173-192.
14. Dafalias, Y.F., "Modeling Cyclic Plasticity: Simplicity Versus Sophistication," Mechanics of Engineering Materials, Eds. Desai and Gallagher, John Wiley and Sons, 1984, pp. 153-178.
15. Krieg, R.D., "A Practical Two Surface Plasticity Theory," ASME Journal of Applied Mechanics, Vol. 42, 1975, pp. 641-646.
16. McDowell, D.L., "A Two Surface Model for Transient Nonproportional Cyclic Plasticity: Part I - Development of Appropriate Equations," ASME Journal of Applied Mechanics, Volume 52, 1985, pp. 298-302.
17. McDowell, D.L., "A Two Surface Model for Transient Nonproportional Cyclic Plasticity: Part II - Comparison of Theory with Experiments," ASME Journal of Applied Mechanics, Volume 52, 1985, pp. 303-308.
18. Lamba, H.S., and Sidebottom, O.M., "Cyclic Plasticity for Nonproporti onal Paths: Part 2 - Comparison with Predictions of Three Incremental Plasticity Models," ASME Journal of Engineering Materials and Technology, Vol. 100, 1978, pp. 104-111.
19. McDowell, D.L., "An Experimental Study of the Structure of Constitutive Equations for Nonproportional Cyclic Plasticity," ASME Journal of Engineering Materials and Technology, Vol. 107, 1985, pp. 307-315.
20. James, G.H., Imbrie, P.K., Hill, P.S., Allen, D.H., and Haisler, W.E., "An Experimental Comparison of Several Current Viscoplastic Constitutive Models at Elevated Temperature," ASME J. Engineering Materials and Technology, Vol. 109, 1987, pp. 130-139.
21. Chen, H. S., Gilman, J. and Head, J., "Dislocation Multipoles and Their Role in Strain Hardening ", Journal of Applied Physics, Vol. 35, 1964, pp. 2502-2514.
22. Gillis, P.P. and Gilman, J.J., "Dynamical Dislocation Theory of Crystal Plasticity : Part II. Easy Glide and Strain Hardening," Journal of Applied Physics, Vol. 36, No. 11, Nov. 1963, pp. 3380-3386.

23. Solomon, A.A. and Nix, W.D., "Interpretation of High Temperature Plastic Deformation in Terms of Measured Effective Stresses," Acta Metallurgica, Vol. 18, Aug. 1980, pp. 863-876.
24. Ahlquist, C.N. and Nix, W.D., "The Measurement of Internal Stresses During Creep of Al and Al-Mg Alloys," Acta Metallurgica, Vol. 19, April 1971, pp. 373-385.
25. Gibeling, J.C. and Nix, W.D., "The Description of Elevated Temperature Deformation in Terms of Threshold Stresses and Back Stresses: A Review," Mat. Science and Engineering, Vol. 45, 1980, pp. 123-135.
26. Lowe, T. C., and Miller, A. K., "Improved Constitutive Equations for Modeling Strain Softening- Part I: Conceptual Development," ASME J. Engr. Materials and Technology, Vol. 106, 1984, pp. 337-342.
27. Lowe, T. C., and Miller, A. K., "Improved Constitutive Equations for Modeling Strain Softening- Part II: Predictions for Aluminum," ASME J. Engr. Materials and Technology, Vol. 106, 1984, pp. 343-348.
28. Tsou, J.C. and Quesnel, D.J., "Internal Stress Measurements During the Saturation Fatigue of Polycrystalline Aluminum," Mat. Science and Engineering, Vol. 56, 1982, pp. 289-299.
29. Oytana, C., Delobelle, P., and Mermet, A., "Constitutive Equations St udy in Biaxial Stress Experiments," J. Engineering Materials and Technology, Vol. 104, 1982, pp. 1-11.
30. Meyers, A.M., and Chawla, K.K., Mechanical Metallurgy, Prentice-Hall, Inc., 1984.
31. McDowell, D.L., Moosbrugger, J.C., Doumi, M., and Jordan, E.H., "Some Implications for Cyclic Plastic and Viscoplastic Equations Based on Nonproportional Loading Experiments," presented at 3rd Symposium on Nonlinear Constitutive Relations for High-Temperature Applications, NASA, University of Akron, June 11-13, 1986.
32. Nouailhas, D., "A Viscoplastic Modelling Applied to Stainless Steel Behavior, " in Constitutive Laws for Engr. Materials: Theory and Applications, Vol. I, Eds. Desai, Krempl, Kiousis and Kundu, Tucson, Arizona, 1987, pp. 717-724.
33. McDowell, D.L., Ho, K.I., and Stalley, J., "An Anisotropic, Damage-Coupled Viscoplastic Model for Creep-Dominated Cyclic Loading," presented at 3rd Int. Symp. on Nonlinear Fracture Mechanics, Knoxville, TN, Nov. 1986.
34. McDowell, D.L., Ho, K.I., and Moosbrugger, J.C., "Continuum Damage Representation of Creep-Dominated, Nonproportional Cyclic Loading," to be presented at Int. Seminar on High Temp. Fracture Mechanisms and Mechanics, Dourdan, France, Oct. 13-15, 1987.
35. Phillips, A., and Lee, C.W., "Yield Surfaces and Loading Surfaces. Experiments and Recommendations," International Journal of Solids and Structures, Vol. 15, 1979, pp. 715-729.
36. Krempl, E., and Lu, H., 1984, "The Hardening and Rate-Dependent Behavior of Fully Annealed AISI Type 304 Stainless Steel Under Biaxial In-Phase and Out-of-Phase Strain Cycling at Room Temperature," ASME Journal of Engineering Materials and Technology, Vol. 106, pp. 376-382.
37. Krempl, E., "Models of Viscoplasticity, Some Comments on Equilibrium (Back) Stress and Drag Stress," Report MML 87-2, Mechanics of Materials Laboratory, Rensselaer Polytechnic Institute, February 1987.

38. Krempl, E., and Yao, D., "The Viscoplasticity Theory Based on Overstress Applied to Ratchetting and Cyclic Hardening," Report MML 87-3, Mechanics of Materials Laboratory, Rensselaer Polytechnic Institute, March 1987.
39. McDowell, D.L., "An Evaluation of Recent Developments in Hardening and Flow Rules for Rate-Independent, Nonproportional Cyclic Plasticity," to appear in ASME J. Applied Mechanics, Paper No. 87-APM-37, 1987.
40. Clifton, R.J., "Dynamic Plasticity," ASME J. Applied Mechanics, Vol. 50, Dec. 1983, pp. 941-952.
41. McDowell, D. L., and Moosbrugger, J. C., "A Rate-Dependent Bounding Surface Model," work in progress, 1987.
42. Yoder, P.J., and McDowell, D.L., "Bounding-Surface Plasticity in Strain Space," submitted to Acta Mechanica, Dec. 1986.
43. Abrahamson, T. E., "Modeling the Inelastic Behavior of Type 304 Stainless Steel With a Unified Creep-Plasticity Theory", PhD Thesis, University of Illinois at Urbana-Champaign, Urbana, Illinois, 1983.
44. McDowell, D.L., "Simple Experimentally Motivated Cyclic Plasticity Model," ASCE J. Engineering Mechanics, Vol. 113, No. 3, 1987, pp. 378-397.
45. Ohashi, Y., and Tanaka, E., and Ooka, M., "Plastic Deformation Behavior of Type 316 Stainless Steel Subject to Out-of-Phase Strain Cycles," ASME J. Engineering Materials and Technology, Vol. 107, 1985, pp. 286-292.
46. Chaboche, J.L., "Cyclic Plasticity Modeling and Rachetting Effects," in Constitutive Laws for Engr. Materials: Theory and Applications, Vol. I, Eds. Desai, Krempl, Kiousis and Kundu, Tucson, Arizona, 1987, pp. 47-58.

LIST OF FIGURES

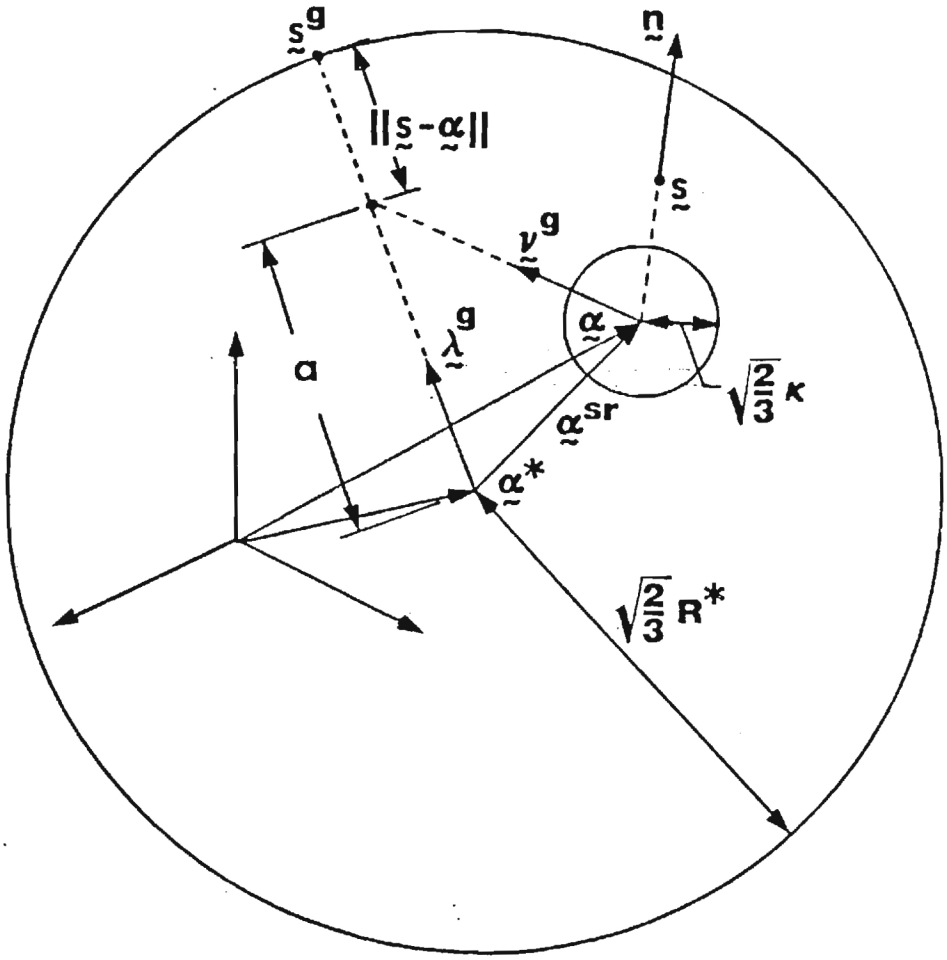

Figure 1. Geometric interpretation of the rate-dependent bounding surface model in the deviatoric stress space.

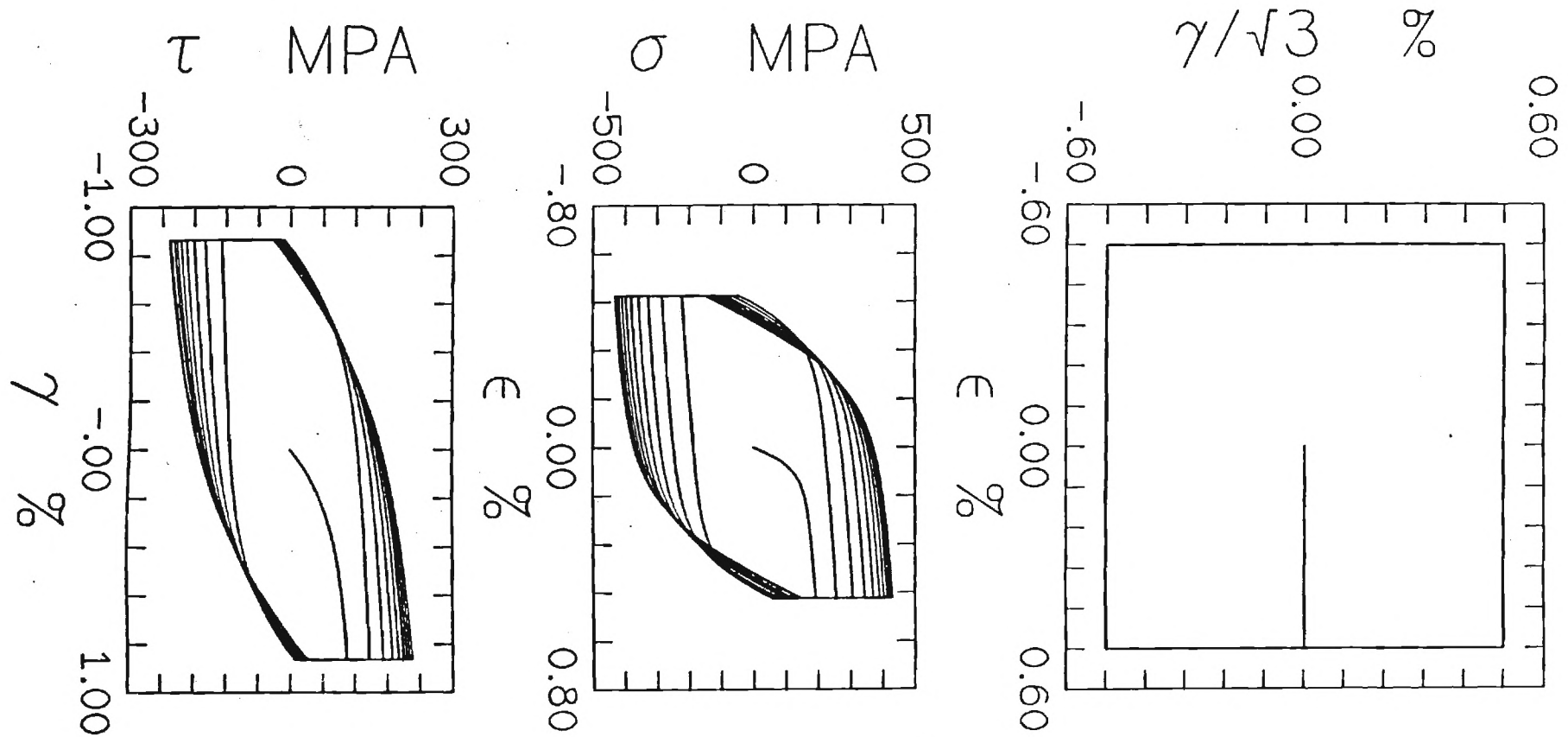

Figure 2. Nonproportional cyclic strain-controlled history (first 10 cycles) :
(a) Strain path imposed in axial strain - shear strain space,
(b) Model prediction for axial stress vs. axial strain response,
(c) Model prediction for shear stress vs. Shear strain response,

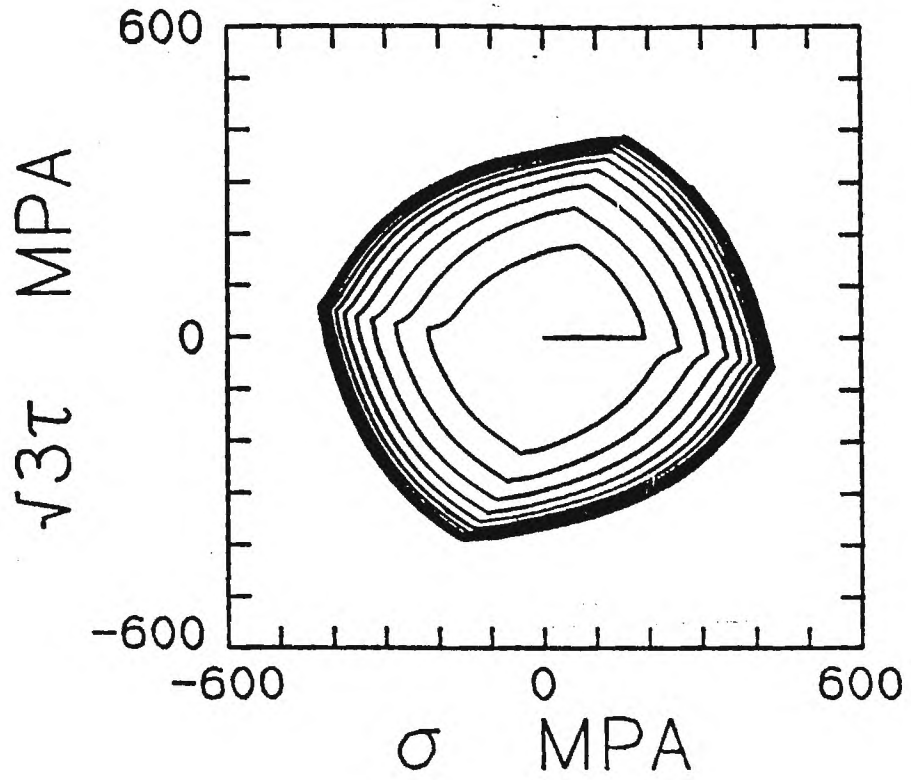

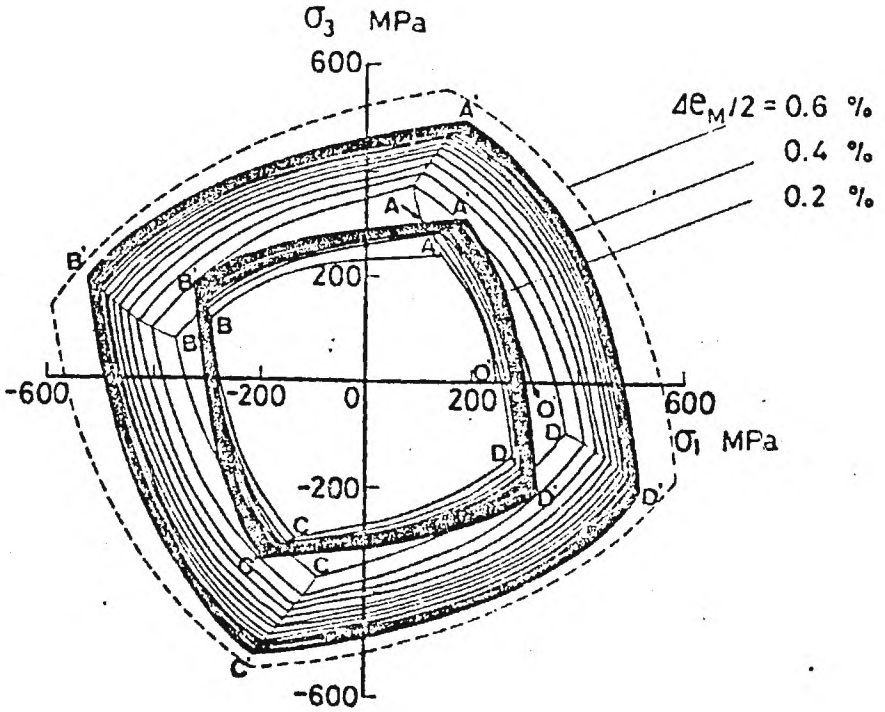

Figure 3. Nonproportional cyclic strain-controlled history (first 10 cycles) for history shown in Figure 2: Stress space response; model prediction (upper) and experimental results of Ohashi et al. [45] for geometrically similar strain space paths imposed on type 316 stainless steel at room temperature (lower). Note that $\sigma_1=\sigma$, $\sigma_3=\sqrt{3}\tau$ and $\Delta e_M/2=\Delta\epsilon/2$.

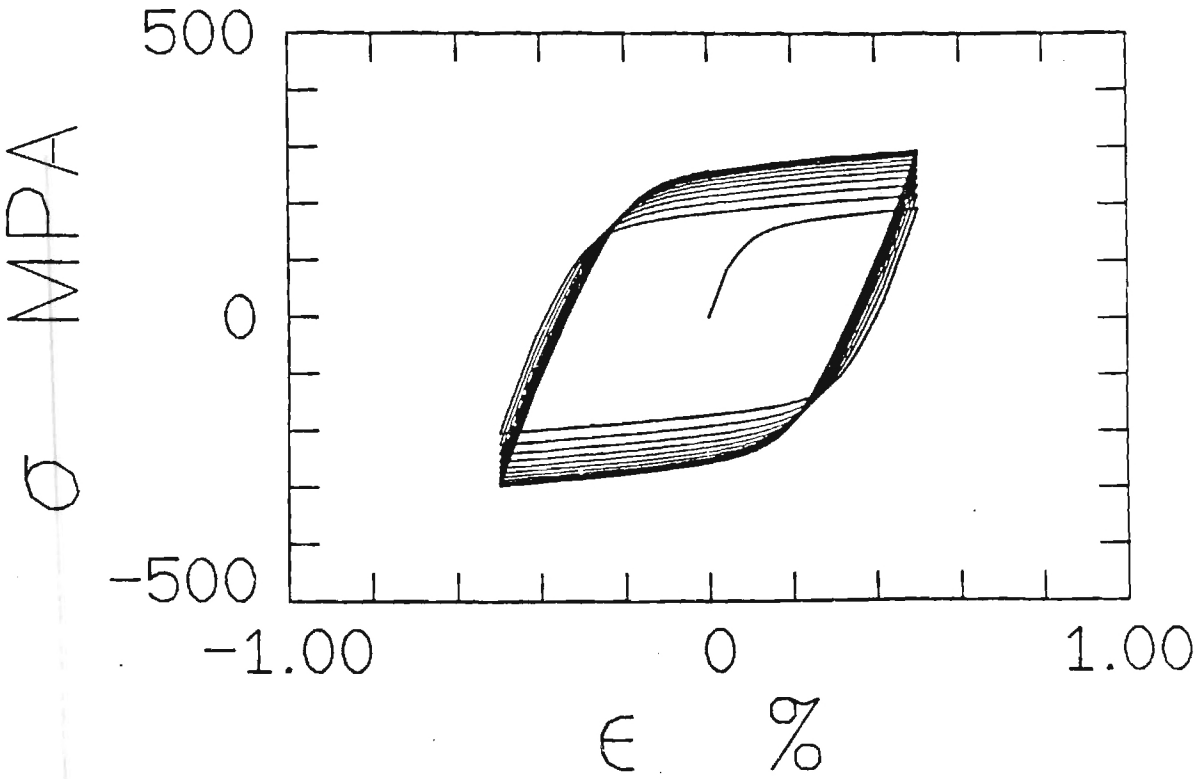

Figure 4. Predicted response for a uniaxial cyclic strain-controlled history at a strain amplitude of 0.5% (first 10 cycles).

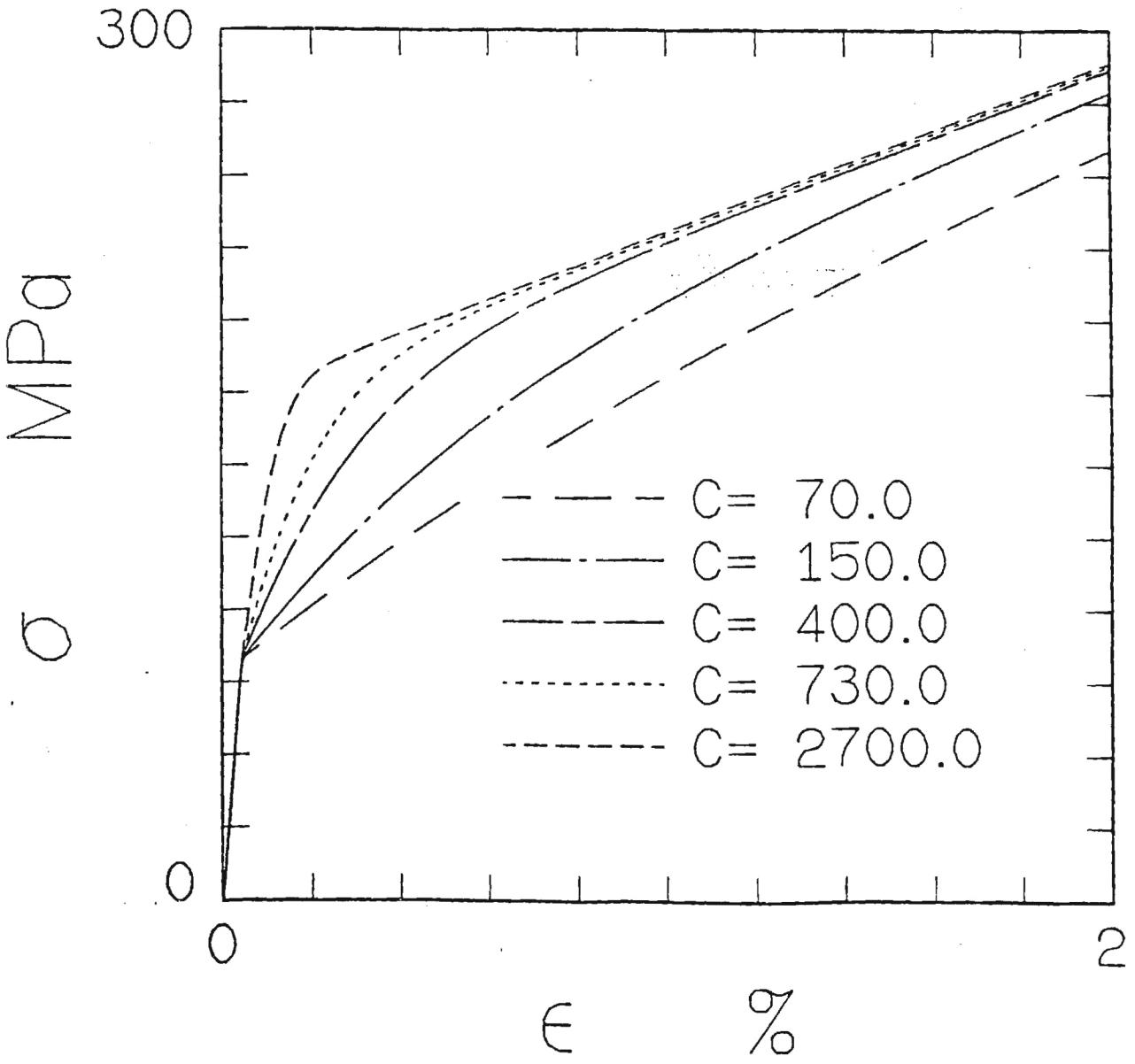

Figure 5. Model behavior for a constant strain rate monotonic test using various constant values of C; δ^g dependence is not included.

A GENERALIZED RATE-DEPENDENT BOUNDING SURFACE MODEL

D.L. McDowell
Associate Professor

J.C. Moosbrugger
Graduate Research Assistant

Georgia Institute of Technology
Atlanta, Georgia 30332

ABSTRACT

The usual format of unified creep-plasticity models with direct hardening/dynamic recovery is briefly reviewed. A rate-dependent bounding surface theory is proposed and its relationship to these "conventional" unified theories is explored. Tensorial state variables in the model are related to thermal and athermal, short and long range obstacles to dislocation motion. Several interesting features regarding multiaxial generalization, nonproportional loading and asymptotic behaviors are discussed. The definition of the image point in the new model is generalized to allow inclusion of arbitrary directional indices for kinematic hardening.

INTRODUCTION

Classical constitutive models for rate-independent inelastic or viscous flow of initially isotropic, polycrystalline metals assume the existence of inelastic or viscous potentials, respectively, which govern the inelastic strain rate and evolution of any internal variables. In cases where the inelastic strain rates vary significantly across regimes which could either be considered rate-independent or viscous, there are two approaches. First, the inelastic and viscous potentials may be summed with no coupling as in classical models. The alternative is to couple the potentials either through internal variable coupling or via combination into a single, rate-dependent potential.

The latter approach is the focus of so-called unified creep- inelasticity or state variable models in which the inelastic strain rate encompasses straining associated with overcoming viscous (thermal) and predominately plastic (athermal) barriers (1-8). Typically, one of the major problems with such unified approaches is the difficulty encountered in accurately predicting viscous or creep behavior when the material constants and parameters are primarily determined from higher strain rate data or vice versa. In addition, the predominate use of uniaxial tests has led to inaccuracies in modeling material behavior under nonproportional loading. The viewpoint taken here is that careful examination of experimental behaviors over a wide range of strain rates, including biaxial nonproportional histories, in conjunction with micromechanical considerations can lead to a more general unified framework.

It is useful to consider a conceptual framework for existing models. Typically, two internal variables are chosen as a minimum set. One, associated with kinematic hardening or deformation induced anisotropy is often termed the backstress, internal stress or equilibrium stress and is associated with the fluctuating stress field produced by the accumulation of dislocation lines at or near glide obstacles in the operant slip planes. The other internal variable is associated with isotropic hardening effects. In rate-independent plasticity, it is typically associated with the yield surface dimension. In the unified theories it is analogously included, most often, as a viscous drag stress, implying that the inherent resistance to dislocation glide is dependent upon the deformation history. These internal variables are associated with microstructurally local stresses produced by dislocation rearrangements.

As a somewhat specific form, consider the isothermal framework employed by Walker (7) and Chaboche (8), albeit with slightly different functional dependencies. These theories are selected as representative of a direct hardening/dynamic recovery format. For simplicity, we restrict consideration to the small strain case. The inelastic strain rate $\dot{\underset{\sim}{\varepsilon}}^{in}$ and internal or equilibrium stress rate $\dot{\underset{\sim}{\alpha}}$ are given by

$$\dot{\underset{\sim}{\varepsilon}}^{in} = f(||\underset{\sim}{s} - \underset{\sim}{\alpha}||, K)\ (\underset{\sim}{s} - \underset{\sim}{\alpha}) \qquad (1)$$

$$\dot{\underset{\sim}{\alpha}} = C(\rho)\ \left[a'\underset{\sim}{n} - h(\rho)\underset{\sim}{\alpha}\right]\ ||\dot{\underset{\sim}{\varepsilon}}^{in}|| - R(||\underset{\sim}{\alpha}||)\ \underset{\sim}{\alpha} \qquad (2)$$

where

$$||\dot{\underset{\sim}{\varepsilon}}^n|| = (\dot{\underset{\sim}{\varepsilon}}^n : \dot{\underset{\sim}{\varepsilon}}^n)^{1/2}, \qquad (3)$$

$R(||\underset{\sim}{\alpha}||)$ is a static thermal recovery function, and $\rho = \int ||\dot{\underset{\sim}{\varepsilon}}^n|| dt$.

It should be noted that C is considered independent of ρ in nearly all viscoplastic theories of this form. The static thermal recovery term provides a Bailey-Orowan (7) format for the balance of microstructural hardening and recovery processes.

The term $-Ch\underset{\sim}{g}||\underset{\sim}{g}||$ in equation (2) is referred to as a dynamic recovery term and provides nonlinear kinematic hardening behavior even at high inelastic strain rates where static thermal recovery effects are negligible. This term was first proposed by Armstrong and Frederick (10). The isotropic hardening parameter is denoted by K and depends on the accumulated inelastic strain path length, i.e. $K = \hat{K}(\rho)$. Likewise, as seen in equation (2), the nonlinear kinematic hardening is in general dependent on ρ. The coefficient of direct hardening, a', is generally regarded as isothermally constant. The inelastic strain rate function f usually is expressed as a power law or exponential-type function of effective overstress $||\underset{\sim}{s} - \underset{\sim}{g}||$ normalized by K.

It should be noted that hardening effects associated with accumulation of inelastic strain are reflected in both the flow rule through K and in the evolution of $\underset{\sim}{g}$ through the ρ-dependent coefficients. Both $C(\rho)$ and $a'(\rho)$ saturate to constant values as $\rho \to \infty$. At strain rates high enough to neglect static thermal recovery and at "large" strains, $||\underset{\sim}{g}||$ achieves the rate-independent limit $||\underset{\sim}{g}|| = a'(\rho)$ in the limit as $\rho \to \infty$. Hence, the asymptotic or saturation behavior of $\underset{\sim}{g}$ at high strain rates is assumed to be independent of inelastic strain path history and strain rate.

The equivalence with a two surface Mroz-type hardening theory with a bounding surface has been established for a kinematic internal variable whose evolution is prescribed by the hardening/dynamic recovery format of equation (2) with $h(\rho) = 1$; this equivalence was first pointed out by Marquis (11) and was subsequently discussed by Chaboche and Rousselier (12). This equivalence is extremely important in view of the accuracy of correlations obtained with two surface theories based on a Mroz-type kinematic hardening rule for multiaxial nonproportional cyclic plasticity (13-18). Furthermore, it reveals that isotropic hardening in the above formulation may appear in both the flow rule and the kinematic hardening rule; its presence in the former affects the inelastic strain rate and in the latter affects the rate of kinematic hardening. Based on this equivalence with a simple two surface theory form and with the previously demonstrated inaccuracy of Prager hardening for $\underset{\sim}{g}$ (19) in multiaxial experiments, the dynamic recovery term is viewed as essential for proper multiaxial generalization. We should note, of course, that this term has already been established as necessary for proper correlation of experimental uniaxial data (c.f. James et al. (20)). Based on experimental observations, it appears that a heuristic necessary condition for multiaxial generalization of any rate-dependent theory is that it collapse to a multiple loading surface interpretation with Mroz- or near Mroz-type kinematic hardening behavior; inclusion of the dynamic recovery term is necessary to satisfy this condition.

With the foregoing equivalence with bounding surface theory established, it is necessary to appeal to microstructural considerations to obtain physically based multiaxial generalizations. Such generalizations should comply with (i) the presence of thermal and athermal obstacles to dislocation motion with different amplitudes and spatial periodicities, (ii) rate-dependence of dislocation substructures, and (iii) the possibility of tensorial indices other than $\underset{\sim}{g}$ for dynamic recovery associated with dislocation cross-slip or climb around obstacles. These three features will be respectively addressed by

(i) decomposition of $\underset{\sim}{g}$ into thermal and athermal, predominately short and long range components, respectively;
(ii) rate-dependence of the direct hardening coefficient for the internal stress component associated with dislocation interactions with thermal, predominately short range barriers; and
(iii) generalization of the definition of the "image point" on the bounding surface toward which the short range internal stress may translate.

All of these features are addressed in the context of a rate-dependent bounding surface model in the next section.

RATE-DEPENDENT BOUNDING SURFACE MODEL

Short and Long Range Internal Stresses

We adopt the view that the net force on mobile dislocations required to achieve a given mean velocity is isothermally invariant; it is the rate of directional (kinematic) material hardening (due to the interaction of mobile dislocations with other dislocations and other microstructural defects) which changes with deformation history, resulting in increasing flow stress, for example, under cyclic hardening conditions. The isotropic or nondirectional hardening affects the size of the stress space domain in which the internal stress can evolve rather than the initial "yielding" behavior. The coupling of viscous and plastic effects is accomplished via distinction between internal stress fields associated with thermal barriers to dislocation glide and those which are primarily athermal. This distinction arises from recognition that obstacles to dislocation glide may or may not be bypassed depending on the relative magnitude of the activation energy associated with the prevailing bypass mechanism.

We refer to the work of Chen, Gilman and Head (21), Gillis and Gilman (22), Solomon and Nix (23) and Ahlquist and Nix (24) regarding the influence of the internal stress field on mean dislocation velocity. Though the total internal stress field associated with dislocation arrangement is necessarily self-equilibrated, the component of internal stress which is manifested in macroscopic response, as viewed by Solomon and Nix and by the authors, is related to the magnitude and frequency of the peaks of the actual distribution rather than the mean values in any grain. This component of internal stress can, in fact, produce inelastic strain rate in the absence of macroscopically applied stress. Lowe and Miller (26-27), among others, have recognized the role of short and long range barriers in the development of internal stress fields. They cite the work of Mughrabi who observed distinct long and short wavelength periodicities in the curvature of free primary dislocations in neutron irradiated copper as direct microstructural evidence. Short range barriers

(several Burgers vectors in extent) are considered to be primarily of a thermal nature. That is, thermally activated processes can assist dislocations in bypassing or penetrating these barriers. Long range barriers are considered to be primarily of an athermal nature, i,e. the activation energies associated with the processes by which dislocations can bypass or penetrate these barriers are high and characterized by weak temperature dependence.

There is experimental evidence (23,24,28-29,31) indicating that the magnitude of internal stress $\underset{\sim}{g}$ is a very significant fraction of the applied stress. Though $\underset{\sim}{g}$ is not observable in the strict sense, its magnitude may be estimated indirectly via the flow potential. The reported experimental estimates of $\underset{\sim}{g}$ are typically on the order of 60% to 80% of the magnitude of the applied stress $||\underset{\sim}{s}||$ at various rates of prestrain.

The short range, predominately thermal barriers provide the rate-controlling feature of viscoplastic, rate-sensitive deformation behavior. Dislocations moving in the vicinity of short range barriers are alternately hindered and assisted by the fluctuating short range internal stress fields set up by pile-ups at precipitates, entanglements, etc. There is a marked transitory short range microstructural rearrangement associated with a change of macroscopic strain rate or loading direction, in contrast to the rather more slowly evolving long range microstructure. This argument is very similar to the distinction drawn by Lowe and Miller (26-27) between very short range, thermal and short range, athermal internal stresses. At extremely high strain rates typical of shock loading, for example, the dislocation density is extremely high and the cell structure is very fine (30). These nonlinear, strain rate-dependent changes in the character of the stalemating capability of short range barriers can be appropriately included in the direct hardening term in equation (2) through coefficient a'.

In addition, isotropic hardening associated with immobilization of dislocations at short range obstacles affects the rate of stalemating processes at the short range barriers; hence, the hardening rate of the short range internal stress increases as the immobile dislocation density increases. This effect may be incorporated in coefficient a' through dependence on the inelastic strain path history, for example.

The notion that the viscous drag force should be reflected by the short range internal stress introduces the possibility that the overstress is not necessarily a strong function of inelastic strain rate, as implied by theories which assume that the internal stress hardening functions are linear in strain rate. The validity of either viewpoint, however, is extremely difficult to assess on the basis of only uniaxial experiments since the directional indices for all of the terms are collinear. Since the evolution of short range internal stress in the former approach is highly transient and nonlinearly strain rate-dependent, uniaxial unloading or stress dip experiments to determine the internal stress may be subject to error unless great care is given to precise control and temporal resolution of data acquistion. Nonproportional loading experiments, in contrast, provide more information regarding the internal stress magnitude since the inelastic strain rate is collinear with $(\underset{\sim}{s} - \underset{\sim}{g})$. Analyses we have conducted on experimental data on Ni-base superalloy Hastelloy X at 650°C (31) subjected to sinusoidal, cyclic nonproportional tension-torsion loading at different effective strain rates indicated that the internal stress is a very significant fraction of the peak applied effective stress (~ 60% to 80%) and that the coefficients of the direct hardening/dynamic recovery terms were rate-dependent. Consequently, the overstress was not as large nor did it vary with strain rate as much as predicted with rate-independent coefficients. These tests were conducted at strain rates high enough to validate neglect of static thermal recovery terms. Additionally, analysis of nonproportional cyclic loading experiments on type 304 stainless steel by McDowell (16-17) revealed that the magnitude of the internal stress $\underset{\sim}{g}$ even after a tremendous amount of cyclic hardening was approximately 70% to 80% of the peak applied effective stress.

Obviously, a complete micromechanical treatment of the various processes involved and the coupling between them is beyond the scope of any continuum model. In the continuum model to be discussed here, we will attempt to describe the macroscopic material behavior through a viscoplastic potential which captures strain rate sensitivity over a wide range of strain rates. Coupling of viscous and plastic effects is accomplished by prescribing evolution equations for two kinematic hardening internal variables. One is associated with material hardening due to interaction of mobile dislocations with short range barriers. The other is associated with interactions of mobile dislocations with long range barriers. These interactions are described by the sum of these two kinematic hardening variables,

$$\underset{\sim}{\alpha} = \underset{\sim}{\alpha}^{sr} + \underset{\sim}{\alpha}^{*} \tag{4}$$

which represents the center of a viscoplastic potential surface in deviatoric stress space. Short and long range internal stresses are denoted by $\underset{\sim}{\alpha}^{sr}$ and $\underset{\sim}{\alpha}^{*}$, respectively. The evolution equations for these kinematic hardening variables reflect the dominant thermal or athermal nature of associated short or long range barriers. The postulated evolution equation for the short range internal stress will lead to a rate-dependent bounding surface of a von-Mises form which bounds the region of evolution of the short range internal stress in deviatoric stress space.

Rate-Dependent Bounding Surface Interpretation

The interpretation of the proposed preceding framework in terms of a rate-dependent bounding surface model is surprisingly direct and concise. In this section, we introduce a bounding surface formulation with a generalized image point for kinematic hardening of the short range internal stress. The rate-dependent flow rule is

$$\dot{\underset{\sim}{\epsilon}}^{n} = \left[\frac{3}{2}\right]^{1/2} A\langle J_{\alpha} - \kappa\rangle^{n} \exp\left[B\langle J_{\alpha} - \kappa\rangle^{n+1}\right] \underset{\sim}{n} \tag{5}$$

where

$$J_{\alpha} = \left[\frac{3}{2}(\underset{\sim}{s} - \underset{\sim}{\alpha}):(\underset{\sim}{s} - \underset{\sim}{\alpha})\right]^{1/2} = \left[\frac{3}{2}\right]^{1/2} ||\underset{\sim}{s} - \underset{\sim}{\alpha}|| \tag{6}$$

and

$$\underset{\sim}{n} = \frac{\underset{\sim}{s} - \underset{\sim}{\alpha}}{||\underset{\sim}{s} - \underset{\sim}{\alpha}||} \tag{7}$$

There is no consistency condition to be met in the rate-dependent case, i.e. the stress point may lie outside of the rate-independent yield surface $J_{\alpha}(\underset{\sim}{s}-\underset{\sim}{\beta}) = \kappa$. Here, A, B and n are regarded as constants in the isothermal case. We admit the possibility that κ may be a repository for isotropic hardening although, as discussed later, we do not seek to place the emphasis on this point offered by the vast majority of unified theories. This flow rule, as discussed by Nouailhas (32), approximates the hyperbolic sine function often used for more accurate correlation of strain rate sensitivity over a wide range of inelastic strain rates. Essentially, the exponential flow potential results in a variable viscosity exponent, when viewed in terms of more conventional power law representations. It should be noted that Lowe and Miller (26-27) have similarly based the flow potential on the sum of short and long range internal stresses.

The hardening rates for long and short range internal stresses are respectively given by

$$\dot{\underset{\sim}{\alpha}}^{*} = C^{*}\,\dot{\underset{\sim}{\epsilon}}^{n} - \underset{\sim}{N}^{*}(\underset{\sim}{\alpha}^{*}) \tag{8}$$

$$\dot{\underset{\sim}{\alpha}}^{sr} = C(\delta^{g})\left[\, a\underset{\sim}{\lambda}^{g} - \underset{\sim}{\alpha}^{sr}\right] ||\dot{\underset{\sim}{\epsilon}}^{n}|| - \underset{\sim}{N}^{sr}(\underset{\sim}{\alpha}^{sr}) \tag{9}$$

where $\underset{\sim}{N}^{*}$ and $\underset{\sim}{N}^{sr}$ are static thermal recovery functions and parameters δ^{g} and $\underset{\sim}{\lambda}^{g}$ are associated with the bounding surface defined by $J_{\alpha}(\underset{\sim}{s}-\underset{\sim}{\beta}^{*}) = R^{*}$. Note the similarity of the evolution law for short range internal stress with that for $\underset{\sim}{\beta}$ in the framework outlined in equations (1)-(3). Note that coeficient "a" in equation (9) in general includes isotropic hardening associated with both short and long range barriers. In addition, "a" is in general strain rate-dependent to incorporate rate-dependence of the saturation dislocation density. These features of the model will be discussed later.

Define the bounding surface radius R^{*} and the image point $\underset{\sim}{s}^{g}$ on the bounding surface by

$$\left[\frac{2}{3}\right]^{1/2} R^{*} = a + ||\underset{\sim}{s} - \underset{\sim}{\alpha}|| \tag{10}$$

$$\underset{\sim}{s}^{g} = \left[\frac{2}{3}\right]^{1/2} R^{*}\underset{\sim}{\lambda}^{g} + \underset{\sim}{\alpha}^{*} = (a + ||\underset{\sim}{s} - \underset{\sim}{\alpha}||)\underset{\sim}{\lambda}^{g} + \underset{\sim}{\alpha} - \underset{\sim}{\alpha}^{sr} \tag{11}$$

where "a" is the coefficient of the direct hardening term in equation (9). The norm of the vector from $\underset{\sim}{\beta}^{sr}$ to the image point configuration, as shown geometrically in Figure 1, may be expressed in terms of internal variables within the present model framework, i.e.

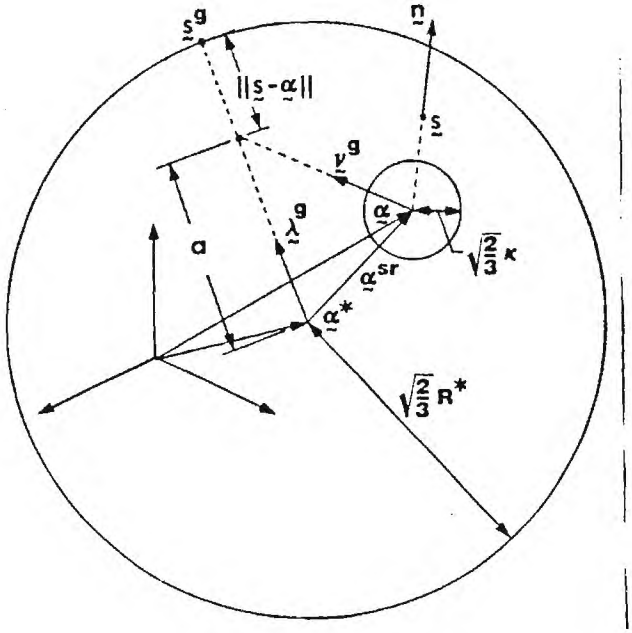

Fig. 1 Geometric interpretation of the rate-dependent bounding surface model in the deviatoric stress space.

$$\delta^{g} = ||\, a\underset{\sim}{\lambda}^{g} - \underset{\sim}{\alpha}^{sr}\,|| \tag{12}$$

and the unit vector $\underset{\sim}{\nu}^{g}$ in this direction is given by

$$\underset{\sim}{\nu}^{g} = \frac{a\underset{\sim}{\lambda}^{g} - \underset{\sim}{\alpha}^{sr}}{\delta^{g}} \tag{13}$$

As $\delta \to 0$, $||\underset{\sim}{\beta}^{sr}|| \to a$ which attributes to "a" the meaning of saturation level of short range internal stress. Obviously, from equation (10), "a" is a component of the bounding surface radius. The bounding surface in this framework can be associated with saturation of internal stress and continuing hardening at long range obstacles.

It has been consistently noted (19-39) in studies of rate-independent nonproportional loading data that a hardening modulus based on the Mroz distance vector, i.e. the special case $\underset{\sim}{\lambda} = \underset{\sim}{\mu}$, provides good correlation of data. In other words, the nonproportionality of the next loading increment affects the inelastic strain rate. In the current rate-dependent framework, this dependence on δ^{g} (which is also rate-dependent) is admitted through $C(\delta^{g})$. From equations (10) and (13), it is clear that equation (9) may be written as

$$\dot{\underset{\sim}{\alpha}}^{sr} = \delta^{g}\, C(\delta^{g})\, ||\dot{\underset{\sim}{\epsilon}}^{n}||\, \underset{\sim}{\nu}^{g} - \underset{\sim}{N}^{sr}(\underset{\sim}{\alpha}^{sr}) \tag{14}$$

The hardening rule in equation (14) is essentially equivalent to that offered by McDowell et al. (33-34) for modeling creep-plasticity interaction of type 304 stainless steel at 593°C, although in that earlier work the idenification with the direct hardening/dynamic recovery format was not made. Furthermore, in this earlier work by McDowell, the flow potential was made to depend only on the short range internal stress as defined in this work.

A generalized image point formulation may permit more accurate representation of dislocation rearrangements over a wide range of strain rates. Experiments (19,35,39) have shown that the direction of the rate of $\underset{\sim}{\alpha}$ may be more closely related to that of the deviatoric stress rate than the inelastic strain rate, at least within some ranges of strain rates or loading regimes. Perhaps the most compelling reason for mathematical generalization of the image point concept is the possibility of deriving a particular (not necessarily Mroz-type) image point from first principles, e.g. a mechanically and micromechanically consistent analysis of slip for a polycrystalline aggregate subjected to nonproportional loading. Such a development would also serve as a more fundamental foundation for bounding surface theory in addition to its proven capability for experimental correlation.

Figure 1 depicts the geometrical interpretation of this bounding surface theory in the deviatoric stress plane.

A very important additional aspect of this approach is the inclusion of rate-dependence and isotropic hardening in the bounding surface through parameter "a". The hardening coefficient "a" may be written as

$$a = a_o\left[F(\theta) + \Sigma(q, \Lambda, \theta, ||\underset{\sim}{\alpha}^{sr}||) + \varsigma F\dot{\Sigma}\right] \qquad (15)$$

where a_o is a temperature-dependent constant and Σ is a temperature-dependent history functional of inelastic strain amplitude q, nonproportionality factor Λ (as described elsewhere (15-16)), overstress $\theta = ||\underset{\sim}{s}-\underset{\sim}{\alpha}||$, and the magnitude of short range internal stress. The term $a_o\Sigma$ is the component of "a" which is affected by isotropic hardening and is representative of the average immobile dislocation density at both short and long range barriers of predominately athermal character. Hence, the possibility that isotropic hardening depends on inelastic strain rate history is included. Parameter ς prescribes the coupling between isotropic hardening and the instantaneous strain rate. From the work of Krempl and Lu (36), $\varsigma = 0$ for type 304 stainless steel at room temperature and there is no coupling between the viscous and plastic components; as pointed out by Krempl, ς is not necessarily zero for all materials (37). Krempl (37) also points out the general impropriety of including isotropic hardening effects in the flow rule since this implies that the viscous overstress versus inelastic strain rate relation is always affected by isotropic hardening. The present theory interprets this coupling chiefly as an effect on the short range internal stress rate; although the flow rule with constant κ cannot instantaneously reflect this coupling with a sudden change in strain rate, the rapid evolution of the short range internal stress may render extremely difficult differentiation of the results of the two approaches based on uniaxial tests only. The present theory assumes that isotropic hardening processes affect viscous drag force on dislocations predominately via g^{sr} rather than attenuation of overstress via κ. Such a distinction is most easily assessed by analysis of results from multiaxial nonproportional loading histories; as discussed in a previous section, multiaxial nonproportional experimental evidence exists to motivate this inclusion of isotropic hardening (36,39) and rate-dependence (31) in the evolution equation for g^{sr}. Krempl (37-38) also introduces the possibility of including both rate-dependence and isotropic hardening in the coefficient of direct hardening for the equilibrium or internal stress rate.

Function F introduces the nonlinear effect of effectively increasing activation energy of thermal barriers with increasing inelastic strain rate in addition to a decrease in mean free path between short range obstacles; in other words, the directional hardening is strain rate-dependent because the set of effective stalemating obstacles is not invariant with strain rate. Function F can be directly interpreted as the strain rate sensitivity of the asymptotic or bounding, i.e. "large" strain, stress-strain response. The function F also can reflect inverse strain rate sensitivity.

For very high strain rates at which the flow potential is quite nonlinear in overstress J_α, this feature permits description of the highly workhardened microstructure and the corresponding high internal stress field, in contrast to the strain rate invariant directional hardening incorporated in numerous other theories. Refer to Clifton (40) for a review of the operative dislocation mechanisms at high strain rates.

The present model is complete with prescription of specific forms for $C(\delta g)$, F, Σ and recovery functions $\mathcal{N}^{sr}$ and $\mathcal{N}^*$.

Creep, Stress Relaxation, and High Strain Rate Behaviors

Since the current model applies to a continuum of inelastic strain rates ranging from the creep rates to high strain rates, it is necessary to examine the asymptotic behavior of the model in these regimes. We present an abbreviated outline of asymptotic behaviors in this paper.

Consider first the asymptotic behavior of the rate-dependent model at high enough strain rates to neglect static thermal recovery effects. The magnitude of the short range internal stress saturates in the asymptotic regime of flow stress to

$$||\underset{\sim}{\alpha}^{sr}|| = a \qquad (16)$$

which is obviously a function of both isotropic hardening and inelastic strain rate or overstress. Hence, in this approach there is no rate-independent form for the state variable g at high strain rates in contrast to several analogous theories (7-8).

The transient nature of creep and stress relaxation is dependent on overstress $||\underset{\sim}{s} - \underset{\sim}{g}||$. Hence, both the transient, short range and steady long range hardening processes embedded in g contribute. Since the growth of g is nonlinear and depends on inelastic strain rate, creep or stress relaxation behavior will obviously depend on prior loading history. For example, creep tests conducted at the same stress levels after different prior loading histories will exhibit different transient responses.

Let us first consider the stress (load)-controlled creep test. After primary creep transients reflecting rearrangement of dislocation structures at short range obstacles have subsided, steady state conditions will be reached. Steady state corresponds to saturation of the internal stress $\underset{\sim}{g}$, i.e.

$$\dot{\underset{\sim}{\alpha}} = \underset{\sim}{0} = C\dot{\underset{\sim}{\epsilon}}^{*}\underset{\sim}{n} + C\left[a\underset{\sim}{\lambda}^{g} - \underset{\sim}{\alpha}^{sr} \right]||\dot{\underset{\sim}{\epsilon}}^{n}|| - \underset{\sim}{N}^{sr}(\underset{\sim}{\alpha}^{sr}) - \underset{\sim}{N}^{*}(\underset{\sim}{\alpha}^{*}) \tag{17}$$

such that the static thermal recovery functions must balance all hardening processes. In the approach to steady state creep conditions it would generally be expected that the internal stress would approach collinearity with the deviatoric stress, i.e. $\underset{\sim}{\lambda}^{g} \rightarrow \underset{\sim}{n}$. Since the hardening vs. recovery processes at short and long range barriers are physically distinct, we may assume that both the long and short range internal stresses eventually saturate at some steady state. However, the asymptotic approach to the steady state may occur at different rates for the long and short range backstresses. Most relevant observations indicate that dislocation arrangements at short range barriers approach steady state fairly quickly, with this evolution reflected in the primary creep behavior. On the other hand, the long range internal stress may approach a steady state more slowly. The net effect is that the creep response may appear to have reached steady state at rather small strains, but may never quite reach such a state metallurgically nor in terms of the present model since the damage effect may be reflected in the creep response prior to steady state. In an engineering sense, we may operationally define a steady state creep response as corresponding to the minimum creep rate observed in a standard test, i.e. just prior to the tertiary stage. Then we may assume that the balance of hardening and thermal recovery holds for dislocation structures at both short and long range barriers, i.e.

$$C\left[a\underset{\sim}{\lambda}^{g} - \underset{\sim}{\alpha}^{sr} \right]||\dot{\underset{\sim}{\epsilon}}^{n}|| = \underset{\sim}{N}^{sr}(\underset{\sim}{\alpha}^{sr}) \tag{18}$$

$$C\dot{\underset{\sim}{\epsilon}}^{*}\underset{\sim}{n} = \underset{\sim}{N}^{*}(\underset{\sim}{\alpha}^{*}) \tag{19}$$

In view of the nonlinearity of the recovery terms, it is clear that the internal stress at steady state creep is rate-dependent. Furthermore, since the left hand side of equation (18) is nonlinearly rate-dependent, the recovery term $\underset{\sim}{N}^{sr}$ need not necessarily be as large as in most theories, nor of the same nonlinear form.

Primary creep behavior is largely related to the overstress-dependent parameter C which governs transient response of the short range internal stress. The marked transient rate of stress relaxation during strain hold periods is also heavily dependent on C, while the static thermal recovery terms govern the rate of recovery at long times as discussed by Walker (7); it should be noted that large static thermal recovery terms can lead to unrealistic stress relaxation at long times in conventional unified theories. The creep and relaxation behaviors are analogous processes both physically and in the constitutive equations; essentially, only the boundary conditions are different.

At very high strain rates (e.g. $> 10^{1} - 10^{2}$ sec^{-1}), formulations in which C and "a" are constants essentially lead to a strain rate-independent evolution of $\underset{\sim}{g}$. This implies that the resistance to dislocation motion is offered by rate-independent barriers. The present model considers a "viscous" resisting force associated with the viscoplastic component of the internal stress, $\underset{\sim}{g}^{sr}$, which increases in concert with the applied stress. This rate-dependent increase in the strength of short range barriers may be attributed to decreased mean free path of stalemating events and to inertial forces on dislocations as discussed by Clifton (40); the latter effects may be extremely localized and quite unstable.

There is a fundamental physical difference between the two approaches. Namely, the first approach suggests that the hardened microstructure, reflected by $\underset{\sim}{g}$, is essentially invariant with respect to strain rate once static thermal recovery terms can be safely neglected. This infers that the set of obstacles or mechanisms which resist dislocation motion and the nature of these obstacles is invariant with respect to strain rate. Yet, as mentioned earlier, the dislocation density and cell size of specimens tested at extremely high strain rates is markedly different from that of specimens tested at moderate strain rates to the same level of strain. The extent of microstructural hardening is significantly greater and of a different spatial character at the very high strain rate. Clifton (40) attributes this chiefly to increasing mobile dislocation density at increasing strain rate. This can be reflected physically through rate-dependence of the internal stress evolution, in particular in the dependence of Σ on overstress.

It may also be shown (41) that neglect of rate-dependence in coefficient "a" and static thermal recovery terms results in a rate-independent bounding surface formulation which includes kinematic hardening of both the yield surface and bounding surface. Interestingly, this particular formulation involves both a Prager-type and image point directed kinematic hardening increment for the yield surface (42).

SOME IMPLICATIONS OF THE BOUNDING SURFACE FORMULATION

Some important features of the bounding surface model will be examined in this section with some brief illustrative numerical calculations. Special attention is focused on the dependence of coefficient C in equation (9) on δ^{g} and associated implications for accurate modeling of the initial yielding portion of the stress-strain response.

Figures 2-6 illustrate some examples of model behavior for uniaxial and for multiaxial cyclic strain-controlled histories and will be discussed shortly. In these calculations, we choose $C(\delta^{g})$ of the form

$$C(\delta^{g}/2a) = C_{o}\left\{1 + C_{f}\left[1 - \exp\left[-C_{d}(\delta^{g}/2a)^{m}\right]\right]\right\} \tag{20}$$

where δ^{g} in this case is defined in accordance with a Mroz-type rule, i.e. $\underset{\sim}{\lambda}^{g} = \underset{\sim}{n}$.

It should be emphasized that the model constants were determined from several sources (14-16,43-44) in order to be somewhat representative of the behavior of type 304 and 316 stainless steels for the purpose of illustrating certain features of the model. They do not, however, represent an optimal set for accurately describing the actual behavior of either material at a particular temperature and range of strain rates since this is not the intent of the present work. Hence, the methodology of determination of constants reported here is of an inherently approximate nature; refer to Ref. (33) for details of more precise isothermal characterization of a given material. Constants A, B and n were determined from constant strain rate monotonic test results reported by Abrahamson (43) with the assumption that

$$||\underset{\sim}{s} - \underset{\sim}{g}|| = 0.4\,\sigma_f \qquad (21)$$

where σ_f is the flow stress at 4% plastic strain. This assumption is based on the approximate asymptotic level of $\underset{\sim}{g}$ noted in experiments (23-25,29,31,39).

Rate-dependence in the coefficient of the direct hardening term for the short range backstress is included via dependence of the limit surface radius on overstress, i.e.

$$a = (2/3)^{1/2} R^* - ||\underset{\sim}{s} - \underset{\sim}{g}|| \qquad (22)$$

$$R^* = R_1^* + R_2^* \qquad (23)$$

$$R_2^* = M\, J_\alpha^{m_1} \qquad (24)$$

Isotropic hardening effects, including dependence on inelastic strain path length and nonproportionality of the loading history, are included through evolution of R_1^* by incorporating the model due to McDowell (44) arrived at through the analysis of data from nonproportional cyclic strain controlled histories imposed on type 304 stainless steel at room temperature (19,39), i.e.

$$\dot{R}_1^* = \bar{\mu}\left[\bar{R}_1^*(\Lambda) - R_1^*\right]||\dot{\underset{\sim}{\epsilon}}^p|| \qquad (25)$$

where

$$\bar{R}_1^* = R_o + h_1(\Lambda)^{h_2} \qquad (26)$$

and Λ denotes dependence on nonproportionality of the loading history. The definition of R_1^* in equation (26) is taken from Ref. (44) with the simplification h_2 = constant in this work. The value of h_2 is taken as representative of the level of nonproportionality associated with a biaxial path to be considered in this study.

An initial limit surface radius was taken to be $R_1^* = 34.5$ MPa and a constant effective strain rate of 0.002 sec^{-1} was used for all calculations. Note that $\zeta = 0$ in this formulation, as supported by experiments on austenitic stainless steels (36). Again, it is emphasized that the model constants are selected to be representative in only an approximate way of a wide range of temperatures and strain rates for austenitic types 304/316 stainless steels in the absence of static thermal recovery effects. A summary of model constants selected for example calculations is as follows:

κ = 10 MPa	$\underset{\sim}{N}^* = \underset{\sim}{0}$, $\underset{\sim}{N}^{sr} = \underset{\sim}{0}$
$\bar{\mu}$ = 10	C^* = 3000 MPa
ν = 0.29 (elastic Poisson's ratio)	
G = 75.2 X 10^3 MPa (elastic shear modulus)	
A = 3.6 X 10^{-10}	B = 2.73 X 10^{-10}
n = 4.5	m_1 = 0.85
C_o = 72	M = 1.34
C_f = 36	R_o = 175 MPa
C_d = 10	h_1 = 175 MPa
m = 1.8	h_2 = 0.6

Units of stress and time are MPa and sec, respectively.

Referring to Figures 2-3, it is clear that the present framework is suitable for representation of nonproportional cyclic loading histories. A strain-controlled, room temperature tension-torsion square path history enforced on a thin-walled tubular, type 304 stainless steel specimen by Ohashi et al. (45) is shown with the results of the rate-dependent bounding surface theory juxtaposed. Though the amplitudes of the predicted and experimental results are not in precise agreement, owing to the approximate nature of the parameter selection procedure which was independent of these particular experimental results, the character of the response is accurately predicted. This is not surprising, of course, since the bounding surface theory is expected to perform well for such nonproportional cyclic loading histories (16-19,39,44). The dependence of C on $\delta\underset{\sim}{g}$ in the current model, to be discussed in the next paragraph, and the generalized image point offer the potential for very precise correlation of the detailed features of nonproportional loading histories.

In Figure 4, the cyclic hardening behavior characteristic of this class of materials from the annealed condition is displayed by the model for constant amplitude cycling at ± 0.5% strain. The smooth transition from initial yielding to the asymptotic response is noted in particular. It must be emphasized that the radius κ of the purely elastic regime is extremely small as noted above. This smooth transition emerges primarily from the dependence of C on $\delta\underset{\sim}{g}$ in equation (20). It must be emphasized that this dependence is not embodied in current unified theories, but is extremely relevant to the practical problems of modeling mean stress relaxation and rachetting at cyclic strain amplitudes of small magnitude. For example, Chaboche and co-workers (32,46) effectively decompose the internal stress $\underset{\sim}{g}$ into an arbitrary number (usually two) of components which evolve with independent hardening/dynamic recovery rules to more accurately capture the work-hardening response just after initial yielding at each reversal. In the present theory, this is accomplished in essence by the introduction of the two tensorial variables $\underset{\sim}{g}^{sr}$ and $\underset{\sim}{g}^*$; however, the introduction of dependence of C on $\delta\underset{\sim}{g}$ is the key to accurate modeling of the transition from initial yielding to asymptotic behavior in the context of a single direct hardening/dynamic recovery evolution equation for $\underset{\sim}{g}^{sr}$. The component $\underset{\sim}{g}^*$ defines the asymptotic response exclusively. A continuous

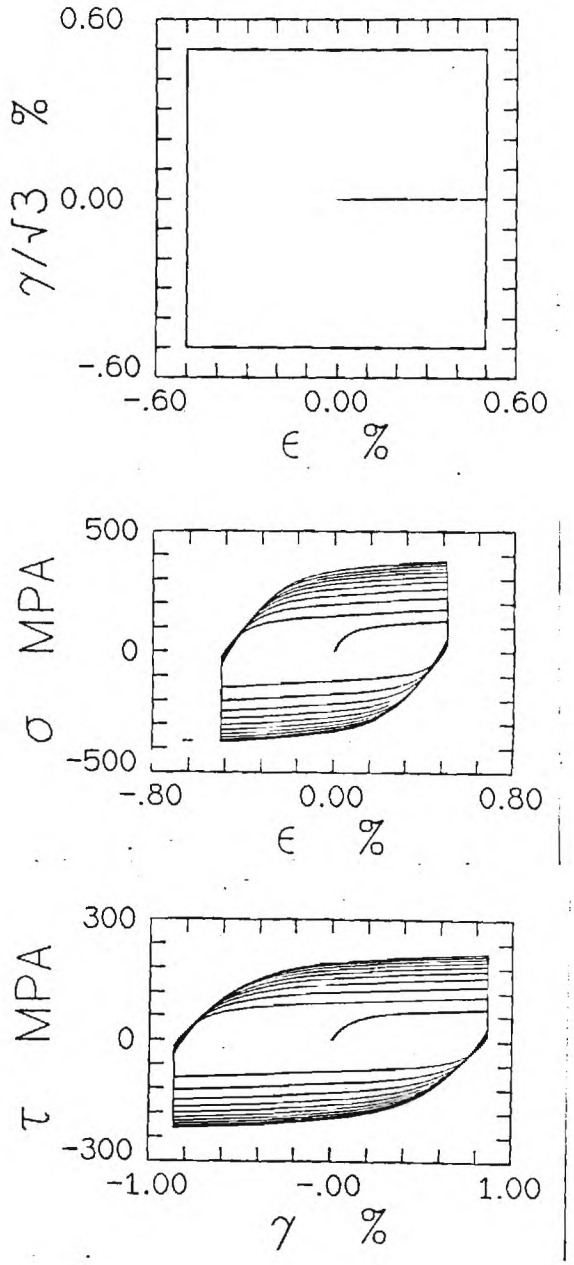

Fig. 2 Nonproportional cyclic strain-controlled history (first 10 cycles) :
(a) Strain path imposed in axial strain - shear strain space,
(b) Model prediction for axial stress vs. axial strain response,
(c) Model prediction for shear stress v.. Shear strain response,

dependence on $\delta\xi$ is reflected in $C(\delta\xi)$ in the spirit of rate-independent two surface theories. Furthermore, it is most likely necessary to decompose the internal stress ξ into more than two components à la Chaboche to achieve the accuracy and generality offered by the current framework with $C(\delta\xi)$. Finally, the decomposition offered herein is based on short and long range internal stresses, motivated by dislocation arguments; Chaboche and associates evidently decomposed ξ to obtain a better fit to experimental data.

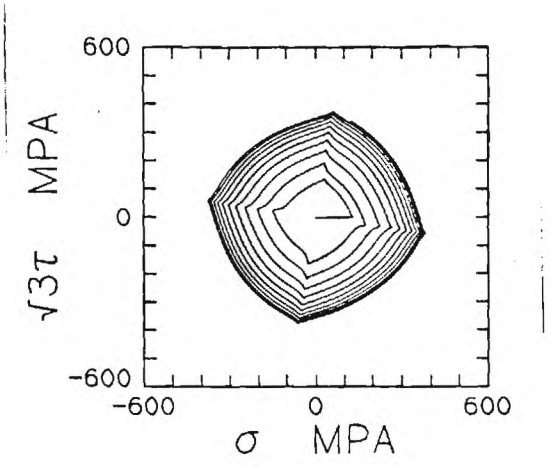

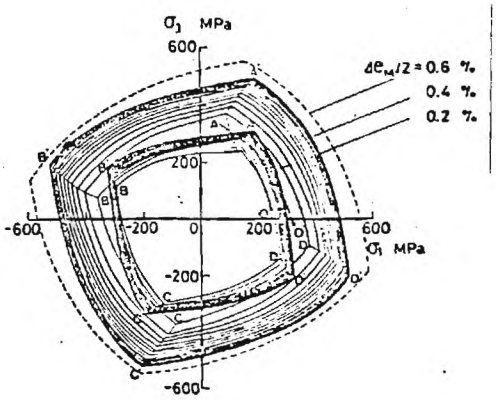

Fig. 3 Nonproportional cyclic strain-controlled history (first 10 cycles) for history shown in Figure 2: Stress space response; model prediction (upper) and experimental results of Ohashi et al. (45) for geometrically similar strain space paths imposed on type 316 stainless steel at room temperature (lower). Note that $\sigma_1=\sigma$, $\sigma_3=\sqrt{3}\tau$ and $\Delta e_M/2=\Delta\epsilon/2$.

To illustrate the consequences of the dependence of C on $\delta\xi$, model computations were made for strain-controlled, monotonic uniaxial tests with C = constant and with $C = C(\delta\xi)$. In Figure 5, the responses are shown for C = constant ($C_d = 0$) for various C values. It is noted that the approach to the asymptotic or bounding behavior may be varied with C in this case, but the "initial yielding" behavior is strongly affected; even moderate C values, for example, lead to a marked discontinuity in the stress-strain response at small strains. The use of high C values to minimize this discontinuity results in unrealistically rapid approach to asymptotic behavior, a feature often noted in current unified theories. Figure 6 depicts the range of

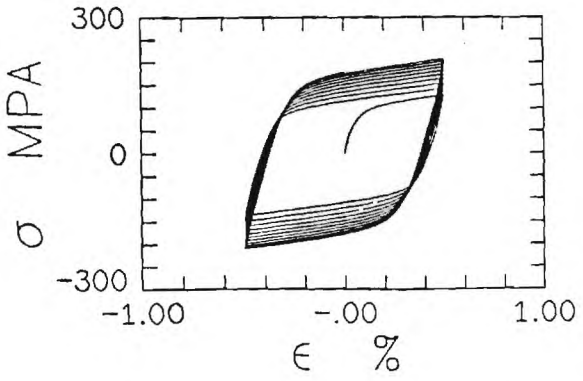

Fig. 4 Predicted response for a uniaxial cyclic strain-controlled history at a strain amplitude of 0.5% (first 10 cycles).

stress-strain behaviors which can be achieved with C = $C(\delta\bar{\varepsilon})$ by varying C_d in equation (20) with C_o, C_f and m listed above; in contrast to Figure 5, note that both a high initial tangent modulus and a smooth transition from elastic behavior to elastic-viscoplastic behavior is obtained for a range of C_d values, whereas this cannot be accomplished with any constant C value. Hence, the full nonlinear transition may be described accurately by the

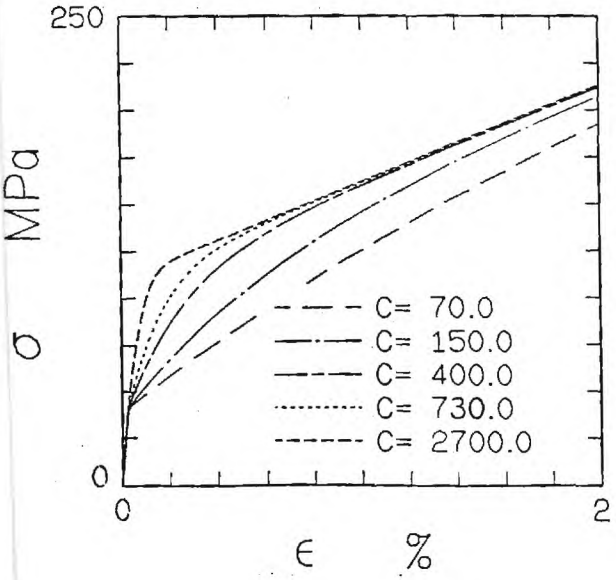

Fig. 5 Model behavior for a constant strain rate monotonic test using various constant values of C; $\delta\bar{\varepsilon}$ dependence is not included.

evolution of the short range internal stress. This of course has important implications for prediction of stress relaxation, rachetting, and inelastic strain ranges for creep-fatigue calculations under both proportional and nonproportional loading histories of typically small to moderate strain amplitude or magnitude.

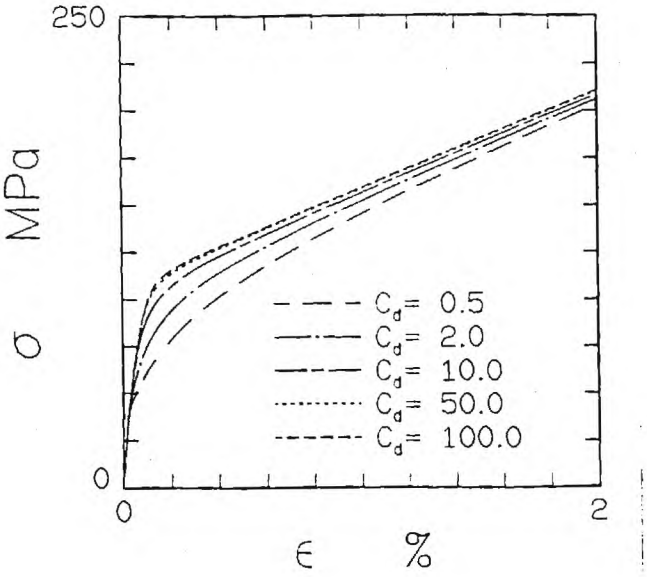

Fig. 6 Model behavior for a constant strain rate monotonic test using various values of C_d (equation (20)) with C_o, C_f and m equal to the values given in the text.

In this work, we have discussed behavior for only a single strain rate for rather restricted histories when static thermal recovery is negligible. Some of the subtleties of the current approach have been highlighted. The model captures cyclic behavior, including nonproportional loading paths, and the full elastic-viscoplastic transition to asymptotic stress-strain response. The creep behavior has been discussed elsewhere (33-34).

CONCLUSIONS

A rate-dependent bounding surface model has been proposed as an accurate multiaxial generalization of unified creep-plasticity theory. Its relationship to several existing unified theories with hardening/dynamic recovery format is explored. Several key departures from these existing theories are noted, motivated by experimental observations. The definition of the image point associated with the bounding surface in the new model is generalized to allow inclusion of arbitrary directional indices for kinematic hardening. In addition, the bounding surface radius is allowed to depend on both the inelastic strain rate and the effective inelastic strain path length. As a result, there is no unique rate-independent asymptotic behavior at high strain rate. Furthermore, static thermal recovery terms are not required to balance a direct hardening term linear in inelastic strain rate, a requirement of many existing theories which limits accuracy of combined correlation of both cyclic and creep behaviors.

ACKNOWLEDGMENTS

The authors are grateful for the support of the U.S. National Science Foundation (NSF MSM-8601889; MSM-8552714) for support of this work.

REFERENCES

1. Lindholm, U.S., Chan, K.S., Bodner, S.R., Weber, R.M., Walker, K.P., and Cassenti, B.N., "Constitutive Modeling for Isotropic Materials," NASA CR-174980, SwRI-7476/30, 1985.
2. Pugh, C. E., and Robinson, D.N., "Some Trends in Constitutive Equation Model Development for High-Temperature Behavior Model Development for High-Temperature Behavior of Fast-Reactor Structural Alloys," Nuc. Engr. and Design, Vol. 48, 1978, pp. 269-276.
3. Krieg, R. D., Swearengen, J. C., and Rohde, R. W., "A Physically-Based Internal Variable Model for Rate-Dependent Plasticity," Inelastic Behavior of Pressure Vessel and Piping Components (Eds. Chang and Krempl), PVP-PB-028, ASME, 1978, pp. 15-28.
4. Lagneborg, R., "A Modified Recovery-Creep Model and its Evaluation," Metal Science Journal, Vol. 6, 1972, pp. 127-133.
5. Bodner, S.R., and Partom, Y., "Constitutive Equations for Elastic-Viscoplastic Strain Hardening Materials," ASME J. of Applied Mechanics, Vol. 42, 1975, pp. 385-389.
6. Hart, E.W., "Constitutive Relations for Non-Elastic Deformations of Metals," J. Eng. Mat. and Technology, Trans. ASME, Volume 98, 1976.
7. Walker, K.P., "Research and Development Program for Nonlinear Structural Modeling with Advanced Time-Temperature Dependent Constitutive Relationships," NASA Report CR-165533, NASA Lewis RC, Nov. 1981.
8. Chaboche, J.L., "Description Thermodynamicque et Phénomenologique de la Viscoplasticité Cyclique avec Endommagement," Publication No. 1978-3 of the Office National d'Etudes et de Researches Aerospatiales, France, 1978.
9. Chaboche, J.L., "Viscoplastic Constitutive Equations for the Description of Cyclic and Anisotropic Behaviour of Metals," Bull. de l' Acad. Polonaise des Sciences, Série Sc. et Techn., Vol. 25, No. 1, 1977, pp. 33-42.
10. Armstrong, P.J., and Frederick, C.O., "A Mathematical Representation of the Multiaxial Bauschinger Effect," C.E.G.B. Report RD/B/N 731, 1966.
11. Marquis, D., "Sur un Modèle de Plasticité rendant compte du Comportement Cyclique," 3ème Congrès Francais de Mécanique, Nancy, 1979.
12. Chaboche, J. L., and Rousselier, G., "On the Plastic and Viscoplastic Constitutive Equations- Part I: Rules Developed With Internal Variable Concept," ASME J. Pressure Vessel Technology, Vol. 105, 1983, pp. 153-158.
13. Dafalias, Y.F., and Popov, E.P., "A Model of Nonlinearly Hardening Materials for Complex Loading," Acta Mechanica, Vol. 21, 1975, pp. 173-192.
14. Dafalias, Y.F., "Modeling Cyclic Plasticity: Simplicity Versus Sophistication," Mechanics of Engineering Materials, Eds. Desai and Gallagher, John Wiley and Sons, 1984, pp. 153-178.
15. Krieg, R.D., "A Practical Two Surface Plasticity Theory," ASME Journal of Applied Mechanics, Vol. 42, 1975, pp. 641-646.
16. McDowell, D.L., "A Two Surface Model for Transient Nonproportional Cyclic Plasticity: Part I - Development of Appropriate Equations," ASME Journal of Applied Mechanics, Volume 52, 1985, pp. 298-302.
17. McDowell, D.L., "A Two Surface Model for Transient Nonproportional Cyclic Plasticity: Part II - Comparison of Theory with Experiments," ASME Journal of Applied Mechanics, Volume 52, 1985, pp. 303-308.
18. Lamba, H.S., and Sidebottom, O.M., "Cyclic Plasticity for Nonproportional Paths: Part 2 - Comparison with Predictions of Three Incremental Plasticity Models," ASME Journal of Engineering Materials and Technology, Vol. 100, 1978, pp. 104-111.
19. McDowell, D.L., "An Experimental Study of the Structure of Constitutive Equations for Nonproportional Cyclic Plasticity," ASME Journal of Engineering Materials and Technology, Vol. 107, 1985, pp. 307-315.
20. James, G.H., Imbrie, P.K., Hill, P.S., Allen, D.H., and Haisler, W.E., "An Experimental Comparison of Several Current Viscoplastic Constitutive Models at Elevated Temperature," ASME J. Engineering Materials and Technology, Vol. 109, 1987, pp. 130-139.
21. Chen, H. S., Gilman, J. and Head, J., "Dislocation Multipoles and Their Role in Strain Hardening ", Journal of Applied Physics, Vol. 35, 1964, pp. 2502-2514.
22. Gillis, P.P. and Gilman, J.J., "Dynamical Dislocation Theory of Crystal Plasticity : Part II. Easy Glide and Strain Hardening," Journal of Applied Physics, Vol. 36, No. 11, Nov. 1963, pp. 3380-3386.
23. Solomon, A.A. and Nix, W.D., "Interpretation of High Temperature Plastic Deformation in Terms of Measured Effective Stresses," Acta Metallurgica, Vol. 18, Aug. 1980, pp. 863-876.
24. Ahlquist, C.N. and Nix, W.D., "The Measurement of Internal Stresses During Creep of Al and Al-Mg Alloys," Acta Metallurgica, Vol. 19, April 1971, pp. 373-385.
25. Gibeling, J.C. and Nix, W.D., "The Description of Elevated Temperature Deformation in Terms of Threshold Stresses and Back Stresses: A Review," Mat. Science and Engineering, Vol. 45, 1980, pp. 123-135.
26. Lowe, T. C., and Miller, A. K., "Improved Constitutive Equations for Modeling Strain Softening-Part I: Conceptual Development," ASME J. Engr. Materials and Technology, Vol. 106, 1984, pp. 337-342.
27. Lowe, T. C., and Miller, A. K., "Improved Constitutive Equations for Modeling Strain Softening-Part II: Predictions for Aluminum," ASME J. Engr. Materials and Technology, Vol. 106, 1984, pp. 343-348.
28. Tsou, J.C. and Quesnel, D.J., "Internal Stress Measurements During the Saturation Fatigue of Polycrystalline Aluminum," Mat. Science and Engineering, Vol. 56, 1982, pp. 289-299.
29. Oytana, C., Delobelle, P., and Mermet, A., "Constitutive Equations Study in Biaxial Stress Experiments," ASME J. Engineering Materials and Technology, Vol. 104, 1982, pp. 1-11.
30. Meyers, A.M., and Chawla, K.K., Mechanical Metallurgy, Prentice-Hall, Inc., 1984.
31. McDowell, D.L., Moosbrugger, J.C., Doumi, M., and Jordan, E.H., "Some Implications for Cyclic Plastic and Viscoplastic Equations Based on Nonproportional Loading Experiments," presented at 3rd Symposium on Nonlinear Constitutive Relations for High-Temperature Applications, NASA, University of Akron, June 11-13, 1986.
32. Nouailhas, D., "A Viscoplastic Modelling Applied to Stainless Steel Behavior, " in Constitutive Laws for Engr. Materials: Theory and Applications, Vol. I, Eds. Desai, Krempl, Kiousis and Kundu, Tucson, Arizona, 1987, pp. 717-724.
33. McDowell, D.L., Ho, K.I., and Stalley, J., "An Anisotropic, Damage-Coupled Viscoplastic Model for Creep-Dominated Cyclic Loading," presented at 3rd Int. Symp. on Nonlinear Fracture Mechanics,

Knoxville, TN, Nov. 1986.
34. McDowell, D.L., Ho, K.I., and Moosbrugger, J.C., "Continuum Damage Representation of Creep-Dominated, Nonproportional Cyclic Loading," to be presented at Int. Seminar on High Temp. Fracture Mechanisms and Mechanics, Dourdan, France, Oct. 13-15, 1987.
35. Phillips, A., and Lee, C.W., "Yield Surfaces and Loading Surfaces. Experiments and Recommendations," International Journal of Solids and Structures, Vol. 15, 1979, pp. 715-729.
36. Krempl, E., and Lu, H., 1984, "The Hardening and Rate-Dependent Behavior of Fully Annealed AISI Type 304 Stainless Steel Under Biaxial In-Phase and Out-of-Phase Strain Cycling at Room Temperature," ASME Journal of Engineering Materials and Technology, Vol. 106, pp. 376-382.
37. Krempl, E., "Models of Viscoplasticity, Some Comments on Equilibrium (Back) Stress and Drag Stress," Report MML 87-2, Mechanics of Materials Laboratory, Rensselaer Polytechnic Institute, February 1987.
38. Krempl, E., and Yao, D., "The Viscoplasticity Theory Based on Overstress Applied to Ratchetting and Cyclic Hardening," Report MML 87-3, Mechanics of Materials Laboratory, Rensselaer Polytechnic Institute, March 1987.
39. McDowell, D.L., "An Evaluation of Recent Developments in Hardening and Flow Rules for Rate-Independent, Nonproportional Cyclic Plasticity," ASME J. Applied Mechanics, Vol. 54, 1987, pp. 323-334.
40. Clifton, R.J., "Dynamic Plasticity," ASME J. Applied Mechanics, Vol. 50, Dec. 1983, pp. 941-952.
41. McDowell, D. L., and Moosbrugger, J. C., "A Rate-Dependent Bounding Surface Model," work in progress, 1987.
42. Yoder, P.J., and McDowell, D.L., "Bounding-Surface Plasticity in Strain Space," revised for publication in Acta Mechanica, September 1987.
43. Abrahamson, T. E., "Modeling the Inelastic Behavior of Type 304 Stainless Steel With a Unified Creep-Plasticity Theory", PhD Thesis, University of Illinois at Urbana-Champaign, Urbana, Illinois, 1983.
44. McDowell, D.L., "Simple Experimentally Motivated Cyclic Plasticity Model," ASCE J. Engineering Mechanics, Vol. 113, No. 3, 1987, pp. 378-397.
45. Ohashi, Y., and Tanaka, E., and Ooka, M., "Plastic Deformation Behavior of Type 316 Stainless Steel Subject to Out-of-Phase Strain Cycles," ASME J. Engineering Materials and Technology, Vol. 107, 1985, pp. 286-292.
46. Chaboche, J.L., "Cyclic Plasticity Modeling and Rachetting Effects," in Constitutive Laws for Engr. Materials: Theory and Applications, Vol. I, Eds. Desai, Krempl, Kiousis and Kundu, Tucson, Arizona, 1987, pp. 47-58.

REVISED

Presented at Int. Seminar on High Temp.
Fracture Mechanisms and Mechanics,
Dourdan, FRANCE Oct. 13-15, 1987

CONTINUUM DAMAGE REPRESENTATION OF CREEP-DOMINATED, NONPROPORTIONAL CYCLIC LOADING

D.L. McDowell, K. Ho and J.C. Moosbrugger

George W. Woodruff School of Mechanical Engineering
Georgia Institute of Technology
Atlanta, GA 30332
USA

SYNOPSIS

The problem of high temperature creep damage in initially isotropic, polycrystalline metals has received considerable attention. Fundamentally, two distinct approaches have emerged which seek to address the evolution of damage at different size scales. The first approach, traditionally encompassing time-fraction rules and remaining life curves is directed toward description of creep-rupture phenomena under variable stress loading histories. The second approach, the "micro-mechanical" treatment, seeks to derive expressions for nucleation and/or growth of voids on grain boundaries with suitable prescription of rupture criteria.

This work is concerned with a continuum approach for modeling of physical grain boundary damage under multiaxial, nonproportional, creep-dominated loading histories. Such histories necessitate description of the anisotropic nature of creep damage accumulation since the rupture time is greatly affected by damage anisotropy. In this work, a general framework for continuum creep damage evolution is presented which extends the work of Murakami and Ohno [1-2], Trampczynski et al. [3-4], and Leckie and Onat [5-6].

CREEP DAMAGE GROWTH LAW

In this paper, we adopt the notion that a spatial distribution of grain boundary cavitation and triple-point cracking may be represented as a continuum quantity. Since creep damage is a bulk phenomenon, such a description is quite reasonable as confirmed by results of homogenization theory [7]. Precedental works of Kachanov [8] and Rabotnov [9] are noted among many others.

In the approach taken by Murakami and Ohno [1-2], a symmetric second rank damage rate tensor was assumed. This results, of course, in a second rank tensor damage distribution regardless of the nonproportionality of the applied loading history. Experiments conducted by Trampczynski, Hayhurst and Leckie [3-4], however, reveal that the creep damage distribution for some materials is highly dependent on principal stress orientation; a second rank tensor representation of physical damage is inadequate. Krajcinovic [10-11] suggests that the directional distribution of physical damage is most appropriately modeled as a dual vector; such a vector can represent, for example, the discontinuity in loading/unloading stiffness exhibited by cracked brittle materials by virtue of crack closure. Leckie and Onat [5-6] suggest stronger conditions, based on damaged material symmetry arguments, which require that a vectorial distribution of damage on the

unit sphere be even with respect to $\underset{\sim}{n}$, i.e.

$$\omega(\underset{\sim}{n}) = \omega(-\underset{\sim}{n}) \tag{1}$$

where $\underset{\sim}{n}$ is a unit vector normal to the unit sphere and $\omega(\underset{\sim}{n})$ is the distribution of damage. If the damage is manifested as an array of cracks, for example, ω may be defined as the area fraction of cracks associated with crack face unit normal vector $\underset{\sim}{n}$ [12]. Leckie and Onat have shown that $\omega(\underset{\sim}{n})$ may be represented by an expansion of even rank symmetric tensors.

In this work, we adopt the symmetry arguments of Leckie and Onat. For grain boundary creep damage, we assume that the orientation and magnitude of damage is defined by the unit normal vector and damaged area fraction of each grain boundary facet, i.e.

$$\omega(\underset{\sim}{n}) = \frac{1}{S_g(\underset{\sim}{n})} \int_V dS_{gd}(\underset{\sim}{n}) \tag{2}$$

where $S_g(\underset{\sim}{n})$ is the total grain boundary facet area in volume V with unit normal vector $\underset{\sim}{n}$, and $dS_{gd}(\underset{\sim}{n})$ is the differential damaged grain boundary facet area associated with unit vector $\underset{\sim}{n}$. The form given in equation (2) permits experimental estimation of $\omega(\underset{\sim}{n})$ from macroscopically homogeneously deformed specimens; for a continuum representation, we may think of the volume of integration as passing to an infinitesimal, i.e. $V \to \delta V$.

Following the development of Leckie and Onat [5-6], we may define the damage distribution $\omega(\underset{\sim}{n})$ in terms of a set $\underset{\sim}{\Gamma}$ of even rank, irreducible tensors obtained from the distribution of damage on the unit sphere. The effect of the current state of damage on damage rate is introduced via stress intensification associated with loss of load bearing area by defect formation and distribution, defect stress concentration, and defect interaction. Effective stress $\underset{\sim}{S}$ may be expressed as a second rank tensor function of Cauchy stress $\underset{\sim}{\sigma}$ and a fourth rank operator $\underset{\sim}{M}(\underset{\sim}{\Gamma})$, i.e.

$$\underset{\sim}{S} = \hat{\underset{\sim}{S}}(\underset{\sim}{M}(\underset{\sim}{\Gamma}), \underset{\sim}{\sigma}) \tag{3}$$

Regarding practical application of such an approach, we may select a "minimal" set $\underset{\sim}{\Gamma}$ based on acceptable approximation of the damage accumulation processes and the rupture criterion. For proportional loading, $\underset{\sim}{\Gamma}$ of rank two may be a sufficient approximation for anisotropic material damage. For nonproportional loading, however, the appropriate rank of $\underset{\sim}{\Gamma}$ depends on both the nonproportionality of the loading history and the nature of the damage distribution.

In this work, we make the simplifying assumption that the principal axes of the Cauchy stress and effective stress coincide, which may be true for proportional loading even up to large cavity volume fractions. However, for nonproportional loading such an assumption suggests a limitation to relatively small cavity volume fractions to ensure that the rotation of the effective stress with respect to the Cauchy stress is suitably small. With this assumption we may express $\underset{\sim}{M}$ in the principal stress coordinate frame as

$$M_{ijkl}(\underset{\sim}{\Gamma}) = \phi_{ij}(\underset{\sim}{\Gamma})\ \delta_{ik}\delta_{jl} \quad \text{(no sum on i and j)} \tag{4}$$

with

$$\underset{\sim}{\phi} = \sum_{j=1}^{3} \Omega^{(j)}\ \underset{\sim}{n}^{(j)} \otimes \underset{\sim}{n}^{(j)} \tag{5}$$

where $\underset{\sim}{\phi}$ is the damage effect tensor with principal components $\Omega^{(j)}$ and eigenvectors $\underset{\sim}{n}^{(j)}$ collinear with those of $\underset{\sim}{\sigma}$. We do not attempt herein to make a direct connection between the definition of $\underset{\sim}{\phi}$ and loss of cross-sectional area in the Cauchy tetrahedron as do Murakami and Ohno [1-2], recognizing that the actual damage distribution is not in general represented by a second rank tensor; rather, $\underset{\sim}{\phi}$ is viewed as an approximation of the intensification effect of grain boundary damage on the current principal stresses and hence influences damage rate.

In this work, we consider only infinitesimal strains and small rotations. Furthermore, the cavity volume fraction is assumed small so that the assumption of equivalence of the principal coordinate frames for effective and Cauchy stresses may be approximately made. Such an assumption is not as physically restrictive as it might seem in view of the typically small cavity volume fraction up to the rupture event. This does not imply that the damage distribution is isotropic, but that the damage rate is tensorially dictated by the current principal directions of $\underset{\sim}{\sigma}$. This results in an anisotropic damage distribution for proportional or nonproportional loading. Density changes associated with damage are neglected, although they may be included as discussed by Chaboche [13]. Isothermal conditions are assumed. We define the growth rate of ω as a function of $\underset{\sim}{\phi}$ and $\underset{\sim}{\sigma}$ in the following simple way:

$$\dot{\omega}(\underset{\sim}{n}) = \xi(\sigma^*) \left[\eta\, \chi^{(1)} \left\{\Omega^{(1)}\right\}^{l(\sigma^*)} + \right. \tag{6}$$

$$\left. (1-\eta) \sum_{j=1}^{3} \chi^{(j)} \left\{\Omega^{(j)}\right\}^{l(\sigma^*)} \left\{ \underset{\sim}{n} \cdot \underset{\sim}{n}^{(j)} \otimes \underset{\sim}{n}^{(j)} \cdot \underset{\sim}{n} \right\} \left\{ \underset{\sim}{n} \cdot \underset{\sim}{n}^{(j)} \right\}^{2P} \right]$$

$$= \dot{\omega}(\underset{\sim}{n})_{\text{isotropic}} + \dot{\omega}(\underset{\sim}{n})_{\text{anisotropic}}$$

which corresponds to the magnitude in direction $\underset{\sim}{n}$ (obtained by 2(P+1) contractions with $\underset{\sim}{n}$) of the symmetric, anisotropic damage rate tensor $\dot{\underset{\sim}{\Gamma}}$ of rank 2(P+1), i.e.

$$\dot{\underset{\sim}{\Gamma}} = \xi(\sigma^*) \left[\eta\, \chi^{(1)} \left\{\Omega^{(1)}\right\}^{l(\sigma^*)} \overset{P+1}{\underset{i=1}{\otimes}} \underset{\sim}{I} + \right. \tag{7}$$

$$\left. (1-\eta) \sum_{j=1}^{3} \chi^{(j)} \left\{\Omega^{(j)}\right\}^{l(\sigma^*)} \overset{2(P+1)}{\underset{i=1}{\otimes}} \left\{\underset{\sim}{n}^{(j)}\right\} \right]$$

where ξ and l are functions of the isochronous stress σ^* (surface of constant rupture time), $\underset{\sim}{n}^{(j)}$ is the unit vector in the j^{th} principal stress direction, σ_j, $\underset{\sim}{n}^{(j)} \cdot \underset{\sim}{n} = n_k^{(j)} n_k$, P is an integer representative of the order of the anisotropic damage distribution, and η is the fraction of damage rate in the $\underset{\sim}{n}^{(1)}$ direction which is isotropic; η is bounded by $0 \leq \eta \leq 1$ and may also be a function of σ^* as discussed later. The value of P is either zero or a positive integer. $\underset{\sim}{I}$ is the identity tensor. The $\Omega^{(j)}$ are the principal components of the damage effect tensor $\underset{\sim}{\phi}$. Factor $\chi^{(j)}$ excludes contribution of compressive principal stresses to the damage rate, i.e.

$$\chi^{(j)} = \left\langle \underset{\sim}{n}^{(j)} \cdot \frac{\underset{\sim}{\sigma}}{|\sigma_j|} \cdot \underset{\sim}{n}^{(j)} \right\rangle \tag{8}$$

where σ_j are the ordered principal stresses with $\sigma_1 \geq \sigma_2 \geq \sigma_3$, and the Macauley bracket $\langle F \rangle = F$ if $F > 0$; $\langle F \rangle = 0$ otherwise. The scalar product of two second rank tensors $\underset{\sim}{A}$ and $\underset{\sim}{C}$ is defined by $(\underset{\sim}{A}:\underset{\sim}{C}) = (A_{ij}C_{ij})^{1/2}$, and the outer product is denoted by $\otimes$; outer products repeated multiplicatively (P+1) and 2(P+1) times are inferred by the summation on $\otimes$ in equation (7).

Several forms may be proposed for $\Omega^{(j)}$. One possibility is that the anisotropic damage rate in principal stress direction $\underset{\sim}{n}^{(j)}$ depends only on the extent of damage in that direction, $\omega(\underset{\sim}{n}^{(j)})$, i.e.

$$\Omega^{(j)} = \frac{1}{1 - \omega(\underset{\sim}{n}^{(j)})} \tag{9}$$

which is a direct anisotropic generalization of the Kachanov-Rabotnov damage approach [14]. Another possibility is that the anisotropic damage rate in the $\underset{\sim}{n}^{(j)}$ direction also depends on η. Such dependence would introduce a significant departure from the spirit of equation (9) only if η is a function of σ^*. We may choose to allow $\Omega^{(j)}$ to depend on $\eta\omega(\underset{\sim}{n}^{(j)})$, recognizing that this quantity provides a lower bound on the damage oriented orthogonal to the $\underset{\sim}{n}^{(j)}$ direction. A simple way to introduce nonlinear dependence on η is by defining a symmetric, second rank tensor $\underset{\sim}{\zeta}^{(j)}$ defined uniquely by each $\omega(\underset{\sim}{n}^{(j)})$, in analogy to the definition proposed by Murakami and Ohno [1], as

$$\underset{\sim}{\zeta}^{(j)} = \left[\underset{\sim}{I} - \underset{\sim}{\Pi}(\underset{\sim}{n}^{(j)}) \right]^{-1} \tag{10}$$

where $\underset{\sim}{\Pi}$ is defined by

$$\underset{\sim}{\Pi}(\underset{\sim}{n}^{(j)}) = \omega(\underset{\sim}{n}^{(j)}) \left[\eta + (1 - \eta)\, \underset{\sim}{n}^{(j)} \otimes \underset{\sim}{n}^{(j)}\right] \tag{11}$$

The $\underset{\sim}{\phi}$ components in this case are expressed as $\Omega^{(j)} = (\underset{\sim}{\zeta}^{(j)}:\underset{\sim}{\zeta}^{(j)})^{1/2}$, i.e.

STANDARD PAGE DEPTH

LONG PAGE DEPTH

$$\Omega^{(j)} = \left[\frac{1}{(1 - \omega(\underset{\sim}{n}^{(j)}))^2} + \frac{2}{(1 - \eta\omega(\underset{\sim}{n}^{(j)}))^2} \right]^{1/2} \tag{12}$$

Essentially, this equation assumes that the stress intensification effect associated with each of the damage values $\omega(\underset{\sim}{n}^{(j)})$ is represented by a symmetric, second rank tensor defined by $\omega(\underset{\sim}{n}^{(j)})$, but dependent on η. The scalar multiplier $\Omega^{(j)}$ directly affects evolution of the ω distribution, as seen in equation (6). It should be noted that for isotropic hardening, the damage rate equation assumes the classical Kachanov-Rabotnov form. It is assumed in equation (6) that the evolution of the isotropic component of the ω distribution is dictated by the effect of the damage in the tensile principal stress directions; the isotropic component of damage exists because of constraints between contiguous grains which are affected by relative orientation, extent of grain boundary sliding, etc. As reflected in the isochronous stress, the dilatational and distortional stress invariants affect the rate of creep damage accumulation in addition to the tensile principal stresses.

It is necessary to introduce a specific definition for the isochronous stress. As discussed by Hayhurst et al. [3-4] and Lemaitre and Chaboche [15-18], the isochronous stress is a level surface in stress space denoting equivalent rupture times; it is a function of the maximum principal stress, the second invariant of deviatoric stress, and the hydrostatic stress. Based on the rather extensive experimental work of Huddleston [19], who considered several materials and various biaxiality ratios, the isochronous stress is defined as

$$\sigma^* = \frac{3}{2} S_1 \left(\frac{2}{3} \frac{\sigma_e}{S_1} \right)^a \exp\left[b\{1 + f(J_1)\langle -J_1/|J_1|\rangle\}\left(\frac{J_1}{S_s} - 1\right) \right] \tag{13}$$

where

$$S_1 = \sigma_1 - \frac{1}{3}\sigma_{kk} \tag{14}$$

$$\sigma_e = \left[(3/2)\underset{\sim}{s} : \underset{\sim}{s} \right]^{1/2} \tag{15}$$

$$\underset{\sim}{s} = \underset{\sim}{\sigma} - \frac{1}{3}\sigma_{kk}\,\underset{\sim}{I} \tag{16}$$

$$S_s = \left[\sigma_1^2 + \sigma_2^2 + \sigma_3^2 \right]^{1/2} \tag{17}$$

$$J_1 = \sigma_{kk} \tag{18}$$

It should be noted that this form of the isochronous stress is a slightly altered form of that proposed by Huddleston. Very little data were available in the biaxial regime with an in-plane compressive principal stress of greater magnitude than the tensile stress, i.e. a negative J_1. The approach offered by

Huddleston is hence modified by inclusion of the term $(1+f(J_1)\langle -J_1/|J_1|\rangle)$, which must be experimentally determined.

This form of the isochronous stress has been rather thoroughly supported by a variety of biaxial creep experiments on tubular specimens of type 304 stainless steel at 593°C at ORNL, including axial tension, equi-biaxial tension (axial tension and pressure), internal pressure, torsion, axial tension and torsion, and axial compression and torsion. It should be noted that this form of σ^* was verified for loading magnitudes which would be expected to lead to matrix power law creep governed grain boundary damage accumulation.

It is important to examine the role of exponent P in governing the anisotropy of the damage distribution. P = 0 only if the actual damage distribution $\omega(\underline{n})$ takes the form of a symmetric second rank tensor. This is approximately the case for type 304 stainless steel at 593°C as will be discussed later. For an isotropically damaging material with $\eta = 1$, the second term in equations (6)-(7) does not apply since the anisotropic component of the damage rate is zero. The results of Trampczynski et al. [3-4] for copper indicate a high degree of anisotropy, and hence a larger value of P.

Obviously, the integrated damage distribution $\omega(\underline{n})$ will depend on whether the loading history is proportional or nonproportional. Rotation of the principal stress eigenvectors will in general result in multiple "peaks" in the damage distribution with respect to a fixed material coordinate system. From a practical viewpoint, depending on the rank of the tensorial damage distribution, it may be desirable to express the distribution either precisely in terms of tensor components or approximately in terms of ω values at a discrete number of points on the unit sphere. In the latter case, an interpolation algorithm may be necessary to estimate the ω value in any arbitrary direction. The former representation is desirable for second and perhaps even fourth rank damage tensors, while the latter would seem the only practical route for distributions of higher rank.

Omission of the functional dependence of l on σ^* in equations (6)-(7) would imply that time fraction and damage (for proportional loading) are uniquely related, which does not allow description of multiple isochronous stress level sequence effects (nonlinear damage accumulation) [16-18] if the rupture criterion is stress-independent. In this paper, we will be concerned with correlation of experiments performed at constant isochronous stress and hence do not require explicit stress level-dependence of l, but such dependence offers no particular difficulty. This dependence is physically necessitated by the stress level-dependence of cavity growth mechanisms as reflected in void growth mechanisms maps [20-22], and is supported by experiments cited by Chaboche et al. [16-17] in which the measured damage growth is retarded as a function of time fraction t/t_R as the isochronous stress level increases. The deleterious effects of low-high stress level sequences and the accumulation of greater creep damage under low stress than high stress conditions at the same time fraction are well-documented [23]. In view of the stress-dependence of cavity growth mechanisms (c.f. [20-22]) and the associated differences in void aspect ratios and constraints in regimes of diffusion-dominated versus matrix power law creep-dominated void growth, it may be necessary to admit dependence of the anisotropy of the damage distribution on stress, i.e. $P = P(\sigma^*)$ and $\eta = \eta(\sigma^*)$.

If the microstructure is unstable and aging effects such as precipitation or coarsening exist, it is necessary to include these effects via description of precipitation/coarsening kinetics. The function $\xi(\sigma^*)$ in equations (6)-(7) is based on the assumption of a fixed number of void nucleation sites and a stable microstructure. As discussed by Leckie and Onat [5-6], a separate evolution equation may be introduced for void nucleation rate. Certainly, void nucleation rate may be associated with intersections of slip bands with grain boundaries and with the precipitation of grain boundary carbides, so that inelastic rate of deformation and diffusion kinetics must both be considered. In this study, we will present correlation with isothermal creep histories at only a constant isochronous

stress level for each material such that aging effects are implicitly embedded in the constants and parameters of the evolution equations for damage and creep deformation. For histories involving significant changes in isochronous stress or temperature, consideration must be given to explicit state variables representing, for example, precipitate size and spacing. Aging is an important consideration for predicting long term rupture performance based on short term tests, though it is not the subject of this paper; proper description of aging effects warrants careful parallel studies.

Another key element of the damage formulation is the rupture criterion. Previous discussion has assumed that ω_{max} = constant at rupture. It is clear from previous work [5-6,23] that the extent of creep damage just prior to the final rupture event depends on stress level. If a stress level-dependent rupture criteria is adopted, then the damage at rupture is not constant and the time fraction at any given damage level, even for constant λ, depends on the isochronous stress for proportional loading. A stress level-dependent rupture criterion is more difficult to implement since experimental investigation of the damage distribution at different stress levels is quite involved. Existing data are somewhat sketchy and incomplete. The logical approximation to the physically more precise stress level-dependent rupture criterion is the first approach, i.e. the assumption of a constant damage at failure. This approximation is most likely suitable, even for variable load histories, since the damage growth is highly nonlinear only near the final rupture event. Therefore, from a practical viewpoint, the use of a constant damage at rupture is likely to be sufficient, especially in view of the inherent scatter in creep rupture tests. Hence, the rupture criterion

$$\omega_{max} = \max_{\text{all } \underset{\sim}{n}} \omega(\underset{\sim}{n}) = 1 \tag{19}$$

is selected in this work. It should be noted, however, that the definition of damage offered in equation (2) in conjunction with equation (19) does not imply that the area fraction of cavitated grain boundaries is unity at rupture; the area fraction of cavitated segments normal to $\underset{\sim}{n}$ is unity. For a highly anisotropically damaging material, the total area fraction of cavitated grain boundaries may be quite low. It can be shown, for example, that the area fraction of damaged grain boundary segments upon satisfaction of equation (19) for uniaxial loading is expressed as the mean value of $\omega(\underset{\sim}{n})$ over the unit sphere as

$$f_h = \frac{2(P+1)\eta + 1}{2P + 3} \tag{20}$$

For example, for $\eta = 0$ and $P = 1$ ($\underset{\sim}{\Gamma}$ of rank four), $f_h = 0.2$ at rupture. If the damage is isotropic, $\eta = 1$ and $f_h = 1$ at rupture. If $\underset{\sim}{\Gamma}$ is second rank, $P = 0$ and $f_h = (2\eta + 1)/3$, i.e. the hydrostatic component of $\underset{\sim}{\Gamma}$.

Finally, it should be noted that under conditions of finite strain, the damage distribution must evolve in reference to a material coordinate frame, necessitating an appropriate finite strain formulation [1-2,13] and consideration of material density changes [13,24].

CORRELATION WITH NONPROPORTIONAL CREEP HISTORIES

It is necessary to implement the foregoing damage formulation in a viscoplastic constitutive framework of desired sophistication and accuracy. In this section, we

will first discuss the selected form of the coupling with a rather general viscoplastic model framework. Then we will specialize to unified creep-plasticity and power-law creep constitutive laws for comparison of high temperature, nonproportional creep rupture experiments conducted on type 304 stainless steel and pure copper, respectively.

The constitutive model for rate-dependent deviatoric inelasticity must be coupled with the damage distribution just presented. An isothermal framework for achieving this coupling for small cavity volume fractions is as follows:

viscoplastic flow rule:
$$\dot{\underset{\sim}{\epsilon}}^{n} = f(\underset{\sim}{s}D,\ \underset{\sim}{\alpha}D,\ \kappa) \tag{21}$$

hardening rules:

kinematic:
$$\dot{\underset{\sim}{\alpha}}D = H_{\alpha}(\underset{\sim}{s}D,\ \underset{\sim}{\alpha}D,\ K^{*})\ ||\dot{\underset{\sim}{\epsilon}}^{n}||\ \underset{\sim}{\nu} - R_{\alpha}(\underset{\sim}{\alpha}D)\ \underset{\sim}{\alpha}D \tag{22}$$

isotropic:
$$\dot{\kappa} = G_{\kappa}(\underset{\sim}{s}D,\ \underset{\sim}{\alpha}D,\ \kappa)\ ||\dot{\underset{\sim}{\epsilon}}^{n}|| - R_{\kappa}(\kappa) \tag{23}$$

$$\dot{K}^{*} = G_{R^{*}}(\underset{\sim}{s}D,\ \underset{\sim}{\alpha}D,\ K^{*})\ ||\dot{\underset{\sim}{\epsilon}}^{n}|| - R_{K^{*}}(K^{*}) \tag{24}$$

Here deviatoric stress $\underset{\sim}{s} = \underset{\sim}{\sigma} - (\sigma_{kk}/3)\underset{\sim}{I}$, and backstress $\underset{\sim}{\alpha}$ is deviatoric. The inelastic strain $\underset{\sim}{\epsilon}^{n}$ includes both conventional creep and plastic strain as in other unified theories. The backstress reflects, in a general sense, directional internal stress fields associated with dislocation entanglements at both thermal and athermal barriers. Scalar state variables K^{*} and κ introduce strain hardening/softening effects in the backstress evolution and flow rules, respectively. Equations (21)-(24) include a hardening/recovery format typical of existing unified creep-plasticity approaches (c.f. [25-32]). Additionally, the directional index $\underset{\sim}{\nu}$ may be selected to correspond to a hardening/dynamic recovery format in the first term for $\underset{\sim}{\alpha}$, as shown by Rousellier and Chaboche [33-34].

Note that the effect of damage is reflected by a multiplicative factor D and the product $\underset{\sim}{s}D$, for example, can be thought of as an effective stress for the viscoplastic deformation. As stated by Leckie [5-6] and viewed herein as a tentative approximation, experiments show that the influence of the damage tensor on the creep rate is isotropic and monotonically increasing, even into the tertiary regime. This has been demonstrated even for materials which damage in a highly anisotropic manner [6]. In detailed experiments on intentionally perforated specimens, Murakami [2] has shown that the influence of cavity volume fraction on stress-strain response is isotropic for cavity fractions up to a few percent, a typical range for engineering alloys up to rupture. These results, of course, are necessary to admit scalar D to couple damage with the deformation response; obviously, D must be related to the mean value of the w distribution, i.e.

$$D = \hat{D}(\Psi) \tag{25}$$

where Ψ is defined by

$$\Psi = \frac{1}{4\pi} \int_{A_u} \omega(\underset{\sim}{n})\, dA \qquad (26)$$

Note that the effect of damage on the tertiary creep rate will remain unaltered upon rotation of the principal stress axes with this formulation as is experimentally observed [3-6].

A very useful recursion formula may be derived by considering the mean value over the unit sphere of the damage rate distribution, i.e.

$$\dot{\Psi} = \eta\, \dot{\omega}(\underset{\sim}{n}^{(1)}) + \sum_{j=1}^{3} \frac{1}{(2P+3)} \left[\dot{\omega}(\underset{\sim}{n}^{(j)}) - \eta\, \dot{\omega}(\underset{\sim}{n}^{(1)}) \right] \qquad (27)$$

with the initial (undamaged) condition $\Psi(0) = 0$, where

$$\dot{\omega}(\underset{\sim}{n}^{(j)}) = \xi(\sigma^*) \left[\eta\, \chi^{(1)} \left\{ \Omega^{(1)} \right\}^{l(\sigma^*)} + (1-\eta)\, \chi^{(j)} \left\{ \Omega^{(j)} \right\}^{l(\sigma^*)} \right] \qquad (28)$$

In the more general case of larger cavity volume fractions [2], we must define an appropriate effective stress $\underset{\sim}{S}^c$ derived from an operation of a fourth rank tensor $\underset{\sim}{\underset{\sim}{I}}(\phi)$ on the applied stress

$$\underset{\sim}{S}^c = \frac{1}{2} \left\{ \underset{\sim}{\underset{\sim}{I}} : \underset{\sim}{\sigma} + \left(\underset{\sim}{\underset{\sim}{I}} : \underset{\sim}{\sigma} \right)^T \right\} \qquad (29)$$

where $\underset{\sim}{\underset{\sim}{I}}(\phi)$ may be expressed in terms of ϕ and its scalar invariants vis-à-vis the representation theorem for isotropic tensor functions [35]; the constants in this representation may be selected to fit experimental results. In addition, an effective backstress $\underset{\sim}{\beta}^c$ must be analogously defined through a fourth rank tensor transformation; such a representation would obviously be quite complex, providing strong impetus for the aforementioned assumption of the isotropy of the damage effect on creep deformation. As pointed out by Chaboche, inclusion of damage in the viscoplastic potential would result in an additional damage coefficient which leads to volumetric inelastic strain. It should be noted that $\underset{\sim}{S}^c$ and $\underset{\sim}{\beta}^c$ would replace $D\underset{\sim}{S}$ and $D\underset{\sim}{\beta}$ in equations (21)-(24) in the case of large cavity fractions.

It should be mentioned that the elastic compliance is also affected by the presence of creep damage, although an explicit form for this dependence is not presented in this work. Let T be absolute temperature. Assuming the Helmholtz free energy density can be decomposed into elastic and viscous components [11,13],

$$\psi = \psi^e(\underset{\sim}{\epsilon}^e, \underset{\sim}{\Gamma}, T) + \psi^v(\underset{\sim}{\alpha}, \kappa, K^*, \underset{\sim}{\Gamma}, T) \qquad (30)$$

along with $\underset{\sim}{\epsilon} = \underset{\sim}{\epsilon}^e + \underset{\sim}{\epsilon}^n$ leads to the thermoelastic relation

$$\underset{\sim}{\sigma} = \rho \frac{\partial \psi}{\partial \underset{\sim}{\epsilon}^e} \tag{31}$$

which obviously depends on the damage distribution through $\underset{\sim}{\Gamma}$.

The coupling of damage with two significantly different viscoplastic formulations is discussed next.

A. Rate-Dependent Bounding Surface Formulation: Type 304 Stainless Steel at 593°C

For multiaxial cyclic plasticity, it has previously been demonstrated that a bounding surface approach [36-41] provides very good correlation of nonproportional deformation behavior. Since such behavior is of concern to nonproportional cyclic histories, a recently introduced [42] strain-hardening model based on a rate-dependent bounding surface with a Mroz translation rule for backstress is adopted. Key features of this theory include isotropic hardening reflected through growth of the bounding surface rather than a scalar parameter in the flow rule, and rate-dependence of the backstress evolution even at high strain rates. These features contrast with conventional unified creep-plasticity models (c.f. [25-32]). Rate-dependence is reflected primarily through bounding surface dependence on overstress, strain-hardening is reflected through growth of the bounding surface, and smooth yielding response is obtained through use of the Mroz distance vector in the backstress hardening rate coefficient.

Briefly, the damage-coupled bounding surface model can be stated in multiaxial form as

$$\dot{\underset{\sim}{\epsilon}}^n = \frac{3}{2} K \langle \bar{\sigma} D - K_o \rangle^n \exp(Z \langle \bar{\sigma} D - K_o \rangle^{n+1}) \; (\underset{\sim}{s} - \underset{\sim}{\alpha})/\bar{\sigma} \tag{32}$$

where

$$\bar{\sigma} = [(3/2)(\underset{\sim}{s} - \underset{\sim}{\alpha}) : (\underset{\sim}{s} - \underset{\sim}{\alpha})]^{1/2} = \sqrt{3/2} \; ||\underset{\sim}{s} - \underset{\sim}{\alpha}|| \tag{33}$$

$$\bar{\alpha} = [(3/2) \; \underset{\sim}{\alpha} : \underset{\sim}{\alpha}]^{1/2} \tag{34}$$

Here deviatoric stress $\underset{\sim}{s} = \underset{\sim}{\sigma} - (\sigma_{kk}/3)\underset{\sim}{I}$, backstress $\underset{\sim}{\alpha}$ is deviatoric, and we have defined $n = K_o$ = constant. The inelastic strain $\underset{\sim}{\epsilon}^n$ includes both conventional creep and plastic strain as in other unified theories. The effective overstress and backstress are denoted as $\bar{\sigma}$ and $\bar{\alpha}$, respectively. The exponential term was proposed by Nouailhas [43] for description of high strain rate events.

The competition between hardening and static thermal recovery terms in the backstress rate equation is introduced in this bounding surface formulation in the following way:

$$\dot{\underset{\sim}{\alpha}} D = H(\bar{\alpha} D, \delta) \; ||\dot{\underset{\sim}{\epsilon}}^n|| \underset{\sim}{\nu} - R(\bar{\alpha} D) \underset{\sim}{\alpha} D \tag{35}$$

where

$$H(\bar{\alpha}D,\delta) = \beta_o + \beta_1 \exp(-\beta_4\langle 1-\beta_3\left(\frac{\delta}{R^*}\right)\rangle^{\beta_5}) + \beta_2\exp(-\beta_6\bar{\alpha}^* D) \tag{36}$$

$$\delta = \sqrt{3/2}\ ||\ \sqrt{2/3}\ R^*\underset{\sim}{N} - \underset{\sim}{s}||\ , \quad \underset{\sim}{N} = (\underset{\sim}{s} - \underset{\sim}{\alpha})/||\underset{\sim}{s} - \underset{\sim}{\alpha}|| \tag{37}$$

$$\bar{\alpha}^* = (R^* - \delta - \bar{\sigma}) \tag{38}$$

$$R(\bar{\alpha}D) = \beta_7 \exp(-\beta_8\bar{\alpha}D)\ (\bar{\alpha}D)^{\beta_9} \tag{39}$$

It should be noted that in this particular formulation with the bounding surface fixed at the origin, the restriction $\delta > 0$ is enforced at a constant strain rate to avoid contact of the stress point with the bounding surface. This is achieved by driving the exponential term effectively to zero at a non-zero δ/R^* ratio. If the bounding surface were allowed to translate, this restriction would not apply; such a generalization is currently being carried out.

The specific form for $D(\Psi)$ selected for this model is

$$D(\Psi) = 1 + C\ \Psi^m \tag{40}$$

The radius of the bounding surface, R^*, evolves with accumulated plastic strain (creep hardening) and responds through the effective overstress to changes in inelastic strain rate to reflect the rate-dependence of the asymptotic state of $\underset{\sim}{\alpha}$, i.e.

$$R^* = \beta_{10}\ \rho\ [1 + \beta_{12}\ \bar{\sigma}^{\beta_{13}}] \tag{41}$$

where

$$\dot{\rho} = \beta_{11}\ (\rho_{mf} - \rho)\ \sqrt{2/3}\ ||\dot{\underset{\sim}{\epsilon}}^n|| \tag{42}$$

with initial condition $\rho(0) = \rho_o$. As seen in equation (41), this formulation clearly exhibits both viscous overstress and backstress effects, motivated by experiments which reveal rate-dependent dislocation structures even at high strain rates.

The directional index for the backstress hardening rate is a rate-dependent Mroz form

$$\underset{\sim}{\nu} = \left[\frac{\sqrt{2/3}\ R^*\ \underset{\sim}{N} - \underset{\sim}{s}}{\sqrt{2/3}\ \delta}\right] \tag{43}$$

The bounding surface and the surface of constant dimension K_o which prescribes elastic response are shown in Fig. 1 along with the vector $\underset{\sim}{\nu}$ in deviatoric stress space. It should be noted that the damage effect D is applied to R^* in addition to

tensorial stress quantities since R^* is related to the saturated or asymptotic value of stress [44].

In this formulation, $K, K_o, Z, n, C, m, \beta_o, \beta_1, \beta_2, \beta_3, \beta_4, \beta_5, \beta_6, \beta_7, \beta_8, \beta_9, \beta_{10}, \beta_{11}, \beta_{12}, \beta_{13}$, and ρ_{mf} are isothermal material constants. Non-isothermal generalization can be achieved primarily by invoking temperature dependence of the backstress recovery term [28] and some of the constants, although this is not necessary in the current isothermal work. Note that K_o does not evolve, resulting in a domination of the inelastic response by evolution of the backstress. This feature allows the overstress tensor to properly model inelastic strain rate direction for rapidly changing nonproportional loading directions or for a departure from a previous loading path for which steady state creep conditions were reached as discussed by McDowell [42] and Lowe and Miller [45-46].

The hardening function which governs smooth transition from a very "stiff" region of backstress rate to an asymptotic response is the second term in equation (36) where the Mroz distance vector is normalized by bounding surface radius. Constants $\beta_1, \beta_4, \beta_5$, and β_3 govern this transition and are selected to match a monotonic, strain-controlled uniaxial test at a single strain rate in addition to a cyclic, strain-controlled uniaxial test at a single strain rate. The cyclic test is used primarily to determine β_3, which ensures that the normalization will be satisfactory for both monotonic and cyclic behavior. Constant β_o describes asymptotic response and constants β_2 and β_6 are employed in a second-order term to model the backstress level dependence of hardening rate observed experimentally when hardening dominates recovery. Constants ρ_{mf} and β_{11} introduce strain hardening into the model and can be determined either from a uniaxial monotonic or cyclic test. Constants β_{10}, β_{12}, and β_{13} are determined from flow stress/strain rate sensitivity data at the temperature of interest; since strain rate sensitivity of R^* is directly related to that of stress in this model, these constants can be determined in a straightforward manner after the constants in the flow rule have been defined to fit a range of desired (observed) backstress behavior obtained from "dip" tests, multiaxial creep or cyclic plasticity experiments involving a sudden change in inelastic strain rate direction, etc. Constants C and m are determined by matching the integrated inelastic strain rate behavior with tertiary creep data.

Interrupted creep tests are generally necessary to assess exponent l at a given isochronous stress level; l can also be determined in an approximate way by periodically unloading from the creep curve [15-18] or by matching the integrated damage-coupled creep equations (32)-(43) with observed onset of tertiary response assuming m = 1 in equation (40). The value m = 1 arises from the Murakami study [2] mentioned earlier. Stress exponent k is easily identified as the slope of the $\log(t_R)$ vs. $\log(\sigma)$ curve obtained from uniaxial tests. Isotropic damage fraction η is identified as the ratio of the transverse damage to the longitudinal damage in a uniaxial test, and is identified by quantitative metallographic techniques described elsewhere [42].

At the isochronous stress level of this study, cavity growth is governed by matrix power law creep. Hence, we define

$$\xi(\sigma^*) = B \left[\sigma^* \right]^k \qquad (44)$$

Once k is known, coefficent B can be found at the isochronous stress level associated with l by integrating and matching rupture times from uniaxial tests with the assumed rupture criterion $w_{max} = 1$.

Tension-torsion tests were conducted at ORNL on thin-walled tubular specimens of type 304 stainless steel (ORNL Ref. heat 9T2796) at 593°C. The specimens were annealed in argon at 1093°C for 30 minutes, and were subsequently air cooled at >100°C/min to room temperature. Refer to Huddleston [19] for further experimental details.

For an isochronous stress of 176.1 MPa at 593°C, the constants are B = 2.71×10^{-28} sec^{-1} and l = 4.8. Units of stress and damage rate are MPa and sec^{-1}, respectively. Constants independent of isochronous stress include k = 8.5551 and η = 0.61. Quantitative evaluation of the grain boundary damage distribution for these biaxial experiments revealed that the damage distribution is suitably described by a second rank tensor [42] which sets P = 0. Exponent l was estimated by matching the tertiary response of uniaxial tests with the integrated damage-coupled creep equations.

The details may be found elsewhere [42] regarding the determination of the constants for the rate-dependent bounding surface model for type 304 stainless steel at room temperature. In summary, the material constants at 593°C for the damage-coupled creep-plasticity model are:

$K = 5 \times 10^{-48}$	$\beta_5 = 1.25$	$\beta_{12} = 0.225$
$K_o = 13.8$	$\beta_6 = 0.0196$	$\beta_{13} = 1.91$
$n = 30$	$\beta_7 = 1.552 \times 10^{-19}$	$\rho_{mf} = 517$
$\beta_o = 1104$	$\beta_8 = -0.0207$	$\rho_o = 145$
$\beta_1 = 6.9 \times 10^6$	$\beta_9 = 5.088$	$C = 0.32$
$\beta_2 = 1044$	$\beta_{10} = 0.00361$	$m = 1$
$\beta_3 = 1.18$	$\beta_{11} = 7.0$	$Z = 0$
$\beta_4 = 23.16$		

where the units of stress are in MPa and time in sec.

The coordinate system employed for the stress analysis of the tubular specimens is shown in Fig. 2. Model predictions and experimental data for three different biaxial creep experiments are shown in Figs. 3-5. In these figures, inelastic axial and tensorial shear strain components are plotted versus time in addition to the axial and shear stress history. It is noted that the rupture time is generally well-predicted as is the inelastic strain upon initial loading and subsequent secondary and tertiary creep rates. The inelastic strain and rupture behavior is well-predicted for proportionally loaded specimen GT-1. The rupture time for specimen GT-4A is somewhat overpredicted for a simple nonproportional loading history, though the strain at rupture and the tertiary character are in reasonable agreement. The correlation obtained for GT-6, a somewhat complex creep-dominated cyclic loading history, is quite good. In all these experiments, the isochronous stress was held constant at 176.15 MPa and the principal stress directions were rotated at some point(s) in the loading history as shown in the figures.

B. Simple Power Law Creep: Pure Copper at 250°C

Trampczynski et al. [3-4] have conducted nonproportional loading experiments on commercially pure copper thin-walled tubular specimens at 250°C and have found in this case that damage is highly anisotropic, i.e. $\eta \simeq 0$. Both by metallurgical examination and by comparison of rupture times with uniaxial and proportional specimens at the same isochronous stress level, they concluded that damage accumulation in copper could be treated as highly decoupled with respect to several discrete loading directions in a nonproportional sequence history. It should be noted that Murakami and Ohno have applied their second rank tensor model to this data set as an approximation, although the physical damage distribution in this case is not accurately represented by a second rank tensor.

The grain boundary metallographs [3] indicate that the appropriate representation of grain boundary cracking at rupture in these specimens is fully anisotropic, $\eta = 0$, and that the deviation of damaged cavity facet normals about the maximum principal stress direction(s) is extremely small, i.e. $P > 0$. Since the maximum principal stress governs the fully anisotropic damage response in this case, a = b = 0 in the general isochronous stress form, i.e.

FIRST LINE OF TEXT

$$\sigma^* = \frac{3}{2} S_1 \tag{45}$$

For axial torsional loading of a thin-walled tube, $\sigma^* = \sigma_1$. The anisotropic damage rate equation may be written in this case as

$$\dot{\omega}(\underset{\sim}{n}) = \xi(\sigma^*) \sum_{j=1}^{3} \left\{\Omega^{(j)}\right\}^{l(\sigma^*)} \chi^{(j)} \left\{ \underset{\sim}{n}\cdot\underset{\sim}{n}^{(j)} \otimes \underset{\sim}{n}^{(j)}\cdot\underset{\sim}{n} \right\} \left\{ \underset{\sim}{n}\cdot\underset{\sim}{n}^{(j)} \right\}^{2P} \tag{46}$$

where again the cavity growth is dominated by matrix power law creep, so that $\xi(\sigma^*)$ is defined as in equation (44). Since only one principal stress is tensile for this particular biaxial loading configuration,

$$\dot{\omega}(\underset{\sim}{n}) = B\,(\sigma_1)^k \left\{\Omega^{(1)}\right\}^{l(\sigma^*)} \chi^{(1)} \left\{ \underset{\sim}{n}\cdot\underset{\sim}{n}^{(1)} \otimes \underset{\sim}{n}^{(1)}\cdot\underset{\sim}{n} \right\} \left\{ \underset{\sim}{n}\cdot\underset{\sim}{n}^{(1)} \right\}^{2P} \tag{47}$$

$$\underset{\sim}{\zeta}^{(1)} = \left\{ \underset{\sim}{I} - \underset{\sim}{n}^{(1)} \otimes \underset{\sim}{n}^{(1)}\, w(\underset{\sim}{n}^{(1)}) \right\}^{-1} \tag{48}$$

$$\Omega^{(1)} = \left[\underset{\sim}{\zeta}^{(1)} : \underset{\sim}{\zeta}^{(1)} \right]^{1/2} = \left[\left[\frac{1}{1 - w(\underset{\sim}{n}^{(1)})} \right]^2 + 2 \right]^{1/2} \tag{49}$$

For copper, we choose to consider a less sophisticated constitutive model for the creep deformation. The coupling with damage for power law creep is given by

$$\dot{\underset{\sim}{\varepsilon}}^{n} = \frac{3}{2} \left[\frac{\sigma_e D}{A} \right]^n \frac{\underset{\sim}{s}}{\sigma_e} \tag{50}$$

where D in this case is selected as

$$D = \left[1 + C\,\psi^m\right]^{1/n} \tag{51}$$

although the form given earlier could also be used.

From Trampczynski et al. [3], n = 6.95. From Murakami and Ohno [1] and Trampczynski [3], k = 5.52 and l = 5.6. At the isochronous stress level to be considered in this study, a mean rupture time of 315 hours is expected for uniaxial creep conditions at 250°C. The constants A = 195, B = 1.913×10^{-14}, C = 3.0, and m = 6.0 were selected to provide the best fit to the secondary and tertiary response of the nonproportional biaxial history shown in Fig. 6 with the additional constraint that t_R = 315 hours for any proportional tension-torsion loading path.

STANDARD PAGE DEPTH

LONG PAGE DEPTH

It should be noted that the units of stress and time are MPa and hours, respectively, for the above set of constants. In this sense, the general shape of the tertiary response achieved by the theory shown in Fig. 6 is not truly predicted, although the rupture time is.

The value of P was selected as a significantly large integer to result in significant decoupling of the bimodal peaks of the damage distribution resulting from an occasional 33.7° rotation of the applied maximum principal stress as discussed by Trampczynski et al. [3]. As P increases, the damage distribution assumes a more highly anisotropic, directional character; as a consequence, the predicted rupture life increases for nonproportional loading histories. In the experiments on copper conducted by Trampczynski et al. [3], two maximum principal stress orientations were alternatively enforced at an angle of ±16.87° from the tube longitudinal direction. Hence, the tensile principal stress was periodically rotated within the plane of the specimen wall via change of the sign of the applied torque, though the principal stress magnitude was held fixed at 46.8 MPa.

In this work P = 6 was selected to ensure little interaction of the damage accumulated in the two directions, as physically observed. The experimental and theoretical results are compared in Figs. 6-7 for two nonproportional loading histories. In these plots, the engineering creep shear strain is plotted rather than the tensorial creep shear strain. Note the correlation offered by the theory, which exhibits the same general trends as the second rank tensor approach of Murakami and Ohno [1-2]. In these figures, the inelastic strain upon initial loading and the primary strain during the first loading event are eliminated from the presentation of the experimental data since the power law creep equation does not consider these components. No attempt was made, however, to eliminate the transient inelastic strains which occur at each subsequent loading reversal. This accounts for much of the error in creep strain evident in Fig. 7 for the complex loading history. This disagreement would not exist with an appropriately sophisticated inelastic strain rate law, such as the one offered in the previous section. The life is reasonably well-correlated for both histories.

CONCLUSIONS

The present study has demonstrated that anisotropic creep damage can be successfully treated within the framework of continuum damage mechanics, even for creep-dominated cyclic loading histories typical of nuclear components. A damage distribution with even symmetry has been introduced on the unit sphere which evolves in rate form as a symmetric tensor of rank necessary to match physically measured damage distributions. The approach is motivated by the treatment of even rank tensor distributions forwarded by Leckie and Onat [5-6], and contains as a subset the specific tensorial definitions of damage adopted in the anisotropic theories of Chaboche (rank four) [13,18,24] and Murakami and Ohno [1-2] (rank two).

A general form of coupling with damage has been suggested for an internal variable inelasticity framework and specific forms have been investigated for type 304 stainless steel at 593°C and pure copper at 250°C with the assumption of small cavity volume fractions. A novel bounding surface cyclic viscoplasticity theory has been offered for multiaxial creep-plasticity deformation as one of these specific forms. Good correlation of rupture time, secondary creep, and tertiary creep has been obtained for proportional and nonproportional, isothermal, constant isochronous nominal stress loading histories.

ACKNOWLEDGMENTS

The authors are grateful to Martin Marietta Energy Systems and the U.S. National Science Foundation (NSF MSM-8601889; MSM-8552714) for support of this work.

REFERENCES

1. Murakami, S., and Ohno, N., "A Continuum Theory of Creep and Creep Damage," Creep in Structures, IUTAM, 1980, pp. 422-444 (Eds. Ponter and Hayhurst).
2. Murakami, S., "Notion of Continuum Damage Mechanics and its Application to Anisotropic Creep Damage Theory," ASME J. of Engineering Materials and Technology, Vol. 105, April 1983, pp. 99-105.
3. Trampczynski, W. A., Hayhurst, D.R., and Leckie, F.A., "Creep Rupture of Copper and Aluminum Under Non-Proportional Loading," J. Mech. Phys. Solids, Vol. 29, No. 5/6, 1981, pp. 353-374.
4. Trampczynski, W. A., and Hayhurst, D.R., "Creep Deformation and Rupture Under Non-Proportional Loading," Creep in Structures, IUTAM, Eds. Ponter and Hayhurst, 1980, pp. 388-405.
5. Leckie, F. A., and Onat, E. T., "Tensorial Nature of Damage Measuring Internal Variables," Physical Non-Linearities in Structural Analysis, IUTAM, 1980, pp. 140-155 (Eds. Hult and Lemaitre).
6. Leckie, F. A., "The Constitutive Equations for High Temperatures and Their Relationship to Design," Proc. Int. Conf. on Constitutive Laws for Engineering Materials, Eds. Desai and Gallagher, Univ. of Arizona, Tucson, Jan. 1983, p. 93.
7. Duvaut, C., "Analyse Fonctionnelle - Méchanique des Milieu Continus-Homogénéisation", Theoretical and Applied Mechanics, North-Holland, Amsterdam, 1976.
8. Kachanov, L., Fundamental of Fracture Mechanics, Nauka, Moscow, 1974.
9. Rabotnov, Y. N., Creep Problems in Structural Members, Amsterdam, North Holland Publishing Co., 1969.
10. Krajcinovic, D., "Creep of Structures - A Continuous Damage Mechanics Approach," J. Structural Mechanics, 11(1), 1983, pp. 1-11.
11. Krajcinovic, D., and Fonseka, G.U., "The Continuous Damage Theory of Brittle Materials," Parts 1 and 2, ASME J. Appl. Mech., Vol. 48, 1981, pp. 809-824.
12. Costin, L. S., and Stone, C. M., "Implementation of a Finite Element Damage Model for Rock," in Constitutive Laws for Engr. Materials: Theory and Applications, Vol. II, Eds. Desai, Krempl, Kiousis and Kundu, Tucson, Arizona, USA, 1987, pp. 829-840.
13. Chaboche, J. L., "Continuum Damage Mechanics: Present State and Future Trends," ONERA T.P. n°1986-53, Séminaire International sur l'Approche Locale de la Rupture, Moret-sur-Loing, June 3-5, 1986.
14. Chow, C. L., and Wang, J., "An Anisotropic Theory of Elasticity for Continuum Damage Mechanics," Int. J. Fracture, 33, 1987, pp. 3-16.
15. Chaboche, J. L., "Continuous Damage Mechanics - A Tool to Describe Phenomena Before Crack Initiation," Nuclear Engr. and Design, Vol. 64, 1981, pp. 233-247.
16. Lemaitre, J., and Chaboche, J. L., "Aspect Phénoménologique de la Rupture par Endommagement," J. de Mécanique Appliquée, Vol. 2, No. 3, 1978, pp. 317-365.
17. Lemaitre, J., and Chaboche, J. L., "A Non-Linear Model of Creep-Fatigue Damage Cumulation and Interaction," Mechanics of Visco-Plastic Media and Bodies, Ed. Jan Hult, Springer, Berlin, 1975, pp. 297-301.
18. Chaboche, J. L., "Le Concept de Contrainte Effective Appliqué a l'élasticité et a la Viscoplasticité en Présence d'un Endommagement Anisotrope," Coll. Euromech. 115, Grenoble, 1979 (CNRS, 1982).
19. Huddleston, R. L., "An Improved Multiaxial Creep-Rupture Strength Criterion," ASME J. Pressure Vessels and Piping, Paper 84-PVP-106, 1984.
20. Miller, D. A., and Langdon, T. G., "Independent and Sequential Cavity Growth Mechanisms," Scripta Metallurgica, Vol. 14, 1980, pp. 143-148.

21. Svensson, L. E., and Dunlop, G. L., "Mechanisms for the Growth of Intergranular Creep Cavities," Creep in Structures, IUTAM, 1980, pp. 445-462 (Eds. Ponter and Hayhurst).
22. Cocks, A.C.F., and Ashby, M.F., "On Creep Fracture by Void Growth," J. Progress in Materials Science, Vol. 27, 1981, pp. 189-245.
23. Woodford, D.A., "Creep Damage and the Remaining Life Concept," ASME J. Engr. Materials and Technology, Vol. 101, Oct. 1979, pp. 311-316.
24. Chaboche, J. L., "Anisotropic Creep Damage in the Framework of Continuum Damage Mechanics," Nucl. Engr. Des., 79, 1984, pp. 309-319.
25. Pugh, C. E., and Robinson, D.N., "Some Trends in Constitutive Equation Model Development for High-Temperature Behavior Model Development for High-Temperature Behavior of Fast-Reactor Structural Alloys," Nuc. Engr. and Design, Vol. 48, 1978, pp. 269-276.
26. Krieg, R. D., Swearengen, J. C., and Rohde, R. W., "A Physically-Based Internal Variable Model for Rate-Dependent Plasticity," Inelastic Behavior of Pressure Vessel and Piping Components (Eds. Chang and Krempl), PVP-PB-028, ASME, 1978, pp. 15-28.
27. Lagneborg, R., "A Modified Recovery-Creep Model and its Evaluation," Metal Science Journal, Vol. 6, 1972, pp. 127-133.
28. Miller, A., "An Inelastic Constitutive Model for Monotonic, Cyclic, and Creep Deformation," ASME J. of Engineering Materials and Technology, Vol. 98, 1976, pp. 97-113.
29. Ponter, A.R.S., and Leckie, F.A., "Constitutive Relationships for the Time-Dependent Deformation of Metals," J. Eng. Mat. and Technology, Trans. ASME, Volume 98, 1976.
30. Hart, E.W., "Constitutive Relations for Non-Elastic Deformations of Metals," J. Eng. Mat. and Technology, Trans. ASME, Volume 98, 1976.
31. Chan, K.S., Bodner, S.R., Walker, K.P., and Lindholm, U.S., "A Survey of Unified Constitutive Theories," Proc. 2nd Symp. on Nonlinear Constitutive Relations for High Temperature Applications, NASA Lewis Research Center, June 13-15, 1984.
32. Walker, K. P., "Research and Development Program for Nonlinear Structural Modeling with Advanced Time-Temperature Dependent Constitutive Relationships," NASA Report CR-165533, NASA Lewis RC, Nov. 1981.
33. Chaboche, J. L., and Rousselier, G., "On the Plastic and Viscoplastic Constitutive Equations- Part I: Rules Developed With Internal Variable Concept," ASME J. Pressure Vessel Technology, Vol. 105, 1983, pp. 153-158.
34. Chaboche, J. L., and Rousselier, G., "On the Plastic and Viscoplastic Constitutive Equations- Part II: Application of Internal Variable Concepts to the 316 Stainless Steel," ASME J. Pressure Vessel Technology, Vol. 105, 1983, pp. 159-164.
35. Wang, C. C., "A New Representation Theorem for Isotropic Functions: An Answer to Professor G. F. Smith's Criticism of My Paper on Representations for Isotropic Functions," Arch. Rat. Mech. Anal., Vol. 36, 1970, pp. 198-223.
36. Dafalias, Y.F., and Popov, E.P., "A Model of Nonlinearly Hardening Materials for Complex Loading," Acta Mechanica, Vol. 21, 1975, pp. 173-192.
37. Dafalias, Y.F., "The Concept and Application of the Bounding Surface in Plasticity Theory," Physical Non-Linearities in Structural Analysis, Eds. J. Hult and J. Lemaitre, IUTAM Symposium, Senlis, France, Springer Verlag, 1981, pp. 56-63.
38. Tseng, N.T., and Lee, G.C., "Simple Plasticity Model of the Two-Surface Type," ASCE Journal of Engineering Mechanics, Vol. 109, No. 3, June 1983, pp. 795-810.
39. Mroz, Z., "An Attempt to Describe the Behaviour of Metals Under Cyclic Loads Using a More General Workhardening Model," Acta Mechanica, Vol. 7, 1967, pp. 199-212.
40. McDowell, D. L., "A Two Surface Model for Transient Nonproportional Cyclic Plasticity: Part 1," ASME J. Applied Mechanics paper No. 85-APM-9, 1985.

41. McDowell, D. L., "A Two Surface Model for Transient Nonproportional Cyclic Plasticity: Part 2," ASME J. Applied Mechanics Paper No. 85-APM-10, 1985.
42. McDowell, D. L., Ho, K. I., and Stalley, J., "An Anisotropic, Damage-Coupled Viscoplastic Model for Creep-Dominated Cyclic Loading," presented at Third Int. Symp. on Nonlinear Fracture Mech., Knoxville, TN, Nov. 1986.
43. Nouailhas, D., "A Viscoplastic Modelling Applied to Stainless Steel Behavior, " in Constitutive Laws for Engr. Materials: Theory and Applications, Vol. II, Eds. Desai, Krempl, Kiousis and Kundu, Tucson, Arizona, USA, 1987, pp. 717-724.
44. McDowell, D. L., and Moosbrugger, J. C., "A Rate-Dependent Bounding Surface Model," work in progress, 1987.
45. Lowe, T. C., and Miller, A. K., "Improved Constitutive Equations for Modeling Strain Softening- Part I: Conceptual Development," ASME J. Engr. Materials and Technology, Vol. 106, 1984, pp. 337-342.
46. Lowe, T. C., and Miller, A. K., "Improved Constitutive Equations for Modeling Strain Softening- Part II: Predictions for Aluminum," ASME J. Engr. Materials and Technology, Vol. 106, 1984, pp. 343-348.

LIST OF FIGURES

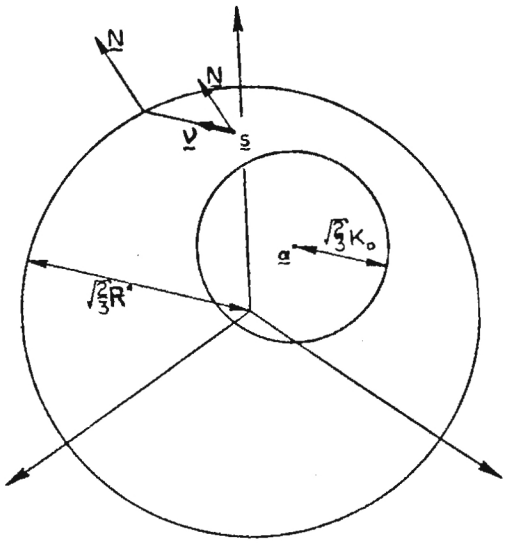

FIG. 1- Bounding and loading surfaces in deviatoric stress space.

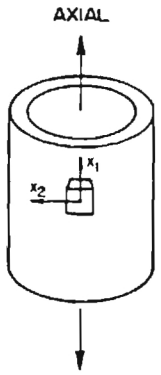

FIG. 2- Coordinate system for the thin-walled tubular tension torsion specimen; x_1 and x_2 are the axial and circumferential coordinates, respectively, at the specimen mid-plane.

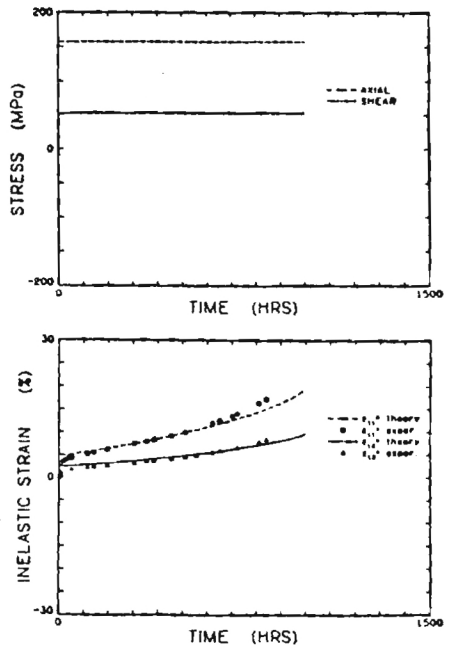

FIG. 3- Type 304 stainless steel at 593°C: applied biaxial nominal stress history (top) and predicted versus experimental inelastic strains (bottom) for specimen GT-1. Actual and predicted rupture times are 892 hr and 998 hr, respectively.

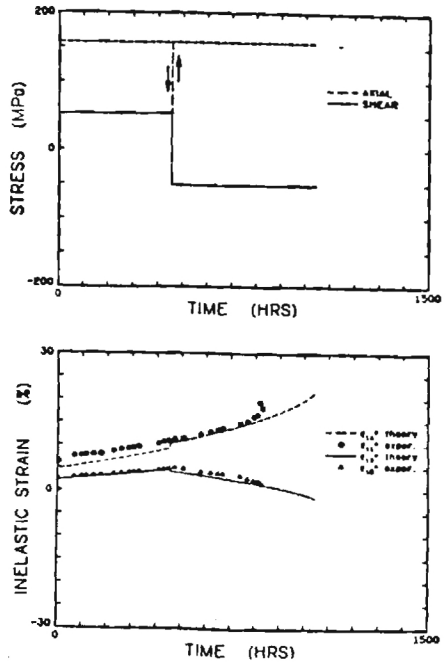

FIG. 4- Type 304 stainless steel at 593°C: applied biaxial nominal stress history (top) and predicted versus experimental inelastic strains (bottom) for specimen GT-4A. Actual and predicted rupture times are 851 hr and 1043 hr, respectively.

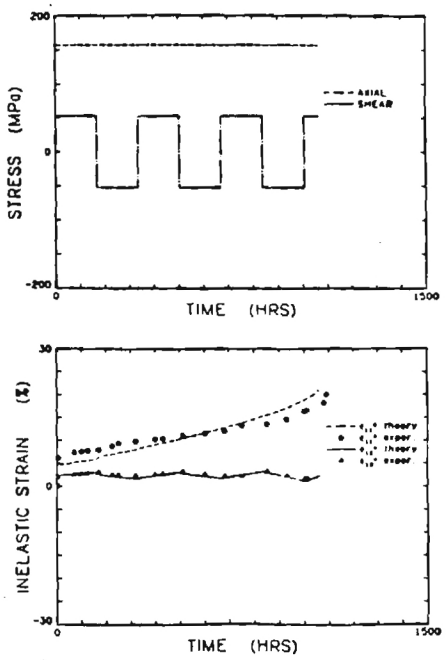

FIG. 5- Type 304 stainless steel at 593°C: applied biaxial nominal stress history (top) and predicted versus experimental inelastic strains (bottom) for specimen GT-6. Actual and predicted rupture times are 1088 hr and 1060 hr, respectively.

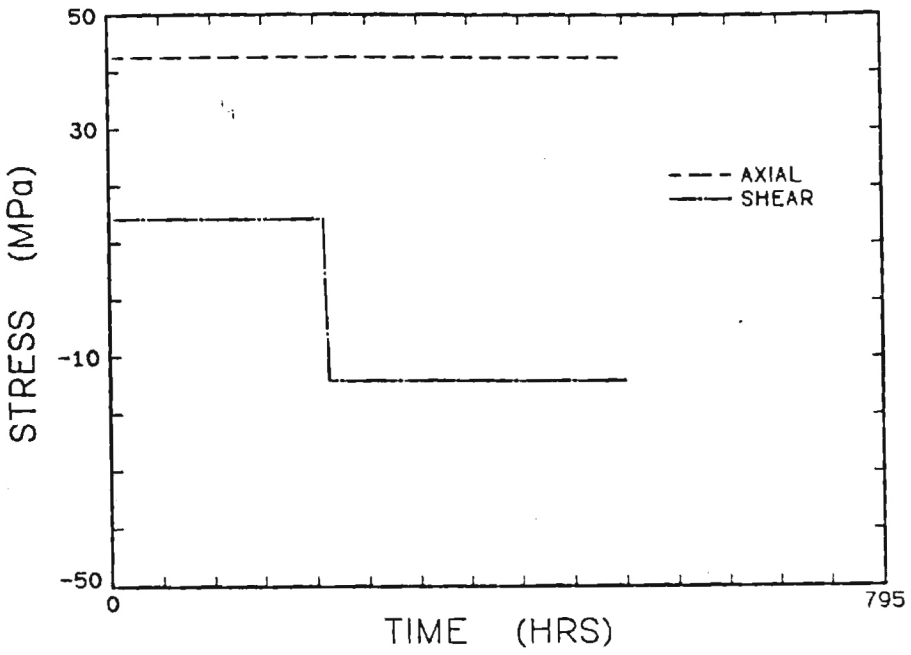

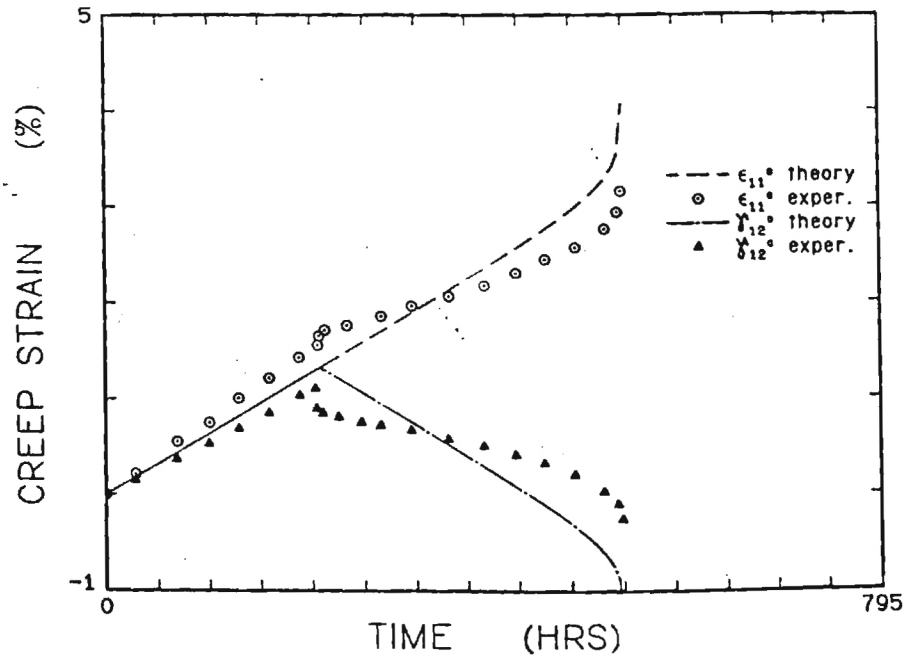

FIG. 6- Copper at 250°C: applied biaxial nominal stress history (top) and predicted versus experimental [3] creep strains (bottom) for a history with a single reversal.

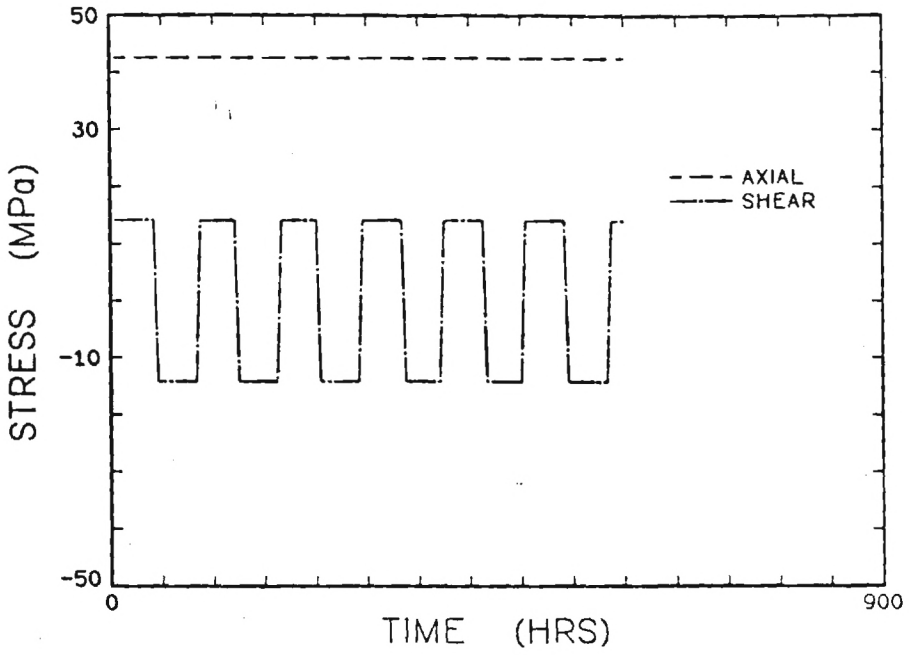

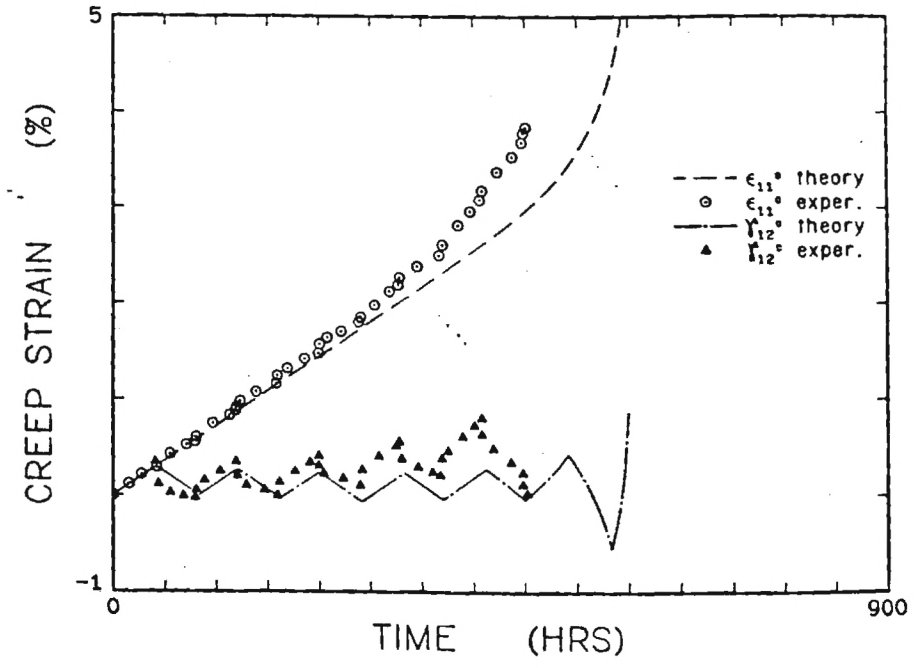

FIG. 7- Copper at 250°C: applied biaxial nominal stress history (top) and predicted versus experimental [3] creep strains (bottom) for a history with multiple reversals.

E-25-M 10

FINAL REPORT ON NSF GRANT NO. MSM-8601889

EXTENSION OF STATE VARIABLE THEORIES TO HIGH TEMPERATURE MULTIAXIAL CYCLIC LOADING

Submitted to Division of Mechanics, Structures
and Materials Engineering

National Science Foundation
1800 G. Street, N.W.
Washington, D.C. 20550
March 1989

Submitted by

DAVID L. MCDOWELL
Associate Professor
The George W. Woodruff School of Mechanical Engineering
Georgia Institute of Technology
Atlanta, GA 30332

NATIONAL SCIENCE FOUNDATION
Washington, D.C. 20550

FINAL PROJECT REPORT
NSF FORM 98A

PLEASE READ INSTRUCTIONS ON REVERSE BEFORE COMPLETING

PART I—PROJECT IDENTIFICATION INFORMATION

1. Institution and Address	2. NSF Program	3. NSF Award Number
Georgia Tech Research Corporation Georgia Institute of Technology Atlanta, GA 30332-0420	ENG-MSM	MSM-8601889
	4. Award Period From 7/1/86 To 12/31/88	5. Cumulative Award Amount $115,393

6. Project Title

Extension of State Variable Theories to High Temperature Multiaxial Cyclic Loading

PART II—SUMMARY OF COMPLETED PROJECT *(FOR PUBLIC USE)*

The objective of this two year program was to conduct high temperature axial-torsional cyclic loading experiments to study the structure of state variable viscoplasticity approaches for more general loading paths than previously examined.

An axial-torsional testing capability was developed for test temperatures up to 800°C-900°C. A unique set of experiments was conducted on type 304 stainless steel at room temperature and Ni-Base superalloy Waspalloy with two different microstructures at 600°C; these experiments included complex cyclic, proportional and nonproportional loading paths at different strain rates. As a result of these and other experimental investigations, a viscoplastic bounding surface theory was formulated. Bounding surface theory had previously been fruitfully applied to multiaxial inelastic deformation of rate-independent metals. The theory is interpreted in terms of evolution of short and long range, thermal and athermal components of backstress which correspond to elastic dislocation interactions at various size scales. Rate-dependence is decomposed between the flow rule and the short range backstress evolution; the latter repository for rate-dependence reflects thermally activated dislocation cross slip. Likewise, isotropic hardening effects are decomposed between the drag stress in the flow rule and the amplitudes of backstress as motivated by experiments and micromechanical arguments. Analysis of the rich set of experimental data obtained is a continuing task beyond this program.

PART III—TECHNICAL INFORMATION *(FOR PROGRAM MANAGEMENT USES)*

1. ITEM *(Check appropriate blocks)*	NONE	ATTACHED	PREVIOUSLY FURNISHED	TO BE FURNISHED SEPARATELY TO PROGRAM	
				Check (✓)	Approx. Date
a. Abstracts of Theses		X			
b. Publication Citations		X			
c. Data on Scientific Collaborators		X			
d. Information on Inventions	X				
e. Technical Description of Project and Results		X			
f. Other *(specify)*					

2. Principal Investigator/Project Director Name *(Typed)*	3. Principal Investigator/Project Director Signature	4. Date
David L. McDowell	4/5/89	4/5/89

SUMMARY

The objective of this two year program was to conduct high temperature axial-torsional cyclic loading experiments to study the structure of state variable viscoplasticity approaches for more general loading paths. In summary, the accomplishments are as follows:

(i) the development of axial-torsional testing capability for thin-walled tubes at temperatures up to 800°C-900°C;

(ii) the couching of bounding surface theory, previously applied to the problem of multiaxial inelastic deformation of rate-independent metals, within the context of rate-dependent, viscoplastic behavior;

(iii) completion of a unique set of experiments on type 304 stainless steel at room temperature and Ni-Base superalloy Waspaloy with two different microstructures at 650°C, including complex cyclic, proportional and nonproportional loading paths at different strain rates;

(iv) the awarding of a doctorate in connection with this research;

(v) refereed papers and presentations.

It should be noted that two distinctive high temperature materials were selected for this study. Type 304 stainless steel was selected on the basis of the rather extensive existing uniaxial database and relevance to the power industry; it is a ductile, tough, low strength material. Originally, a test temperature of 600°C was forecast for this material, but uniaxial investigations at this temperature revealed essentially no strain rate dependence due to dynamic strain aging effects. Since this alloy is significantly rate-dependent at room temperature, a room temperature testing program was conducted. In contrast, Waspaloy is a γ-γ' strengthened Ni-base superalloy which exhibits rather high strength levels but is significantly rate-sensitive at 650°C; in addition, this material is rather well-characterized uniaxially at this temperature. It is somewhat of a model material for studying behavior of Ni-base superalloys in the sense that its practical upper-

use temperature is in the vicinity of 650°C-700°C. This enables studies of deformation response with more accurate control of temperature in the gage section than would be obtained with higher temperature Ni-base superalloys.

IMPORTANT ADVANCES

(i) High-Temperature Multiaxial Testing Facility

A computer-controlled, high temperature axial-torsional load frame was installed. To conduct the experiments in this project, we developed rather sophisticated software for automated test control and data acquisition which permitted loading at any arbitrary constant effective strain rate along user-defined strain- or stress-controlled loading paths in the axial-torsional subspace for thin-walled tubular specimens.

(ii) Viscoplastic Bounding Surface Theory

A rate-dependent bounding surface model was developed in an effort to generalize unified creep-plasticity models to a theoretical framework which has successfully correlated cyclic stress-strain response under multiaxial nonproportional loading. It was shown that the presence of a dynamic recovery term in the backstress evolution equation is necessary for compatibility with a bounding surface approach. The bounding surface approach was further refined by: (a) generalization of the concept of the image point for kinematic hardening, (b) rate-dependence of the direct hardening coefficient in the short range backstress evolution equation as motivated by rate-dependence of dislocation cross slip, and (c) decomposition of the backstress into short and long range, thermal and athermal components, respectively. These developments are in accordance with those in the materials science literature, albeit from the general multiaxial cyclic loading viewpoint rather than the uniaxial tensile test perspective. This rate-dependent bounding surface model is in essence a generalization of some of the more accurate viscoplastic overstress

models which have been developed largely in association with NASA and NSF sponsored programs in the last decade.

Much of the insight into the relationship between state variable theories of viscoplasticity and bounding surface approaches for metals were obtained by considering the physics of dislocation interactions at various subgrain size scales. As expressed in the Ph.D. dissertation of J. Moosbrugger and in related publications this past year (enclosed), we have identified the decomposition of backstress into components which pertain to dislocation interactions with short range and long range barriers. The former involve thermally activated processes and the latter, which typically have high activation energy, are predominately athermal in accordance with the materials science literature. Isotropic hardening, which relates to substructure development and increase in dislocation density, has been incorporated into the evolution of appropriate backstress components in addition to the drag stress in the flow rule. This differs from existing theories which assume that isotropic hardening affects only the flow rule. Moreover, rate dependence is also partitioned between the flow rule and the short range backstress evolution; the former is associated with slip system stress relaxation associated with thermally activated cross slip as pointed out in a paper recently submitted for presentation at the Canadian Fracture Conference in May 1989 (enclosed). In this paper, we have related the structure of the theory developed in Moosbrugger's Ph.D. thesis to dislocation level events using the single slip theory of Aifantis, a simplified form of continuum slip theory. It is shown that the partitioning schemes for hardening and rate-dependence outlined in the proposed model have strong basis in dislocation behavior. In fact, the precise form for backstress evolution proposed in Moosbrugger's thesis is derived on the basis of quite simple slip system constitutive laws in this paper.

(iii) Experiments

These theoretical developments have been accompanied by tension-torsion experiments designed to differentiate between isotropic hardening in the flow rule and backstress rate or between rate-dependence in the flow rule or backstress rate.

Experiments were conducted on both 304 stainless steel at room temperature and Ni-base superalloy Waspaloy at 650°C which employed nonproportional cyclic loading at different strain rates with and without instantaneous strain rate and loading direction changes. Such tests are valuable since the backstress (and its components) are tensorial variables and the inelastic strain rate is noncollinear with backstress. This permits evaluation of the instantaneous versus gradual strain rate sensitivity attributable to the flow rule and backstress rate, respectively.

Based on analysis of the 304 data, we have concluded that almost all of the cyclic hardening is actually associated with the elevation of backstress rather than the drag stress in the flow rule. Furthermore, the drag stress is much smaller than the 0.1% cyclic yield strength of the material. Since the drag stress can be thought of in the rate-independent sense as defining the yield surface radius, this result actually conflicts with almost all previous formulations, which have incorporated isotropic hardening in the drag stress. The result may be anticipated since, as shown in our micromechanical single slip work, the drag stress is related to the intrinsic lattice resistance which, for FCC metals, is weakly dislocation density dependent and rather small in magnitude.

We also see evidence of the decomposition between rate-dependence in the flow rule and in the backstress evolution rate based on experiments which involved coincident nonproportional strain path trajectories and strain rate changes. By correlation of 304 data, we estimate that most of the rate-dependence for this material at room temperature is embedded in backstress evolution rather than in the flow rule.

Two different lots of Waspaloy were intentionally subjected to two different heat treatments which resulted in fine grain and large grain structure. The precipitate size also differed. The differences in cyclic viscoplastic response of these two different microstructures at high temperature were very interesting and should aid in further efforts to tie the microstructure to mechanical response. Differences were observed in rate-sensitivity, isotropic hardening under proportional and nonproportional loading, etc.

A detailed description of experimental results obtained through this program appears in the Appendix, along with discussion of some important aspects of observed behaviors.

Analysis of these rather voluminous, interesting sets of data will continue for some time and should result in numerous important distinctions and findings to be published.

(iv) Student/Staff Involvement

John C. Moosbrugger earned his doctorate in December 1988. His dissertation, entitled "A Rate-Dependent Bounding Surface Model for Nonproportional Cyclic Viscoplasticity," introduced a decomposition of rate-dependence between the flow rule and the kinematic hardening rate. In addition to the modeling in his thesis, John conducted the type 304 stainless steel experiments. Dr. Moosbrugger's work has been presented before the international community of viscoplasticity researchers and has been received favorably. John is now an Assistant Professor in Mechanical and Industrial Engineering at Clarkson University in Potsdam, New York.

The development and operation of the multiaxial testing laboratory is the responsibility of Research Engineer R.L.T. Oehmke, who conducted the Waspaloy experiments.

(v) Papers and Presentations

The following is a list of papers related to this project which were produced/published or submitted during this grant period (enclosed):

1. McDowell, D.L., Ho, Kwang-Il, and Stalley, J., "An Anisotropic, Damage-Coupled Viscoplastic Model for Creep-Dominated Cyclic Loading," presented at the ASTM Third Int. Symp. for Nonlinear Fracture Mechanics, ASTM STP 995, pp. 173-194, 1989.

2. McDowell, D.L. and Moosbrugger, J.C., "A Generalized Rate-Dependent Bounding Surface Model," ASME PVP-Vol. 129, pp. 1-11, 1987.

3. McDowell, D.L., Ho, K., and Moosbrugger, J.C., "Continuum Damage Representation of Creep-Dominated, Nonproportional Cyclic Loading," Int. Seminar on High Temperature Fracture Mechanisms and Mechanics, Dourdan, France, October 1987.

4. Moosbrugger, J.C. and McDowell, D.L., "On a Class of Kinematic Hardening Rules for Nonproportional Cyclic Plasticity," ASME Journal of Engineering Materials and Technology, Vol. 111, 1989, pp. 87-98.

5. Moosbrugger, J.C. and McDowell, D.L., "A Rate-Dependent Bounding Surface Model with a Generalized Image Point for Cyclic Nonproportional Viscoplasticity," under revision for publication in the Journal of the Mechanics and Physics of Solids, May 1988.

6. McDowell, D.L. and Moosbrugger, J.C., "Bounding Surface Interpretation of Rate-Dependent Metallic Behavior under Nonproportional Loading," Proc. Int. Seminar on the Inelastic Behaviour of Solids Models and Utilisation, Besancon, France, Aug. 30 - Sept. 1, 1988.

7. McDowell, D.L. and Moosbrugger, J.C., "Application of Continuum Slip Approaches to Viscoplasticity," to be presented at the 19th Canadian Fracture Conference, Ottawa, Ontario, Canada, May 1989.

The following related presentations were made:

1. "Creep-Dominated, Damage-Coupled Cyclic Viscoplasticity," Oak Ridge National Laboratory, October 1986.

2. "Potential for Materials Characterization Using Multiaxial Nonproportional Testing," ASTM Spring Meeting of Subcommittee E9-04 on Instrumentation, Cincinnati, OH, April, 1987.

3. "Developments in Two Surface Plasticity Theory", Renssaeler Polytechnic Institute, September 22, 1987.

4. "Developments in Two Surface Plasticity Theory", Cornell University, September 23, 1987.

5. "Developments in Two Surface Plasticity Theory", Brown University, September 28, 1987.

6. ""Further Developments in Two Surface Plasticity," University of Kentucky Applied Mechanics Seminar, March, 1988.

7. "Recent Developments in Two Surface Plasticity Theory," Ford Motor Co., Scientific Research, Dearborn, MI, April 11, 1988.

8. "Further Developments in Two Surface Plasticity," Georgia Tech Materials Engineering Seminar, April 19, 1988.

9. Moosbrugger, J.C. and McDowell, D.L., "Consideration of Rate-Dependence and Anisotropy Within the Framework of Bounding Surface Inelasticity," ASME/SES Summer Annual Meeting, Berkeley, CA, June 20-22, 1988.

10. McDowell, D.L. and Moosbrugger, J.C., "Bounding Surface Interpretation of Rate-Dependent Metallic Behavior under Nonproportional Loading," Proc. Int. Seminar on the Inelastic Behaviour of Solids Models and Utilisation, Besancon, France, Aug. 30 - Sept. 1, 1988.

11. "Fundamental Aspects of Bounding Surface Viscoplasticity," Georgia Tech Structural Mechanics Seminar, March 2, 1989.

APPENDIX

EXPERIMENTAL RESULTS

In this appendix, we present a selection of experimental results for both materials studied.

NOMENCLATURE

σ = axial stress

τ = shear stress

ϵ = axial strain

γ = engineering shear strain

ϵ_a = axial strain amplitude

γ_a = engineering shear strain amplitude

β = phase angle

N = cycle number

$\dot{\bar{\sigma}}$ = effective stress rate = $(\dot{\sigma}^2 + 3\dot{\tau}^2)^{1/2}$

$\dot{\bar{\epsilon}}$ = effective strain rate = $(\dot{\epsilon}^2 + \dot{\gamma}^2/3)^{1/2}$

For out-of-phase tests (e.g. Test #1 and Test #4), $\epsilon = \epsilon_a \sin(2\pi n_p/N_s)$ and $\gamma = \gamma_a \sin(2\pi n_p/N_s - \beta)$ where n_p is the strain path segment number ($0 \le n_p \le N_s$) and N_s is the total number of strain path segments in the cycle (N_s = 100 in this study). In this investigation, all nonproportional loading paths, including the sinusoidal paths, were constructed from a collection of straight line segments in the axial-torsional strain space. Sinusoidal out-of-phase strain paths were defined in this manner to admit enforcement of constant effective strain rate along the entire path, rather than admitting a variation in effective strain rate as per the conventional manner of definition. Since a total of 100 segments were used for sinusoidal paths, the curvature of the strain space trajectory appears smooth.

DESCRIPTION OF WASPALOY TESTS

Test #1 consists of 4 blocks with constant strain amplitudes and effective strain rate with 10 cycles per block. For this test, ϵ_a = .0045 and γ_a = .00675 with an effective strain rate of .001 sec^{-1}. However, the phase angle increases in 30° increments per block from 0° to 90°. The test consisted of a total of 12 blocks of which the first 4 are reported here.

Test #4 consists of 4 90° out-of-phase blocks with 25 cycles each. The effective strain rate, .001 sec^{-1}, remains constant for all blocks. However, the strain amplitudes increase as the block number increases. This test actually consists of 8 blocks, only 4 of which are reported here.

Test #5 consists of 4 blocks with 16 cycles in each block and a constant effective strain rate of .001 sec^{-1}. The strain amplitudes remain constant at ϵ_a = .006 and γ_a = .009. Blocks 1 and 3 are in-phase tests while blocks 2 and 4 are 90° out-of-phase.

Test #6 is the only test run in load control instead of strain control. The effective stress rate is 10 MPa/sec. Block #1 consists of 50 proportional cycles between σ_a=460 MPa, τ_a=265 MPa and σ_a=-460 MPa, τ_a=-265 MPa. A 600 second hold period is then executed at σ_a=460 MPa, τ_a=265 MPa.

Block #3 consists of 50 cycles between the endpoints σ=0, τ=0; σ=-460 MPa, τ=-265 MPa; σ=460 MPa, τ=-265 MPa; σ=460 MPa, τ=265 MPa; and return to σ=-460MPa, τ=-265 MPa along the same path. A 600 second hold then occurs at σ=460 MPa, τ=265 MPa.

Block #5 consists of 50 cycles between the endpoints σ=575 MPa, τ=0 MPa; σ=0 MPa, τ=331 MPa; σ=575 MPa, τ=0 MPa at an effective stress rate of 10 MPa/sec. A 600 second hold then takes place at σ=460 MPa, τ=265 MPa. Block #5 is then repeated.

Test #7 for reporting purposes is reduced to three blocks although, at least in terms of the software required, several more blocks were required to implement the test. Block #1 involves strain control between the endpoints ϵ=0, γ=.01 and ϵ=0, γ=-.01 with 600 second hold periods at ϵ=0, γ=.01 during cycles 1, 5, and 10. The specimen is then cycled between ϵ=.006, γ=0 with 600 second hold periods at ϵ=.006, γ=0 during cycles 10, 15, and 20. Finally, the specimen is subjected to cycling between the endpoints

$\epsilon = .006$, $\gamma = .01$; $\epsilon = -.006$, $\gamma = .01$; $\epsilon = -.006$, $\gamma = -.01$; and back to $\epsilon = .006$, $\gamma = .01$. Six-hundred second hold periods occur at the following strain space locations and cycle numbers: $\epsilon = .006$, $\gamma = .01, N = 25$; $\epsilon = -.006$, $\gamma = -.01, N = 30$; $\epsilon = -.006$, $\gamma = 0, N = 35$; and $\epsilon = 0$, $\gamma = -.01$, $N = 40$. The effective strain rate is constant for this test at .001 sec^{-1}.

Test #8 is a dual strain rate test with strain space paths resembling squares with different corner trajectories. The first block is a set-up block of 10 cycles at an effective strain rate of .001 sec^{-1} for the square path between the endpoints $\epsilon = .004$, $\gamma = .007$; $\epsilon = -.004$, $\gamma = .007$; $\epsilon = -.004$, $\gamma = -.007$; $\epsilon = .004$, $\gamma = -.007$; return to $\epsilon = .004$, $\gamma = .007$.

Block #2 consists of 5 cycles with the following endpoints: $\epsilon = .0034$, $\gamma = .006$; $\epsilon = 0$, $\gamma = .0075$; $\epsilon = 0$, $\gamma = .006$; $\epsilon = -.0034$, $\gamma = .006$; $\epsilon = -.0034$, $\gamma = -.006$; $\epsilon = .0034$, $\gamma = -.006$; and back to $\epsilon = .0034$, $\gamma = .006$. The effective strain rate is .001 sec^{-1} for all segments except the corner trajectory and vertical return to the basic square path where the strain rate is .00001 sec^{-1}.

Blocks #3 and #4 are the same as block #2 except the corner trajectories travel to $\epsilon = 0$, $\gamma = .0092$ and $\epsilon = 0$, $\gamma = .0011$ respectively.

The remaining blocks, #5, #6, and #7, duplicate the previous 3 blocks except that the effective strain rate remains constant at .001 sec^{-1} and the trajectory endpoints decrease in shear strain amplitude rather than increase.

MATERIAL

Waspaloy was chosen for this study since baseline uniaxial data at temperatures between 25°C and 800°C was provided by Lerch et al. [A1]. The AMS 5706 Waspaloy was manufactured by Special Metals Corporation as heat # 911671B. The material was supplied in 5.72 cm O.D. hot rolled bar, solution annealed (1010°C, 4 hours and water quenched) before being centerless ground. The manufacturer reported the grain size as 8.

After machining, but before final grinding, the specimens were subjected to the following heat treatment:

For Fine Grain, Large Precipitate specimens (FG-LP)

1010°C +/- 5°C for 2 hours, oil quench, raise to 875°C +/- 10°C for 24 hours.

Nominal grain size is ASTM size 9 (diameter 16μm)

2 precipitate sizes of 900 Å and 3000 Å

For Large Grain, Fine Precipitate specimens (LG-FP)

1100°C +/- 10°C for 2 hours, oil quench, raise to 730°C +/- 10°C for 6 hours.

Nominal grain size is ASTM size 3 (diameter 125 μm)

1 precipitate size of 50-80 Å

These grain and precipitate sizes are as reported by Lerch et al. [A1] for the same material and heat treatment.

TESTING EQUIPMENT

Tests were conducted in an MTS servo-hydraulic load frame with water cooled, hydraulic grips capable of 55 kip axial load and 25 kip-in torque. All tests were conducted with the aid of a DEC MICRO-PDP 11 computer for test data acquisition and control. Additionally, X-Y recorders were used for real time data display and backup data acquisition. An MTS high temperature biaxial extensometer was used for gage section displacement feedback and strain data acquisition. The extensometer was equipped with steel probes for room temperature for economic reasons. High temperature tests necessitated the use of more expensive quartz rod probes.

High temperature tests were conducted with the use of a 7.5 KW induction heater. Several copper load coils were constructed in an iterative process of finding the correct coil geometry to provide 650°C in the gage section with a maximum temperature variation of ±2.5°C. The specimen temperature was controlled using a commercially available temperature controller. A K-type thermocouple connected to the top shoulder of the specimen provided the temperature controller input. The 4-20 ma ouput of the controller provided the power control signal to the induction heater. The controller set point was established by preceding the tests with an actual specimen instrumented with 5

thermocouples; 1 thermocouple on each of the shoulders and 3 thermocouples evenly spaced in the gage section. The induction heater load coil geometry was then adjusted until the temperature distribution in the gage section was deemed satisfactory. Then the shoulder temperatures and controller setpoint were noted. In subsequent tests, the original shoulder temperature was achieved.

CYCLIC HARDENING BEHAVIOR

The fine grain material tends to fail earlier than the coarse grain material. For example, in Test #5, the coarse grain specimen completed the entire test of 8 blocks, while the fine grain specimen failed at the beginning of the 5th block. This phenomenon was also observed in Test #4, among others, and may be attributed to decreased low cycle fatigue resistance of the fine grain material.

Very little hardening was observed in Test #1 for either the fine grain or the coarse grain waspaloy, even in blocks 4 and above where $\beta = 90°$. This may be due to the relatively low strain range for this test. In Test #4, significant hardening was observed for both grain sizes of waspaloy. The coarse grain specimens appear to harden as much as the fine grain specimens, but the stresses required to achieve the same strain amplitudes appear to be greater, probably due to the smaller precipitate size and spacing.

It is noted that the fine grain specimens continually harden in Test #4. Lerch, Jayaraman and Antolovich [A1] reported that the fine grain material was stable at temperatures ranging from 25°C to 800°C with a total strain range from .34% to 1.5% under uniaxial test conditions. It is clear that under biaxial, cyclic, 90° out-of-phase testing, at 650°C, the fine grain specimen continues to harden when the effective strain range is above 1.2%.

Test #8 shows considerable stress relaxation in blocks #2, #3, and #4 at the point where the effective strain rate decreases from 10^{-3} to 10^{-5} sec^{-1}. This occurs at the strain space location $\epsilon = .0034$, $\gamma = .006$,and is not observed in blocks #5, #6, and #7, where the effective strain rate is held constant at 10^{-3} sec^{-1}.

Test #1 indicates a possible inverse rate sensitivity for the fine grain material since the stresses are greater at decreased strain rates for 90° out-of-phase tests as observed in blocks #5-#8. This effect may alternatively be due to continued isotropic hardening. Further analysis is required. The coarse grain material appears to exhibit positive strain rate sensitivity which is especially evident between blocks #7 and #8 where the strain rate changes from 10^{-4} to 10^{-5} with a corresponding decrease in stress.

As mentioned in the main body of the report, analysis of this rather vast set of data will continue for some time.

REFERENCE

A1. Lerch,B.A., Jayarman, N., and Antolovich, S.D., "A Study of Fatigue Damage Mechanisms in Waspaloy from 25 to 800°C", Materials Science and Engineering, 66, pp. 151-166, 1984.

Figure 1: Biaxial Specimen Geometry. All dimensions in mm.

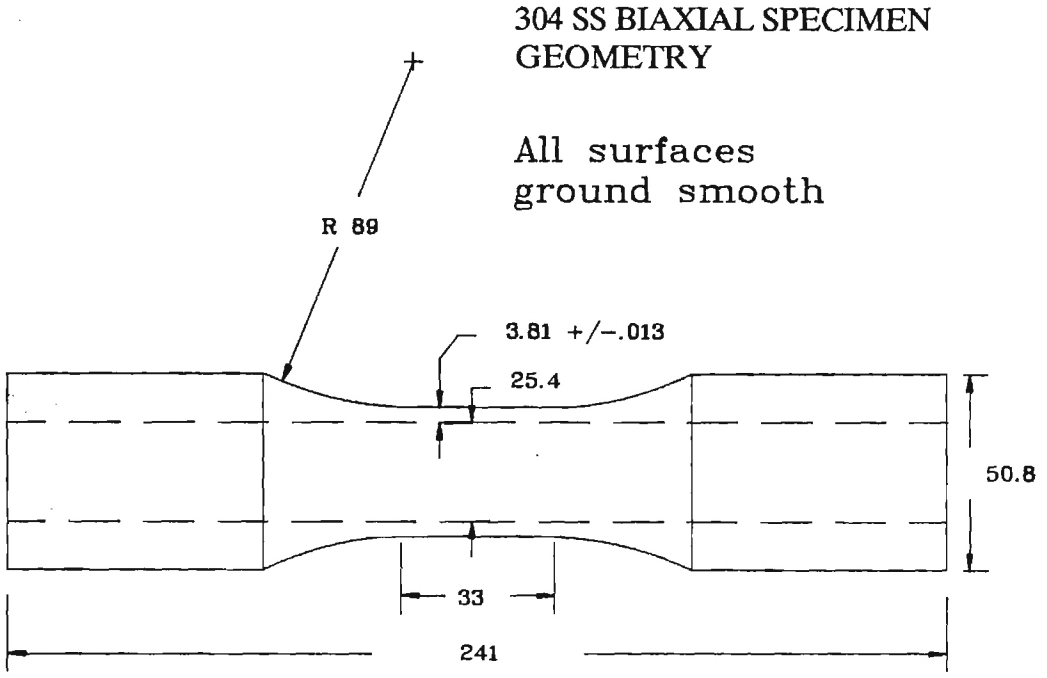

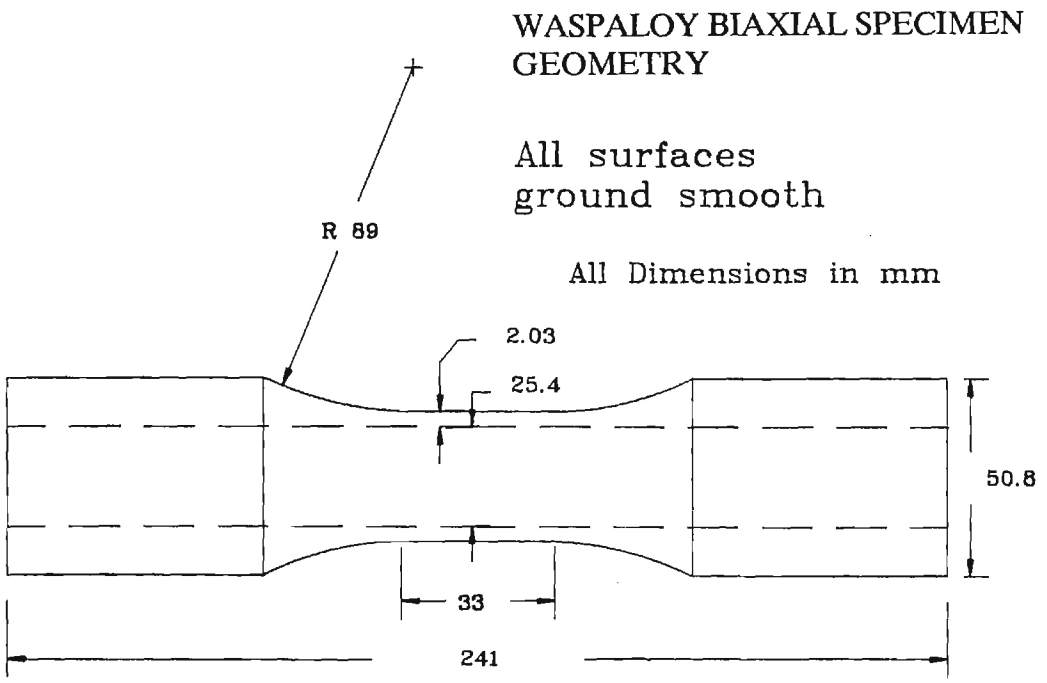

WASPALOY

Figure 2

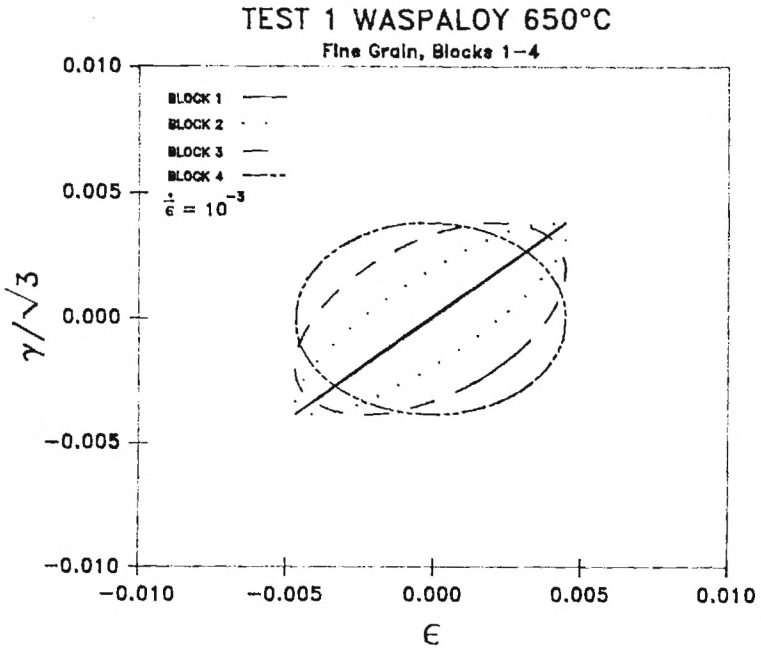
TEST 1 WASPALOY 650°C
Fine Grain, Blocks 1–4
BLOCK 1
BLOCK 2
BLOCK 3
BLOCK 4
$\dot{\epsilon} = 10^{-3}$
$\gamma/\sqrt{3}$
ϵ
0.010
0.005
0.000
−0.005
−0.010
−0.010
−0.005
0.000
0.005
0.010

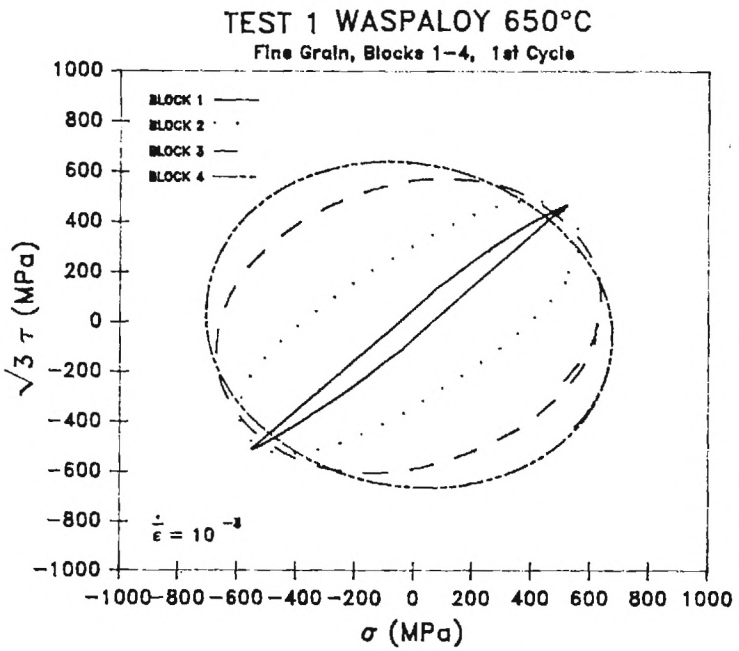
TEST 1 WASPALOY 650°C
Fine Grain, Blocks 1–4, 1st Cycle
BLOCK 1
BLOCK 2
BLOCK 3
BLOCK 4
$\dot{\epsilon} = 10^{-3}$
$\sqrt{3}\,\tau$ (MPa)
σ (MPa)
1000
800
600
400
200
0
−200
−400
−600
−800
−1000
−1000 −800 −600 −400 −200 0 200 400 600 800 1000

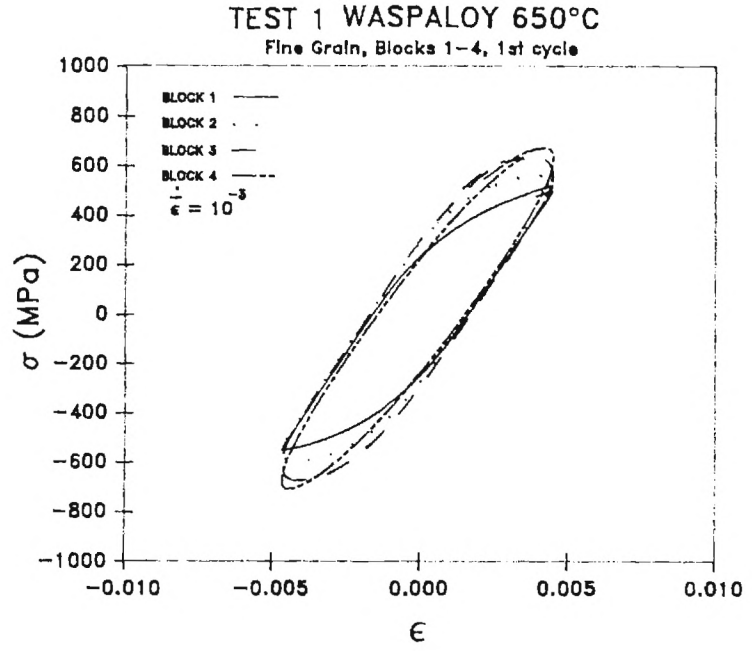
TEST 1 WASPALOY 650°C
Fine Grain, Blocks 1–4, 1st cycle
BLOCK 1
BLOCK 2
BLOCK 3
BLOCK 4
$\dot{\epsilon} = 10^{-3}$
σ (MPa)
ϵ
1000
800
600
400
200
0
−200
−400
−600
−800
−1000
−0.010
−0.005
0.000
0.005
0.010

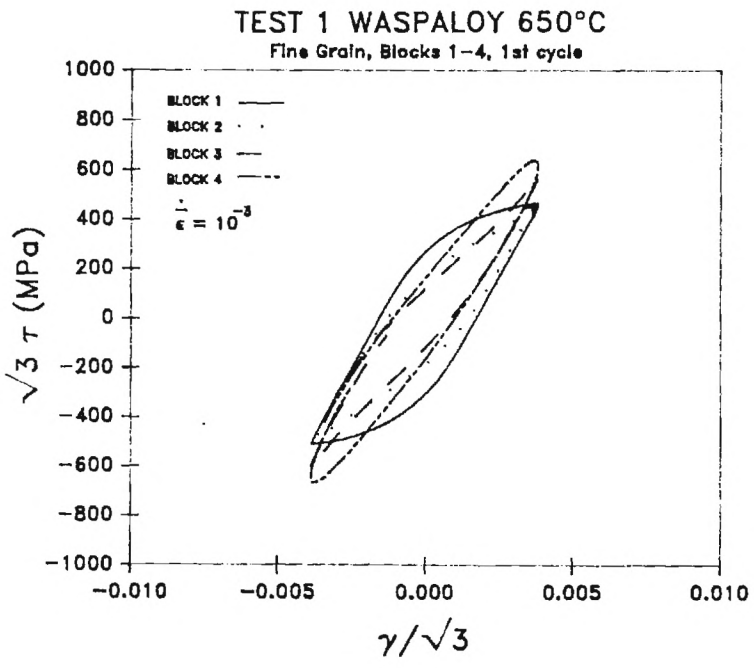
TEST 1 WASPALOY 650°C
Fine Grain, Blocks 1–4, 1st cycle
BLOCK 1
BLOCK 2
BLOCK 3
BLOCK 4
$\dot{\epsilon} = 10^{-3}$
$\sqrt{3}\,\tau$ (MPa)
$\gamma/\sqrt{3}$
1000
800
600
400
200
0
−200
−400
−600
−800
−1000
−0.010
−0.005
0.000
0.005
0.010

Figure 3

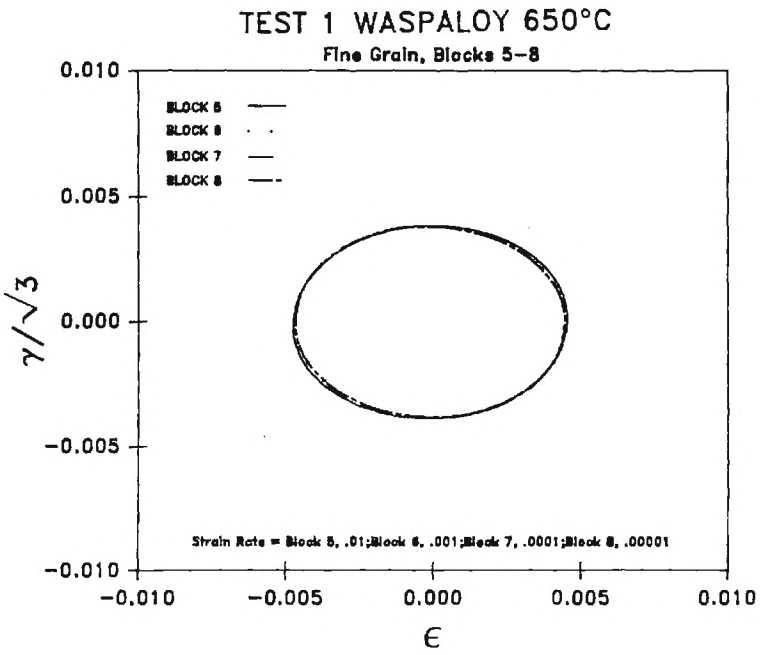
TEST 1 WASPALOY 650°C
Fine Grain, Blocks 5–8
BLOCK 5
BLOCK 6
BLOCK 7
BLOCK 8
Strain Rate = Block 5, .01;Block 6, .001;Block 7, .0001;Block 8, .00001
0.010
0.005
0.000
-0.005
-0.010
γ/√3
-0.010
-0.005
0.000
0.005
0.010
ϵ

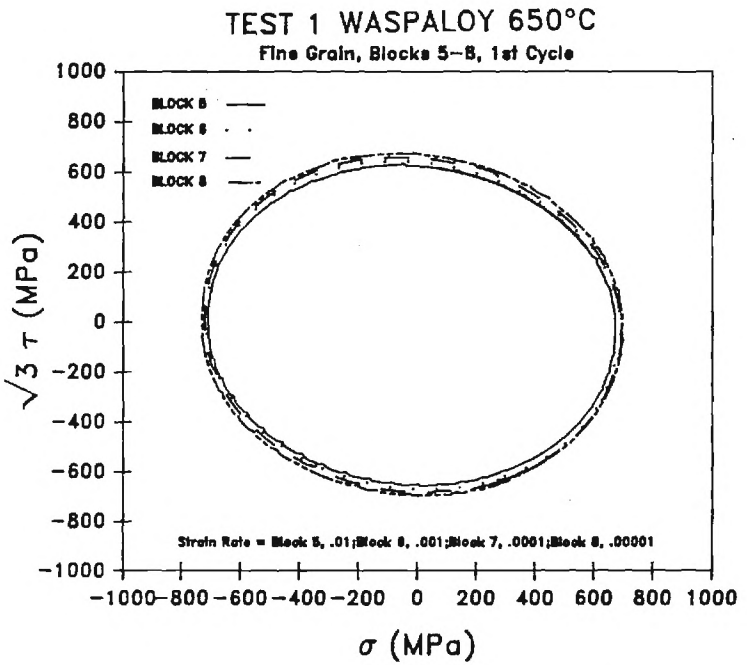
TEST 1 WASPALOY 650°C
Fine Grain, Blocks 5–8, 1st Cycle
BLOCK 5
BLOCK 6
BLOCK 7
BLOCK 8
Strain Rate = Block 5, .01;Block 6, .001;Block 7, .0001;Block 8, .00001
1000
800
600
400
200
0
-200
-400
-600
-800
-1000
√3 τ (MPa)
-1000 -800 -600 -400 -200 0 200 400 600 800 1000
σ (MPa)

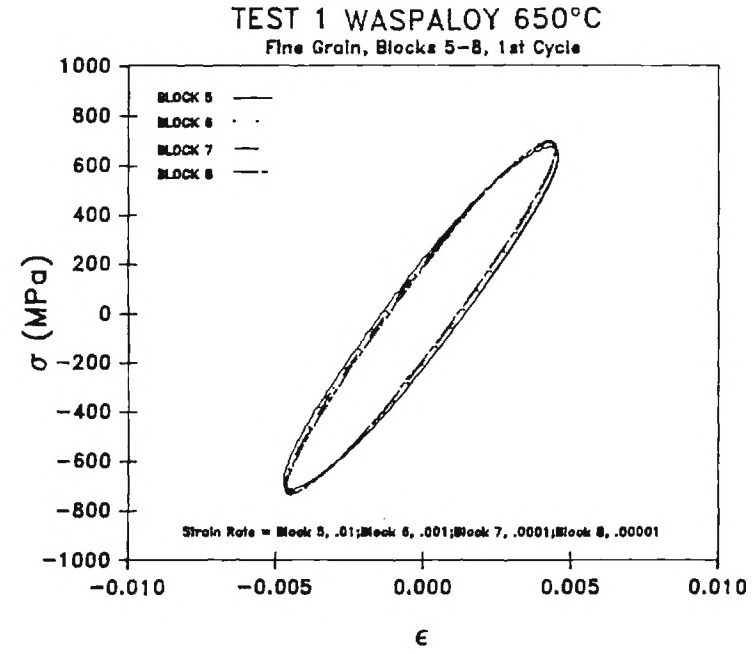
TEST 1 WASPALOY 650°C
Fine Grain, Blocks 5–8, 1st Cycle
BLOCK 5
BLOCK 6
BLOCK 7
BLOCK 8
Strain Rate = Block 5, .01;Block 6, .001;Block 7, .0001;Block 8, .00001
1000
800
600
400
200
0
-200
-400
-600
-800
-1000
σ (MPa)
-0.010
-0.005
0.000
0.005
0.010
ϵ

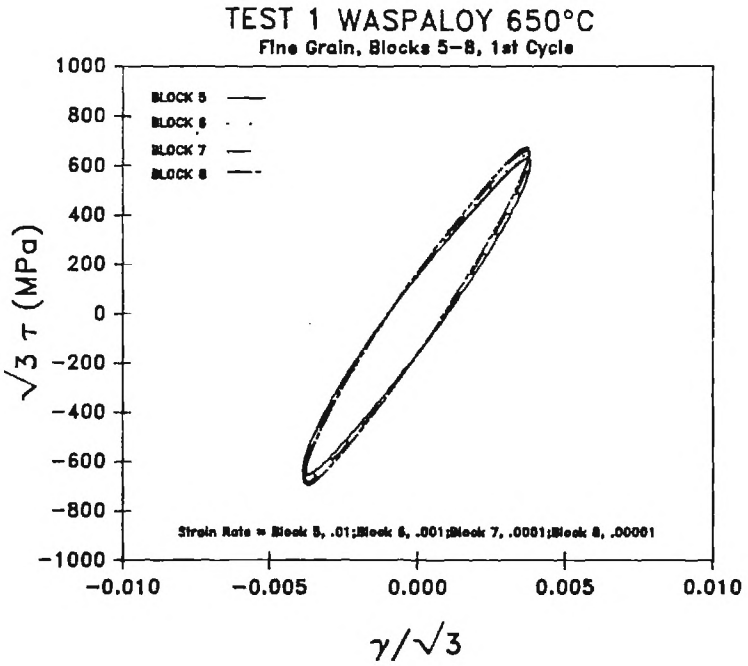
TEST 1 WASPALOY 650°C
Fine Grain, Blocks 5–8, 1st Cycle
BLOCK 5
BLOCK 6
BLOCK 7
BLOCK 8
Strain Rate = Block 5, .01;Block 6, .001;Block 7, .0001;Block 8, .00001
1000
800
600
400
200
0
-200
-400
-600
-800
-1000
√3 τ (MPa)
-0.010
-0.005
0.000
0.005
0.010
γ/√3

Figure 4

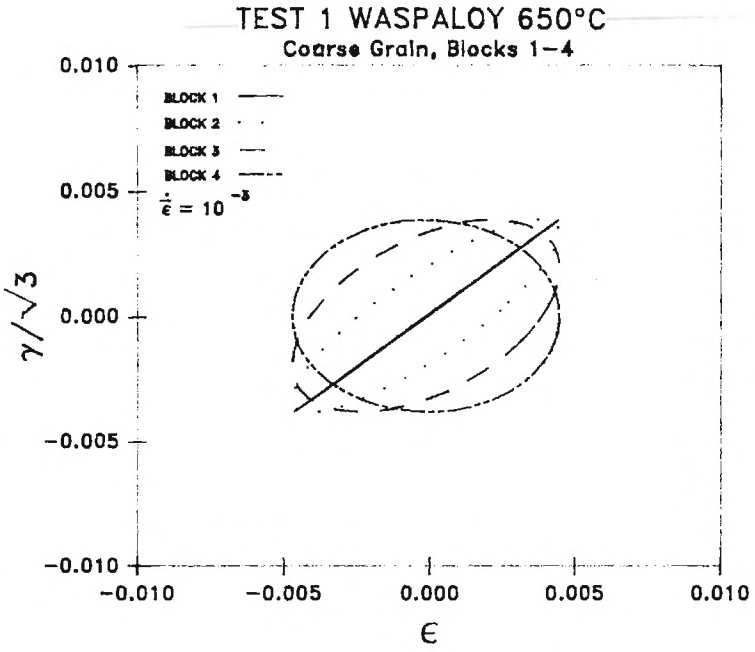
TEST 1 WASPALOY 650°C
Coarse Grain, Blocks 1–4
BLOCK 1
BLOCK 2
BLOCK 3
BLOCK 4
$\dot{\epsilon} = 10^{-5}$
$\gamma/\sqrt{3}$
ϵ
0.010
0.005
0.000
-0.005
-0.010

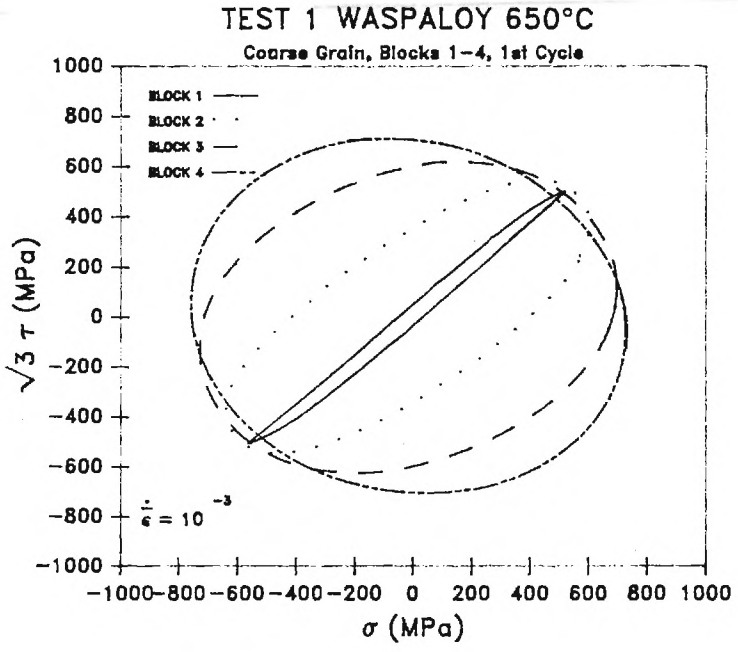
TEST 1 WASPALOY 650°C
Coarse Grain, Blocks 1–4, 1st Cycle
BLOCK 1
BLOCK 2
BLOCK 3
BLOCK 4
$\dot{\epsilon} = 10^{-3}$
$\sqrt{3}\,\tau$ (MPa)
σ (MPa)
1000
800
600
400
200
0
-200
-400
-600
-800
-1000

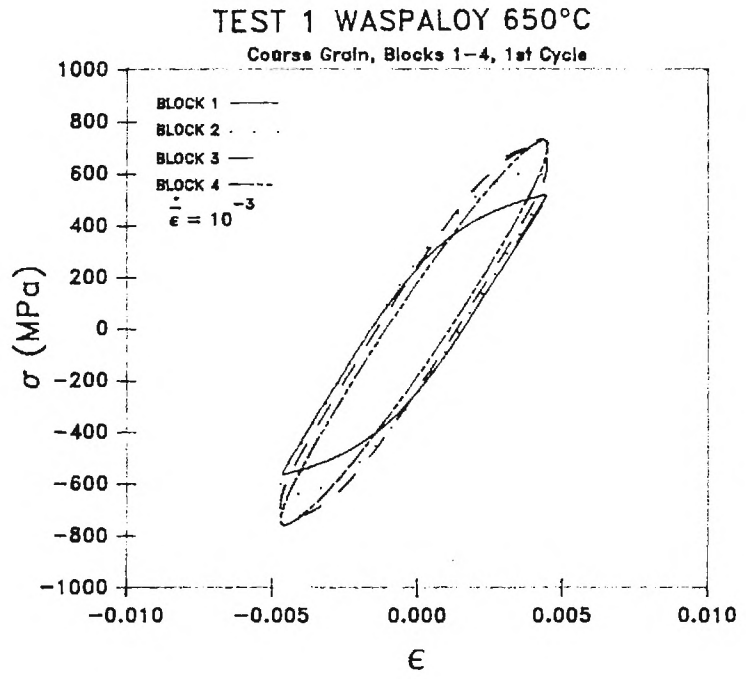
TEST 1 WASPALOY 650°C
Coarse Grain, Blocks 1–4, 1st Cycle
BLOCK 1
BLOCK 2
BLOCK 3
BLOCK 4
$\dot{\epsilon} = 10^{-3}$
σ (MPa)
ϵ
1000
800
600
400
200
0
-200
-400
-600
-800
-1000

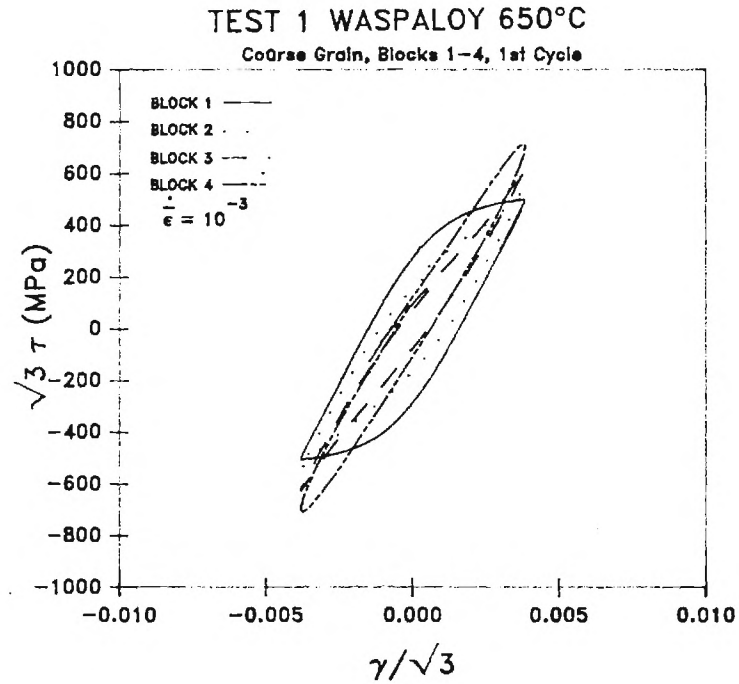
TEST 1 WASPALOY 650°C
Coarse Grain, Blocks 1–4, 1st Cycle
BLOCK 1
BLOCK 2
BLOCK 3
BLOCK 4
$\dot{\epsilon} = 10^{-3}$
$\sqrt{3}\,\tau$ (MPa)
$\gamma/\sqrt{3}$
1000
800
600
400
200
0
-200
-400
-600
-800
-1000

Figure 5

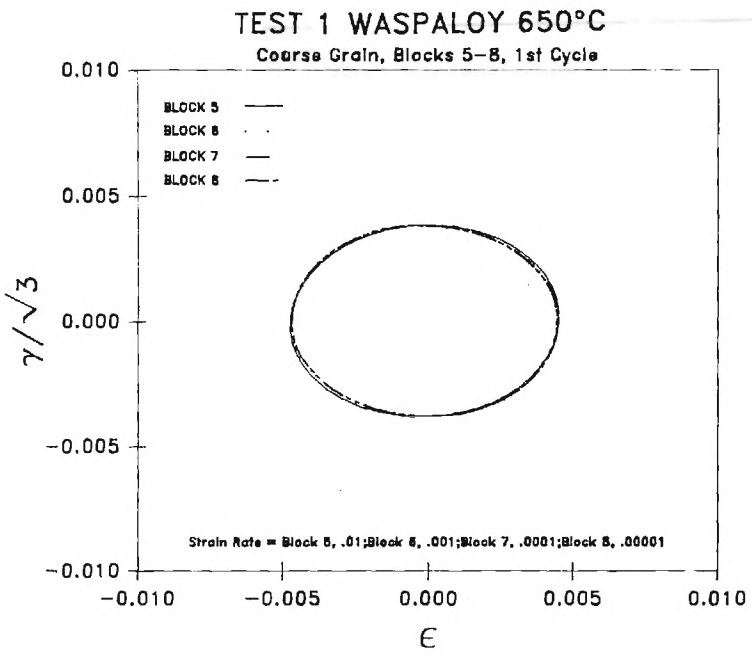
TEST 1 WASPALOY 650°C
Coarse Grain, Blocks 5–8, 1st Cycle
BLOCK 5
BLOCK 6
BLOCK 7
BLOCK 8
Strain Rate = Block 5, .01;Block 6, .001;Block 7, .0001;Block 8, .00001
γ/√3
ϵ
0.010
0.005
0.000
-0.005
-0.010

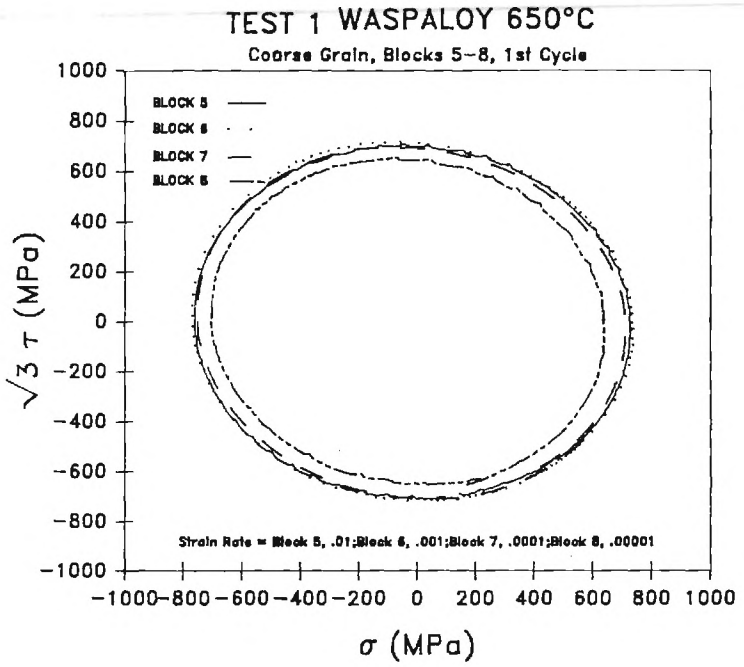
TEST 1 WASPALOY 650°C
Coarse Grain, Blocks 5–8, 1st Cycle
BLOCK 5
BLOCK 6
BLOCK 7
BLOCK 8
Strain Rate = Block 5, .01;Block 6, .001;Block 7, .0001;Block 8, .00001
√3 τ (MPa)
σ (MPa)
1000
800
600
400
200
0
-200
-400
-600
-800
-1000

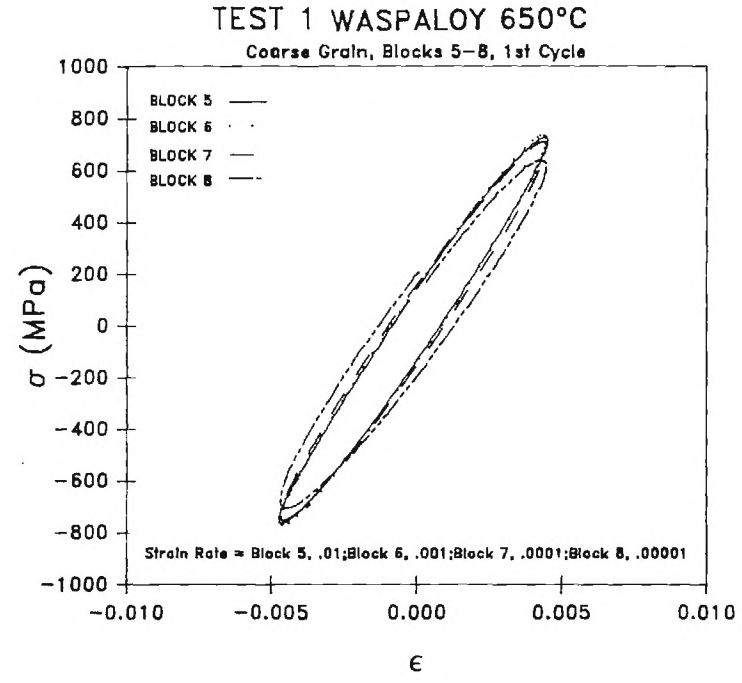
TEST 1 WASPALOY 650°C
Coarse Grain, Blocks 5–8, 1st Cycle
BLOCK 5
BLOCK 6
BLOCK 7
BLOCK 8
Strain Rate = Block 5, .01;Block 6, .001;Block 7, .0001;Block 8, .00001
σ (MPa)
ϵ
1000
800
600
400
200
0
-200
-400
-600
-800
-1000

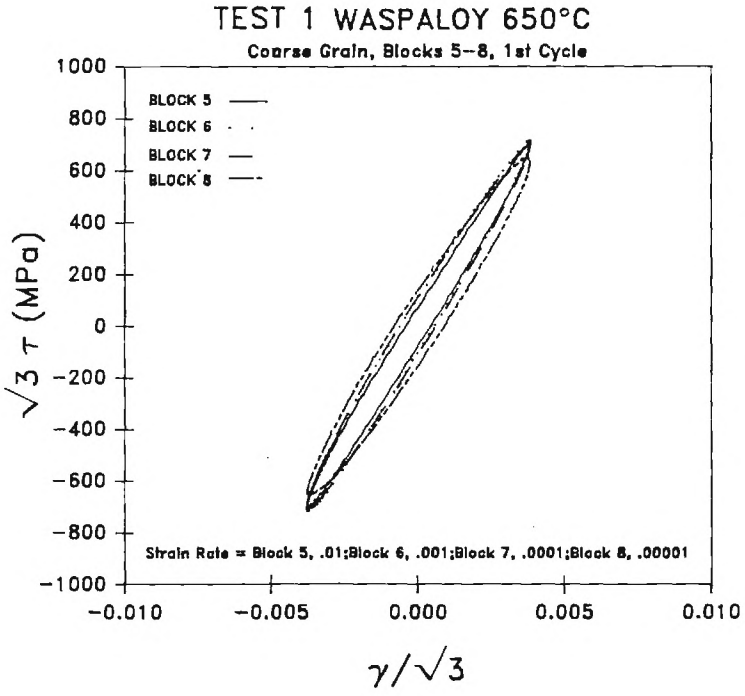
TEST 1 WASPALOY 650°C
Coarse Grain, Blocks 5–8, 1st Cycle
BLOCK 5
BLOCK 6
BLOCK 7
BLOCK 8
Strain Rate = Block 5, .01;Block 6, .001;Block 7, .0001;Block 8, .00001
√3 τ (MPa)
γ/√3
1000
800
600
400
200
0
-200
-400
-600
-800
-1000

Figure 6

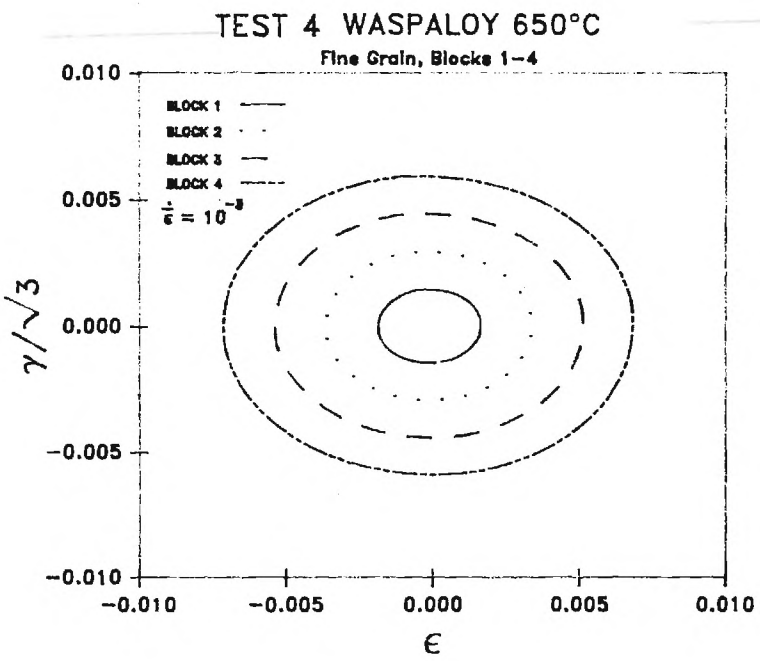
TEST 4 WASPALOY 650°C
Fine Grain, Blocks 1–4
BLOCK 1
BLOCK 2
BLOCK 3
BLOCK 4
$\dot{\epsilon} = 10^{-3}$
$\gamma/\sqrt{3}$
ϵ
0.010
0.005
0.000
-0.005
-0.010

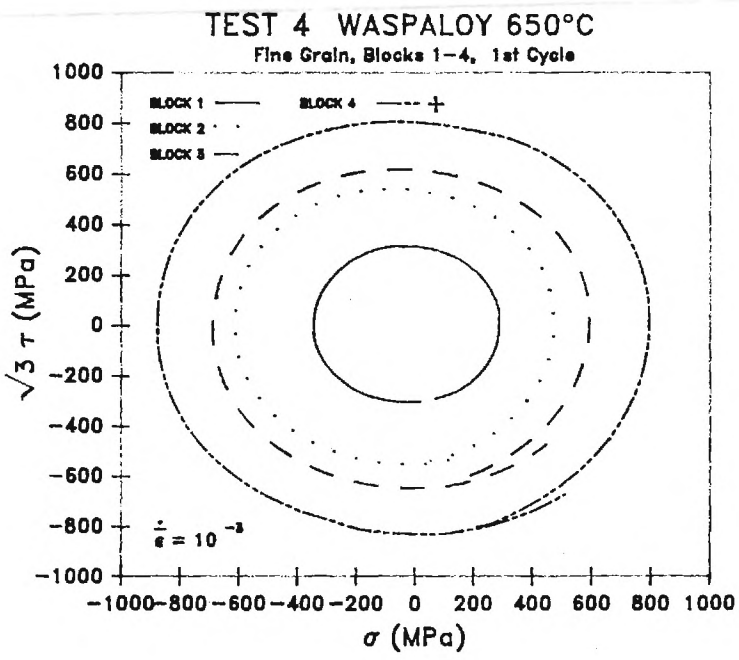
TEST 4 WASPALOY 650°C
Fine Grain, Blocks 1–4, 1st Cycle
BLOCK 1
BLOCK 2
BLOCK 3
BLOCK 4
$\dot{\epsilon} = 10^{-3}$
$\sqrt{3}\,\tau$ (MPa)
σ (MPa)
1000
800
600
400
200
0
-200
-400
-600
-800
-1000

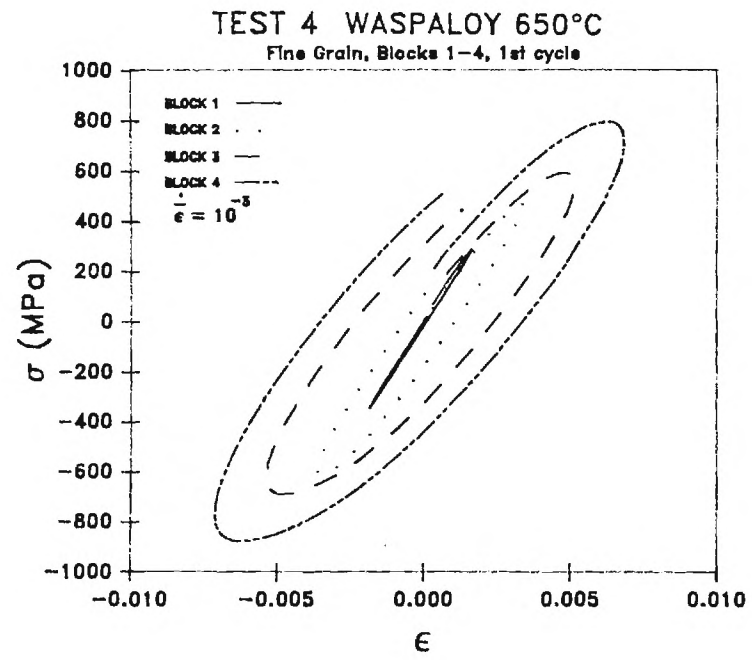
TEST 4 WASPALOY 650°C
Fine Grain, Blocks 1–4, 1st cycle
BLOCK 1
BLOCK 2
BLOCK 3
BLOCK 4
$\dot{\epsilon} = 10^{-3}$
σ (MPa)
ϵ
1000
800
600
400
200
0
-200
-400
-600
-800
-1000

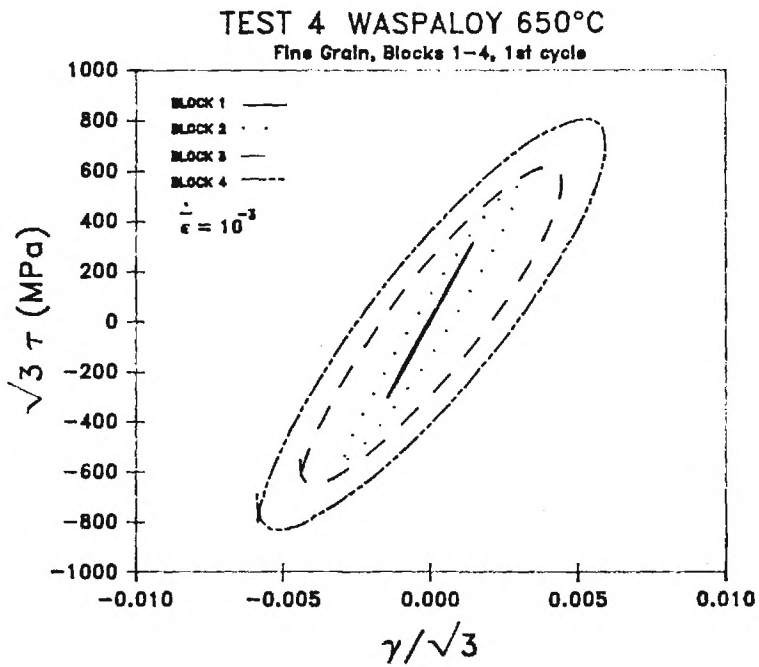
TEST 4 WASPALOY 650°C
Fine Grain, Blocks 1–4, 1st cycle
BLOCK 1
BLOCK 2
BLOCK 3
BLOCK 4
$\dot{\epsilon} = 10^{-3}$
$\sqrt{3}\,\tau$ (MPa)
$\gamma/\sqrt{3}$
1000
800
600
400
200
0
-200
-400
-600
-800
-1000

Figure 7

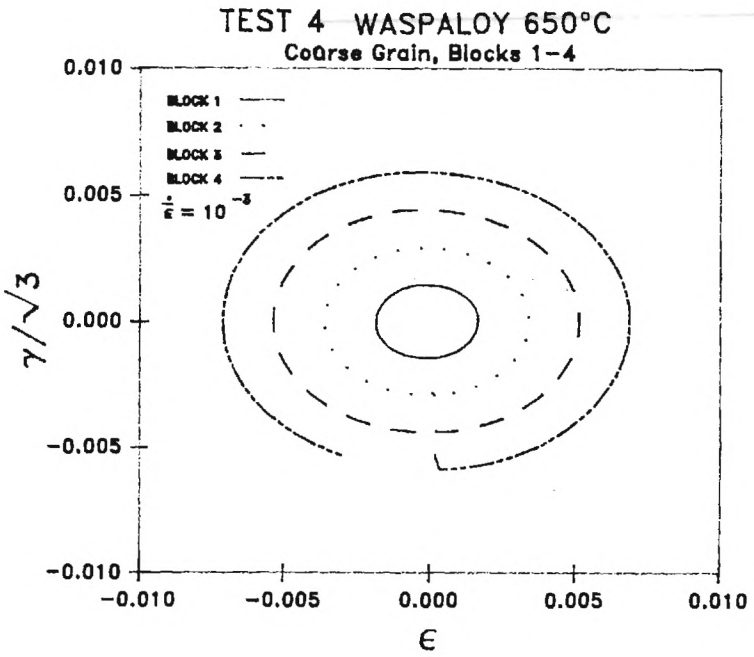
TEST 4 WASPALOY 650°C
Coarse Grain, Blocks 1–4
BLOCK 1
BLOCK 2
BLOCK 3
BLOCK 4
$\dot{\epsilon} = 10^{-3}$
$\gamma/\sqrt{3}$
ϵ
0.010
0.005
0.000
-0.005
-0.010

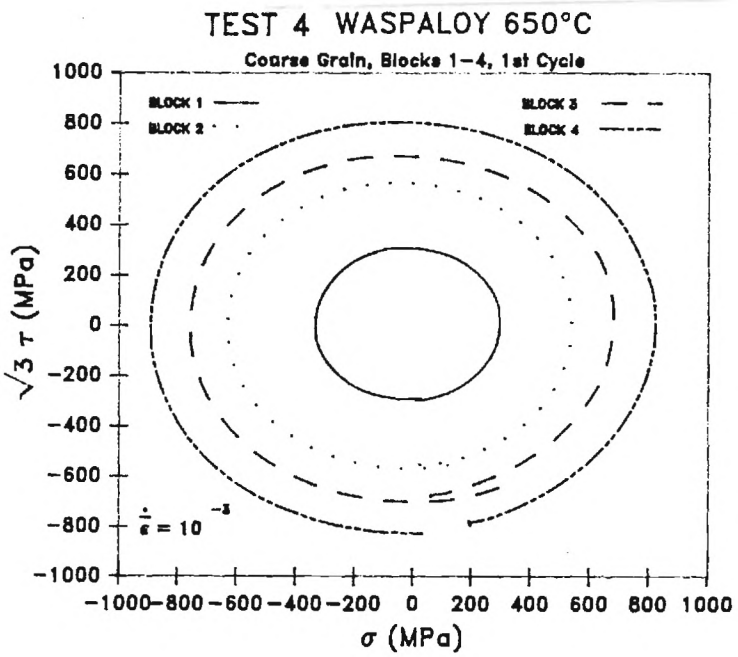
TEST 4 WASPALOY 650°C
Coarse Grain, Blocks 1–4, 1st Cycle
BLOCK 1
BLOCK 2
BLOCK 3
BLOCK 4
$\dot{\epsilon} = 10^{-3}$
$\sqrt{3}\,\tau$ (MPa)
σ (MPa)
1000
800
600
400
200
0
-200
-400
-600
-800
-1000

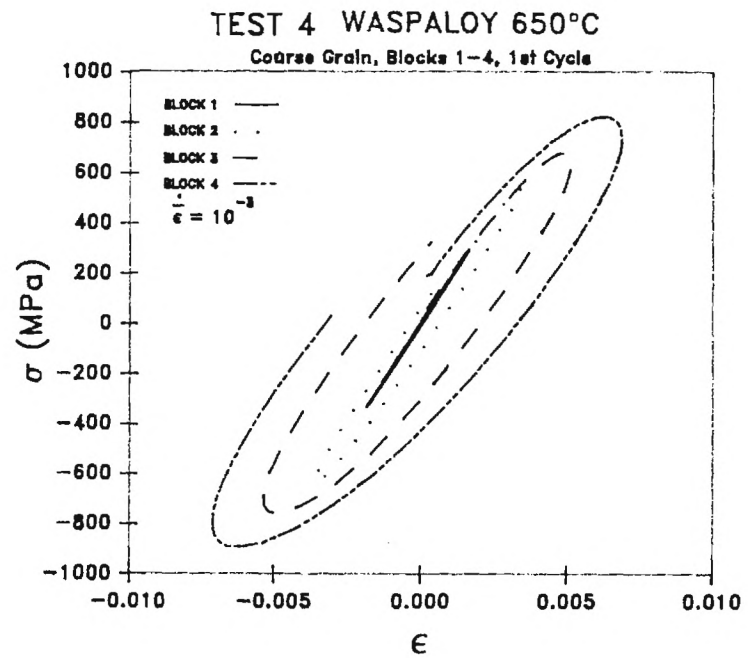
TEST 4 WASPALOY 650°C
Coarse Grain, Blocks 1–4, 1st Cycle
BLOCK 1
BLOCK 2
BLOCK 3
BLOCK 4
$\dot{\epsilon} = 10^{-3}$
σ (MPa)
ϵ
1000
800
600
400
200
0
-200
-400
-600
-800
-1000

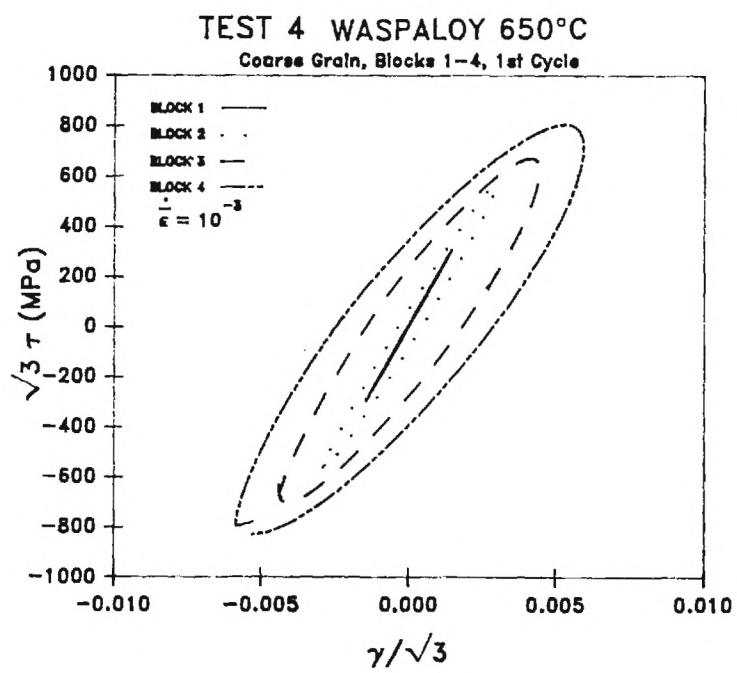
TEST 4 WASPALOY 650°C
Coarse Grain, Blocks 1–4, 1st Cycle
BLOCK 1
BLOCK 2
BLOCK 3
BLOCK 4
$\dot{\epsilon} = 10^{-3}$
$\sqrt{3}\,\tau$ (MPa)
$\gamma/\sqrt{3}$
1000
800
600
400
200
0
-200
-400
-600
-800
-1000

Figure 8

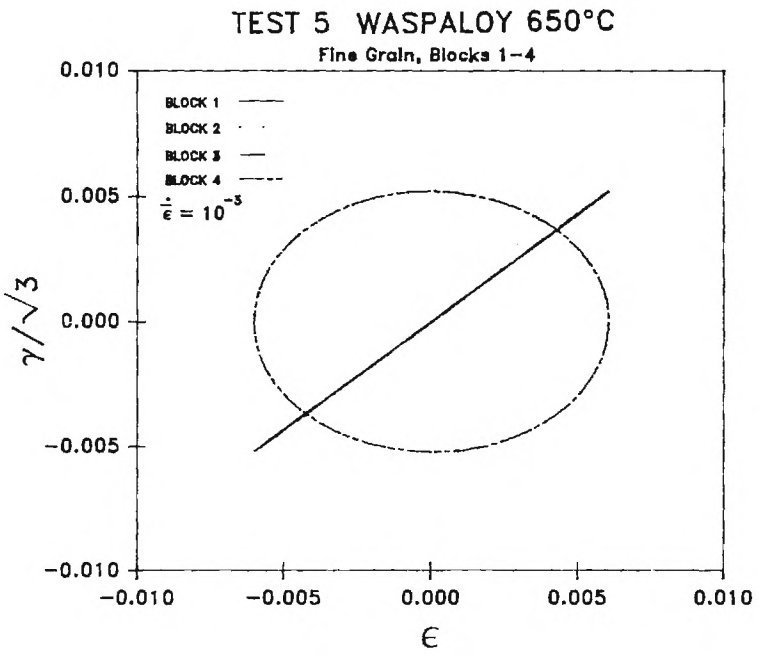
TEST 5 WASPALOY 650°C
Fine Grain, Blocks 1–4
BLOCK 1
BLOCK 2
BLOCK 3
BLOCK 4
$\dot{\epsilon} = 10^{-3}$
$\gamma/\sqrt{3}$
ϵ
0.010
0.005
0.000
−0.005
−0.010

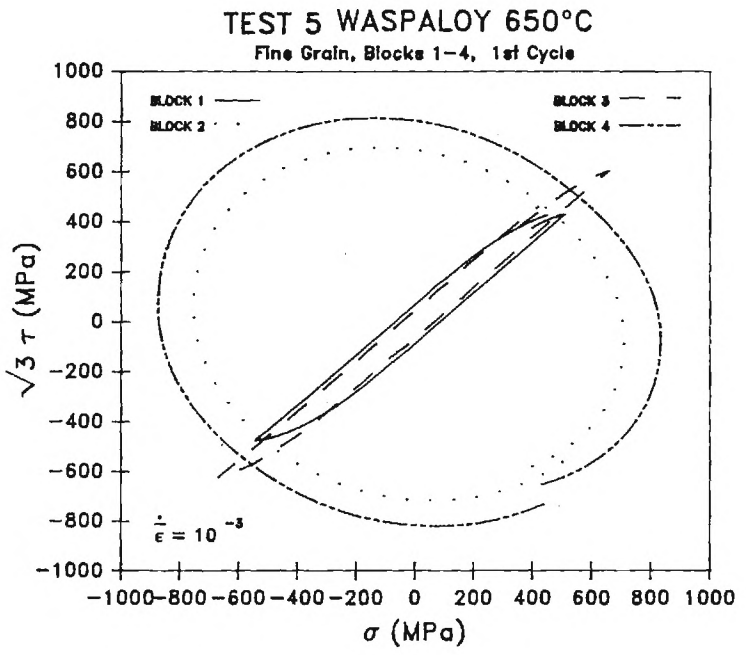
TEST 5 WASPALOY 650°C
Fine Grain, Blocks 1–4, 1st Cycle
BLOCK 1
BLOCK 2
BLOCK 3
BLOCK 4
$\dot{\epsilon} = 10^{-3}$
$\sqrt{3}\,\tau$ (MPa)
σ (MPa)
1000
800
600
400
200
0
−200
−400
−600
−800
−1000

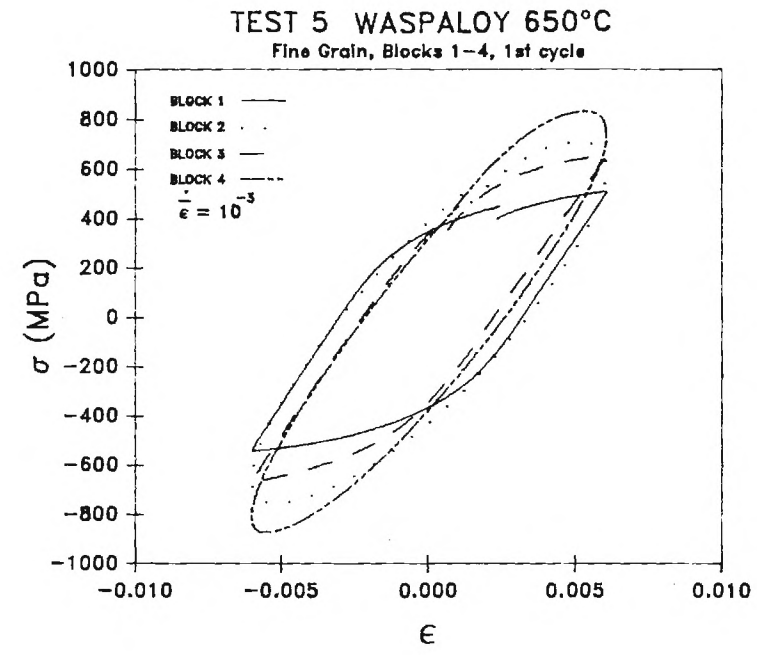
TEST 5 WASPALOY 650°C
Fine Grain, Blocks 1–4, 1st cycle
BLOCK 1
BLOCK 2
BLOCK 3
BLOCK 4
$\dot{\epsilon} = 10^{-3}$
σ (MPa)
ϵ
1000
800
600
400
200
0
−200
−400
−600
−800
−1000

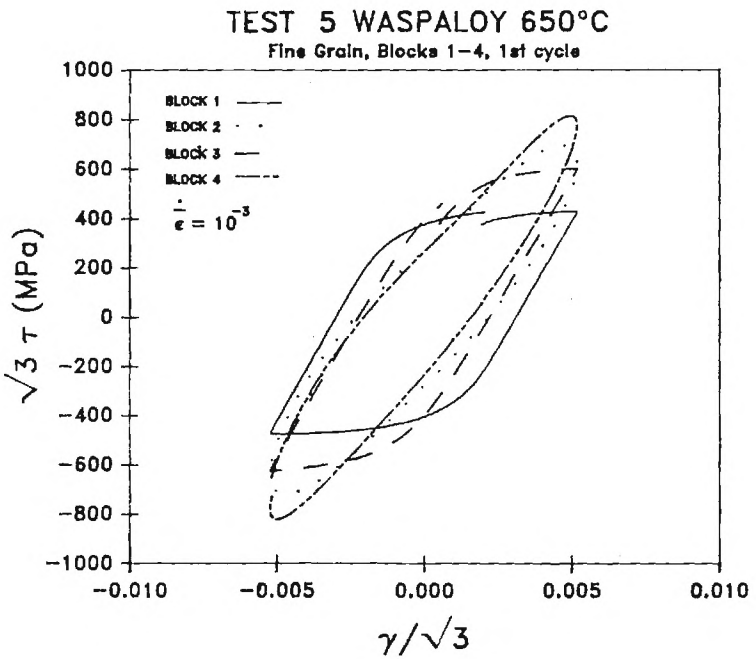
TEST 5 WASPALOY 650°C
Fine Grain, Blocks 1–4, 1st cycle
BLOCK 1
BLOCK 2
BLOCK 3
BLOCK 4
$\dot{\epsilon} = 10^{-3}$
$\sqrt{3}\,\tau$ (MPa)
$\gamma/\sqrt{3}$
1000
800
600
400
200
0
−200
−400
−600
−800
−1000

Figure 9

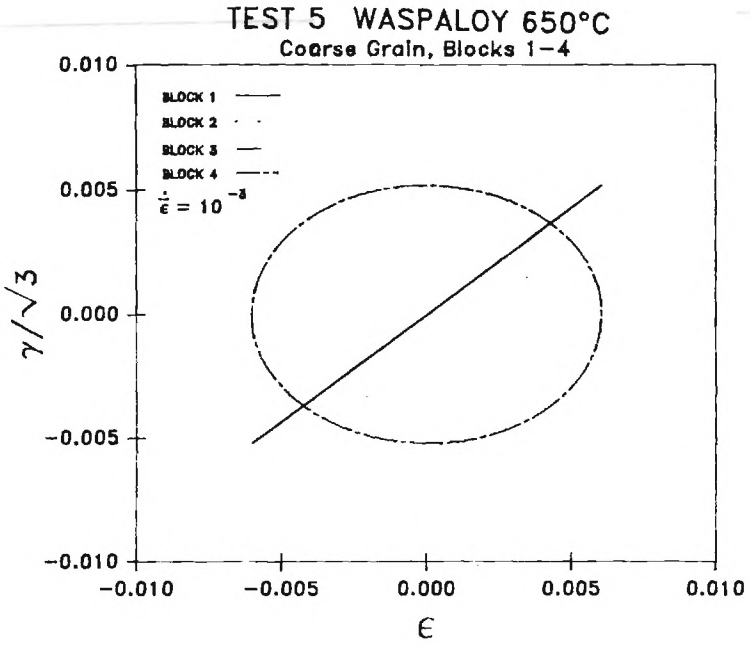
TEST 5 WASPALOY 650°C
Coarse Grain, Blocks 1–4
BLOCK 1
BLOCK 2
BLOCK 3
BLOCK 4
$\dot{\epsilon} = 10^{-3}$
$\gamma/\sqrt{3}$
ϵ
0.010
0.005
0.000
-0.005
-0.010

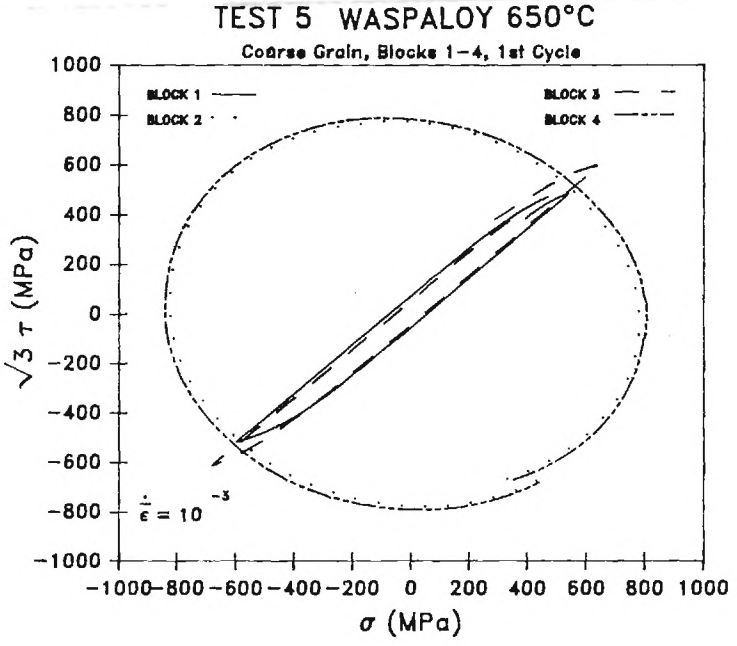
TEST 5 WASPALOY 650°C
Coarse Grain, Blocks 1–4, 1st Cycle
BLOCK 1
BLOCK 2
BLOCK 3
BLOCK 4
$\dot{\epsilon} = 10^{-3}$
$\sqrt{3}\,\tau$ (MPa)
σ (MPa)
1000
800
600
400
200
0
-200
-400
-600
-800
-1000

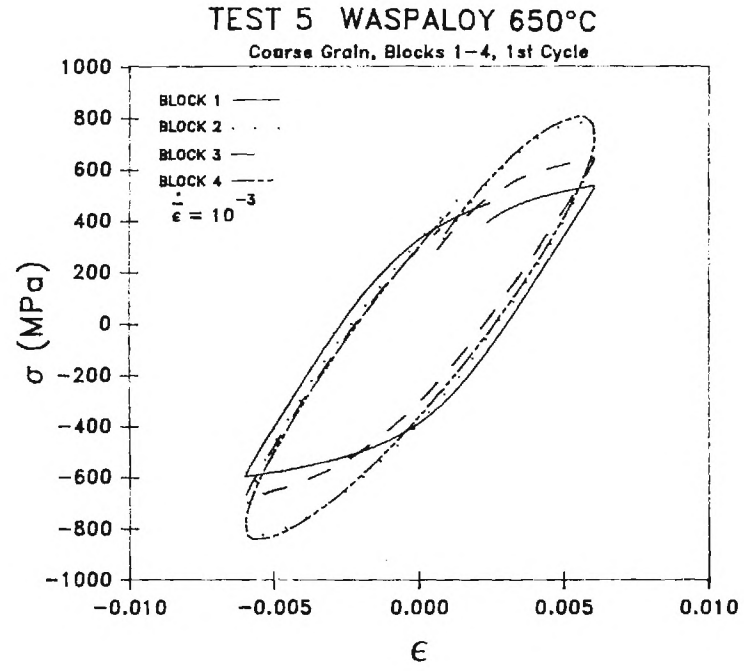
TEST 5 WASPALOY 650°C
Coarse Grain, Blocks 1–4, 1st Cycle
BLOCK 1
BLOCK 2
BLOCK 3
BLOCK 4
$\dot{\epsilon} = 10^{-3}$
σ (MPa)
ϵ
1000
800
600
400
200
0
-200
-400
-600
-800
-1000

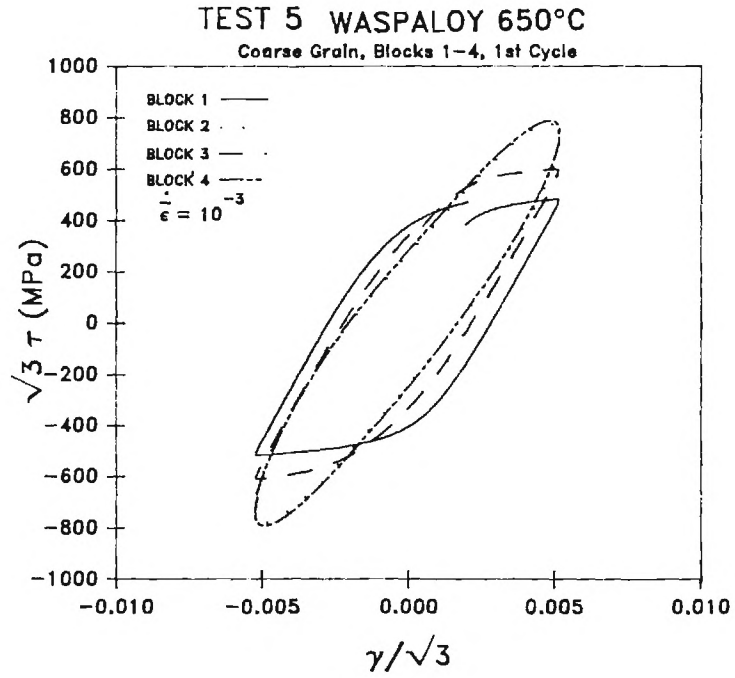
TEST 5 WASPALOY 650°C
Coarse Grain, Blocks 1–4, 1st Cycle
BLOCK 1
BLOCK 2
BLOCK 3
BLOCK 4
$\dot{\epsilon} = 10^{-3}$
$\sqrt{3}\,\tau$ (MPa)
$\gamma/\sqrt{3}$
1000
800
600
400
200
0
-200
-400
-600
-800
-1000

Figure 10

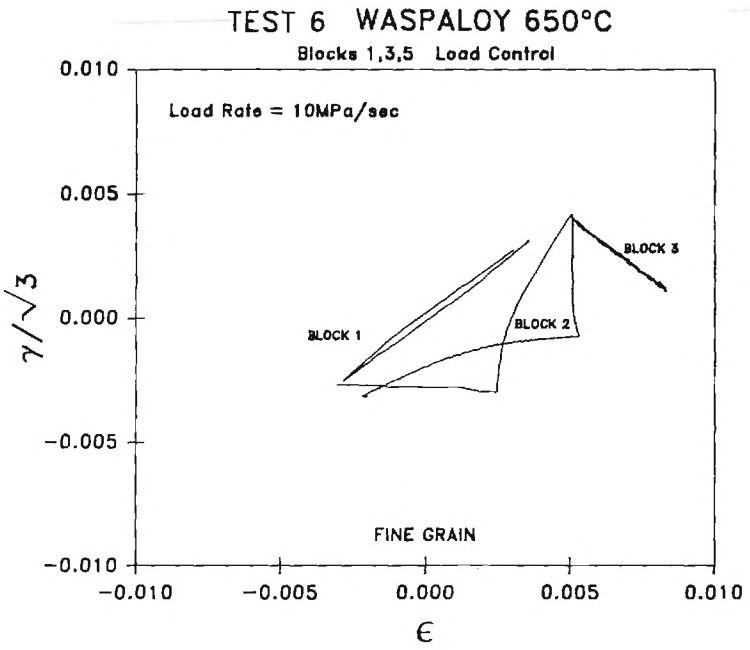
TEST 6 WASPALOY 650°C
Blocks 1,3,5 Load Control
Load Rate = 10MPa/sec
BLOCK 1
BLOCK 2
BLOCK 3
FINE GRAIN
γ/√3
ϵ
0.010
0.005
0.000
-0.005
-0.010

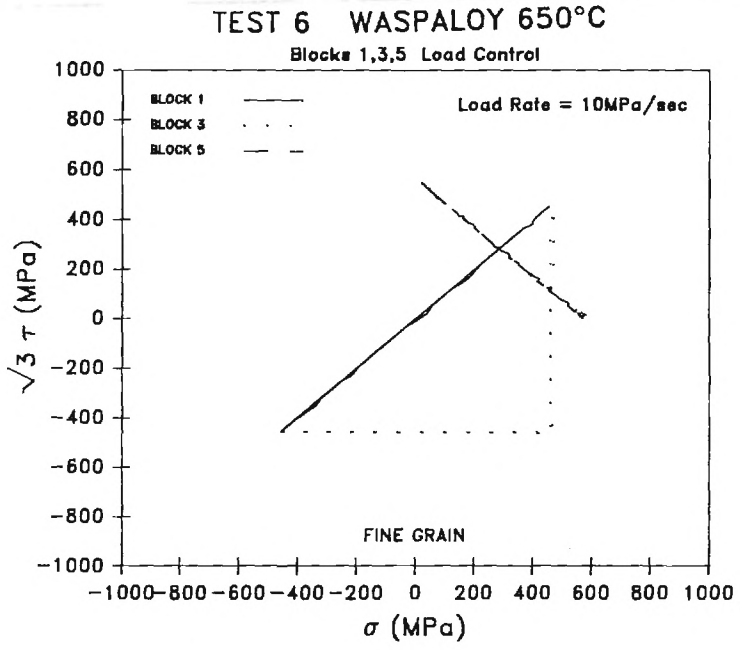
TEST 6 WASPALOY 650°C
Blocks 1,3,5 Load Control
BLOCK 1
BLOCK 3
BLOCK 5
Load Rate = 10MPa/sec
FINE GRAIN
√3 τ (MPa)
σ (MPa)
1000
800
600
400
200
0
-200
-400
-600
-800
-1000

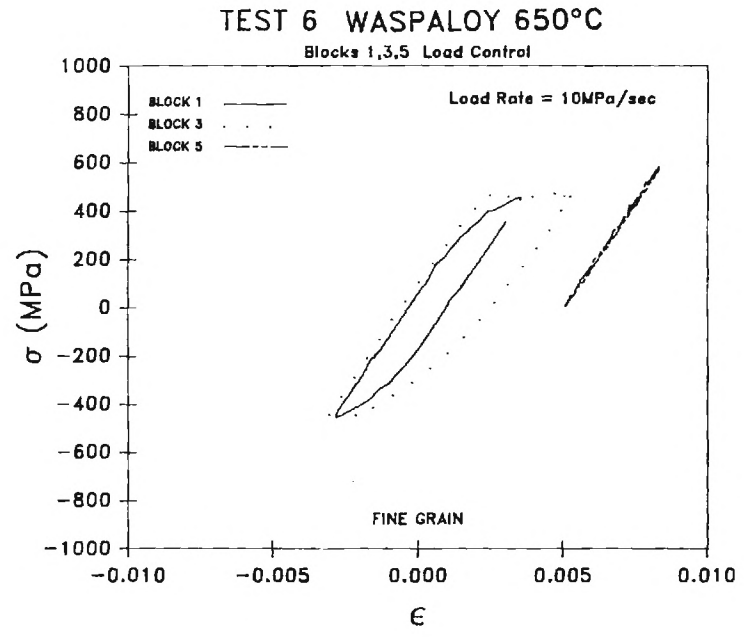
TEST 6 WASPALOY 650°C
Blocks 1,3,5 Load Control
BLOCK 1
BLOCK 3
BLOCK 5
Load Rate = 10MPa/sec
FINE GRAIN
σ (MPa)
ϵ
1000
800
600
400
200
0
-200
-400
-600
-800
-1000
-0.010
-0.005
0.000
0.005
0.010

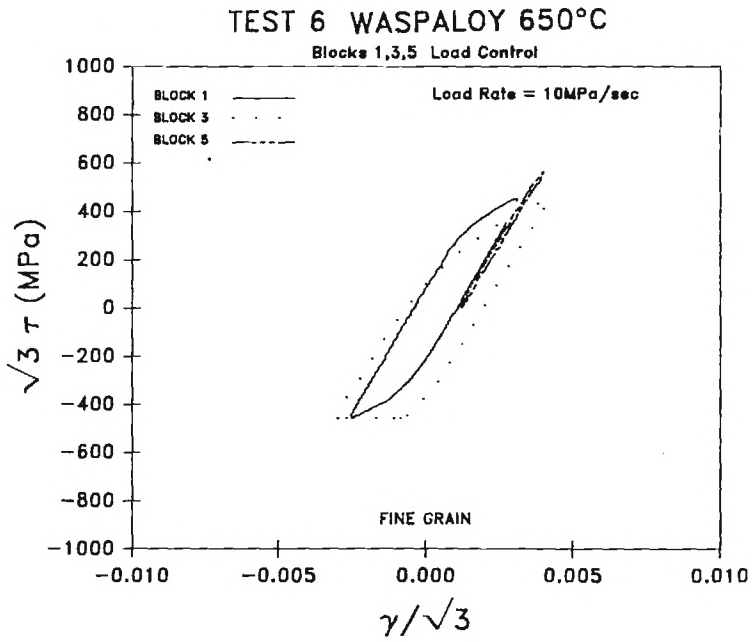
TEST 6 WASPALOY 650°C
Blocks 1,3,5 Load Control
BLOCK 1
BLOCK 3
BLOCK 5
Load Rate = 10MPa/sec
FINE GRAIN
√3 τ (MPa)
γ/√3
1000
800
600
400
200
0
-200
-400
-600
-800
-1000
-0.010
-0.005
0.000
0.005
0.010

Figure 11

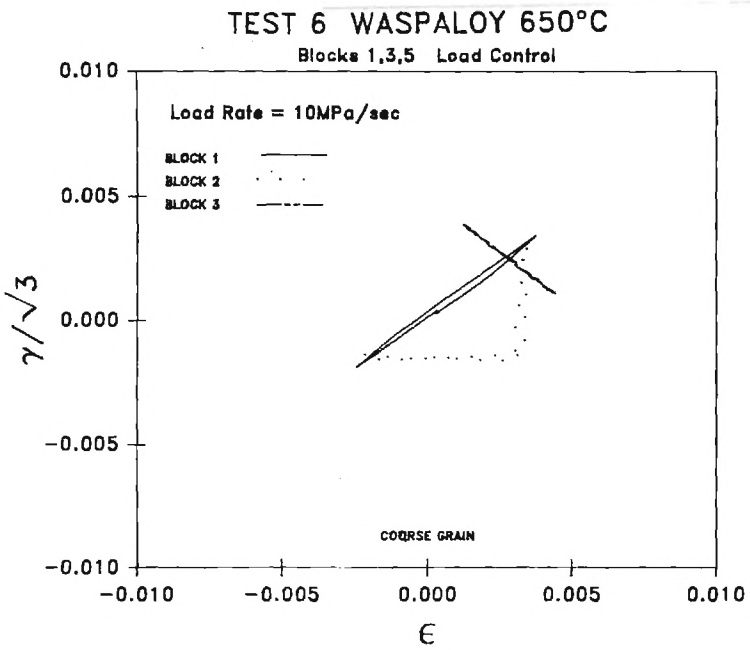
TEST 6 WASPALOY 650°C
Blocks 1,3,5 Load Control
Load Rate = 10MPa/sec
BLOCK 1
BLOCK 2
BLOCK 3
COARSE GRAIN
γ/√3
ϵ
0.010
0.005
0.000
-0.005
-0.010

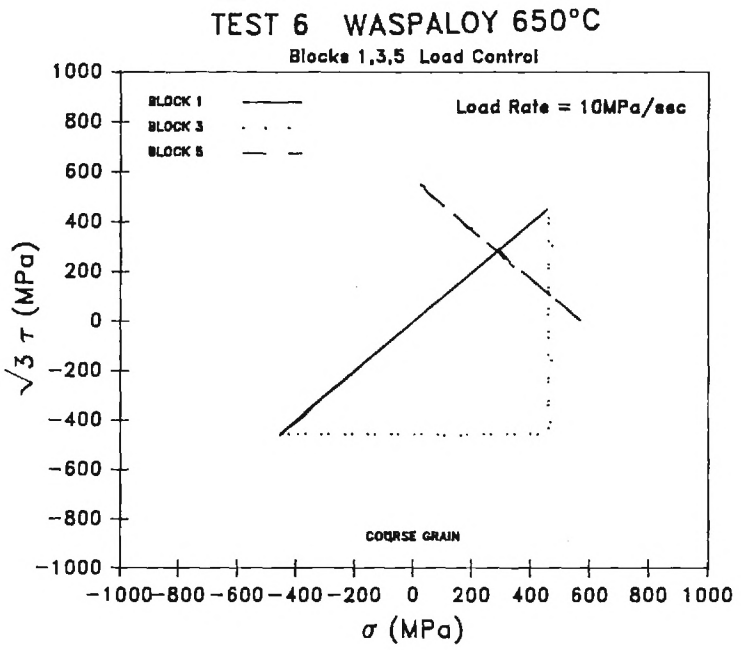
TEST 6 WASPALOY 650°C
Blocks 1,3,5 Load Control
Load Rate = 10MPa/sec
BLOCK 1
BLOCK 3
BLOCK 5
COARSE GRAIN
√3 τ (MPa)
σ (MPa)
1000
800
600
400
200
0
-200
-400
-600
-800
-1000

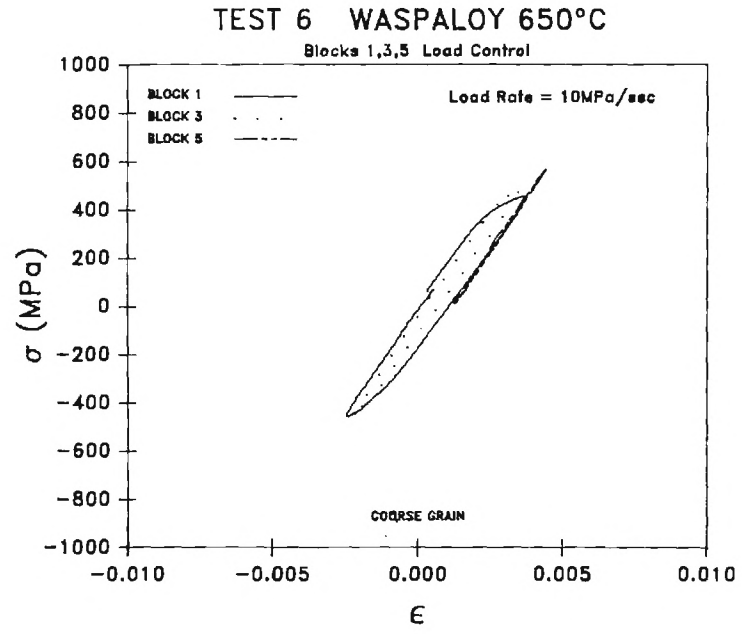
TEST 6 WASPALOY 650°C
Blocks 1,3,5 Load Control
Load Rate = 10MPa/sec
BLOCK 1
BLOCK 3
BLOCK 5
COARSE GRAIN
σ (MPa)
ϵ
1000
800
600
400
200
0
-200
-400
-600
-800
-1000

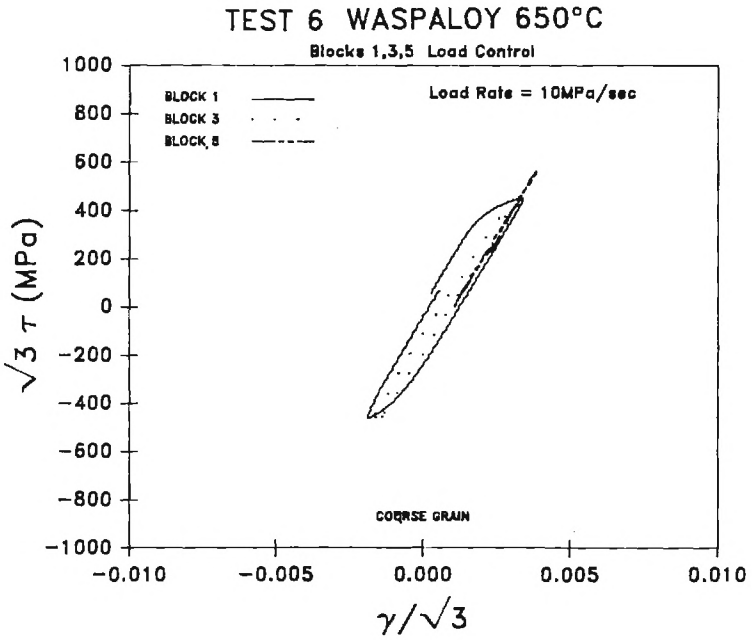
TEST 6 WASPALOY 650°C
Blocks 1,3,5 Load Control
Load Rate = 10MPa/sec
BLOCK 1
BLOCK 3
BLOCK 5
COARSE GRAIN
√3 τ (MPa)
γ/√3
1000
800
600
400
200
0
-200
-400
-600
-800
-1000

Figure 12

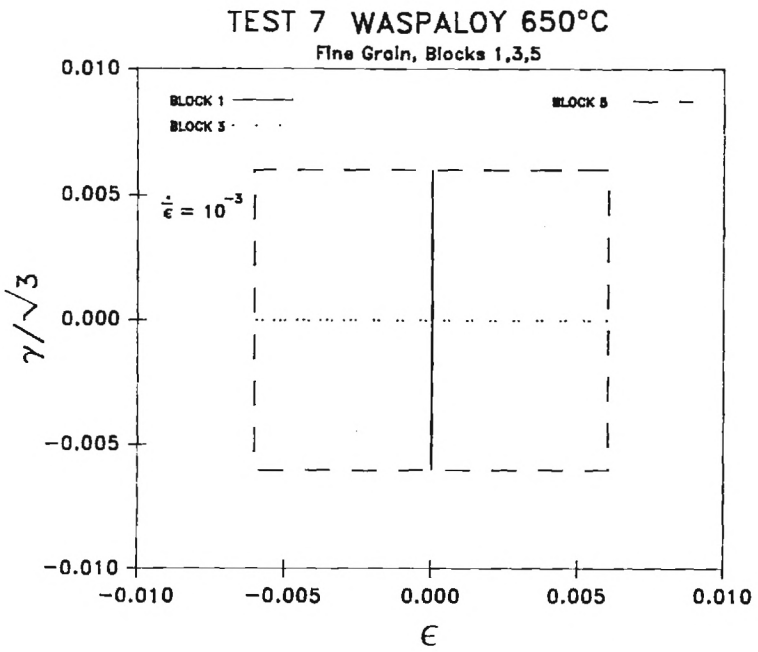
TEST 7 WASPALOY 650°C
Fine Grain, Blocks 1,3,5
BLOCK 1
BLOCK 3
BLOCK 5
$\dot{\epsilon} = 10^{-3}$
$\gamma/\sqrt{3}$
ϵ
0.010
0.005
0.000
-0.005
-0.010

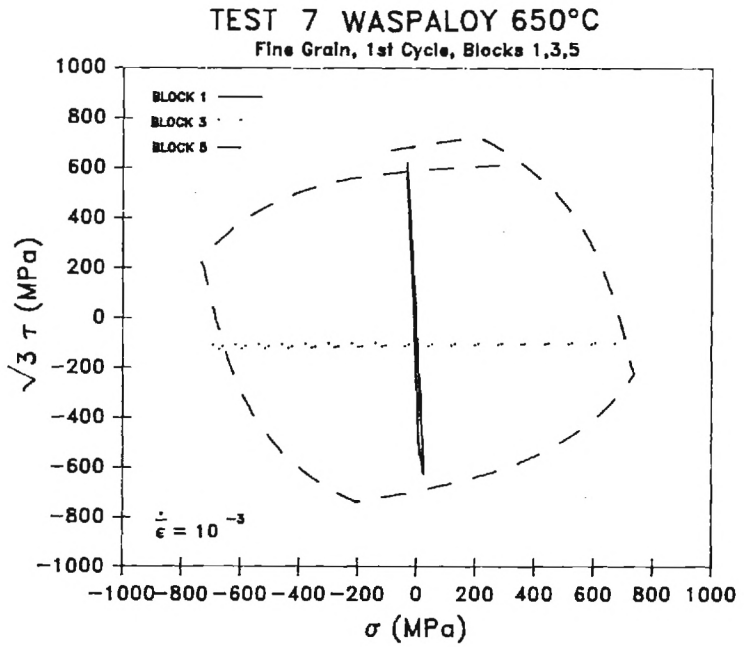
TEST 7 WASPALOY 650°C
Fine Grain, 1st Cycle, Blocks 1,3,5
BLOCK 1
BLOCK 3
BLOCK 5
$\dot{\epsilon} = 10^{-3}$
$\sqrt{3}\,\tau$ (MPa)
σ (MPa)
1000
800
600
400
200
0
-200
-400
-600
-800
-1000

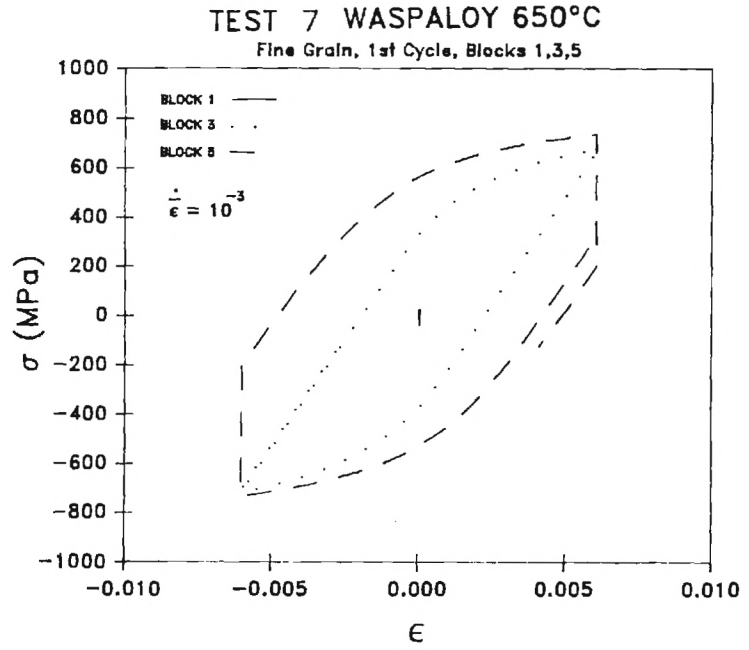
TEST 7 WASPALOY 650°C
Fine Grain, 1st Cycle, Blocks 1,3,5
BLOCK 1
BLOCK 3
BLOCK 5
$\dot{\epsilon} = 10^{-3}$
σ (MPa)
ϵ
1000
800
600
400
200
0
-200
-400
-600
-800
-1000

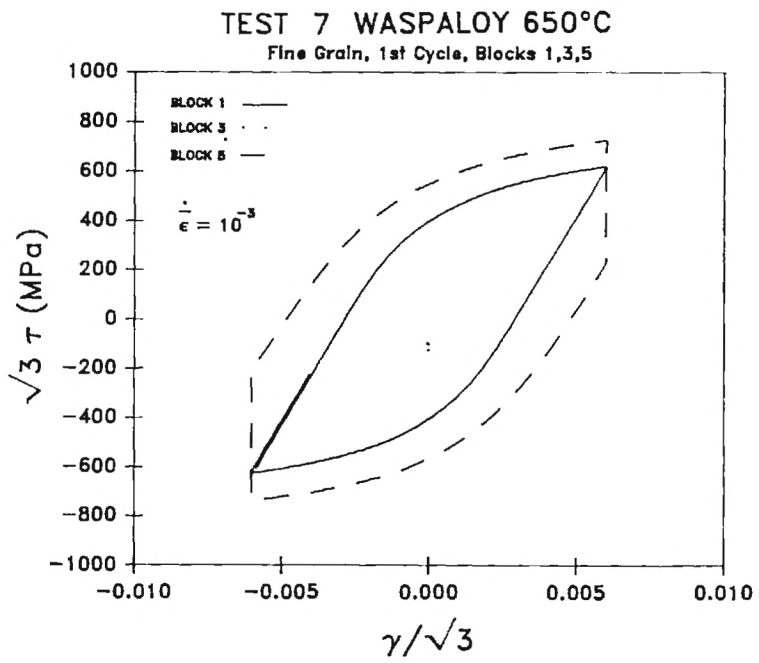
TEST 7 WASPALOY 650°C
Fine Grain, 1st Cycle, Blocks 1,3,5
BLOCK 1
BLOCK 3
BLOCK 5
$\dot{\epsilon} = 10^{-3}$
$\sqrt{3}\,\tau$ (MPa)
$\gamma/\sqrt{3}$
1000
800
600
400
200
0
-200
-400
-600
-800
-1000

Figure 13

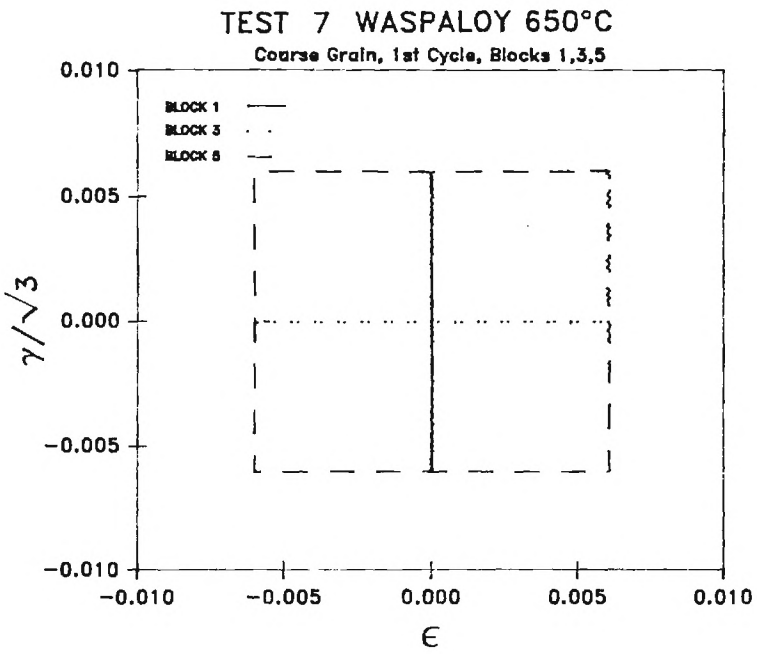
TEST 7 WASPALOY 650°C
Coarse Grain, 1st Cycle, Blocks 1,3,5
BLOCK 1
BLOCK 3
BLOCK 5
0.010
0.005
0.000
-0.005
-0.010
γ/√3
-0.010
-0.005
0.000
0.005
0.010
ϵ

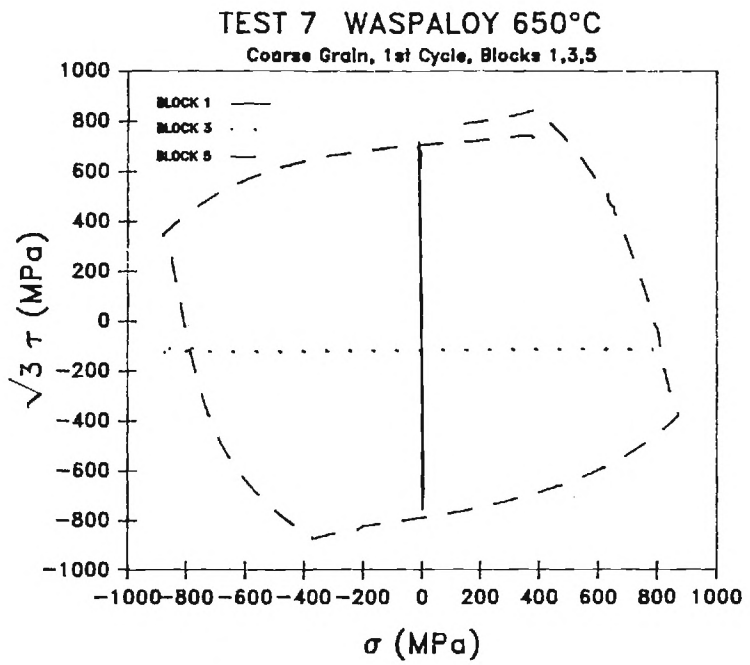
TEST 7 WASPALOY 650°C
Coarse Grain, 1st Cycle, Blocks 1,3,5
BLOCK 1
BLOCK 3
BLOCK 5
1000
800
600
400
200
0
-200
-400
-600
-800
-1000
√3 τ (MPa)
-1000 -800 -600 -400 -200 0 200 400 600 800 1000
σ (MPa)

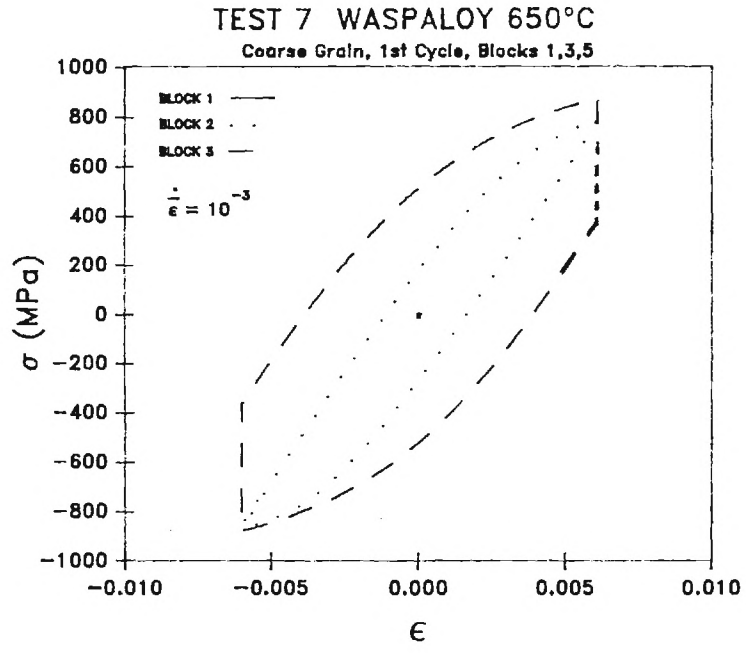
TEST 7 WASPALOY 650°C
Coarse Grain, 1st Cycle, Blocks 1,3,5
BLOCK 1
BLOCK 2
BLOCK 3
$\dot{\epsilon} = 10^{-3}$
1000
800
600
400
200
0
-200
-400
-600
-800
-1000
σ (MPa)
-0.010
-0.005
0.000
0.005
0.010
ϵ

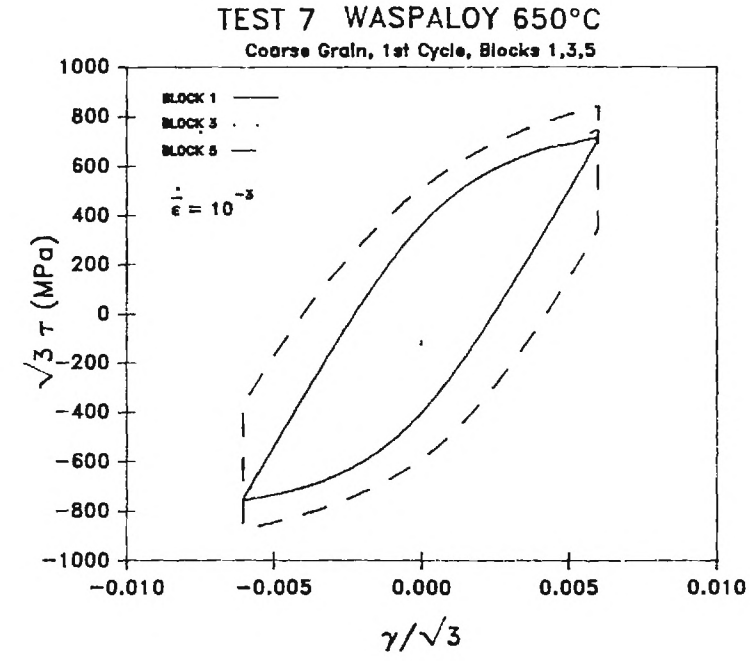
TEST 7 WASPALOY 650°C
Coarse Grain, 1st Cycle, Blocks 1,3,5
BLOCK 1
BLOCK 3
BLOCK 5
$\dot{\epsilon} = 10^{-3}$
1000
800
600
400
200
0
-200
-400
-600
-800
-1000
√3 τ (MPa)
-0.010
-0.005
0.000
0.005
0.010
γ/√3

Figure 14

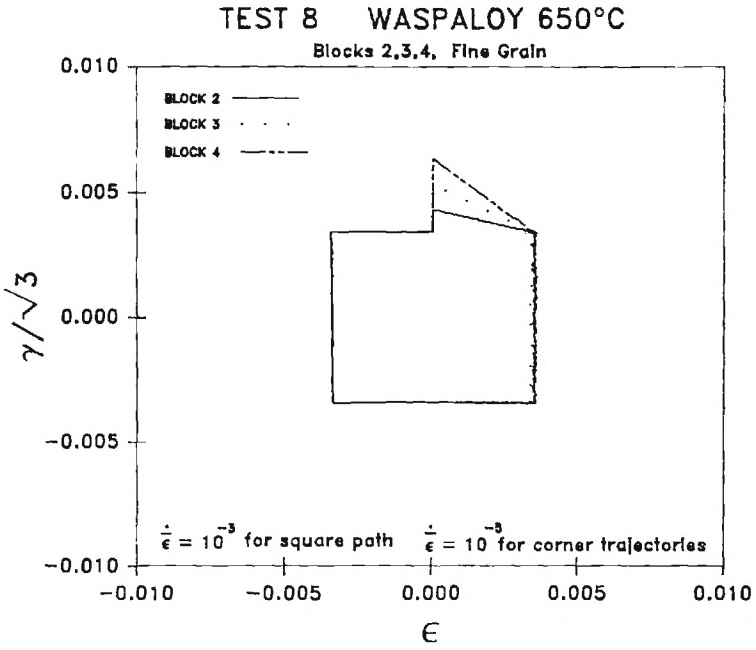
TEST 8 WASPALOY 650°C
Blocks 2,3,4, Fine Grain
BLOCK 2
BLOCK 3
BLOCK 4
$\dot{\epsilon} = 10^{-3}$ for square path $\dot{\epsilon} = 10^{-5}$ for corner trajectories
$\gamma/\sqrt{3}$
ϵ

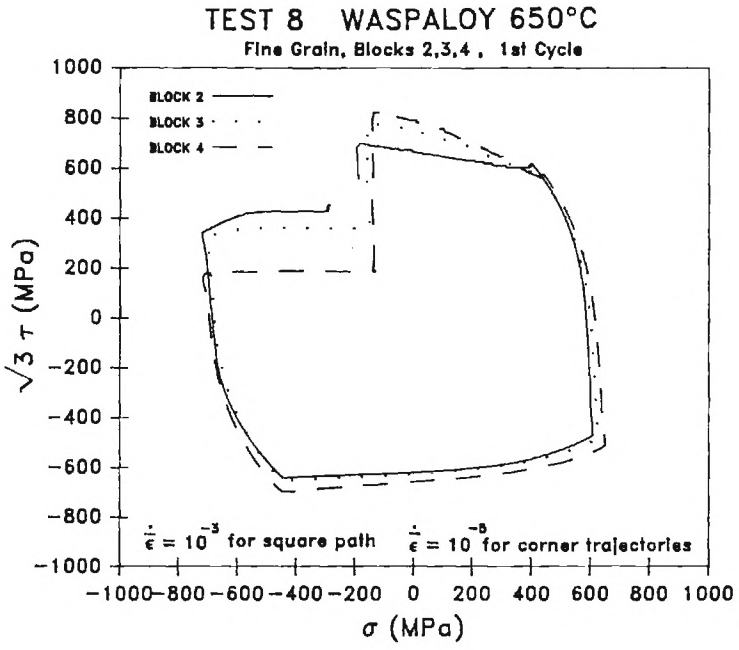
TEST 8 WASPALOY 650°C
Fine Grain, Blocks 2,3,4 , 1st Cycle
BLOCK 2
BLOCK 3
BLOCK 4
$\dot{\epsilon} = 10^{-3}$ for square path $\dot{\epsilon} = 10^{-5}$ for corner trajectories
$\sqrt{3}\,\tau$ (MPa)
σ (MPa)

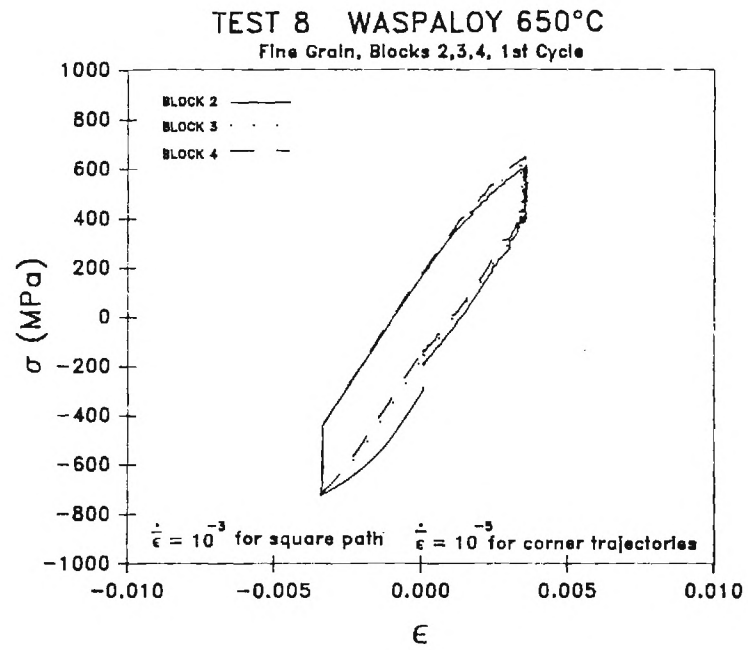
TEST 8 WASPALOY 650°C
Fine Grain, Blocks 2,3,4, 1st Cycle
BLOCK 2
BLOCK 3
BLOCK 4
$\dot{\epsilon} = 10^{-3}$ for square path $\dot{\epsilon} = 10^{-5}$ for corner trajectories
σ (MPa)
ϵ

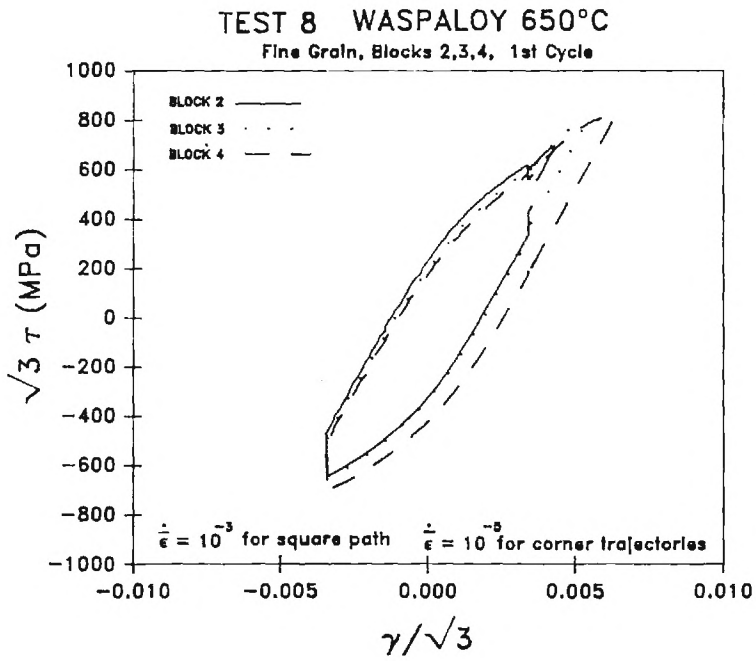
TEST 8 WASPALOY 650°C
Fine Grain, Blocks 2,3,4, 1st Cycle
BLOCK 2
BLOCK 3
BLOCK 4
$\dot{\epsilon} = 10^{-3}$ for square path $\dot{\epsilon} = 10^{-5}$ for corner trajectories
$\sqrt{3}\,\tau$ (MPa)
$\gamma/\sqrt{3}$

Figure 15

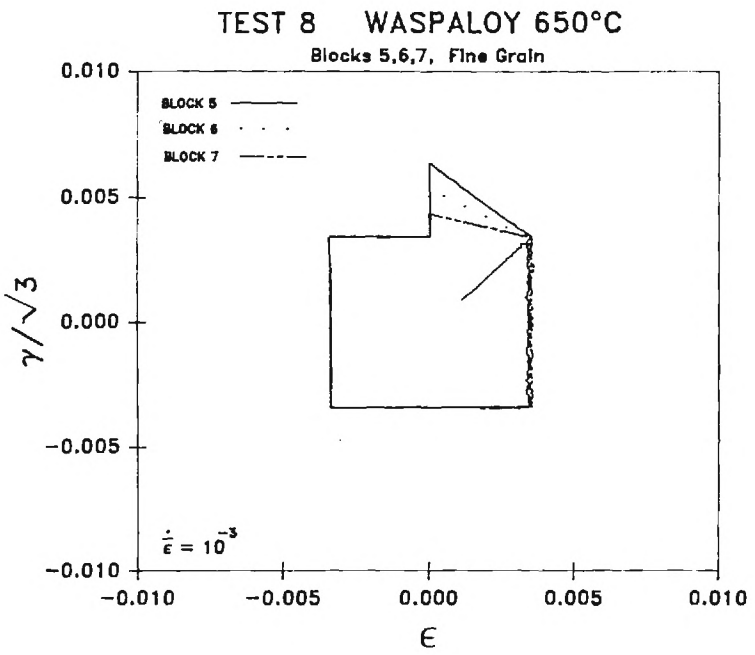
TEST 8 WASPALOY 650°C
Blocks 5,6,7, Fine Grain
BLOCK 5
BLOCK 6
BLOCK 7
$\dot{\epsilon} = 10^{-3}$
$\gamma/\sqrt{3}$
ϵ
0.010
0.005
0.000
-0.005
-0.010

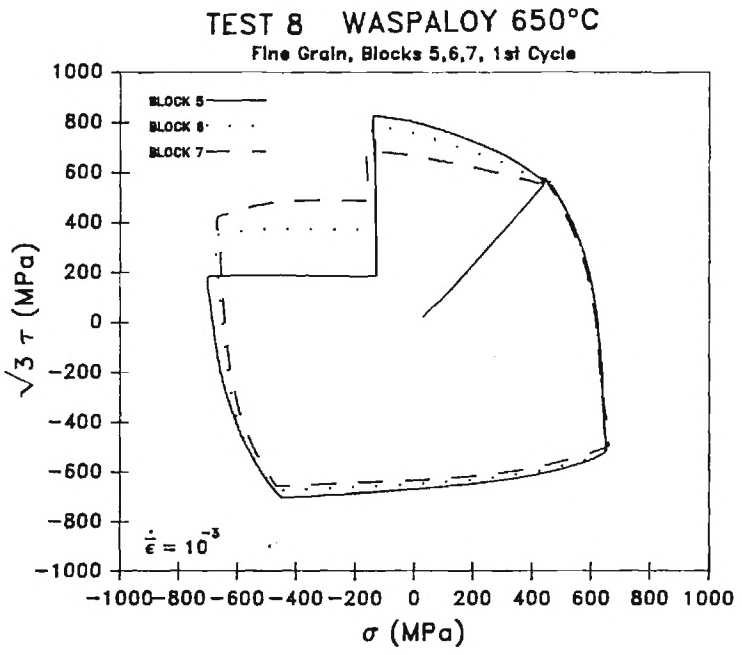
TEST 8 WASPALOY 650°C
Fine Grain, Blocks 5,6,7, 1st Cycle
BLOCK 5
BLOCK 6
BLOCK 7
$\dot{\epsilon} = 10^{-3}$
$\sqrt{3}\,\tau$ (MPa)
σ (MPa)
1000
800
600
400
200
0
-200
-400
-600
-800
-1000

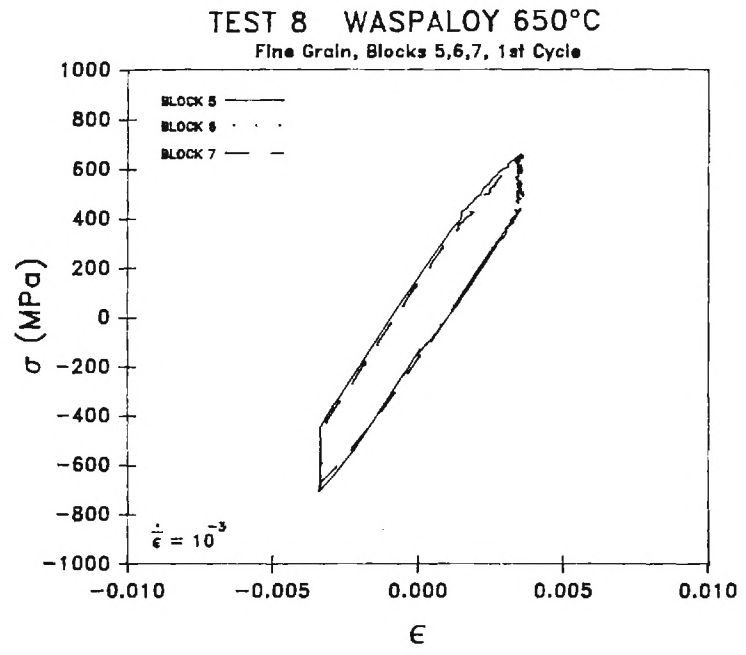
TEST 8 WASPALOY 650°C
Fine Grain, Blocks 5,6,7, 1st Cycle
BLOCK 5
BLOCK 6
BLOCK 7
$\dot{\epsilon} = 10^{-3}$
σ (MPa)
ϵ
1000
800
600
400
200
0
-200
-400
-600
-800
-1000

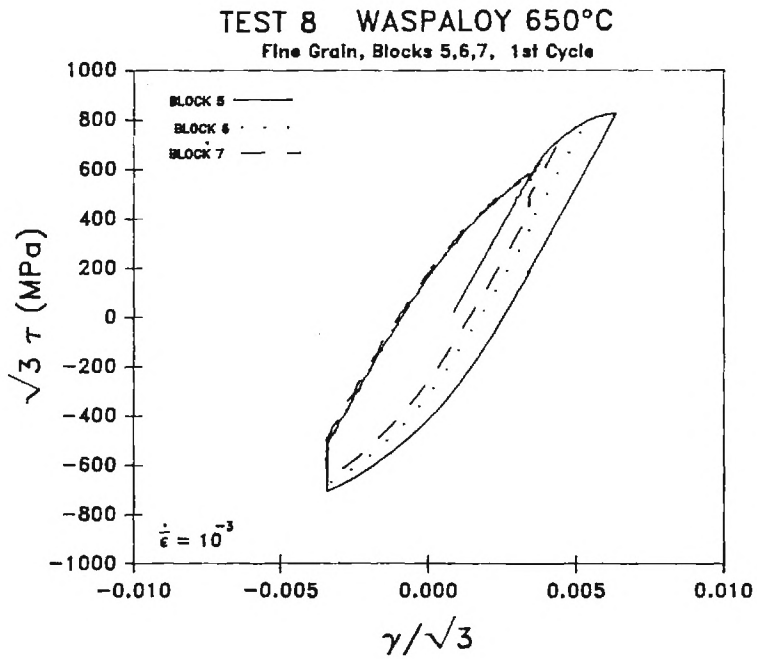
TEST 8 WASPALOY 650°C
Fine Grain, Blocks 5,6,7, 1st Cycle
BLOCK 5
BLOCK 6
BLOCK 7
$\dot{\epsilon} = 10^{-3}$
$\sqrt{3}\,\tau$ (MPa)
$\gamma/\sqrt{3}$
1000
800
600
400
200
0
-200
-400
-600
-800
-1000

Figure 16

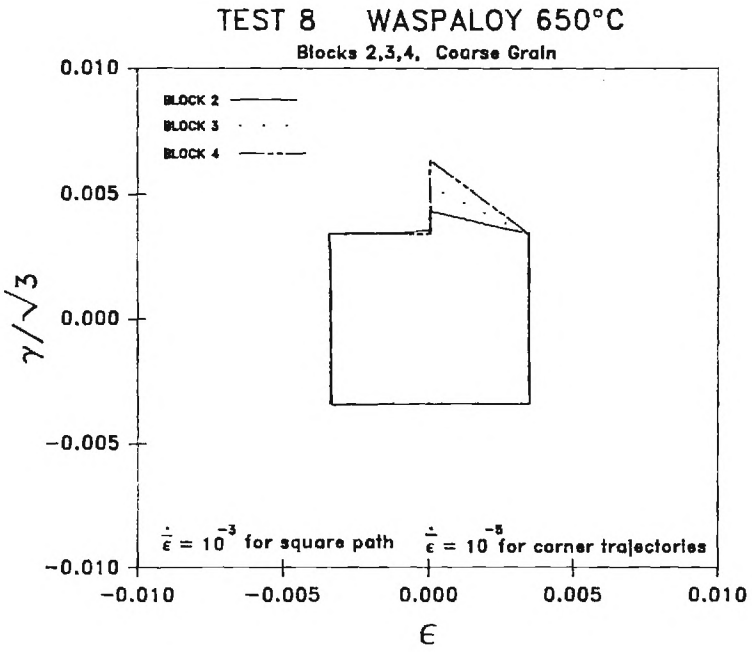
TEST 8 WASPALOY 650°C
Blocks 2,3,4, Coarse Grain
BLOCK 2
BLOCK 3
BLOCK 4
$\dot{\epsilon} = 10^{-3}$ for square path
$\dot{\epsilon} = 10^{-5}$ for corner trajectories
$\gamma/\sqrt{3}$
ϵ

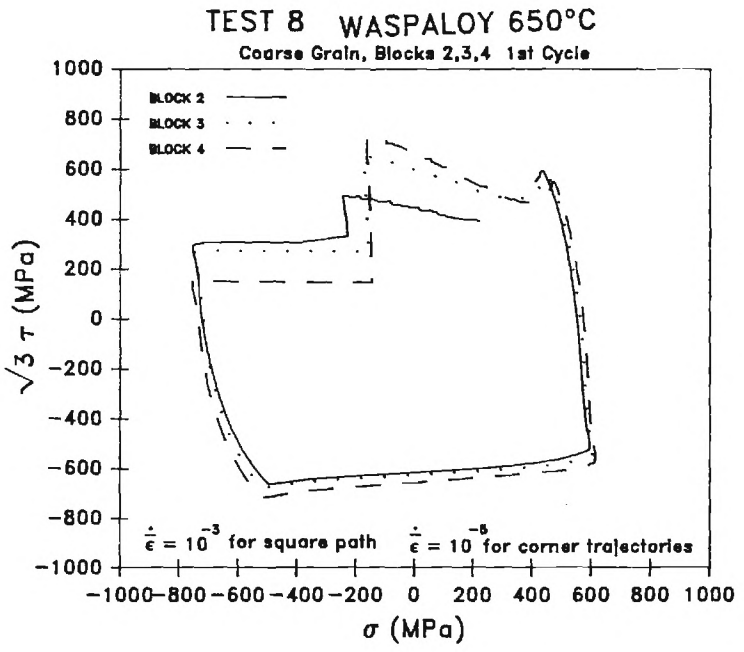
TEST 8 WASPALOY 650°C
Coarse Grain, Blocks 2,3,4 1st Cycle
BLOCK 2
BLOCK 3
BLOCK 4
$\dot{\epsilon} = 10^{-3}$ for square path
$\dot{\epsilon} = 10^{-5}$ for corner trajectories
$\sqrt{3}\,\tau$ (MPa)
σ (MPa)

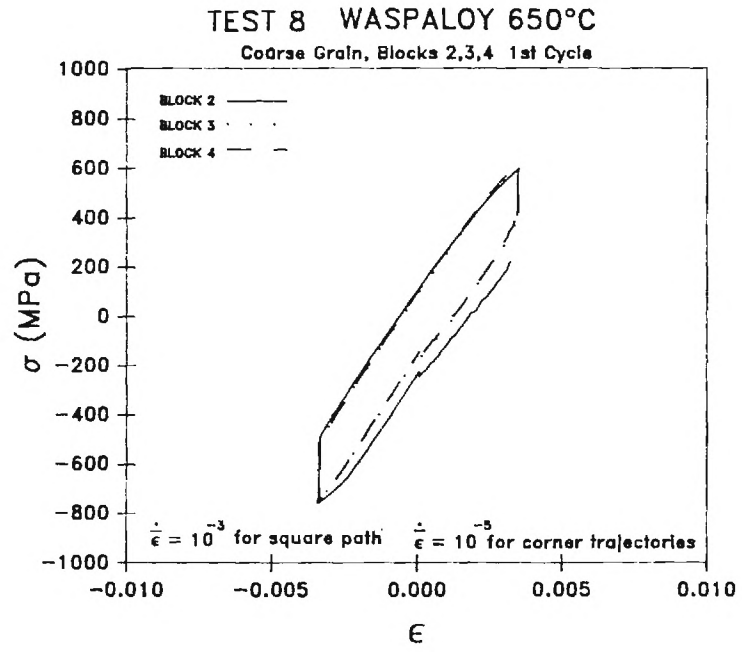
TEST 8 WASPALOY 650°C
Coarse Grain, Blocks 2,3,4 1st Cycle
BLOCK 2
BLOCK 3
BLOCK 4
$\dot{\epsilon} = 10^{-3}$ for square path
$\dot{\epsilon} = 10^{-5}$ for corner trajectories
σ (MPa)
ϵ

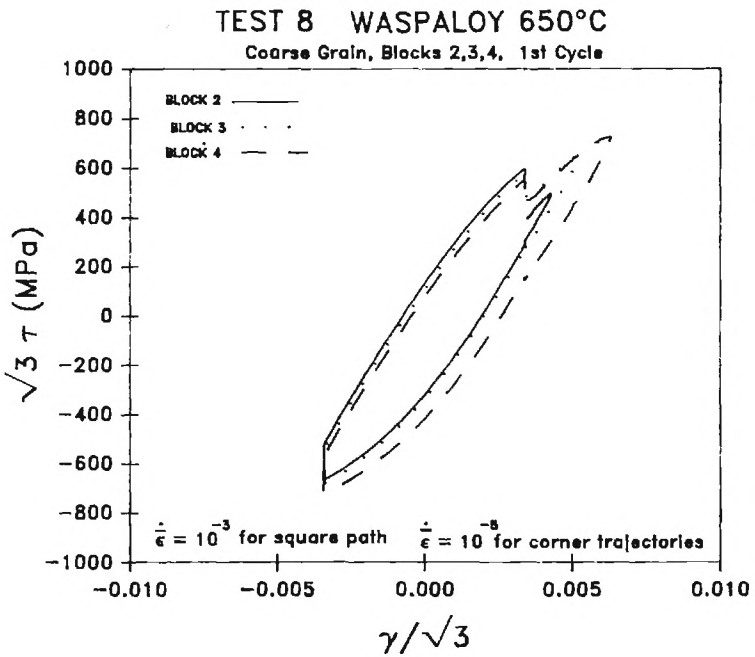
TEST 8 WASPALOY 650°C
Coarse Grain, Blocks 2,3,4, 1st Cycle
BLOCK 2
BLOCK 3
BLOCK 4
$\dot{\epsilon} = 10^{-3}$ for square path
$\dot{\epsilon} = 10^{-5}$ for corner trajectories
$\sqrt{3}\,\tau$ (MPa)
$\gamma/\sqrt{3}$

Figure 17

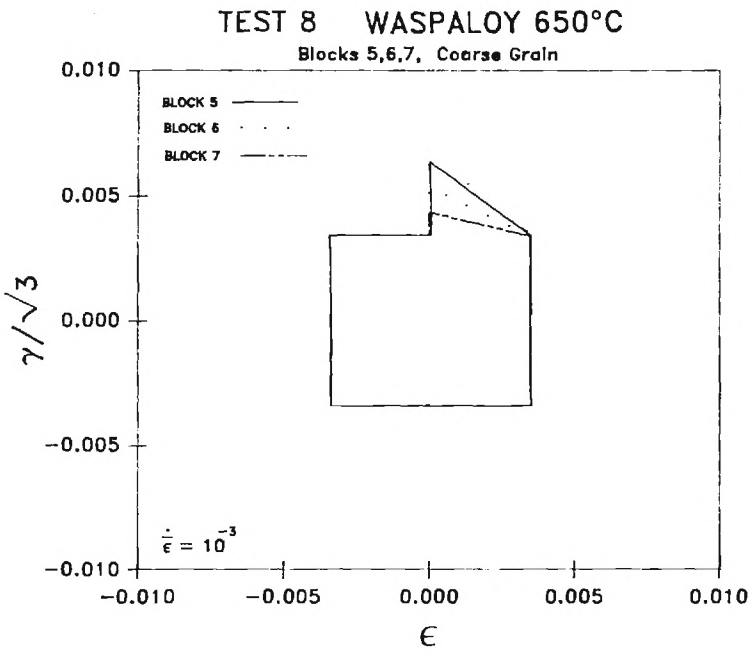
TEST 8 WASPALOY 650°C
Blocks 5,6,7, Coarse Grain
BLOCK 5
BLOCK 6
BLOCK 7
$\dot{\epsilon} = 10^{-3}$
$\gamma/\sqrt{3}$
ϵ
0.010
0.005
0.000
-0.005
-0.010

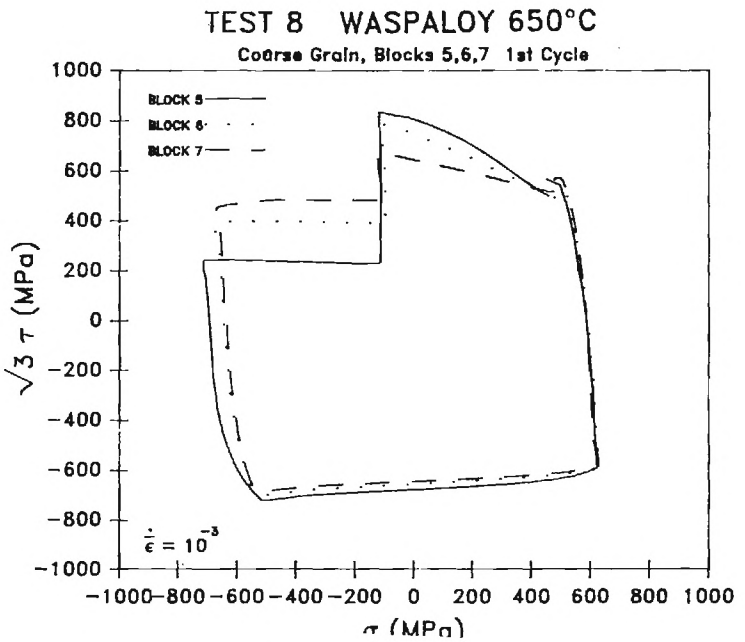
TEST 8 WASPALOY 650°C
Coarse Grain, Blocks 5,6,7 1st Cycle
BLOCK 5
BLOCK 6
BLOCK 7
$\dot{\epsilon} = 10^{-3}$
$\sqrt{3}\,\tau$ (MPa)
σ (MPa)
1000
800
600
400
200
0
-200
-400
-600
-800
-1000

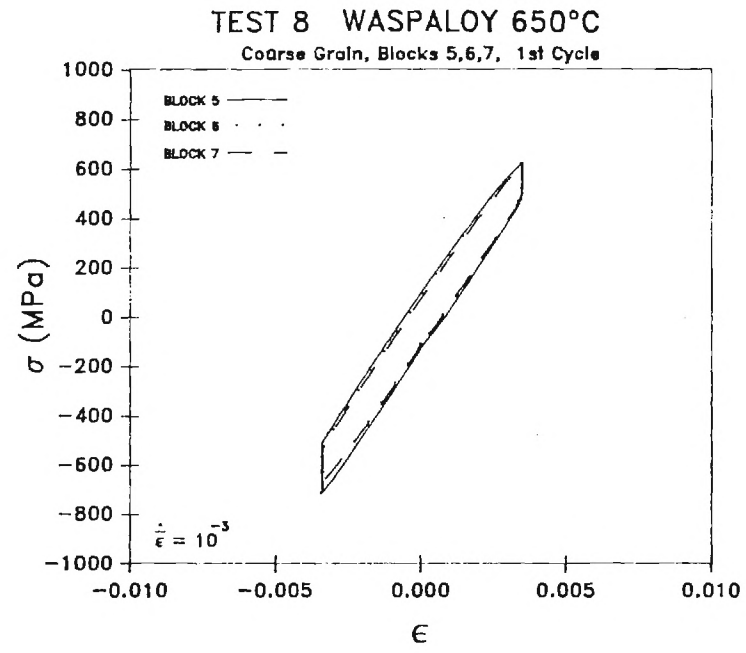
TEST 8 WASPALOY 650°C
Coarse Grain, Blocks 5,6,7, 1st Cycle
BLOCK 5
BLOCK 6
BLOCK 7
$\dot{\epsilon} = 10^{-3}$
σ (MPa)
ϵ
1000
800
600
400
200
0
-200
-400
-600
-800
-1000

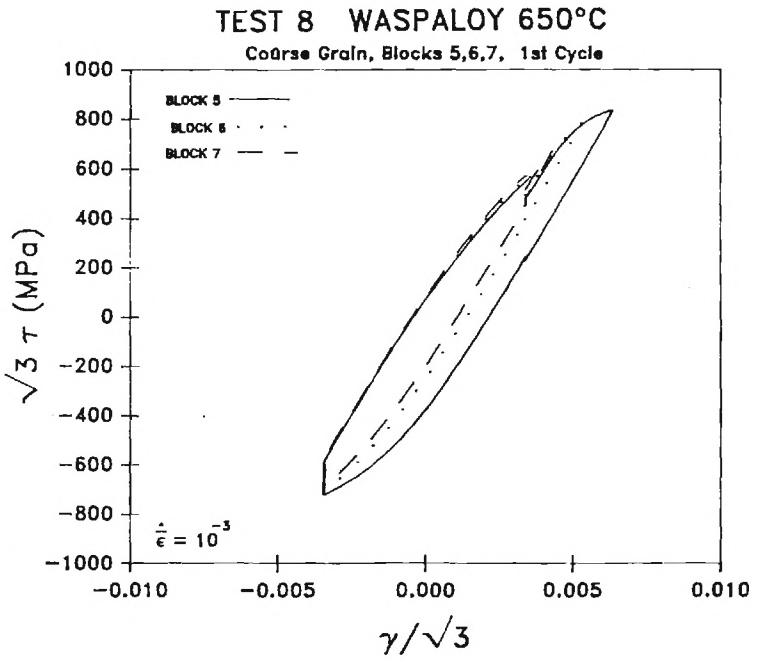
TEST 8 WASPALOY 650°C
Coarse Grain, Blocks 5,6,7, 1st Cycle
BLOCK 5
BLOCK 6
BLOCK 7
$\dot{\epsilon} = 10^{-3}$
$\sqrt{3}\,\tau$ (MPa)
$\gamma/\sqrt{3}$
1000
800
600
400
200
0
-200
-400
-600
-800
-1000

304 STAINLESS STEEL

Table 2-1

304 SS TEST #1

Block Number	Phase Angle β	Number of Cycles	Strain Rate (s^{-1})
1	0	25	10^{-3}
2	$\pi/6$	25	10^{-3}
3	$\pi/3$	25	10^{-3}
4	$\pi/2$	25	10^{-3}
5	$\pi/2$	5	10^{-2}
6	$\pi/2$	5	10^{-3}
7	$\pi/2$	5	10^{-4}
8	$\pi/2$	5	10^{-5}
9	$\pi/2$	5	$10^{-3}/10^{-5}$
10	$\pi/3$	5	$10^{-3}/10^{-5}$
11	$\pi/6$	5	$10^{-3}/10^{-5}$
12	0	5	$10^{-3}/10^{-5}$

$\epsilon = \epsilon_a \sin(n_p/N_s)$, $\gamma = \gamma_a \sin(n_p/N_s - \beta)$, $\epsilon_a = 0.0045$, $\gamma_a = .006$

Note: Blocks 9 - 12 involve cycling at a higher strain rate for half of a cycle and at a lower strain rate for half of a cycle.

Table 2-2

304 SS TEST #4

Block Number	Axial Strain Amplitude ϵ_a	Shear Strain Amplitude γ_a	Number of Ccycles
1	0.0015	0.00225	25
2	0.0030	0.0045	25
3	0.0045	0.00675	25
4	0.0060	0.0090	25
5	0.0045	0.00675	25
6	0.0030	0.0045	25
7	0.0015	0.0030	25
8	0.0060	0.0090	25

$\epsilon = \epsilon_a \sin(2\pi n_p/N_s)$, $\gamma = \gamma_a \sin(2\pi n_p/N_s - \beta)$, $\beta = \pi/2$, $\dot{\bar{\epsilon}} = 10^{-3}\ s^{-1}$

Table 2-3

304 SS TEST #5

Block Number	Phase Angle	Number of Cycles
1	0	25
2	$\pi/2$	25
3	0	25
4	$\pi/2$	25
5	$3\pi/2$	25
6	$\pi/2$	25

$$\epsilon = \epsilon_a \sin(2\pi n_p/N_s),\ \gamma = \gamma_a \sin(2\pi n_p/N_s - \beta)$$

$$\epsilon_a = 0.006,\ \gamma_a = 0.009,\ \dot{\bar{\epsilon}} = 10^{-3}\ s^{-1}$$

Table 2-4

304 SS TEST #6

Block Number		1	2	3	4
Endpoint Sequence σ, τ (MPa)	1 2 3 4 5	$\sigma=\tau=0$ $\sigma=150$ $\tau=-86.6$ $\sigma=150$ $\tau=86.6$ $\sigma=\tau=0$	$\sigma=\tau=0$ $\sigma=150$ $\tau=86.6$ HOLD 2100 s $\sigma=\tau=0$	$\sigma=150$ $\tau=-86.6$ $\sigma=-150$ $\tau=-86.6$ $\sigma=150$ $\tau=-86.6$ $\sigma=150$ $\tau=86.6$ $\sigma=150$ $\tau=-86.6$	$\sigma=150$ $\tau=86.6$ HOLD 2100 s $\sigma=\tau=0$ $\sigma=150$ $\tau=86.6$
Number of Cycles		50	1	50	1
Block Number		5	6	7	8
Endpoint Sequence σ, τ (MPa)	1 2 3 4	$\sigma=0$ $\tau=122.5$ $\sigma=150$ $\tau=0$ $\sigma=0$ $\tau=122.5$	$\sigma=150$ $\tau=86.6$ HOLD 2100 s $\sigma=\tau=0$ $\sigma=150$ $\tau=86.6$	$\sigma=0$ $\tau=122.5$ $\sigma=212.1$ $\tau=0$ $\sigma=0$ $\tau=122.5$	$\sigma=150$ $\tau=86.6$ HOLD 2100 s $\sigma=\tau=0$ $\sigma=150$ $\tau=86.6$
Number of Cycles		50	1	50	1

$\dot{\sigma}$ = 10 MPa/s

Table 2-5

304 SS TEST #8

Block Number		1	2	3	4
Endpoint Sequence ϵ, γ	1 2 3 4 5 6 7	ϵ=0.0000 γ=0.0000 ϵ=0.0060 γ=0.0104 ϵ=-0.0060 γ=0.0104 ϵ=-0.0060 γ=-0.0104 ϵ=0.0060 γ=-0.0104 ϵ=0.0060 γ=0.0104	ϵ=0.0040 γ=0.0069 ϵ=-0.0040 γ=0.0069 ϵ=-0.0040 γ=-0.0069 ϵ=0.0040 γ=-0.0069 ϵ=0.0040 γ=0.0069	ϵ=0.0040 γ=0.0069 ϵ=0.0000 γ=0.0088 ϵ=0.0000 γ=0.0069 ϵ=-0.0040 γ=0.0069 ϵ=-0.0040 γ=-0.0069 ϵ=0.0040 γ=-0.0069 ϵ=0.0040 γ=0.0069	ϵ=0.0040 γ=0.0069 ϵ=0.0000 γ=0.0109 ϵ=0.0000 γ=0.0069 ϵ=-0.0040 γ=0.0069 ϵ=-0.0040 γ=-0.0069 ϵ=0.0040 γ=-0.0069 ϵ=0.0040 γ=0.0069
Number of Cycles		50	5	5	5
Block Number		5	6	7	8
Endpoint Sequence ϵ, γ	1 2 3 4 5 6 7	ϵ=0.0040 γ=0.0069 ϵ=0.0000 γ=0.0139 ϵ=0.0000 γ=0.0069 ϵ=-0.0040 γ=0.0069 ϵ=-0.0040 γ=-0.0069 ϵ=0.0040 γ=-0.0069 ϵ=0.0040 γ=0.0069	ϵ=0.0040 γ=0.0069 ϵ=0.0000 γ=0.0139 ϵ=0.0000 γ=0.0069 ϵ=-0.0040 γ=0.0069 ϵ=-0.0040 γ=-0.0069 ϵ=0.0040 γ=-0.0069 ϵ=0.0040 γ=0.0069	ϵ=0.0040 γ=0.0069 ϵ=0.0000 γ=0.0109 ϵ=0.0000 γ=0.0069 ϵ=-0.0040 γ=0.0069 ϵ=-0.0040 γ=-0.0069 ϵ=0.0040 γ=-0.0069 ϵ=0.0040 γ=0.0069	ϵ=0.0040 γ=0.0069 ϵ=0.0000 γ=0.0088 ϵ=0.0000 γ=0.0069 ϵ=-0.0040 γ=0.0069 ϵ=-0.0040 γ=-0.0069 ϵ=0.0040 γ=-0.0069 ϵ=0.0040 γ=0.0069
Number of Cycles		5	5	5	5

$\dot{\epsilon} = 10^{-3}\ s^{-1}$ except for endpoint sequence 1 - 2, blocks 3 - 5, during which $\dot{\epsilon} = 10^{-5}\ s^{-1}$

Figure 18

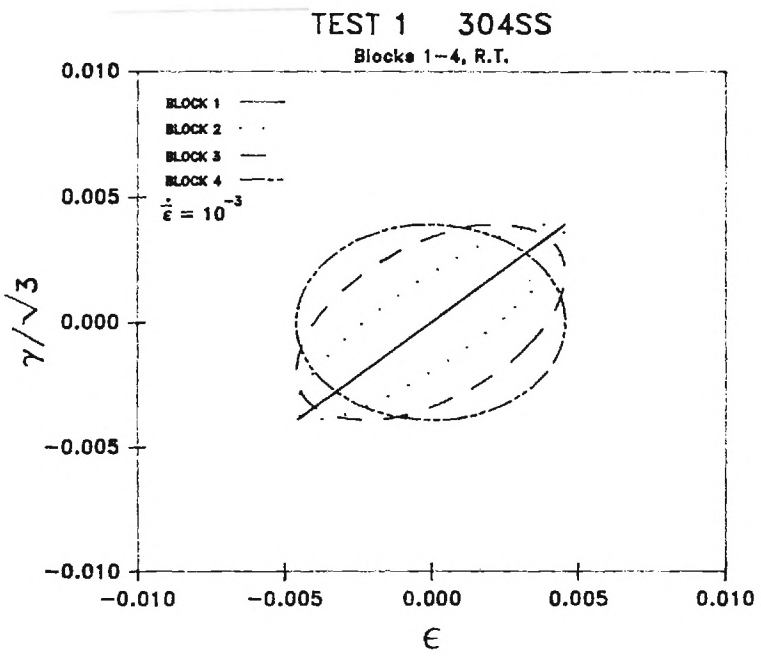
TEST 1 304SS
Blocks 1–4, R.T.
BLOCK 1
BLOCK 2
BLOCK 3
BLOCK 4
$\dot{\epsilon} = 10^{-3}$
$\gamma/\sqrt{3}$
ϵ
0.010
0.005
0.000
−0.005
−0.010

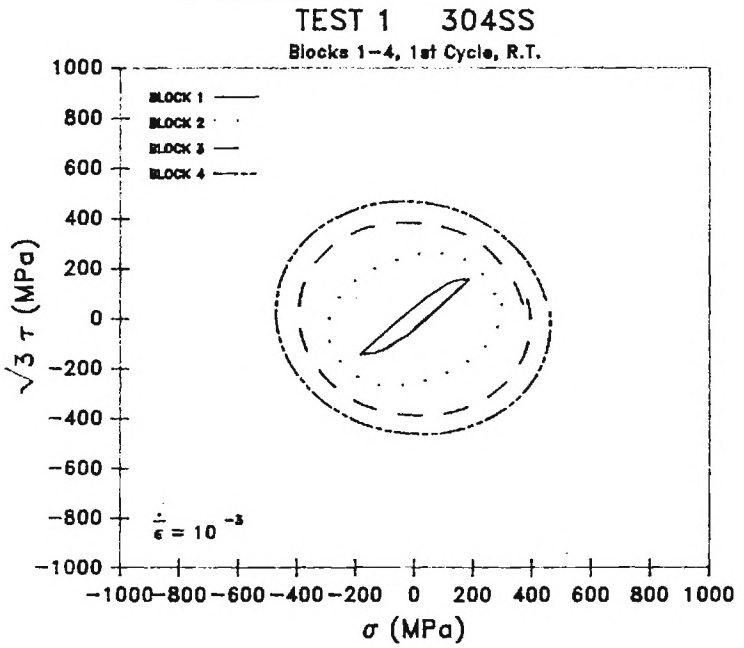
TEST 1 304SS
Blocks 1–4, 1st Cycle, R.T.
BLOCK 1
BLOCK 2
BLOCK 3
BLOCK 4
$\dot{\epsilon} = 10^{-3}$
$\sqrt{3}\,\tau$ (MPa)
σ (MPa)
1000
800
600
400
200
0
−200
−400
−600
−800
−1000

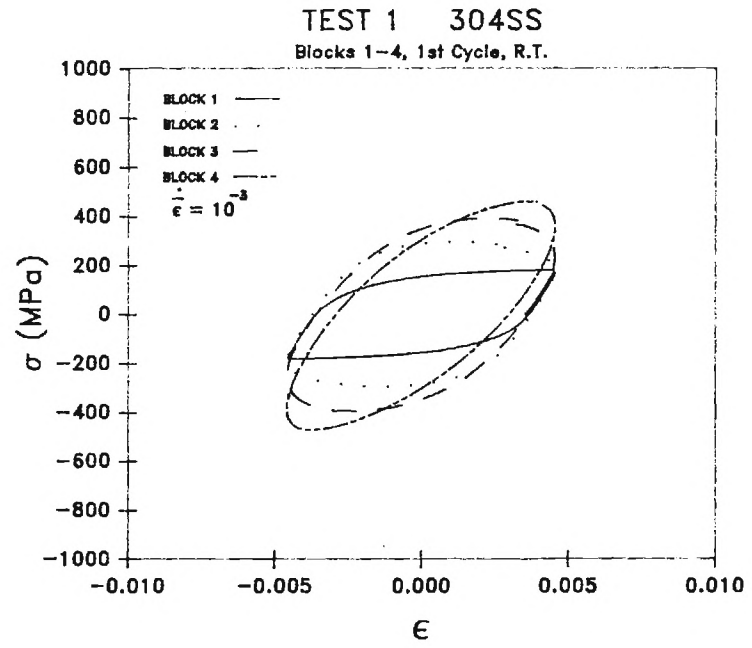
TEST 1 304SS
Blocks 1–4, 1st Cycle, R.T.
BLOCK 1
BLOCK 2
BLOCK 3
BLOCK 4
$\dot{\epsilon} = 10^{-3}$
σ (MPa)
ϵ
1000
800
600
400
200
0
−200
−400
−600
−800
−1000
−0.010
−0.005
0.000
0.005
0.010

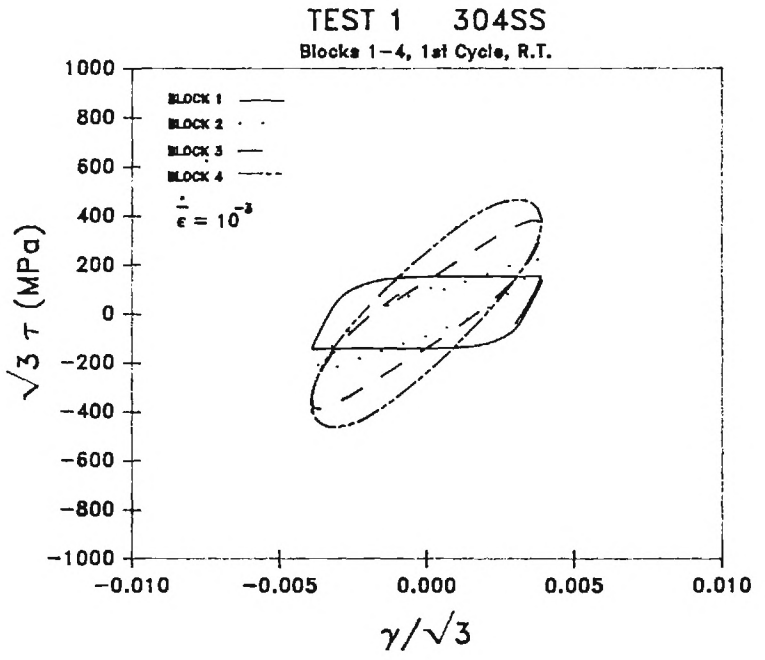
TEST 1 304SS
Blocks 1–4, 1st Cycle, R.T.
BLOCK 1
BLOCK 2
BLOCK 3
BLOCK 4
$\dot{\epsilon} = 10^{-3}$
$\sqrt{3}\,\tau$ (MPa)
$\gamma/\sqrt{3}$
1000
800
600
400
200
0
−200
−400
−600
−800
−1000
−0.010
−0.005
0.000
0.005
0.010

Figure 19

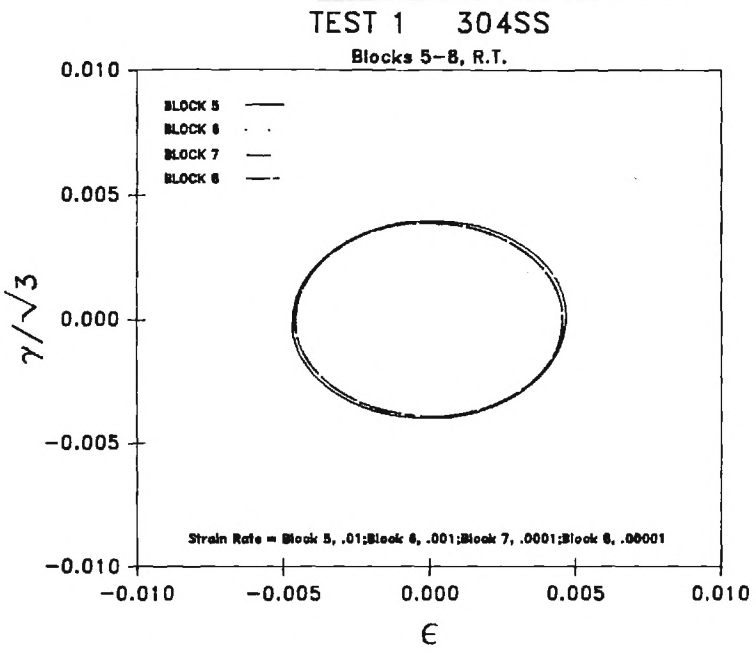
TEST 1 304SS
Blocks 5–8, R.T.
BLOCK 5
BLOCK 6
BLOCK 7
BLOCK 8
Strain Rate = Block 5, .01;Block 6, .001;Block 7, .0001;Block 8, .00001
0.010
0.005
0.000
-0.005
-0.010
-0.010
-0.005
0.000
0.005
0.010
γ/√3
ϵ

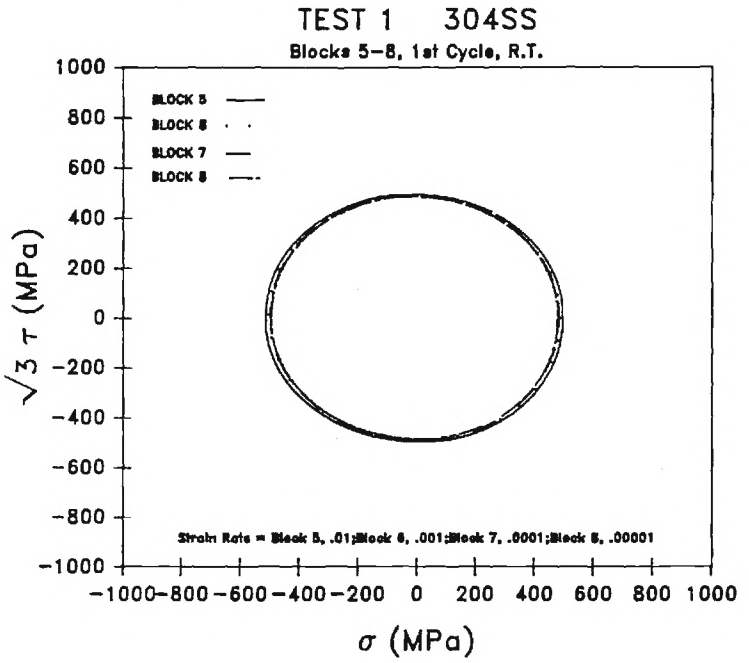
TEST 1 304SS
Blocks 5–8, 1st Cycle, R.T.
BLOCK 5
BLOCK 6
BLOCK 7
BLOCK 8
Strain Rate = Block 5, .01;Block 6, .001;Block 7, .0001;Block 8, .00001
1000
800
600
400
200
0
-200
-400
-600
-800
-1000
-1000 -800 -600 -400 -200 0 200 400 600 800 1000
√3 τ (MPa)
σ (MPa)

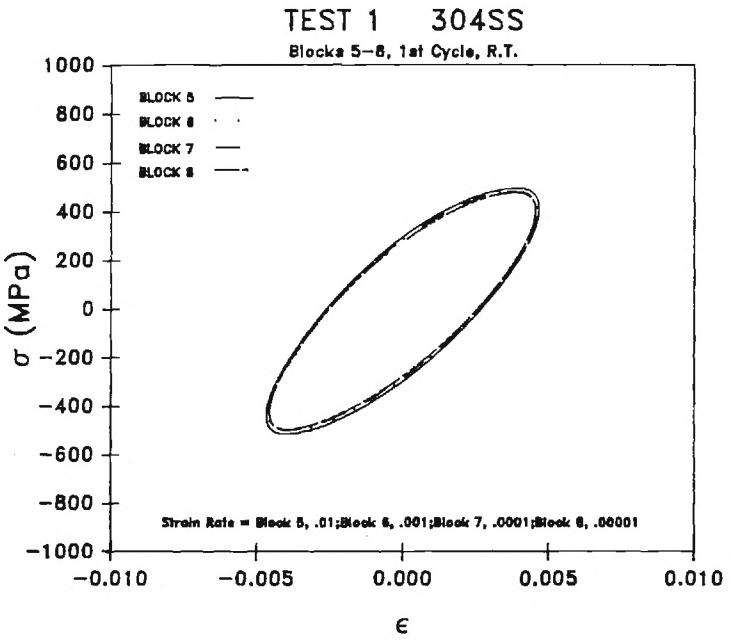
TEST 1 304SS
Blocks 5–8, 1st Cycle, R.T.
BLOCK 5
BLOCK 6
BLOCK 7
BLOCK 8
Strain Rate = Block 5, .01;Block 6, .001;Block 7, .0001;Block 8, .00001
1000
800
600
400
200
0
-200
-400
-600
-800
-1000
-0.010
-0.005
0.000
0.005
0.010
σ (MPa)
ϵ

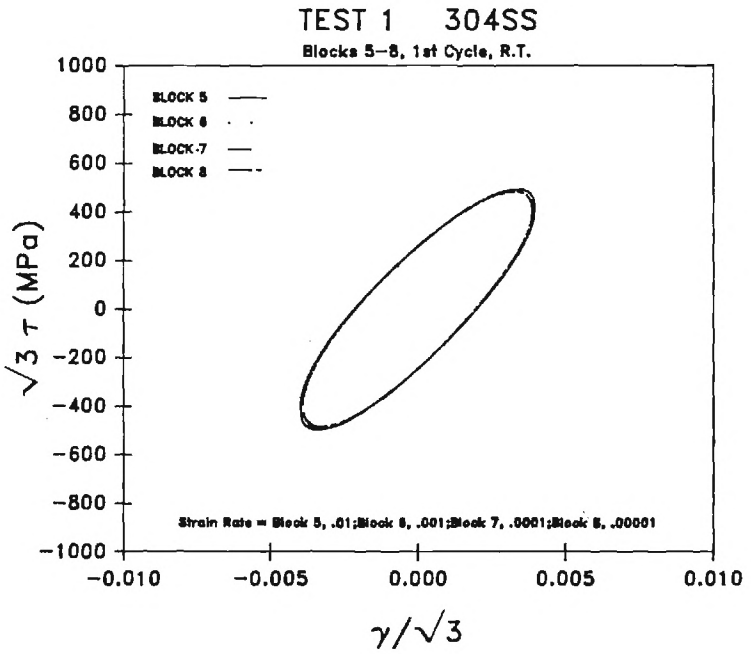
TEST 1 304SS
Blocks 5–8, 1st Cycle, R.T.
BLOCK 5
BLOCK 6
BLOCK 7
BLOCK 8
Strain Rate = Block 5, .01;Block 6, .001;Block 7, .0001;Block 8, .00001
1000
800
600
400
200
0
-200
-400
-600
-800
-1000
-0.010
-0.005
0.000
0.005
0.010
√3 τ (MPa)
γ/√3

Figure 20

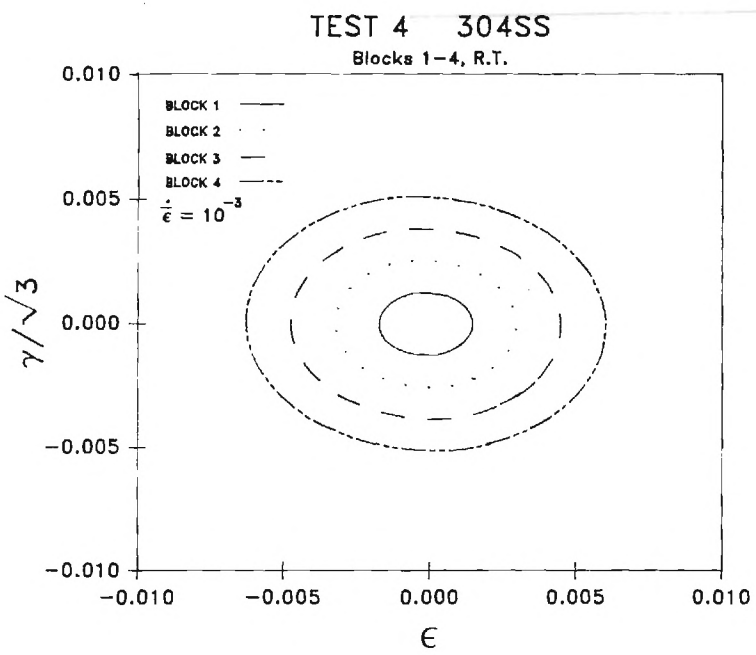
TEST 4 304SS
Blocks 1–4, R.T.
BLOCK 1
BLOCK 2
BLOCK 3
BLOCK 4
$\dot{\epsilon} = 10^{-3}$
$\gamma/\sqrt{3}$
ϵ
0.010
0.005
0.000
-0.005
-0.010

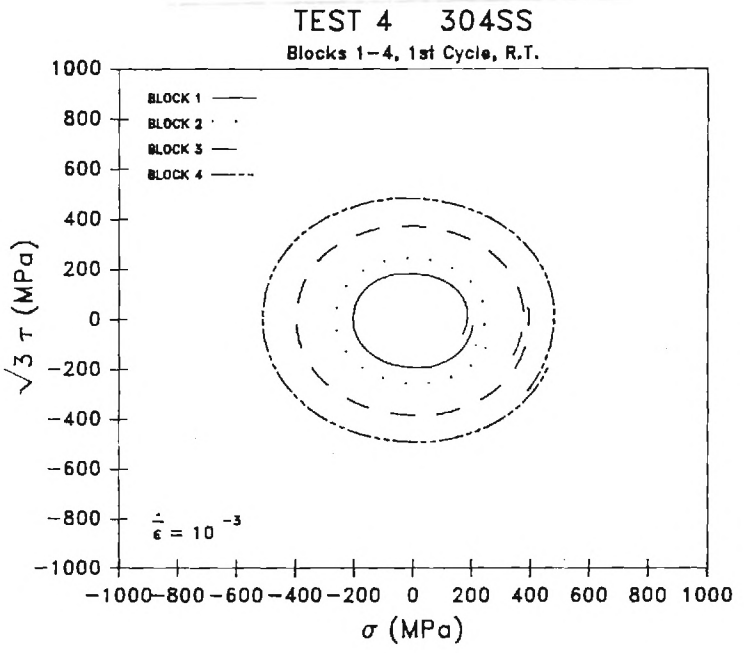
TEST 4 304SS
Blocks 1–4, 1st Cycle, R.T.
BLOCK 1
BLOCK 2
BLOCK 3
BLOCK 4
$\dot{\epsilon} = 10^{-3}$
$\sqrt{3}\,\tau$ (MPa)
σ (MPa)
1000
800
600
400
200
0
-200
-400
-600
-800
-1000

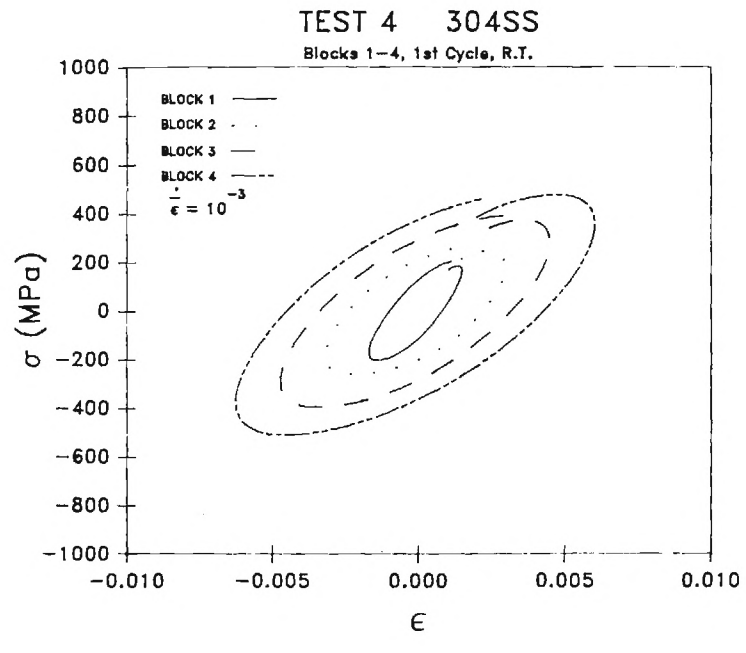
TEST 4 304SS
Blocks 1–4, 1st Cycle, R.T.
BLOCK 1
BLOCK 2
BLOCK 3
BLOCK 4
$\dot{\epsilon} = 10^{-3}$
σ (MPa)
ϵ
1000
800
600
400
200
0
-200
-400
-600
-800
-1000

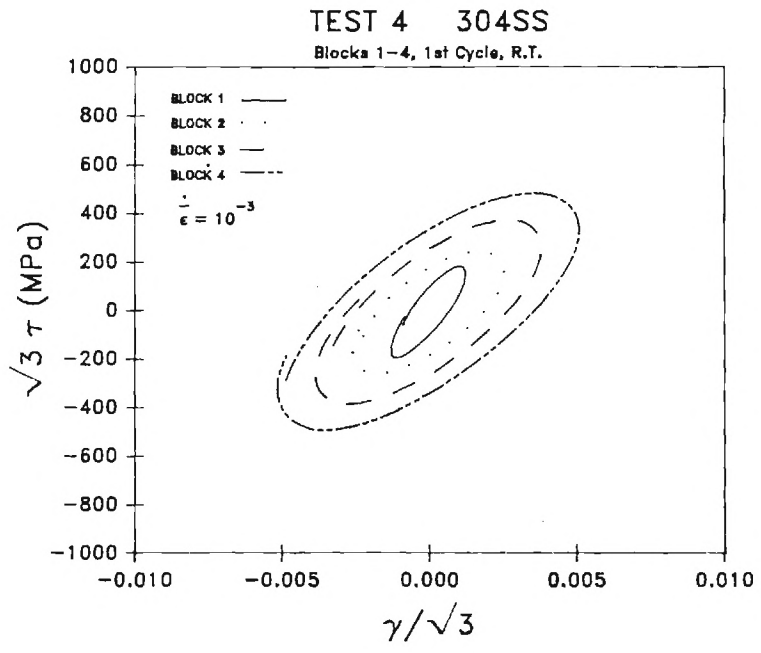
TEST 4 304SS
Blocks 1–4, 1st Cycle, R.T.
BLOCK 1
BLOCK 2
BLOCK 3
BLOCK 4
$\dot{\epsilon} = 10^{-3}$
$\sqrt{3}\,\tau$ (MPa)
$\gamma/\sqrt{3}$
1000
800
600
400
200
0
-200
-400
-600
-800
-1000

Figure 21

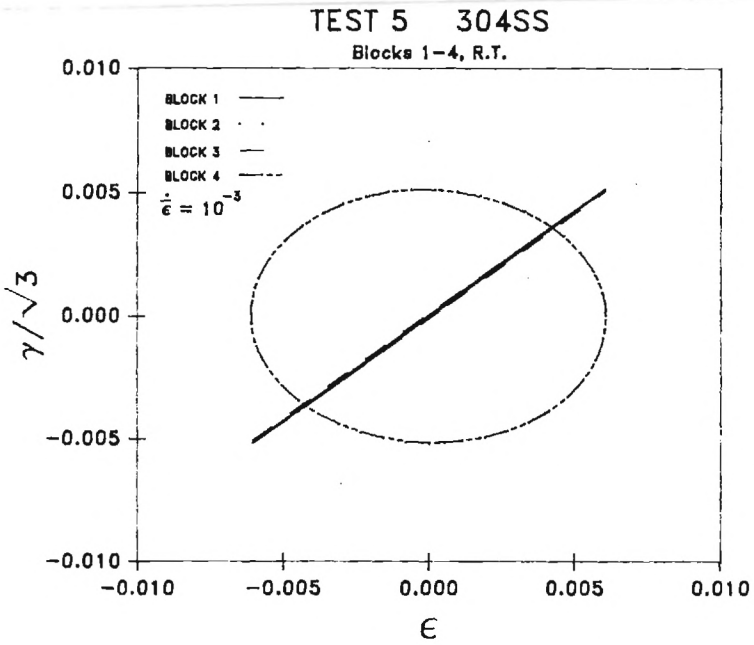
TEST 5 304SS
Blocks 1–4, R.T.
BLOCK 1
BLOCK 2
BLOCK 3
BLOCK 4
$\dot{\epsilon} = 10^{-3}$
$\gamma/\sqrt{3}$
ϵ
0.010
0.005
0.000
-0.005
-0.010

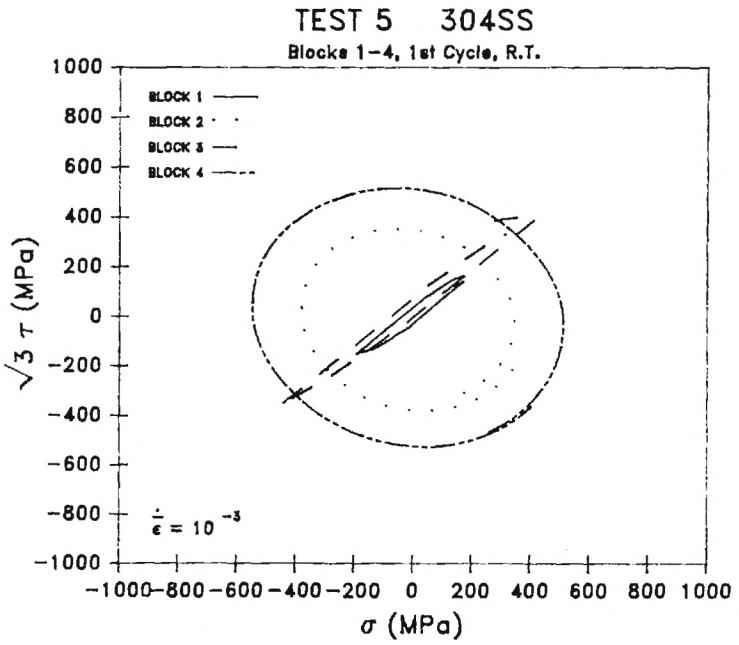
TEST 5 304SS
Blocks 1–4, 1st Cycle, R.T.
BLOCK 1
BLOCK 2
BLOCK 3
BLOCK 4
$\dot{\epsilon} = 10^{-3}$
$\sqrt{3}\,\tau$ (MPa)
σ (MPa)
1000
800
600
400
200
0
-200
-400
-600
-800
-1000

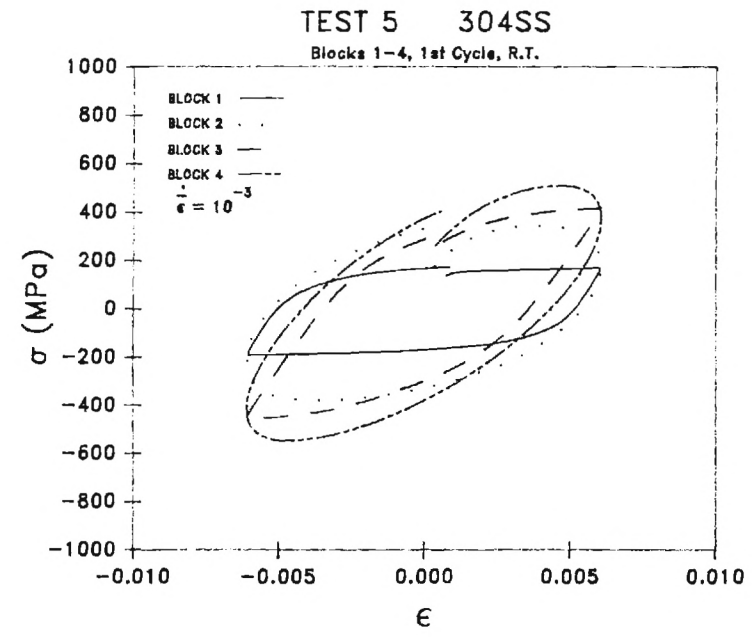
TEST 5 304SS
Blocks 1–4, 1st Cycle, R.T.
BLOCK 1
BLOCK 2
BLOCK 3
BLOCK 4
$\dot{\epsilon} = 10^{-3}$
σ (MPa)
ϵ
1000
800
600
400
200
0
-200
-400
-600
-800
-1000

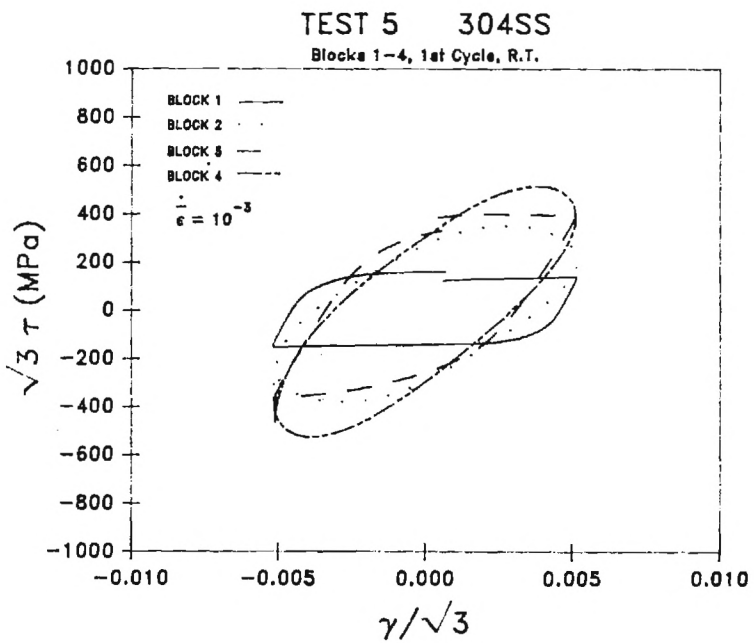
TEST 5 304SS
Blocks 1–4, 1st Cycle, R.T.
BLOCK 1
BLOCK 2
BLOCK 3
BLOCK 4
$\dot{\epsilon} = 10^{-3}$
$\sqrt{3}\,\tau$ (MPa)
$\gamma/\sqrt{3}$
1000
800
600
400
200
0
-200
-400
-600
-800
-1000

Figure 22

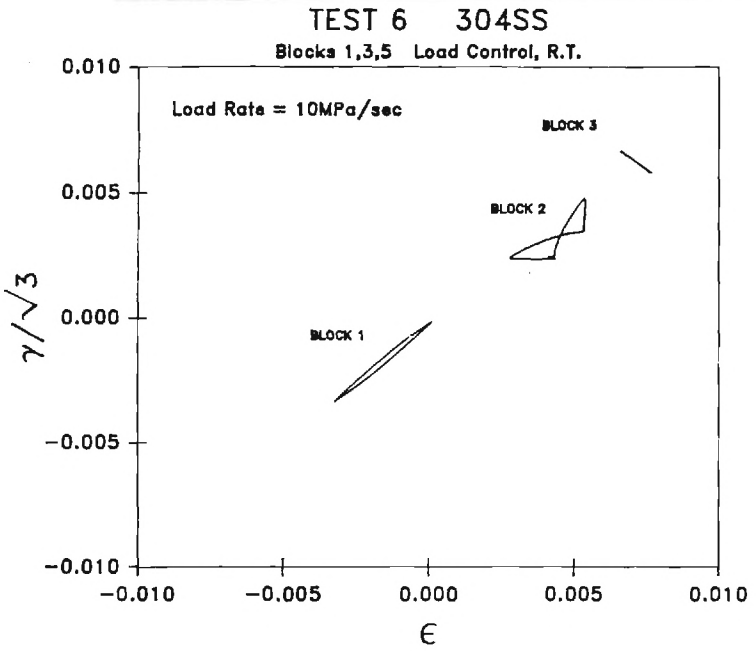
TEST 6 304SS
Blocks 1,3,5 Load Control, R.T.
Load Rate = 10MPa/sec
BLOCK 1
BLOCK 2
BLOCK 3
0.010
0.005
0.000
-0.005
-0.010
γ/√3
-0.010
-0.005
0.000
0.005
0.010
ϵ

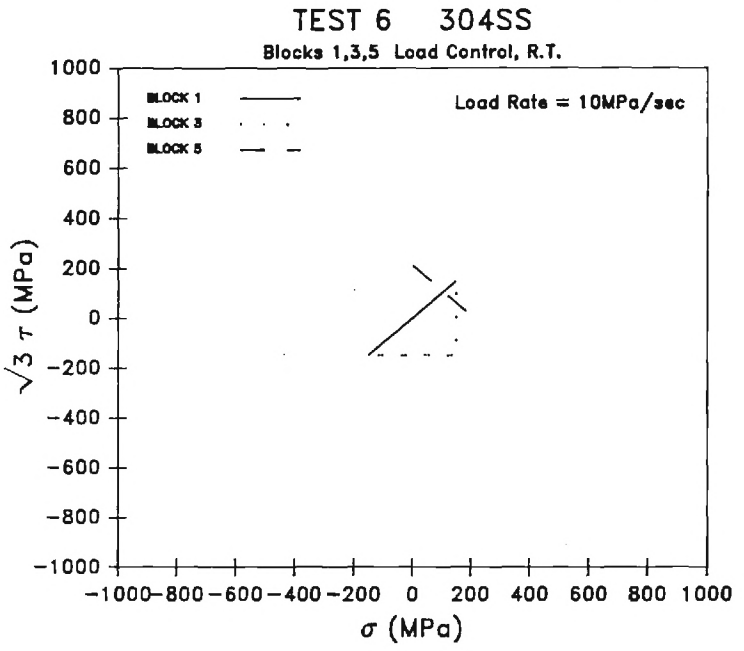
TEST 6 304SS
Blocks 1,3,5 Load Control, R.T.
Load Rate = 10MPa/sec
BLOCK 1
BLOCK 3
BLOCK 5
1000
800
600
400
200
0
-200
-400
-600
-800
-1000
√3 τ (MPa)
-1000 -800 -600 -400 -200 0 200 400 600 800 1000
σ (MPa)

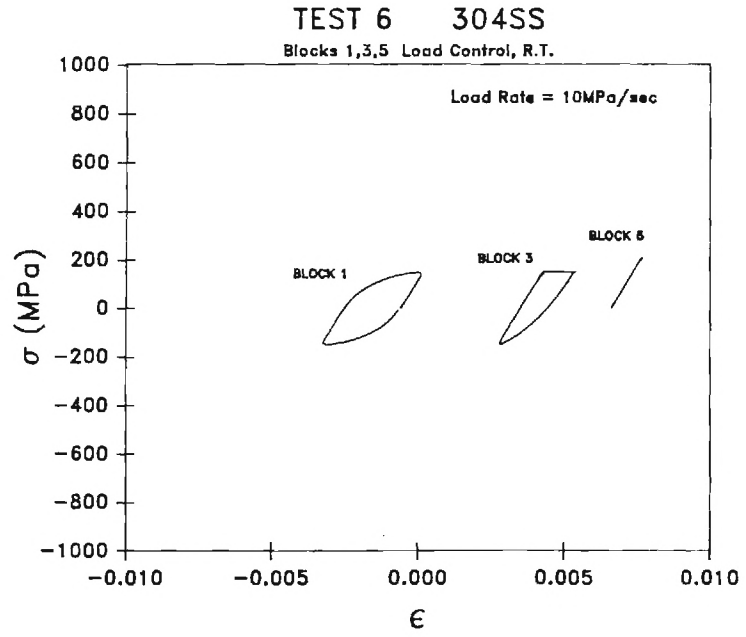
TEST 6 304SS
Blocks 1,3,5 Load Control, R.T.
Load Rate = 10MPa/sec
BLOCK 1
BLOCK 3
BLOCK 5
1000
800
600
400
200
0
-200
-400
-600
-800
-1000
σ (MPa)
-0.010
-0.005
0.000
0.005
0.010
ϵ

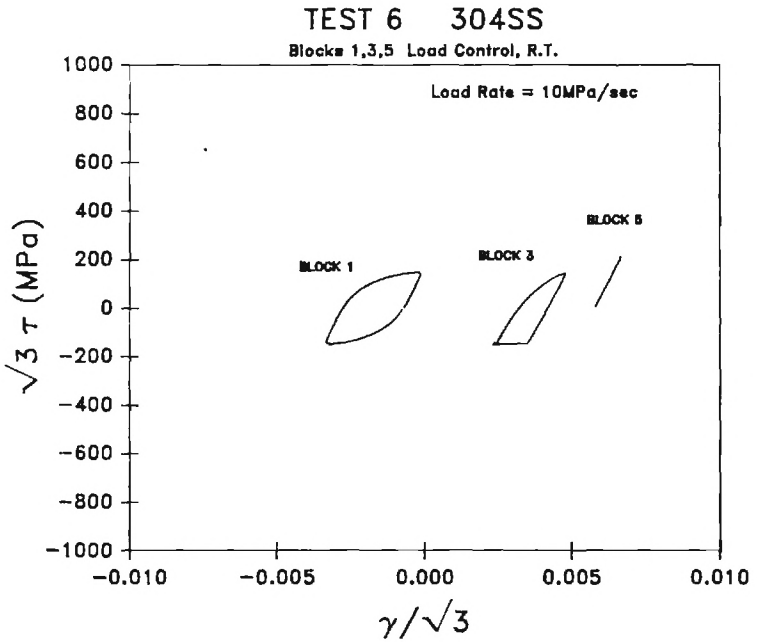
TEST 6 304SS
Blocks 1,3,5 Load Control, R.T.
Load Rate = 10MPa/sec
BLOCK 1
BLOCK 3
BLOCK 5
1000
800
600
400
200
0
-200
-400
-600
-800
-1000
√3 τ (MPa)
-0.010
-0.005
0.000
0.005
0.010
γ/√3

Figure 23

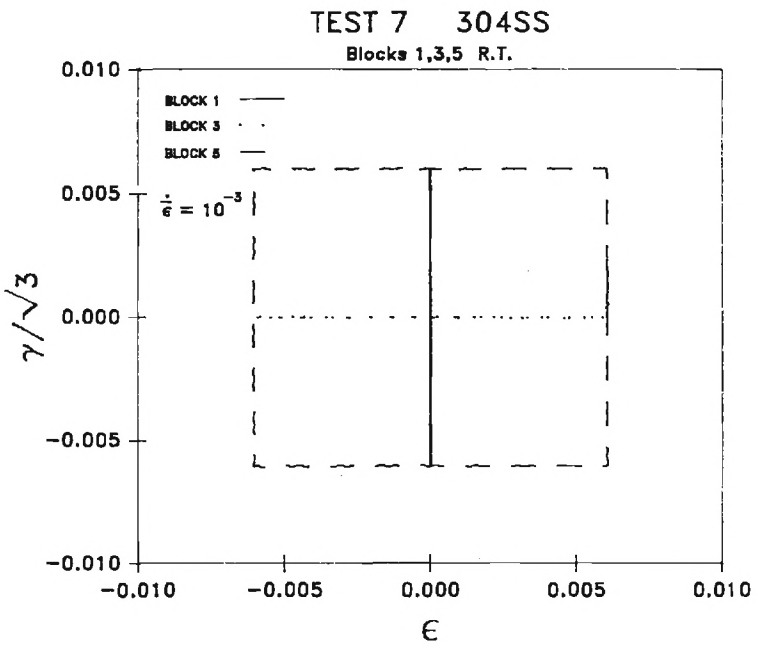
TEST 7 304SS
Blocks 1,3,5 R.T.
BLOCK 1
BLOCK 3
BLOCK 5
$\dot{\epsilon} = 10^{-3}$
$\gamma/\sqrt{3}$
ϵ
0.010
0.005
0.000
-0.005
-0.010

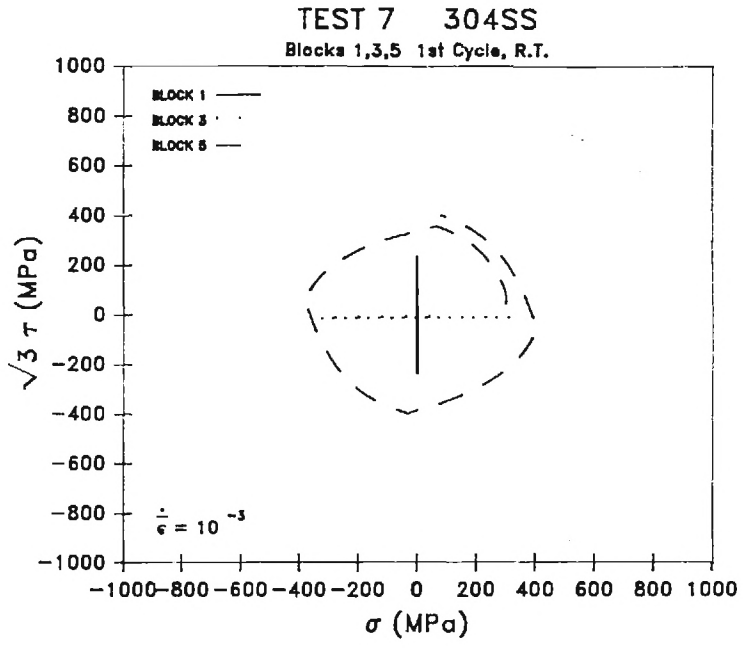
TEST 7 304SS
Blocks 1,3,5 1st Cycle, R.T.
BLOCK 1
BLOCK 3
BLOCK 5
$\dot{\epsilon} = 10^{-3}$
$\sqrt{3}\,\tau$ (MPa)
σ (MPa)
1000
800
600
400
200
0
-200
-400
-600
-800
-1000

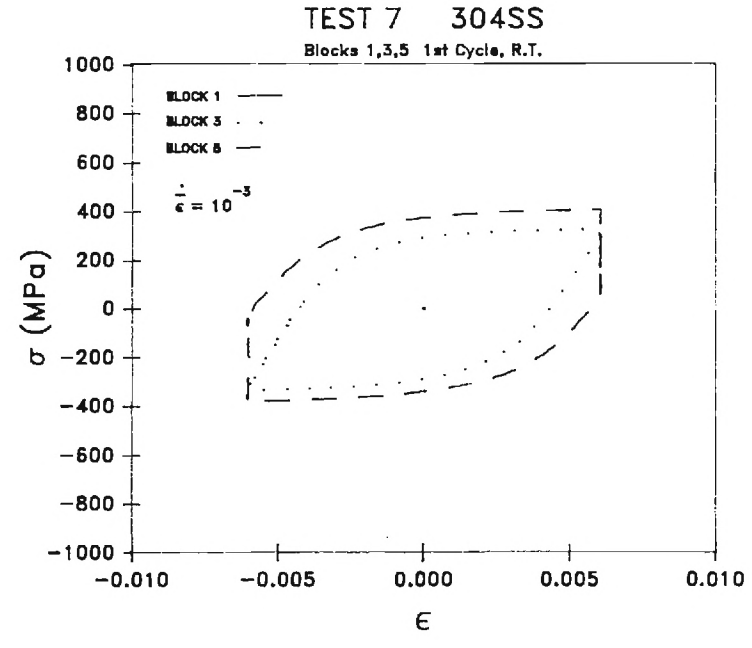
TEST 7 304SS
Blocks 1,3,5 1st Cycle, R.T.
BLOCK 1
BLOCK 3
BLOCK 5
$\dot{\epsilon} = 10^{-3}$
σ (MPa)
ϵ
1000
800
600
400
200
0
-200
-400
-600
-800
-1000
-0.010
-0.005
0.000
0.005
0.010

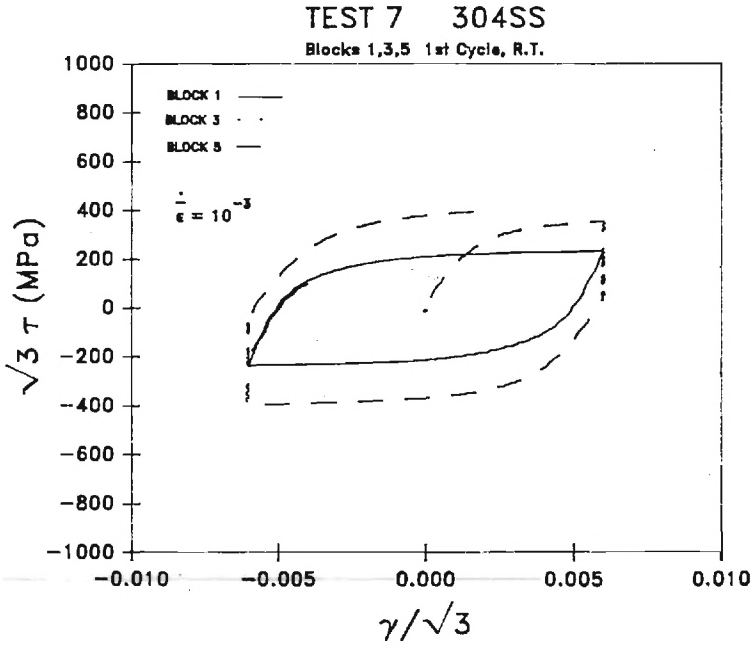
TEST 7 304SS
Blocks 1,3,5 1st Cycle, R.T.
BLOCK 1
BLOCK 3
BLOCK 5
$\dot{\epsilon} = 10^{-3}$
$\sqrt{3}\,\tau$ (MPa)
$\gamma/\sqrt{3}$
1000
800
600
400
200
0
-200
-400
-600
-800
-1000
-0.010
-0.005
0.000
0.005
0.010

Figure 24

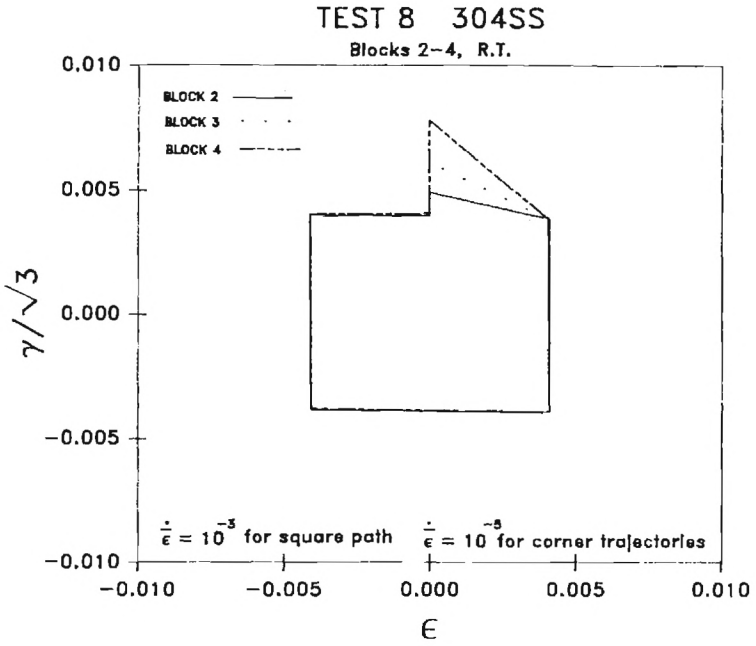
TEST 8 304SS
Blocks 2–4, R.T.
BLOCK 2
BLOCK 3
BLOCK 4
$\dot{\epsilon} = 10^{-3}$ for square path
$\dot{\epsilon} = 10^{-5}$ for corner trajectories
$\gamma/\sqrt{3}$
ϵ

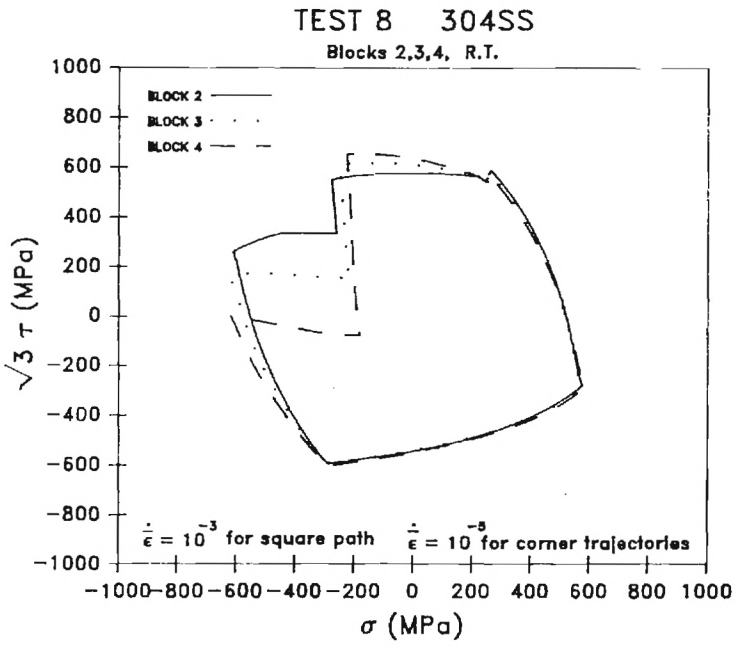
TEST 8 304SS
Blocks 2,3,4, R.T.
BLOCK 2
BLOCK 3
BLOCK 4
$\dot{\epsilon} = 10^{-3}$ for square path
$\dot{\epsilon} = 10^{-5}$ for corner trajectories
$\sqrt{3}\,\tau$ (MPa)
σ (MPa)

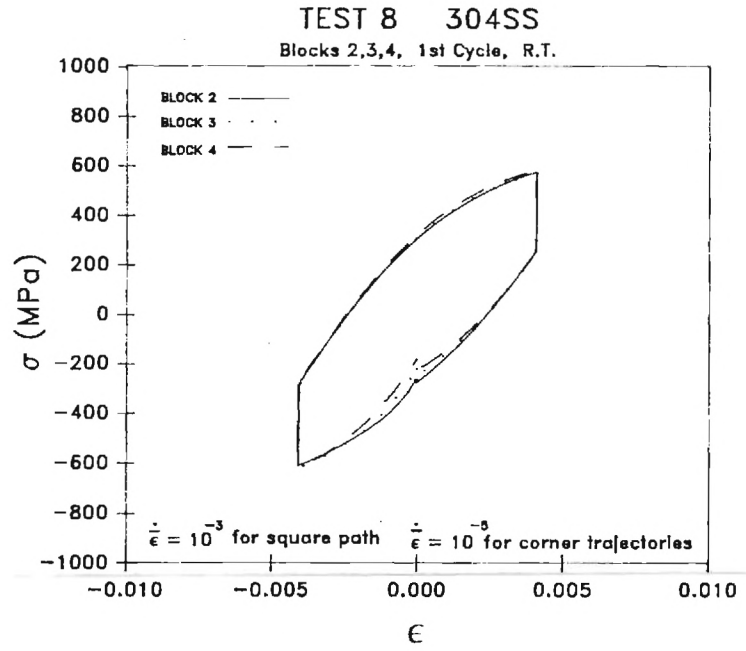
TEST 8 304SS
Blocks 2,3,4, 1st Cycle, R.T.
BLOCK 2
BLOCK 3
BLOCK 4
$\dot{\epsilon} = 10^{-3}$ for square path
$\dot{\epsilon} = 10^{-5}$ for corner trajectories
σ (MPa)
ϵ

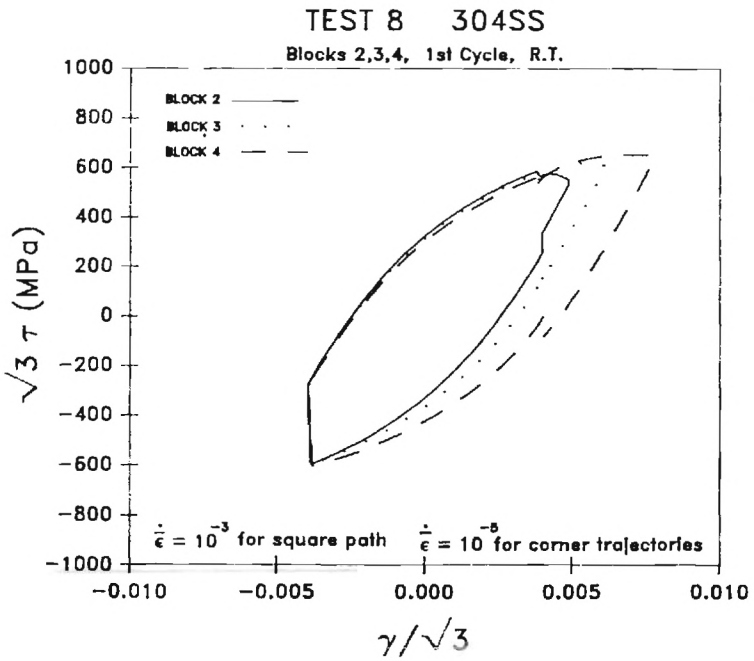
TEST 8 304SS
Blocks 2,3,4, 1st Cycle, R.T.
BLOCK 2
BLOCK 3
BLOCK 4
$\dot{\epsilon} = 10^{-3}$ for square path
$\dot{\epsilon} = 10^{-5}$ for corner trajectories
$\sqrt{3}\,\tau$ (MPa)
$\gamma/\sqrt{3}$

Figure 25

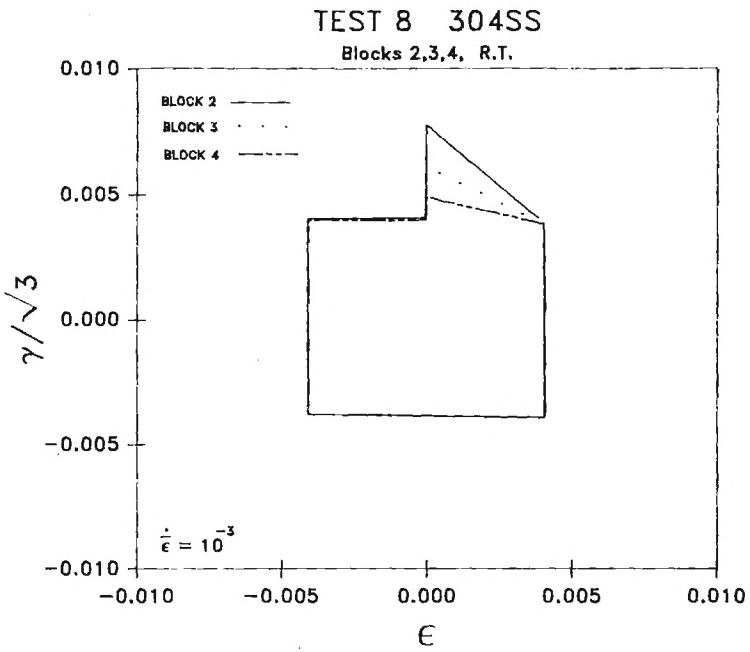
TEST 8 304SS
Blocks 2,3,4, R.T.
BLOCK 2
BLOCK 3
BLOCK 4
$\dot{\epsilon} = 10^{-3}$
$\gamma/\sqrt{3}$
ϵ
0.010
0.005
0.000
-0.005
-0.010

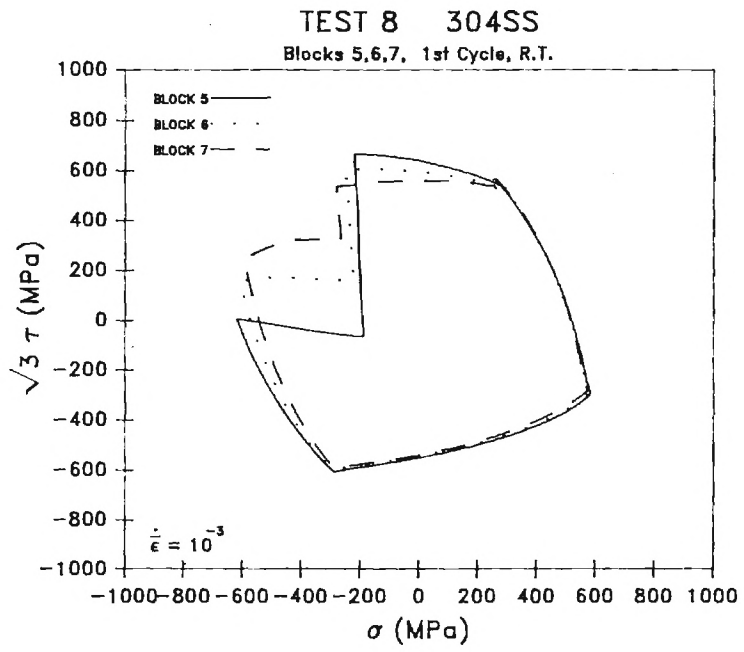
TEST 8 304SS
Blocks 5,6,7, 1st Cycle, R.T.
BLOCK 5
BLOCK 6
BLOCK 7
$\dot{\epsilon} = 10^{-3}$
$\sqrt{3}\,\tau$ (MPa)
σ (MPa)
1000
800
600
400
200
0
-200
-400
-600
-800
-1000

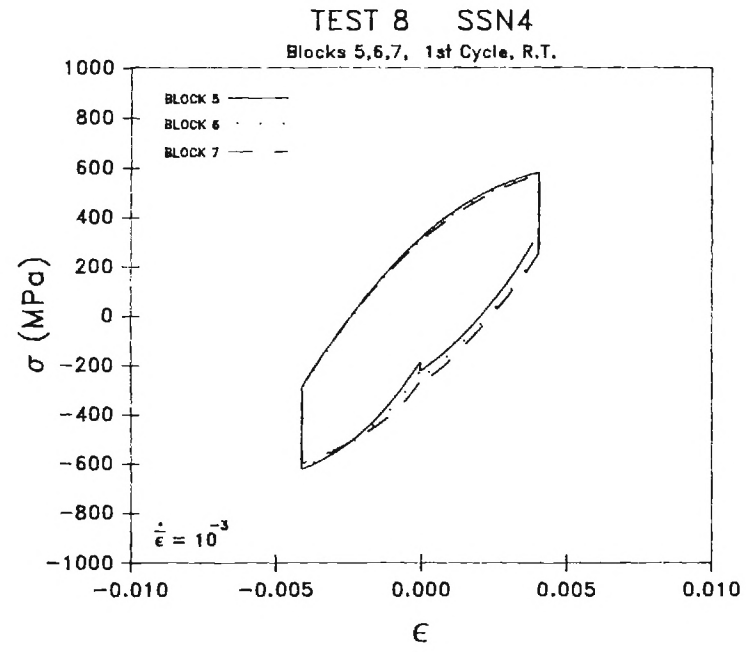
TEST 8 SSN4
Blocks 5,6,7, 1st Cycle, R.T.
BLOCK 5
BLOCK 6
BLOCK 7
$\dot{\epsilon} = 10^{-3}$
σ (MPa)
ϵ
1000
800
600
400
200
0
-200
-400
-600
-800
-1000

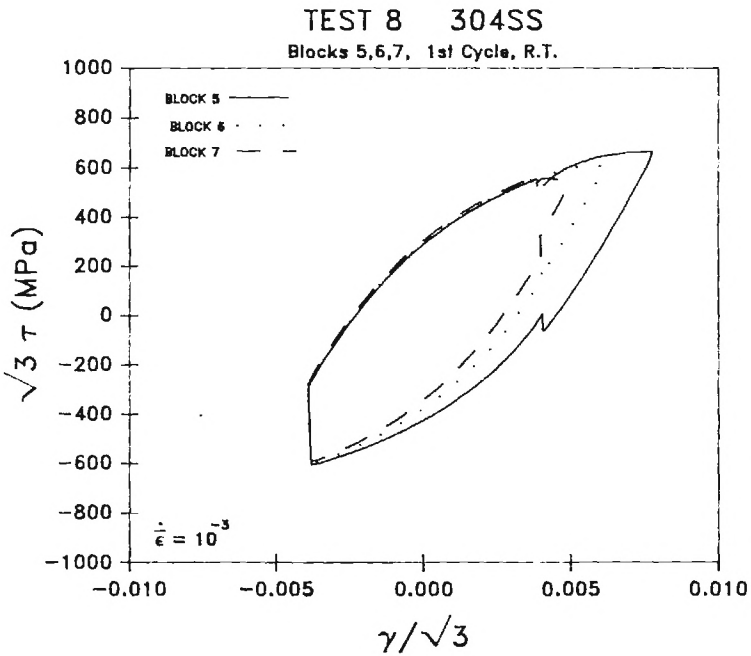
TEST 8 304SS
Blocks 5,6,7, 1st Cycle, R.T.
BLOCK 5
BLOCK 6
BLOCK 7
$\dot{\epsilon} = 10^{-3}$
$\sqrt{3}\,\tau$ (MPa)
$\gamma/\sqrt{3}$
1000
800
600
400
200
0
-200
-400
-600
-800
-1000